

TOWARDS ACCURATE 3D ANALYSIS OF HUMAN MOVEMENT

AN INTEGRATED UWB/MIMU APPROACH



Vinish Yogesh

**TOWARDS ACCURATE 3D ANALYSIS OF
HUMAN MOVEMENT**
AN INTEGRATED UWB/MIMU APPROACH

Vinish Yogesh

The publication of this dissertation was financially supported by Roessingh Research and Development, Roessingh Centrum voor Revalidatie and University of Twente.



**UNIVERSITY
OF TWENTE.**

Cover design: Vinish Yogesh and Sanchana Krishnakumar

Printed by: Ipskamp Printing

Lay-out: Vinish Yogesh

ISBN (print): 978-90-365-6989-7

ISBN (digital): 978-90-365-6990-3

URL: <https://doi.org/10.3990/1.9789036569903>

© 2025 Vinish Yogesh, The Netherlands. All rights reserved. No parts of this thesis may be reproduced, stored in a retrieval system or transmitted in any form or by any means without permission of the author. Alle rechten voorbehouden. Niets uit deze uitgave mag worden vermenigvuldigd, in enige vorm of op enige wijze, zonder voorafgaande schriftelijke toestemming van de auteur

**TOWARDS ACCURATE 3D ANALYSIS OF
HUMAN MOVEMENT**
AN INTEGRATED UWB/MIMU APPROACH

DISSERTATION

to obtain
the degree of doctor at the University of Twente,
on the authority of the rector magnificus,
prof. dr. ir. A. Veldkamp,
on account of the decision of the Doctorate Board
to be publicly defended
on Wednesday 10 December 2025 at 14.45 hours

by

Vinish Yogesh

born on the 26th of March, 1996

in Vythiry, Kerala, India

This dissertation has been approved by:

Promotors

prof.dr. J.H. Buurke

dr.ir. B.J.F. van Beijnum

Graduation Committee:

- Chair / secretary: prof.dr.ir. B.R.H.M. Haverkort
- Promotors: prof.dr. J.H. Buurke
Universiteit Twente, EEMCS, Biomedical Signals
and Systems
dr.ir. B.J.F. van Beijnum
Universiteit Twente, EEMCS, Biomedical Signals
and Systems
- Committee Members: prof.dr.ir. J.R. Buitenweg
Universiteit Twente, EEMCS, Biomedical Signals
and Systems
- prof.dr.ir. G.J.M. Krijnen
Universiteit Twente, EEMCS, Robotics and
Mechatronics
- prof. A. Cereatti PhD
Politecnico di Torino, Department of Electronics
and Telecommunications
- prof. dr. J.H. Van Dieën
Vrije Universiteit Amsterdam
- ir. C.T.M. Baten
Roessingh Research and Development

Permissions for use of images

All adapted or reproduced figures in the General Introduction chapter have been used with proper permissions and in accordance with licensing terms.

Figure	Permission Details
Figure 1.1 (left)	Source: Leonardo da Vinci, <i>Anatomical studies of the shoulder</i> ; Obtained from Wikimedia commons License: Public domain Permission: Reuse permitted without request; attribution included in caption
Figure 1.1 (Right)	Source: Borelli, <i>De motu animalium</i> , Wellcome Collection; Obtained from wellcome collection License: Attribution 4.0 International (CC BY 4.0) Permission: Reuse permitted without request; attribution included in caption
Figure 1.2	Source: Étienne-Jules Marey, <i>Locomotion</i> , (ca. 1870), Reproduced from Abu-Faraj et al. (2015) License: Public domain Permission: Reuse permission conveyed through Copyright clearance center, Inc.; attribution included in caption
Figure 1.4 (Left-Bottom)	Source: AI-generated using OpenAI's DALL·E and edited by author License: Free to use (OpenAI terms) Permission: No permission required; attribution included in caption

Contents

Chapter 1	General Introduction	1
Chapter 2	Integrated UWB/MIMU Sensor System for Position Estimation towards an Accurate Analysis of Human Movement: A Technical Review	21
Chapter 3	UWB Distance Estimation Errors in (Non-)Line of Sight Situations within the Context of 3D Analysis of Human Movement	63
Chapter 4	Novel calibration method for improved UWB sensor distance measurement in the context of application for 3D analysis of human movement	95
Chapter 5	Position estimation based on UWB swarm optimization and comparison against traditional trilateration	123
Chapter 6	Position Estimation with integrated UWB/MIMU sensors in relevance to 3D Analysis of Human Movement	145
Chapter 7	General Discussion	175
	Appendix	200
	Bibliography	208
	Summary	226
	Acknowledgements	238
	About the author and Journal Publications	244
	Progress Range	248

Chapter 1

General Introduction



1.1 Clinical context and motivation

Human movement and mobility are fundamental aspects of daily life, encompassing activities such as walking, running, and other forms of physical activity that enable individuals to interact with their environment. Efficient movement relies on the complex coordination of the musculoskeletal, nervous, and cardiovascular systems [1]. Impairments in gait and mobility can arise from various conditions, including musculoskeletal disorders, osteoarthritis, and neurological conditions such as stroke or spinal cord injuries [1-4]. These impairments can significantly impact an individual's ability to perform everyday tasks, leading to decreased independence and quality of life.

“Lack of activity destroys the good condition of every human being, while movement and methodical physical exercise save it and preserve it.” - Plato

Plato's insightful words emphasize the importance of physical movement and physical activity for a human to live a healthy life. Mobility impairments are associated with higher morbidity and mortality rates, contributing to increased risks of chronic pain, obesity, cardiovascular disease, and mental health issues such as depression and anxiety [5,6].

Physical rehabilitation is a critical component of healthcare and a primary solution for addressing mobility impairments, aiming to restore function and improve quality of life through targeted therapeutic interventions [7]. Rehabilitation encompasses a range of therapies, including physical therapy, occupational therapy, and specialized exercises designed to improve strength, flexibility, balance, and coordination. For instance, rehabilitation for injuries such as ACL involves structured exercise programs to restore joint (knee) stability and strength [8], while osteoarthritis treatment focuses on pain management and joint function improvement through physical therapy and assistive devices [7,9]. By addressing the underlying causes of mobility impairments and promoting optimal movement patterns, rehabilitation not only reduces the immediate impact of these conditions but also mitigates long-term health consequences, enhancing overall well-being.

In order to allow patients to rehabilitate efficiently, it is essential for rehabilitation clinicians to determine the functional status of the joints and to be able to monitor progression during treatment [10]. Instrumented Gait analysis based on optical motion capture systems provides quantitative insights into functional status, thereby aiding clinicians in decision-making and treatments [11]. However, these instrumented optical motion capture systems are restricted to laboratory settings, are very expensive, and are complex to operate, requiring personnel with specialized training. Additionally, the process is time-consuming due to manual post-processing steps such as marker labeling and gap filling, limiting their integration into routine rehabilitation sessions. Therefore, they are not widely used in clinical practice and remain primarily as research tools [12], benefiting only a limited number of patients. In current clinical rehabilitation settings, this determination of functional status is mostly made based on visual observations by a rehabilitation clinician. The rehabilitation clinician can substantiate the visual observations with the results of several standard tests, such as the six-minute walk test, sit-to-stand test, and single-leg stance test. The outcome measures that these tests provide are global and do not provide insight into the underlying mechanisms causing the impairment.

To provide the best possible service to patients who are rehabilitating, it is important to use measurements to gain insight into the kinematics and kinetics, such as the joint angles and the net flexion moment, respectively, of the joint being treated [3]. For example, in patients suffering from knee osteoarthritis, it is important to gain insight into the relative foot placement in relation to the pelvis and the knee abduction and adduction angles [4,5]. The information on kinematics could help them optimize internal load distribution within the knee joint, such that the load within the affected knee is shifted and, as a consequence, slows down further deterioration of the joint. For example, one of the relevant parameters in this context is the foot progression angle, which has been shown to influence medial knee loading and could be modified as a therapeutic intervention, as demonstrated in the work of Wouda et al., 2021 [13]. These kinematic parameters play an important role in the rehabilitation clinician's current thinking process and decision-making, but can only be estimated very indirectly from clinical observations.

In current rehabilitation practice, most decisions on the treatment plan and the effect of the treatment are based on clinical visual observations of the rehabilitation

clinician. Providing them with more accurate objective measurements is expected to significantly contribute to improved clinical decision-making, resulting in:

- An increased chance/possibility of learning how to improve treatment by statistically studying the collective body of acquired monitoring data of all patients [14]
- Decrease in the required number of treatments [14]
- Decreased pressure on the healthcare system and decreased healthcare costs by a reduced number of treatments, improved quality of treatments, and the future possibility of the potential of partial self-care [15]

Introducing measures of human movement to the primary rehabilitation setting could potentially help in better decision-making based on quantitative data, providing insights into patient function. Utilizing these data with regard to the health situation of the patient can support more individualized treatments, thereby reducing healthcare costs and speeding up recovery [15], allowing the patient to participate in society more quickly. However, this potential remains largely unrealized due to limitations in current tools, especially their cost, complexity, and limited applicability outside research environments. A promising pathway forward lies in developing practical and low-cost technologies that can support accurate quantitative human movement assessment in clinical and home-based settings. Wearable sensor systems, in particular, offer a compelling solution for enabling more accessible and ambulatory analysis of human movement [16]. However, they have not yet been fully adopted in clinical practices due to limitations in accuracy. This PhD thesis contributes to the field of wearable 3D analysis of human movement by investigating core technological components that could enable the clinical translation of wearable sensors, where the specific focus is on improving body segment position estimation capabilities through novel combinations of wearable sensing technologies.

This chapter first provides an overview of human movement analysis, outlining the fundamental concepts and significance of studying human movement. It then explores the current tools and systems available for analyzing human movement, including their technological advancements and applications. This is followed by a detailed examination of these systems, focusing on their use in clinical settings and the latest trends in the field. The discussion then shifts to identifying the gaps in both research and clinical practice, highlighting the limitations and challenges faced

by existing movement analysis systems. Finally, the chapter presents the primary goal of the thesis, explaining the research objectives and the methodology employed to achieve these goals.

1.2 Human movement analysis

Human movement analysis is the systematic study of human motion through diverse observational and measurement techniques. Human movement analysis provides objective data about the movement parameters and strategies used, providing a better indication of the quality of human movement [16]. The field of human movement analysis combines principles from biomechanics, physiology, and engineering to understand how the body moves and functions. It plays a crucial role in healthcare, sports, and ergonomics by providing detailed insights into human motion. In clinical settings, it could be used to assess and diagnose movement disorders, plan and evaluate rehabilitation protocols, and monitor progress. For example, gait analysis helps in the management of conditions like cerebral palsy and post-stroke rehabilitation [11]. In sports science, it optimizes performance and reduces injury risk by analyzing athletes' techniques and biomechanics [17]. Ergonomics benefits from movement analysis by designing tools and workspaces that enhance human performance and prevent musculoskeletal injuries [18].

The history of movement analysis dates back more than two millennia, with early observations of animal movement recorded by Aristotle (384-322 B.C.) [19]. He developed theories on the control of animal movement based on his observations. The Renaissance period marked a significant leap forward as Leonardo da Vinci (1452-1519) conducted anatomical studies on the human body by dissections of cadavers [20]. The anatomical sketches of Leonardo not only highlight the surface anatomy but also delve into the underlying mechanisms, offering a comprehensive view that has contributed significantly to the fields of art, medicine, and anatomy (Figure 1.1-Left). Andreas Vesalius (1514-1564) conducted similar anatomical studies, deepening knowledge of human body structure and function. He is also known as the “founder of modern anatomy” for his significant contributions to human anatomical studies [21]. In the 17th century, Galileo Galilei (1564-1642) provided the foundation for modern principles of motion. Giovanni Alfonso Borelli (1608-1679) utilized the motion principles of Galileo to understand human

locomotion, incorporating mathematics and physics (Figure 1.1-Right). He was the first to compute joint forces by applying mechanical principles to human movement, and Borelli is now considered the “Father of Biomechanics” [22]. René Descartes's (1596-1650) and Sir Isaac Newton’s (1643-1727) Enlightenment-era contributions further solidified this approach, describing the body as a mechanical system governed by laws of motion.

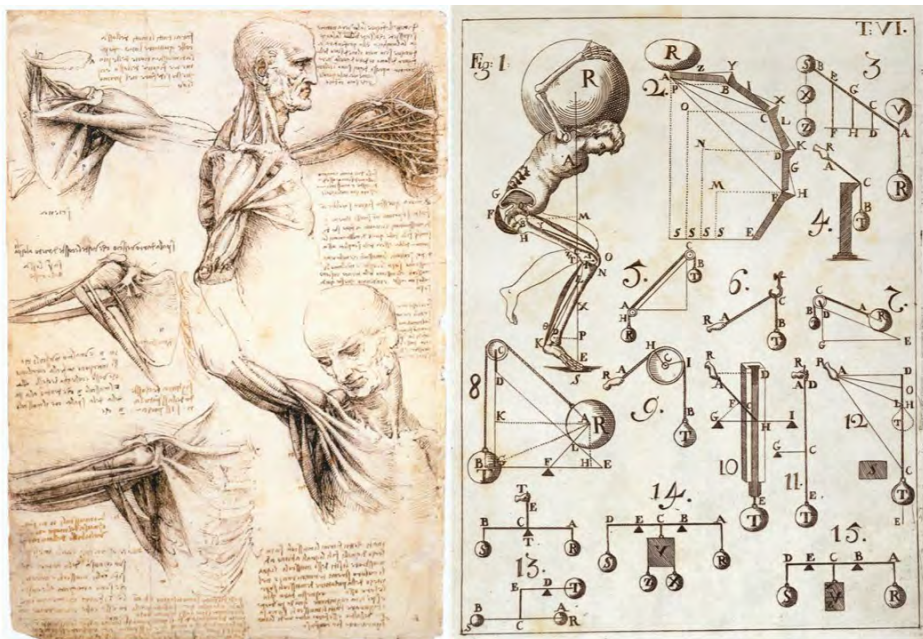


Figure 1.1: (Left)-Sketches by Leonardo da Vinci on human shoulder muscles and the bones, emphasizing intricate anatomical details. Source: Leonardo da Vinci, ‘Anatomical studies of the shoulder’. (Right)-Borelli’s depictions of human biomechanics. Source: Giovanni Alfonso Borelli, ‘De motu animalium’.

The 18th and 19th centuries saw empirical observations and early mathematical models by scientists like Paul J. Barthez and Wilhelm and Eduard Weber contributing to the understanding of gait mechanics [23]. Innovations in cinematography in the late 19th century led to significant advances in movement analysis. Étienne Jules Marey and Eadward Muybridge (1830-1904) provided the first visual analysis of human and animal locomotion, with the use of photography in studying motion dynamics [24]. Marey invented the chronophotograph, and he also built a photographic gun to capture multiple images of a moving subject at 12 frames per second. He utilized a black suit with reflective strips to capture each of

the segments of the human subject, creating a repetitive stick diagram (Figure 1.2). Advances accelerated in the early 20th century with researchers such as Richard Scherb (1880-1955) and Plato Schwartz (1892-1965) developing methods to study muscle action and plantar pressures during gait [25]. The mid-20th century brought significant breakthroughs as Jacqueline Perry and John V. Basmajian pioneered quantitative gait analysis techniques [26] and electromyography [27], providing insights into both normal and pathological aspects of human movement.

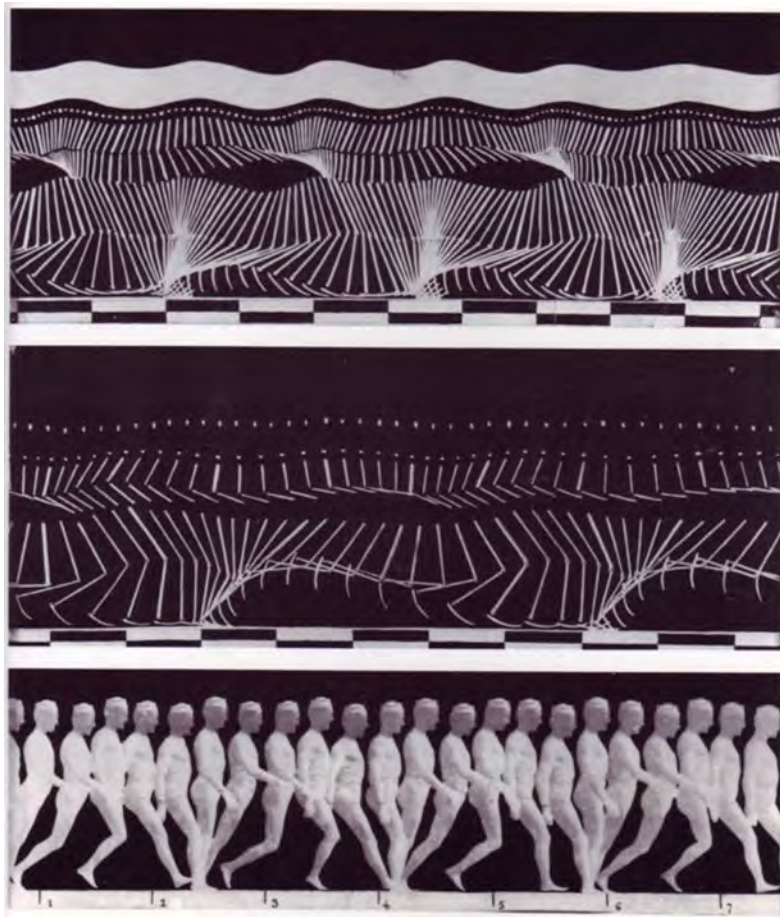


Figure 1.2: Étienne-Jules Marey's chronophotographic sequence of human locomotion, where multiple exposures of a single person's gait are recorded on one plate, visualizing the phases of movement. Source: Public domain image by Marey, 'Locomotion' ca. 1870–1880 reproduced from [22]

The late 20th century witnessed a revolution with the introduction of digital motion capture technologies [28] by David H. Sutherland, John L. Hagy, and David A. Winter. These technologies enabled precise measurement and analysis of human movement, ushering in a new era of biomechanics and clinical gait analysis. The article of Abu-Faraj et al., 2015 [22] provides a detailed history of the evolution of human movement analysis from early 1000 B.C. till the late 20th century. Human motion analysis has evolved from ancient philosophical investigations and empirical observations to sophisticated scientific methodologies. Each era contributed foundational knowledge and technological advancements that have collectively shaped our current understanding of human locomotion. The latest advancements in technology combined with the vast knowledge accumulated over centuries today allow the 3-dimensional analysis of human movement.

1.2.1 Traditional laboratory-based movement analysis

Digital motion capture technology and computer-vision techniques form the basis for the modern-day traditional laboratory-based 3D analysis of human movement (3D AHM). These human movement analysis systems consist of optical marker systems and force plates for the measurement of the kinematic and kinetic parameters of human movement [29,30]. The optical marker system utilizes several digital or infrared cameras to capture images of human movement through the use of reflective markers placed on the human subject (Figure 1.3). These systems are effective in tracking the trajectories of the marker placed on the body with sub-centimeter accuracy [31,32]. These systems are also considered to be the gold standard for measuring body segment positions, orientations, and various other biomechanical parameters like joint angles, base of support, foot clearance, foot progression angles, temporal-spatial gait parameters, range of motion, and trajectories of end-effectors. Using inverse dynamics and joint biomechanical models, joint moments and forces can be estimated with ground reaction force data from force plates serving as input for these computations [33].

Despite the optical motion capture systems being accurate and clinically relevant, these setups are usually expensive, large, and restricted to a fixed location in a laboratory environment [12]. In addition, they also require lengthy preparation

before measurement and complex processing after the measurement, which also includes a manual labelling task, thus requiring longer processing times.



Figure 1.3: A typical laboratory-based optical motion capture system for human movement analysis (Left). A subject with reflective markers strapped onto the body for movement analysis (Right)

It is essential to place the reflective markers precisely on specific anatomical landmarks (Figure 1.3-Right), and a study by McGinley et al. has shown that the inter-session reliability of the marker placement was inconsistent even when the subject and rater were the same [34]. To be able to correctly estimate kinetics, the patient has to place an entire footstep on the force plate without touching the area around the force plate. This constraint may lead patients to (unconsciously) adjust their gait pattern to target the force, potentially altering their natural gait pattern [35]. As the number of trials a patient can perform is limited, and since not every step is successfully landed on the force plates, this yields only a few successful recordings of steps with complete kinematics and force data per session. Alternatively, the force plates are mounted on treadmills to collect data over multiple steps, however, they restrict the person's motion to a straight line. The relevance of how walking on a treadmill differs from walking on solid ground, and whether these differences affect the motion analysis outcomes, remains under debate. These limitations, along with the need for human movement analysis in more natural conditions or other settings than the gait laboratory, such as in rehabilitation therapy or daily-life settings, have directed the research of human movement analysis towards more affordable and wearable sensing alternative methods.

1.2.2 Ambulatory human movement analysis

The technological advancement in inertial sensing has led to the development of Micro Electro Mechanical Systems (MEMS) based Magnetic Inertial Measurement Units (MIMUs), which allow analysis of the kinematics and kinetics, with a cost-effective setup [36]. These wearable MIMU sensors have gained popularity due to their cost-effectiveness, user-friendliness, and compactness. The MIMUs consist of a 3-axis linear accelerometer, a 3-axis rate gyroscope, and a 3-axis magnetometer, which can concurrently measure along 3 axes linear acceleration, angular velocity, and the local magnetic field vector expressed in the sensor’s orthogonal reference frame. These sensors are available both commercially and in custom-built (non-commercial) formats [16]. The commercially available MIMUs, such as Xsens, provide pre-calibrated, wireless or wired sensor units, along with proprietary software for data acquisition, real-time visualization, and post-processing (Figure 1.4). Non-commercial research-grade MIMU sensors may include open-source hardware and software platforms, offering greater flexibility in algorithm development and sensor integration. These sensors are usually mounted on the body through pockets in Lycra measurement suits, elastic bands, Velcro straps, double-sided adhesive tapes, or with medical adhesive tapes, and in some cases with a combination of these methods [37].

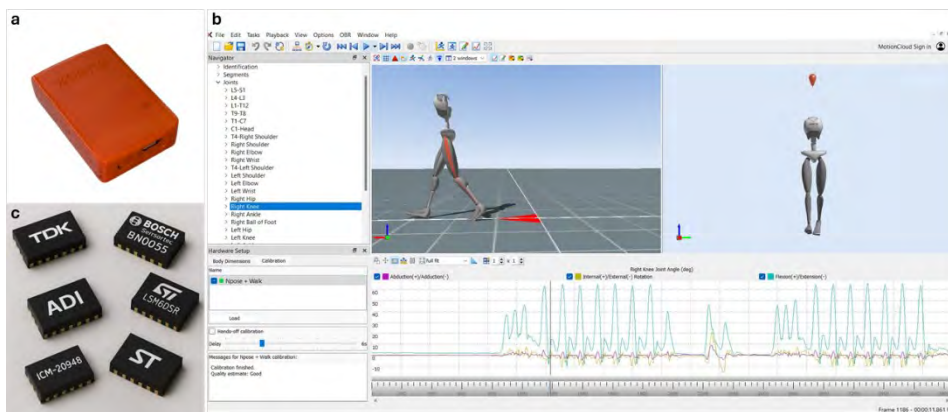


Figure 1.4: (a) Photograph of a single MIMU sensor unit from Xsens Technologies B.V. (b) Screenshot from a commercially available wearable human movement analysis software. (c) Image of 6-axis MIMU sensor chips typically used in the custom-built sensors (AI-generated image).

Using MIMUs for accurate estimation of 3D orientations and rotational kinematics is generally possible by applying sophisticated data fusion algorithms such as Extended Kalman Filters [38,39]. This is achieved by utilizing the redundant movement data obtained from the three sensor modalities of the MIMU [40]. For instance, gyroscopes provide accurate short-term angular velocity measurements, while accelerometers and magnetometers serve as references to correct long-term drift, thus creating a functional redundancy in estimating orientation. However, the accuracy achieved in absolute orientation is affected when the observability of the two natural references (the gravitational force field and the Earth's magnetic fields) used is compromised. This happens for the gravitational field only in specific situations of movement involving prolonged quasi-static accelerations in a magnitude close to, or larger than, gravity, e.g., when making long bends in vehicles or speed skating. This usually does not occur in regular analysis of human movement in rehabilitation or physical therapy. However, the magnetic field observability is often compromised when measuring close to substantial masses of ferromagnetic materials, which frequently occurs in indoor usage, e.g., close to concrete floors [41].

Besides rotational kinematics, 3D linear displacement kinematics can be derived from the MIMU data. With a known starting position, the relative positions can be estimated from the displacement kinematics. However, achieving consistent accuracy in 3D position estimation is challenging due to the substantial integration drift errors caused by the required double integration of the free acceleration signal [42,43]. Unlike the angular estimates, there are no additional displacement data from the sensor system that could be used to counteract this drift through data fusion methods. Only in a few very specific use cases, these errors can be mitigated by using assumptions on aspects of the movement performed by the human. One example is the zero velocity update (ZUVPT) approach, which exploits the fact that in regular (straight) walking, there is a short moment of zero velocity in the foot in each step in the stance phase of gait [44]. Another approach is applying biomechanical constraints to joint kinematics using a biomechanical model of the human body, which incorporates subject-specific parameters such as segment lengths, joint axes, and degrees of freedom [45]. However, these are restricted to the foot for ZUVPT methods and limited to healthy subjects for biomechanical constraints, since patients

often show deviating anthropometrics and exhibit subject-specific movement patterns that severely violate these assumptions.

1.3 Human movement analysis in the current clinical setting

The human movement analysis tools, both the laboratory-based optical motion capture systems and wearable sensor systems, are widely used for clinical research. These clinical research/studies are not regarded as clinical testing because the criteria for clinical research and clinical testing are fundamentally different [29]. Specifically, clinical testing is to make clinical decisions for the patient being tested, while clinical studies are mostly about the conditions affecting patient groups and/or studying the effects of interventions, etc. In the review article by Baker., 2006 [29], he introduces several criteria for biomechanical measures that need to be achieved for the successful use of human movement analysis tools in a clinical setting. The criteria reported by Baker [29] are as follows,

The biomechanical measures of human movement analysis tools should be

- Reproducible
- Stable
- Accurate
- Appropriately validated
- Capable of distinguishing between normal and abnormal
- Must not alter the function it is measuring
- Reported in a form analogous to accepted clinical concepts
- Cost-effective

Optical motion capture systems are the most accurate among all the currently available human movement analysis systems. The relatively high accuracies achievable by these optical motion capture systems make them clinically relevant and are also considered to be sufficient for the clinical decision-making process [46,47]. Despite these systems being highly accurate, only some specialized rehabilitation centers have these laboratory-based optical motion capture systems (e.g., a Vicon or Motion Analysis gait analysis system). These are attributed to the systems not

meeting a few of the criteria indicated by Baker, namely cost-effectiveness, reproducibility, and not altering the function being measured. The reproducibility issues are mainly linked to the marker placement errors, which depend mainly on proper technician training and protocol adherence. Therefore, the reproducibility issue can be avoided by having a highly trained technician and standardized protocols. Concerns about the system altering the function intended to be measured are generally limited to specific movement scenarios. For instance, the patient must step in the middle of a force plate in the measurement laboratory and ensure to remain in the field of view of the cameras, which often influence/alter the natural gait pattern of the patients. The most significant barrier is the high cost linked to the setup and maintenance of these measurement systems, which makes them too expensive to be purchased and managed by a first-line physiotherapy practice. Almost all rehabilitation centers that use these systems are only funded from research budgets and are used mostly for research purposes [12].

The alternative wearable human movement analysis systems are cheaper, portable, and do not alter the function being measured. However, they are susceptible to errors in absolute orientation estimation in situations where the observability of the two natural references is compromised, as explained in Section 1.2.2. Similarly, they are susceptible to errors in estimating positions due to integration drift. Although some sophisticated algorithms improve the accuracy and consistency of orientation estimates, they are based on assumptions of general human movement, which often do not apply to patients who usually have abnormal movement. While for position estimation, they still have a lower accuracy and consistency compared to optical motion capture systems. Because of these reasons, currently, there are no validated ambulatory/wearable medical measuring instruments with which this insight can be obtained objectively, accurately, and reliably suited for use in primary rehabilitation care. Therefore, there is a need for a substantially more accurate and highly consistent wearable system for ambulatory clinical 3D AHM.

1.4 Research on improving ambulatory human movement analysis

There is continuous ongoing research that is aimed at improving the accuracy and consistency of the MIMUs for human movement analysis. For angular data, most of

these improvements involve using more sophisticated algorithms that apply various assumptions and constraints to mitigate error growth, as briefed in Section 1.2.2. Other approaches focus on the controlled use of sensors to avoid situations that cause errors, such as restricting measurements to short durations or few steps, minimizing exposure to ferromagnetic disturbances, and sensor placement strategies [16,48]. Consequently, the accuracy of angular kinematics has significantly improved due to redundant data from multiple sensor sources within the MIMU. However, the 3D position estimates derived from the 3D linear displacement kinematics remain susceptible to large errors and often show temporal instability due to drift accumulation. Also, advancements in algorithm optimization are nearing their limit. Therefore, exploring the addition of supplementary sensors to MIMUs, which can provide redundancy for 3D positional data, is a promising alternative [3]. The addition of additional sensors could provide a better data fusion approach with limited assumptions on the biomechanics of the subject and/or behavior, facilitating a more accurate position estimation in 3D analysis of human movement that could work for patients.

The most commonly proposed sensors for estimation of positions (both in space and on-body) that could be integrated along with the MIMU sensors are, wireless communication modalities such as Wi-Fi, ZigBee, Bluetooth, radio frequency identification (RFID), Ultra-wideband (UWB) [49-53] and other sensors such as GPS [54], ultrasound [55] and infrared (IR) sensors [56] (Figure 1.5). Among the multitude of sensors, the GPS is not suitable for indoor settings [57], which is the common environment for clinical human movement analysis. Within the wireless communication modalities, UWB is considered to be the best in performance and is known to achieve the highest accuracy [58-60], while others are known to have lower accuracy due to external interferences such as reflections and Multi-path interference [61,62]. Apart from UWB, Ultrasound, and IR sensors are also accurate enough to integrate with MIMUs. However, the use of ultrasound in human movement analysis is restricted due to interference issues that arise when multiple ultrasound tags are used simultaneously [63,64], and the applicability of IR is constrained by the necessity for direct Line of Sight (LOS) conditions [63]. Out of the three suitable sensors for integration with MIMU, only IR and ultrasound sensor-integrated MIMUs have been utilized directly for human movement analysis applications, while UWB-

integrated MIMU sensors have been applied exclusively for human tracking applications.

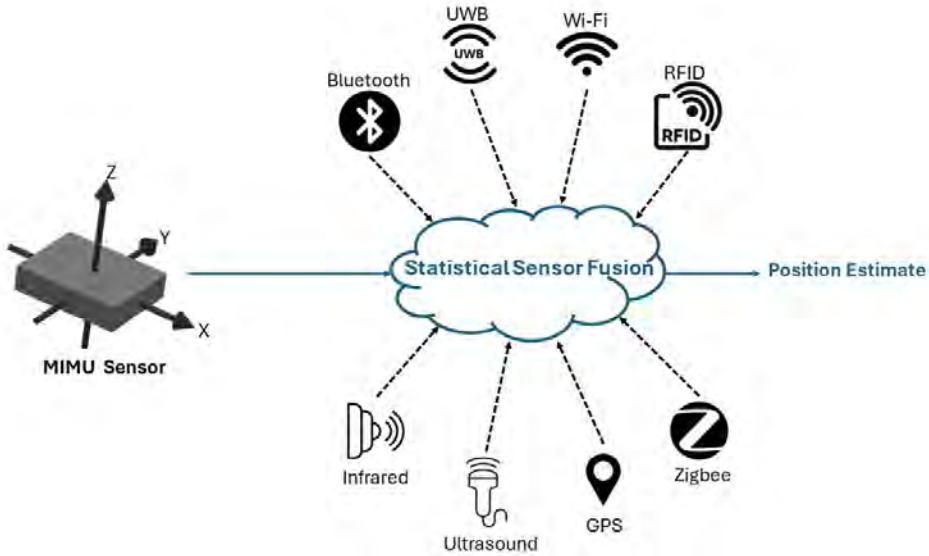


Figure 1.5: Schematic representation of various sensor modalities that can be fused with MIMUs for providing redundant position estimates for data fusion. While this study focuses on UWB as the complementary sensor, other modalities such as GPS, RFID, and ultrasound are alternatives explored in the broader literature.

The integrated UWB/MIMU sensors have great potential for improving accuracy and consistency of position estimates for the 3D analysis of human movement, mainly due to the complementary error characteristics of both these sensors that can offset one another when fused. UWB sensors provide absolute, drift-free position estimates but suffer in accuracy due to Non-Line-of-Sight (NLOS) conditions between the ranging UWB pairs [65]. In contrast, MIMUs offer position estimates relative to their starting position by integrating acceleration, which makes them immune to NLOS but prone to integration drift over time [42]. These complementary error profiles make them ideal candidates for data fusion, where combined use improves accuracy and consistency beyond what each can achieve alone. As a bonus, in wireless solutions, the UWB ranging messages could also double as a means for data transport for both UWB and MIMU data, as their main modus of Operandi is communicating with other sensors at extremely high speeds.

This feature helps integration of UWB to MIMU modules into physical modules to optimize the data fusion approach.

1.5 Problem statement and scope of the thesis

Though the integrated UWB/MIMU sensor system seems to hold the potential for improved position estimation in 3D AHM by addressing the position estimation issues in the current ambulatory system based on MIMU, they have not yet been explored for the analysis of human movement. Instead, they have been used only for human tracking and localization applications. These applications typically operate over large areas and rely on fixed infrastructure, which is not representative of clinical 3D AHM environments. There is no systematic research investigating how UWB behaves within the spatial and anatomical constraints of 3D AHM with only on-body sensors, where short-range on-body measurements and transient NLOS conditions caused by body segments are prevalent. Furthermore, there is a lack of research into the specific calibration procedures and algorithmic strategies necessary for accurate and consistent position estimation using the integrated UWB/MIMU sensor combination in ambulatory human movement analysis, particularly in configurations relevant to 3D AHM.

Realization of this integrated sensor system for clinical adaptation of 3D analysis of human movement would require a structured approach and can be defined in three phases. The first phase would be the core technology development, where it is essential to understand the current capabilities and limitations of integrated UWB/MIMU systems, develop hardware tailored and optimized for human movement analysis, generate foundational knowledge on system behavior in these contexts of 3D AHM, and design robust calibration and data fusion algorithms. The second phase would consist of clinical validation, with the system being tested in real-world clinical environments with patient populations, assessing its ability to produce clinically meaningful movement parameters and refine its usability. The final phase would be the clinical integration, where the technology would be adapted into clinical workflows, explore regulatory approvals, and evaluate its cost-effectiveness and utility in rehabilitation settings.

This PhD thesis is focused exclusively on the first phase of the pathway toward clinical adaptation, which is the core technology development. It does not aim to deliver a final clinical product but instead lays the technical foundation required for future clinical integration. Specifically, this research investigates the feasibility of using integrated UWB/MIMU sensors for improving position estimation in the 3D AHM. The scope includes the development of an integrated sensor system, experimental characterization of UWB performance in relevant conditions, and the formulation of calibration and data fusion algorithms aimed at enhancing accuracy and consistency. The knowledge and methods developed through this work are intended to enable and inform subsequent phases involving clinical validation and real-world deployment.

1.6 Research goal

This research focuses on the development of the integrated UWB/MIMU sensor system and researching their feasibility for accurate, consistent, and drift-free position estimation in ambulatory 3D AHM through research, prototype development, and validation. Therefore, the goal of this research is to “*Develop an integrated UWB/MIMU sensor prototype system along with the smart sensor fusion algorithm, and validate the performance of the integrated system to find out its potential for improving the position estimation accuracy and consistency of the 3D analysis of human movement*”. This research will explore the possibilities to improve the position estimation accuracy and consistency using these integrated sensors, attempting to facilitate ambulatory human movement that is more accurate and consistent, such that they can eventually be realized in future clinical applications.

Achieving this goal requires several intermediate steps, which are defined as the objectives of this study. The objectives of the research are the following:

1. Researching the feasibility of using integrated UWB/MIMU data fusion for clinical human movement analysis, through a comprehensive literature study evaluating the current integrated UWB/MIMU sensor systems and their position estimation accuracies.

2. Develop the integrated UWB/MIMU sensor system and characterize the errors associated with UWB position estimation in situations of human movement analysis.
3. Research and validate strategies to mitigate errors and enhance the UWB sensor system's performance within the integrated sensor system.
4. Research, develop, and validate an algorithm for the optimal integration of UWB and MIMU sensor systems for accurate position estimation.
5. Discuss the performance characteristics and feasibility of using the integrated UWB/MIMU sensor system for estimating positions and its clinical implications.

1.7 Thesis outline

This thesis is structured to progressively address the research objectives defined in Section 1.6, starting from the feasibility analysis of the current system, development, optimization, and final performance validation of the integrated UWB/MIMU sensor system for 3D AHM. Chapter 2 addresses the first objective by evaluating the feasibility of integrated UWB/MIMU systems for clinical 3D AHM through a targeted literature review, identifying both their potential and gaps that limit current applications. Chapter 3 addresses the second objective by developing a custom integrated UWB/MIMU hardware platform and experimentally characterizing the UWB error behavior in 3D AHM situations. Chapters 4 and 5 address the third objective of enhancing UWB performance. Specifically, Chapter 4 introduces a novel calibration method to mitigate the systematic errors present in UWB, while Chapter 5 implements an optimization-based position estimation algorithm that utilizes all the inter-node distances measured by the UWB sensors to improve position estimation accuracy. Chapter 6 addresses the fourth objective by integrating these optimized UWB position estimates with MIMU data using an Extended Kalman Filter (EKF) based approach to achieve accurate, consistent, and drift-free position estimation. Finally, Chapter 7 addresses the fifth objective by synthesizing the main findings, assessing clinical implications, and outlining future research and translation pathways.

A summary of each chapter is provided here:

Chapter 2 provides information about the currently reported capabilities of the Integrated UWB and MIMU sensor system in estimating position, and investigates the potential for the use of these systems for the 3D AHM through a comprehensive literature review. This chapter also identifies the research gaps and limitations that currently restrict the integrated sensor system to only human tracking applications. Furthermore, this chapter addresses the next steps to adapt this technology for human movement analysis.

Chapter 3 describes the developed integrated UWB and MIMU sensor and evaluates the performance of the UWB sensors in position estimation in scenarios of typical 3D AHM. It also includes a detailed assessment of the sensor performance in the scenarios relevant to the intended application of 3D AHM. Additionally, the accuracy-limiting factors of the UWB measurements are investigated in this chapter.

Chapter 4 introduces a calibration method involving a non-linear optimization algorithm to address the systematic errors in the UWB sensors and presents the validation of the developed calibration method with both synthetic (generated with a custom-built data generator) and experimental UWB position measurements.

Chapter 5 presents a position estimation method from the UWB distance measurements based on an optimization technique that utilizes all the inter-node distances between the UWB sensor nodes in a fully connected configuration. This technique was validated using synthetic UWB data (derived from an optical motion capture system). Also, the algorithm performance was compared against the standard trilateration-based position estimation.

Chapter 6 presents a sensor fusion algorithm that combines the UWB and MIMU sensor data optimally to achieve accurate, consistent, and drift-free position estimates. This algorithm is then validated and tested with real MIMU data and synthetic UWB update data (derived from an optical motion capture system) with varying error characteristics in conditions typical in 3D analysis of human movement.

Chapter 7 is the general discussion, which synthesizes the main research findings from the previous chapters and highlights the clinical implications of these research findings. This chapter also proposes future research directions to advance the developed integrated UWB/MIMU sensor system towards clinical application in 3D AHM.

Chapter 2

Integrated UWB/MIMU Sensor System for Position Estimation towards an Accurate Analysis of Human Movement: A Technical Review

This chapter is published as:

Yogesh, V.; Buurke, J.H.; Veltink, P.H.; Baten, C.T.M. Integrated UWB/MIMU Sensor System for Position Estimation towards an Accurate Analysis of Human Movement: A Technical Review. *Sensors* **2023**, *23*, doi:10.3390/s23167277.

Abstract

Integrated Ultra-wideband (UWB) and Magnetic Inertial Measurement Unit (MIMU) sensor systems have been gaining popularity for pedestrian tracking and indoor localization applications, mainly due to their complementary error characteristics that can be exploited to achieve higher accuracies via a data fusion approach. These integrated sensor systems have the potential for improving the ambulatory 3D analysis of human movement (estimating 3D kinematics of body segments and joints) over systems using only on-body MIMUs. For this, high accuracy is required in the estimation of the relative positions of all on-body integrated UWB/MIMU sensor modules. So far, these integrated UWB/MIMU sensors have not been reported to have been applied for full-body ambulatory 3D analysis of human movement. Also, no review articles have been found that have analyzed and summarized the methods integrating UWB and MIMU sensors for on-body applications. Therefore, a comprehensive analysis of this technology is essential to identify its potential for application in 3D analysis of human movement. This article thus aims to provide such a comprehensive analysis through a structured technical review of the methods integrating UWB and MIMU sensors for accurate position estimation in the context of the application for 3D analysis of human movement. The methods used for integration are all summarized along with the accuracies that are reported in the reviewed articles. In addition, the gaps that are required to be addressed for making this system applicable for the 3D analysis of human movement are discussed.

2.1 Introduction

Currently, ambulatory 3D analysis of human movement finds an ever-expanding range of applications in rehabilitation medicine, physical therapy, sports, and ergonomics. The most widely used wearable sensor modality is the Magnetic Inertial Measurement Unit (MIMU), which has gained popularity due to its low cost, ease of use, and portability [38,66]. MIMUs typically comprise a 3-axial linear accelerometer, rate gyroscope, and magnetometer that can simultaneously measure 3D linear acceleration, angular velocity, and the local magnetic field vector in the sensor reference system, respectively [67]. MIMU sensor systems are typically capable of accurately estimating 3D orientation and, by extension, all other 3D rotational kinematics, in a world reference frame by exploiting the redundancy in angular movement data from these three sensor modalities through data fusion algorithms such as the Extended Kalman Filter (EKF) [38-40].

However, the accuracy is limited when the observability of the MIMU sensor's two natural references, which are exploited to relate the sensor reference system to the world reference system, is sub-optimal. These two natural references are the earth's gravity and magnetic fields. Observability of the earth's gravity is only threatened in situations of (prolonged) large or varying free acceleration, like situations of humans in moving vehicles (especially in curves) and in some performance sports (e.g., speed skating). In applications of physical therapy and rehabilitation, this typically does not occur. Observability issues of the earth's magnetic field typically occur in the vicinity of ferromagnetic materials and easily occur in all applications, especially indoors and with sensors close to any constructed floor [41,68]. Also, 3D linear displacement kinematics relative to a starting position can be derived. However, the mostly consistent accuracy achieved for 3D angular kinematics cannot be achieved in 3D position estimation, as this involves double integration of the acceleration signal, causing strong integration drift [42,43]. Since neither the rate gyroscope nor the magnetometer provides additional displacement data, there is no possibility to counteract this drift through data fusion methods, as is performed in the angular estimates. As a consequence, the displacement estimates and the derived position estimates are susceptible to relatively large errors.

Multiple attempts to reduce these errors were made by exploiting assumptions on the movement performed. This is realized, for example, by assuming an instant of zero velocity of the foot in the stance phase of walking in a method called the Zero-Velocity-Update (ZUPT) approach [44,69] or by assuming constraints to the joint 3D kinematics based on a biomechanical model of (part of) the human subject [45]. The application of these methods is (severely) limited by the validity of their assumptions regarding the individual subject's biomechanics or behavior, or situational conditions. As the accuracy problems are due to integration drift, other methods are proposed to limit positional estimates to estimates relative to temporary world frames in cyclical movements short enough to prevent integration errors from becoming substantial [3]. Exploiting the above assumptions can be a solution in some applications, but especially in patients, they have limited applicability, as patients typically perform in an individual-specific pattern, which severely violates these assumptions.

Another possible solution suggested is the addition of additional sensor modalities to the MIMU, seeking to create redundancy for 3D positional data. This would again enable a data fusion approach to tackle the integration drift issues and does not require any assumptions on the subject's biomechanics or behavior, or the situation and/or the short-term cyclicity of the activity, specifically facilitating accurate 3D analysis of human movement in patients. This approach requires adding synchronized ranging sensors to the MIMUs that record the absolute distance between the MIMUs on-body or between the MIMUs on-body and reference ranging sensors positioned around the subject. For a successful application in the 3D analysis of human movement, the position estimates by data fusion of MIMU with some additional sensor modality would require an accuracy that is similar to vision-based systems, which are currently regarded as the 'gold standard'. The accuracy of the vision-based systems is considered to be clinically relevant and sufficient enough for clinical decision-making [46,47]. While no explicit numerical threshold for clinically acceptable accuracy is defined in literature, current consensus papers emphasize the need for precise and verifiable measurements of positions and joint kinematics to ensure clinical validity [70]. Consequently, to approach clinical applicability, data-fusion methods should target sub-centimeter position estimation errors (ca. 1 cm error or better), comparable to those achieved by vision-based

systems that are generally regarded as sufficiently accurate for reliable clinical interpretation [71,72]. In addition, a sufficiently high update rate faster than 1 Hz from the position sensor being used for data fusion is necessary to keep the integration drift errors low [73].

Commonly proposed ranging sensor methods for the estimation of positions in indoor space exploit ultrasound [55] or infrared (IR) sensors [56]. However, ultrasound is not suited for continuous 3D analysis of human movement due to the low-frequency band [63,64], while the IR-based solutions require a direct Line of Sight (LOS), which severely limits their use for wearable 3D analysis of human movement [55,63]. Alternate technologies suggested for ranging are Wi-Fi, ZigBee, Bluetooth, Radio Frequency Identification (RFID), and Ultra-wideband (UWB) [49-53,74]. Among these, UWB is developed with the explicit purpose of ranging, while all the others were developed for communication purposes and only later were they used in ranging applications. Also, of all these methods, the highest accuracies are reported for UWB ranging solutions (errors < 10 cm) [57,58,60,75], with lower accuracies reported for the other solutions [76,77]. These UWB sensors are developed as miniature ranging devices with smart sensor clock-independent Two-Way-Ranging (TWR) algorithms. They use extremely low power and are currently available in single-chip-based packaging [75]. However, their accuracy is still limited, especially in Non-Line-of-Sight (NLOS) conditions [57].

Both MIMUs and UWB have their limitations in accuracy when independently used for the estimation of the (relative) 3D position. However, as the sources of their errors are complementary, it is expected that a data fusion-based integrated estimator would improve position estimation accuracy to a higher level than possible with either of them separately. This is because the MIMUs are prone to drift, but not affected by NLOS, while UWB provides an absolute estimate of distances that is drift-free, but is affected by NLOS. In the last decade, many researchers have exploited the complementary characteristics of UWB and MIMU to achieve accurate position estimates by smart data fusion [78]. All this suggests that, if an accuracy similar to the current lab-based ‘gold standard’ can be achieved with the combination of UWB and MIMU in a set of on-body sensors, applying a data fusion-based approach could have great potential in improving ambulatory 3D analysis of human movement. However, to the knowledge of the authors so far, UWB/MIMU data

fusion applications involving humans are only reported in pedestrian tracking and localization applications. No reports on exploitation for the full-body 3D analysis of human movement with on-body integrated UWB/MIMUs were found by the authors.

To be able to research and develop such an application for 3D analysis of human movement, there is a need to identify the current state-of-the-art research on integrated UWB/MIMU methods for position estimation. Also, a better understanding of the strengths and weaknesses of UWB/MIMU-based estimation, along with the opportunities and threats for successful application in the 3D analysis of human movement with only on-body UWB/MIMUs is essential. To the knowledge of the authors, no comprehensive literature review currently exists that provides the current state-of-the-art research on position estimation of humans (on-body) using these integrated UWB/MIMU sensor systems. Therefore, this paper intends to answer these questions through a technical survey of the literature and provide a summary of methods and algorithms reported in the peer-reviewed literature so far, along with the accuracies and stabilities achieved. As previously identified, integrated UWB/MIMU systems have been primarily applied to pedestrian tracking and navigation tasks rather than direct estimation of human segment or joint positions. Therefore, this review focuses on summarizing existing UWB/MIMU integration methods reported for pedestrian navigation and localization, with the aim of assessing their potential applicability for future human movement analysis.

Thus, the main aim of this paper is to identify the possibilities and limitations of integrated UWB/MIMU sensor systems for achieving accurate position estimates in 3D analysis of human movement applications. This is achieved through a comprehensive technical review of the literature in the past decade. To address this aim, several objectives were formulated:

1. To provide an overview of the current state-of-the-art research on estimation methods of (relative) 3D/2D positions of the human body, human body segments, or joints applying data fusion methods integrating UWB and MIMU sensor technology.
2. To summarize the configurations, protocols, and algorithms used in these estimation methods.

3. To summarize the achieved accuracy and stability reported for these methods.
4. To discuss the strengths and limitations of these methods and their consequences in the context of future application of 3D analysis of human movement.

2.2 Methods

2.2.1 Search Procedure

The literature search was conducted in the databases of Scopus (Elsevier), Web of Science, and PubMed on 2 February 2023. To frame the appropriate search terms, a pre-search was carried out where a list of keywords was identified by considering a set of the most relevant articles that were to be included in the review. Search terms were then grouped into four groups, where the groups were combined using the AND operator, while within the group, the terms were combined with the OR operator. The search terms are listed below:

- Group 1: UWB, ultra-wideband;
- Group 2: IMU, inertial measurement unit, IMMU, inertial magnetic measurement unit, MIMU, magnetic inertial measurement unit, inertial sensors, INS, inertial navigation system, inertial motion capture, accelerometer, gyroscope;
- Group 3: indoor positioning, position, indoor localization, localization, tracking, navigation, indoor navigation, trajectory tracking, distance, motion analysis, movement analysis, dynamic activity, ambulatory, posture, pose, orientation;
- Group 4: sensor fusion, data fusion, filtering algorithm, fusion, filter, Kalman filter, graph optimization, particle filter.

2.2.2 Study Selection

Followed by the initial search of the literature, the titles and abstracts of all the articles found were screened for the inclusion and exclusion criteria. The articles were included when they satisfied the following inclusion criteria:

1. The journal article was published within the last decade, that is between the years 2012 to 2023.
2. The research used the integrated UWB and MIMU sensors alone for estimating positions.
3. The research included experimental validation of the position estimation methods, which were validated against a standard reference system (vision-based systems such as VICON or other means where the ground truth is known).
4. The sensor system was applied for human movement tracking, analysis of human movement, or human localization.
5. The data fusion was based on UWB ranging or position estimates that used multiple sensor nodes instead of localization based on a single UWB sensor that uses the reflected signals similar to radar.

The articles are excluded if:

1. They were not written in English.
2. Additional sensors were used in data fusion along with the UWB/MIMU combination.
3. They were conference proceedings, abstracts, review articles, or letters to editorial.
4. They were applied or used for non-human situations such as drones, robots, etc.

The first two exclusion criteria were straightforward and were to align with this review's goal. The third exclusion criterion for excluding conference proceedings was due to a significant overlap in the data fusion approaches with the journal articles. In addition, these conference articles had limited experimental validation. Therefore, this choice of exclusion ensures clarity and quality of this review. For the fourth exclusion criterion, the focus is exclusively on human body situations, which is to align with this review's objective of assessing the applicability of the existing literature for accurate 3D analysis of human movement. Also, there is a unique effect on ranging accuracy due to on-body placement [76], and thus, this criterion for exclusion also ensures a targeted exploration of methodologies relevant to the intended use-case scenario. Full-text screening of all the shortlisted articles was

performed to validate the inclusion and exclusion criteria and was then reviewed by the researcher (VY).

2.2.3 Data Analysis

The included articles were analyzed in detail to extract information on the methods and their accuracies and stabilities. The information extracted is summarized in Section 2.3. Regarding the achieved accuracy in ranging, the main parameters extracted were Mean Absolute Error (MAE) and Root Mean Square Error (RMSE), along with minimum and maximum errors, if available. Reported Mean Square Error (MSE) values were converted to RMSE for consistent reporting in the tables. Also, if the RMSE and MAE values were reported for the individual axes, then the vector norm of the errors in each axis is computed and also depicted in the table for better comparison to other articles. For articles with the error values not explicitly indicated, it was extracted from the error plots. To facilitate comparison of an accuracy reported through MAE with one reported through RMSE, the reader may use the following relationship: RMSE is equal to $\sqrt{\pi/2}$ times MAE, valid when the errors may be assumed to be uniformly distributed [79], where $\sqrt{\pi/2} \approx 1.5$.

2.3 Results

2.3.1 Search Results

The literature search resulted in the identification of 661 articles in total from all three databases. The flow chart in Figure 2.1 highlights the results of each stage of the reviewing process. The identification of duplicates, initial title/abstract screening, and selection of articles were performed using the Rayyan web application (Rayyan System Inc, Cambridge, MA, USA), an intelligent collaborative research tool for literature reviews. The final included articles were then exported to the reference manager software EndNote X8.2.

Out of the total 661 articles, the duplicates (283 records) were removed, resulting in 378 records for the initial screening stage. The initial screening stage was based on the content of the title and abstract, which resulted in eliminating 318 articles based on the inclusion/exclusion criteria. The articles excluded were based on varying reasons which include: being non-journal articles (209 articles), being not

applied/used for human movement (47 articles), using additional sensors along with the UWB and MIMU used for the data fusion (28 articles), not using either UWB or MIMU in data fusion (24 articles), being reviews/background paper (5 articles), applying only single UWB sensor ranging based on reflected signals (3 articles), not used for position estimation or localization (1 article), and written in another language (1 article). The full text was extracted for the remaining 60 articles to perform a full screening and assessment of eligibility.

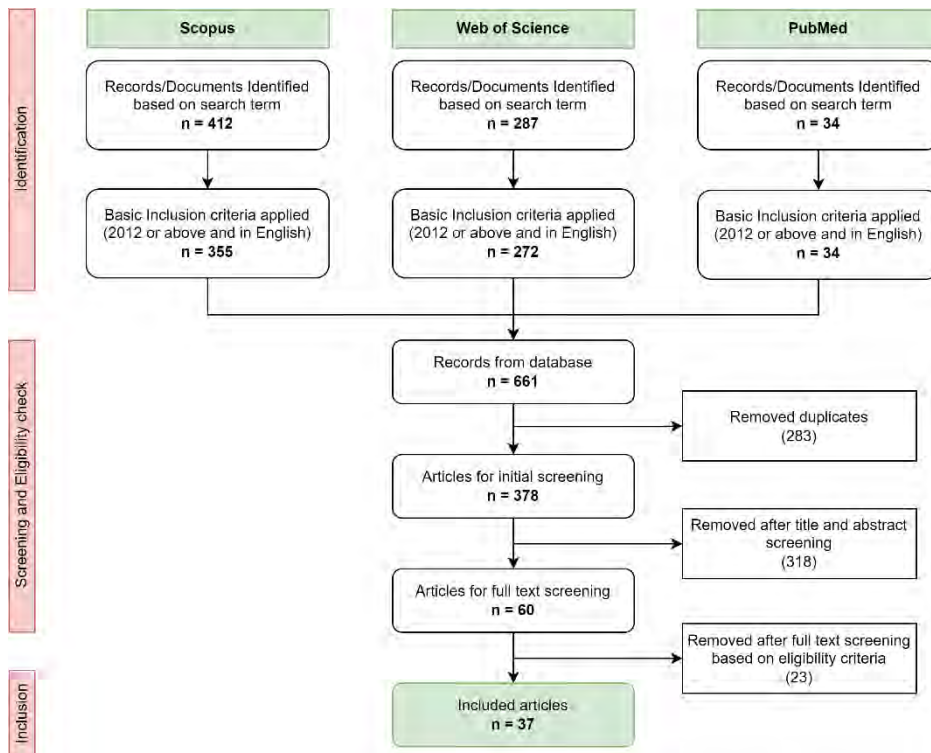


Figure 2.1: Review process flow diagram and inclusion results.

With full-text screening, 23 articles were excluded due to lack of experimental evaluation (4 articles), the full-text being unavailable (3 articles), UWB not being used for data fusion (1 article), and for not being tested/validated on human subjects or other applications (14 records). Finally, a total of 37 articles were included for analysis in this review. A plot of the number of articles published over the years is provided in Figure 2.2. For the year 2023, the number of articles is only based on the first 5 weeks of the year.

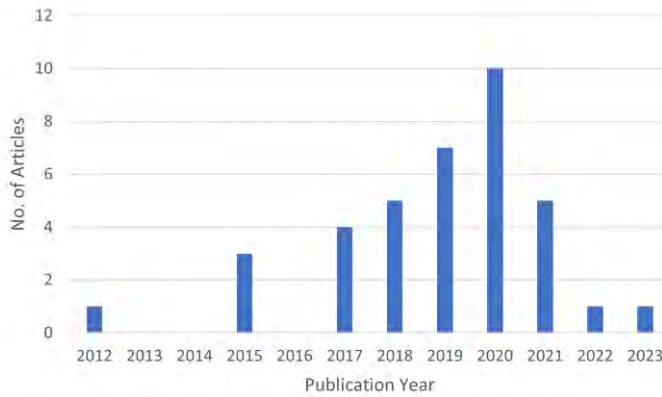


Figure 2.2: Number of relevant publications found per year.

2.3.2 Literature Overview of Integrated UWB/MIMU Sensor System

A summary of all the major data that were extracted from the included records for review is provided in Table 2.1. The extracted information includes the year of publication, sensor specifications, the configuration of the sensors, placement of the sensors on the body, the algorithm used for sensor fusion (method/approach), update parameter used for the fusion, and information regarding sensor hardware integration (separate units, physically attached, or integrated hardware platform). Information that is unavailable or not specified by the articles is marked as “-” in the table.

In the following subsections, the data fusion of the UWB and MIMU reported in the reviewed articles is summarized. The data fusion of the two sensor systems in the articles reviewed consists of a prediction phase where information from one of the sensors is used to estimate the position, which is then followed by an update phase where the information from the additional sensor/s is used to correct for the errors in the estimation of position in the prediction phase. Therefore, the position estimation methods in each of the sensor systems are first described along with their configurations, and sensor placement strategies are described individually. Followed by this, the combination strategy used by the articles for the sensor data fusion is described. If additional improvements in the algorithm for NLOS dealing were reported in the reviewed articles, they are also described.

Table 2.1: Summary of information extracted from each reviewed article.

Author and Year	UWB Sensor	MIMU Sensor	UWB Config.	Update rate		UWB Location	MIMU Location	UWB/MIMU Integration Method	UWB Update Param.	Sensor Attachment
				(sps)						
				MIMU	UWB					
Youssef, Denis et al. 2012 [80]	-	-	4 Anchor and 1 Tag	200	3 to 4	Held in hand	Attached to the subject' s ankles	Loosely coupled EKF	Position	Not rigidly attached
Zihajehzadeh, Yoon et al. 2015 [81]	Ubisense Series 7000	Xsens MTx	4 Anchor and 1 Tag	100	10	Attached to the subject' s waist	Attached to the subject' s waist	Two-step cascaded KF	Position	Rigidly attached
Zihajehzadeh, Yoon et al. 2015 [82]	Ubisense Series 7000	Xsens MVN suit	4 Anchor and 1 Tag	100	16	Attached to the subject' s waist	One unit on the waist and six units for the right and left thighs, shanks, and feet.	Loosely coupled two-step Cascaded KF	Position	Not rigidly attached
Kok, Hol et al. 2015 [83]	NA	Xsens	10 Anchor and 1 Tag	120	10	Attached to the subject' s foot	Attached to the subject' s foot	Maximum a Posteriori (MAP) estimation algorithm	Distance	Rigidly attached
Zihajehzadeh and Park 2017 [68]	Unisense series 7000	Xsens MVN suit	4 Anchor and 3 Tag	100	10	Attached to the subject' s waist and both feet	One unit on the waist and six on the right and left thighs, shanks, and feet.	Multiple layered KF	Position	Rigidly attached
Yoon, Zihajehzadeh et al. 2017 [84]	Unisense series 7000	Xsens MTx	4 Anchor and 1 Tag	100	9.25	Attached to the subject' s waist	One unit on the right and left thigh, shanks, and feet	Cascaded KF	Position	Rigidly attached

Table 2.1: Continued.

Author	Year	Device	Sensors	Anchor and Tag	Count	Attachment	Filter	Distance	Attachment
Chen, Kuang et al.	2017 [85]	-	-	3 Anchor and 1 Tag	-	Attached to the subject's shoulder	Unsecented Kalman Filter (UKF)	Distance	Not rigidly attached
Wang and Li	2017 [60]	DW1000	-	4 Anchor and 1 Tag	128	Attached to the helmet worn on head	PF	Position	Not rigidly attached
Li, Wang et al.	2018 [86]	BeSpoon	MATE9 (Huawei smartphone)	4 Anchor and 1 Tag	-	Held in hand	EKF	Distance	Rigidly attached
Li, Wang et al.	2018 [57]	DWM1000	X-IMU, UK MPU9250	4 Anchor and 1 Tag	128	Attached to the helmet worn on head	Method1: PF Method2: a combination of PF & EKF filter	Position	Not rigidly attached
Wang and Li	2018 [87]	DWM1000	X-IMU, UK MPU9250	4 Anchor and 1 Tag	128	Attached to the helmet worn on head	Graph optimization	Position	Not rigidly attached
Xu, Tian et al.	2018 [88]	-	-	4 Anchor and 1 Tag	-	Attached to a backpack setup carried by the subject	Federated Extended Finite Impulse Response (EFIR) filter	Distance	Not rigidly attached
Xu, Ahn et al.	2018 [89]	DW1000	Acc:ADX1203; Gy:ADXRS620; Magnet: HMC5983	5 Anchor and 1 Tag	-	Attached to a backpack setup carried by the subject	UFIR filter bank	Position	Not rigidly attached
Tian, Wang et al.	2019 [90]	EVB1000/DW1000	Iphone IMU	1 Anchor and 1 Tag	50	Held in hand	PF	Distance	Rigidly attached

Table 2.1: Continued.

Author and Year	UWB Sensor	MIMU Sensor	UWB Config.	Update rate (sps)		UWB Location	MIMU Location	UWB/MIMU Integration Method	UWB Update Param.	Sensor Attachment
				MIMU	UWB					
Xu, Shen et al. 2019 [91]	-	-	4 Anchor and 1 Tag	100	-	Attached to a backpack setup carried by the subject	Attached to the subject's foot	Predictive Adaptive Kalman Filter (PAKF)	Distance	Not rigidly attached
Xu, Ahn et al. 2019 [92]	-	Acc:ADXL203; Gy:ADXRS620; Magnet:MHMC5983	5 Anchor and 1 Tag	-	-	Attached to a backpack setup carried by the subject	Attached to the subject's foot	Predictive UFIR filter	Position	Not rigidly attached
Tian, Wang et al. 2019 [93]	DW1000	iPhone IMU	3 Anchor and 1 Tag	50	-	Held in hand	Held in hand	PF	Distance	Rigidly attached
Ferreira, Fernandes et al. 2019 [94]	DW1000	LSM330DL; Magnet:MHMC5883L	3 Anchor and 1 Tag	100	1 to 2	-	-	EKF	Position	-
Li, Hao et al. 2019 [95]	-	JY901B	4 Anchor and 1 Tag	-	1	Held in hand	-	EKF	Position	-
Wang, Li et al. 2019 [96]	-	MPU9150	7 Anchor and 1 Tag	100	1	Attached to the helmet worn on head	Attached to the subject's foot	Iterative EKF	Distance	Not rigidly attached
Zhang, Zhang et al. 2020 [76]	DWM1000	MPU9250	3 Anchor and 1 Tag	-	-	Attached to the subject's foot	Attached to the subject's foot	KF	position	Rigidly and integrated hardware
Zhang, Tan et al. 2020 [97]	UWB Mm4Plus	JY61 attitude sensor	4 Anchor and 1 Tag	-	-	Attached to the subject's foot	Attached to the subject's foot	EKF	position	Rigidly attached

Table 2.1: Continued.

Xu, Shmaliy et al. 2020 [98]	-	-	4 Anchor and 1 Tag	100	-	Attached to a backpack setup carried by the subject	Attached to the subject's foot	Decision Tree-EFIR filter	Distance	Not rigidly attached
Xu, Li et al. 2020 [99]	-	-	4 Anchor and 1 Tag	-	-	Attached to a backpack setup carried by the subject	Attached to the subject's foot	Least Square-Support Vector Machine (L.S-SVM) assisted UFIR filter	Position	Not rigidly attached
Tian, Wang et al. 2020 [100]	EVB1000/DW1000	iPhone 7 IMU	3 Anchor and 1 Tag	50	3.57	Held in hand	Held in hand	PF	Distance	Rigidly attached
Tian, Wang et al. 2020 [101]	EVB1000/DW1000	iPhone 7 IMU	2 Anchor and 1 Tag	50	3.57	Held in hand	Held in hand	PF	Distance	Rigidly attached
Tian, Wang et al. 2020 [100]	EVB1000/DW1000	iPhone 7 IMU	2 Anchor and 1 Tag	50	3.57	Held in hand	Held in hand	PF	Distance	Rigidly attached
Feng, Wang et al. 2020 [78]	DWM1000/M AX2000	LIS3DH	3 Anchor and 1 Tag 1 Anchor and 1 tag	-	-	-	-	EKF UKF	Distance	- -
Wen, Yu et al. 2020 [77]	PlusOn410	Sarneto, China	5 Anchor and 1 Tag	100	10	Attached to the subject's foot	Attached to the subject's foot	KF	Position	Rigidly attached
Guo, Zhang et al. 2020 [102]	DWM1000	Acc. & Gyr.: ICM20602; Mag: IST8310	3 Anchor and 1 Tag	200	20	Attached to the subject's shoulder	Attached to the subject's shoulder	KF	Distance	Rigidly and integrated hardware

Table 2.1: Continued.

Author and Year	UWB Sensor	MIMU Sensor	UWB Config.	Update rate (sps)		UWB Location	MIMU Location	MIMU Location	UWB/MIMU Integration Method	UWB Update Param.	Sensor Attachment
				MIMU	UWB						
Xu, Shmaliy et al. 2021 [103]	DW1000	Acc:ADX1203;Gyr:ADXRS620;Mag:HMC5983	5 Anchor and 1 Tag	30	3	Attached to a backpack setup carried by the subject	Attached to the subject's foot		EKF filter	Distance	Not rigidly attached
Ali, Liu et al. 2021 [104]	MAX2000/DW1000	MPU6050	4 Anchor and 1 Tag	-	-	Attached to the subject's foot	Attached to the subject's foot		tightly-coupled EKF	Distance	Rigidly and integrated hardware
Kim and Pyun 2021 [105]	DW1000	EBIMU-9DOF	4 Anchor and 1 Tag	50	16	Held in hand at a constant location close to the chest	Held in hand at a constant location close to the chest		KF	Position	Rigidly attached
Wang and Li 2021 [106]	-	MPU9250	5 Anchor and 1 Tag	100	2	Attached to the subject's foot	Attached to the subject's foot		EKF	Distance	Rigidly attached
Xu, Cao et al. 2021 [107]	-	Acc:ADX1203;Gyr:ADXRS620;Mag:HMC5983	4 Anchor and 1 Tag	-	-	Attached to a backpack setup carried by the subject	Attached to the subject's foot		Distributed KF	Distance	Not rigidly attached
Naheem and Kim 2022 [108]	DWM1001C	MPU6050 InvenSense, USA	4 Anchor and 1 Tag	100	10	Attached to the subject's foot	Attached to the subject's foot		loosely coupled EKF	Position	Rigidly attached
Liu, Zhang et al. 2023 [109]	DW1000	-	4 Anchor and 1 Tag	-	-	Body worn; On-body location not mentioned	Body worn; On-body location not mentioned		KF	Position	-

- data not specified in the reviewed articles.

UWB Sensor System Configuration and Measurement

The most commonly used UWB sensor hardware system is the DW/M1000 OR DMW1001 (DecaWave, Dublin, Ireland) [57,60,76,78,87,89,90,93,94,100-105,108-110], which was used in 18 articles, while the Unisense series 7000 was used in 4 articles [68,81,82,84]. The PlusOn 410 UWB [77], UWB Mini4sPlus [97], and BeSpoon [86] were each used in one article. Twelve articles did not report on the UWB sensor that was used in their study [80,83,85,88,91,92,95,96,98,99,106,107]. Detailed information on the sensor systems used, along with their update rates, is provided in Table 2.1. UWB sensors are henceforth referred to as ‘nodes’, and those used in these articles were classified into two classes based on their functionality and named accordingly as ‘anchors’ and ‘tags’. UWB nodes are referred to as anchors when they are placed in fixed known positions around the measurement region and typically form a frame of reference for the position of the tags, while tags are the UWB nodes with an unknown, dynamically changing, position that is worn by the subject [108].

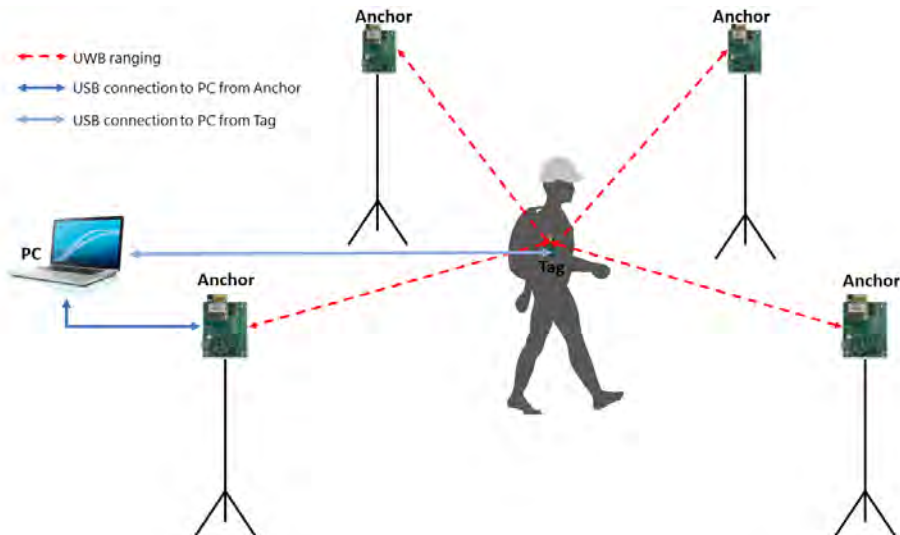


Figure 2.3: Star UWB sensor system configuration.

All the articles reviewed use a ‘star topology’ for the ranging operations (Figure 2.3). In this topology, for each tag, the ranging operations only take place between this individual tag and each anchor, while no ranging operations are performed between tags or between anchors. The alternative ‘swarm topology’ (a topology in which ranging is performed between all node pairs) is not used in any of the articles.

The distances between all of the wearable tags and the fixed anchors were estimated using a variation of the TWR scheme that utilizes the Time of Arrival (ToA) information. The typical TWR scheme is described in detail in [111]. The resulting distance estimates between the tags and anchors were then used to estimate the 2D or 3D position of the tag by the method of trilateration or multilateration, or by an optimization method minimizing least square position errors [112]. For both methods, at least the (required) minimum of three anchors was used to locate each tag in 2D space and at least the (required) minimum of four anchors was used to locate a tag in 3D space [108]. However, in some of the reviewed articles the UWB distance estimates were used as a direct input for their data fusion approach. For these approaches, less than three anchors was enough as there is no need for trilateration to compute positions.

Among the reviewed articles, the number of fixed anchors ranged from 1–10, where the majority of the articles (32 articles) used 3–5 anchors. Two of the articles used seven anchors [96] and ten anchors [83], respectively. Both the articles that used more than five anchors stated that an increase in the number of anchors creates redundancy in the number of ranging, thereby increasing the robustness against situations of NLOS between one or more node pairs. In four articles, the number of anchors was limited to two anchors [100,101] or one anchor [78,90]. These four articles with fewer than three anchors, used only the distance estimates for data fusion and did not estimate positions from UWB. The number of tags on the subject for tracking the motion was always one, except for Zihajehzadeh et al., 2017 [68], where three tags were used. In this article, the additional two UWB tags were used for computing the facing direction (heading) of the subject's body in the horizontal plane, while only the third one was used for position estimation.

MIMU Sensor System Configuration and Measurement

A wide range of MIMUs was used in the reviewed articles and the most commonly used MIMU sensor hardwares are Xsens IMU (Xsens BV, Enschede, Netherlands) [68,81-84], iPhone inbuilt IMU [90,93,100,101,110], and MPU9250/9150 (InvenSense Inc, San Jose, CA, USA) [57,76,87,96,106], which were each used in five articles. Custom-made MIMUs with individual sensors (accelerometer: ADXL203, gyroscope: ADXRS620, and magnetometer: HMC5983) [89,92,103,107] were used in

four articles. Other MIMUs used were MPU6050 (InvenSense Inc, San Jose, CA, USA) [104,108], EBIMU-9DOF [105], JY901B [95], and Starneto [77]. Also, two articles had a custom-built IMU with sensors ICM20602 (Invensense, USA)/IST8310 (iSentek Inc, Taipei, Taiwan) [102] and LSM330DLC (STMicroelectronics, Geneva, Switzerland)/HMC58832 [94]. Two articles used an IMU without a magnetometer, namely LIS3DH (STMicroelectronics, Geneva, Switzerland) [78] and JY61 attitude sensor [97]. All of the MIMUs communicate wirelessly or via a USB connection to a PC or a recorder carried by the subject. The majority of the included articles used a single MIMU on the subject, except for four articles that used more than one MIMU [68,84,85]. Eight articles did not report on the MIMU sensor that was used in their study [60,80,85,88,91,98,99,109].

Two types of position estimation methods were utilized for the MIMU sensor systems in the reviewed articles. The first method, namely the ‘direct strapdown integration method’, estimates the MIMU node displacement relative to the start position by double integration of its free acceleration signal transferred to a global inertial reference frame. This transformation needs the estimated orientation of the MIMU node. Articles in this review using this method did estimate these orientations by data fusion of sensor acceleration, angular velocity, and magnetic field vector data or by data fusion of only sensor acceleration and angular velocity. In addition, some of the articles use the ZUPT algorithm and EKF for improving the position estimates for the IMU placed on the foot, exploiting typical properties of the cyclical movement of the feet in walking. This is illustrated in Figure 2.4, where the blocks with solid lines apply to all, while the dotted lines are applicable for the ones that were relying on the additional ZUPT algorithm and EKF.

The second method used was the Pedestrian Dead Reckoning (PDR) method, where the algorithm detects the heel strike instants and then computes the amount of displacement of the sensor node during each step (heel strike to heel strike) and the direction of displacement separately. The position at the end of the step was then estimated by adding the estimated displacement to the position estimate at the beginning of the step in the estimated direction [85]. A schematic diagram of the PDR algorithm is provided in Figure 2.4. It illustrates that the heel strike instant and the step length were computed based on the acceleration of the sensor, while the heading angle was estimated from either the MIMU orientation, the magnetometer,

or through data fusion of all the combined information (as illustrated with dotted lines in Figure 2.4). The reviewed articles that relied on the PDR algorithm for estimating the position [85,86,90,94,95,100-102,104,105,110] using MIMUs had all adapted the same basic algorithm or with minor improvements. Researchers who are interested to know more details on the general PDR algorithm are referred to [85].

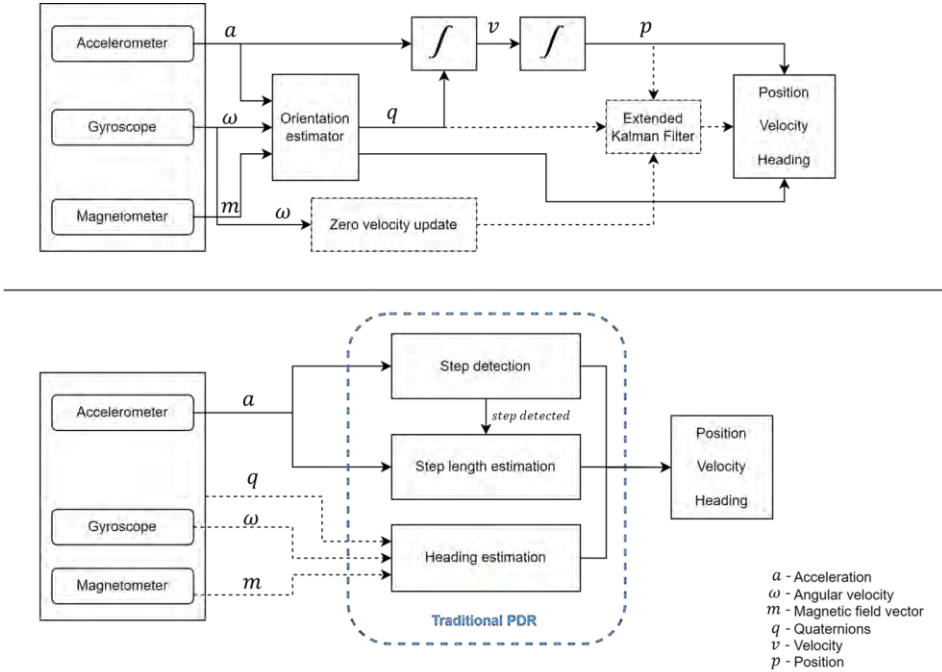


Figure 2.4: Schematic of the MIMU position estimation algorithms applied; Direct strapdown integration method (top) and traditional Pedestrian Dead Reckoning (PDR) algorithm (bottom).

Placement Location of the Sensors on the Body

In the reviewed articles, the UWB and MIMU sensors on the body were not always integrated into a single sensor platform or placed physically tied to each other. The UWB and MIMU were placed at different locations on the body for 15 articles [57,60,80,82,85,87-89,91,92,96,98,99,103,107]. While for another 19 they were physically tied to each other and thus placed at the same location [68,76-78,81,83,84,86,90,93,97,100-102,104-106,108,110]. Among these nineteen articles, only four articles [76,78,102,104] had the MIMU and UWB sensor hardware integrated

into a single sensor platform with one central onboard microcontroller. The placement data were not available for three articles [78,94,109].

As previously mentioned in “UWB Sensor System Configuration and Measurement”, only one UWB tag was placed on the body and was placed mainly on the foot [76,77,83,97,104,106,108], on a shoulder backpack [88,89,91,92,98,99,103,107], or held in hand steady with no swinging [80,86,90,93,95,100,101,110]. Meanwhile, other articles had a placement on the waist [81,82,84], on a head-worn helmet [57,60,87,96], on the shoulder [85,102], or on the chest/trunk [105]. Zihajehzadeh et al. 2017, [68] had three UWB sensors that were placed on the waist and both feet. The mounting locations of the UWB sensors on the body are illustrated in Figure 2.5 (left) with the number of corresponding records.

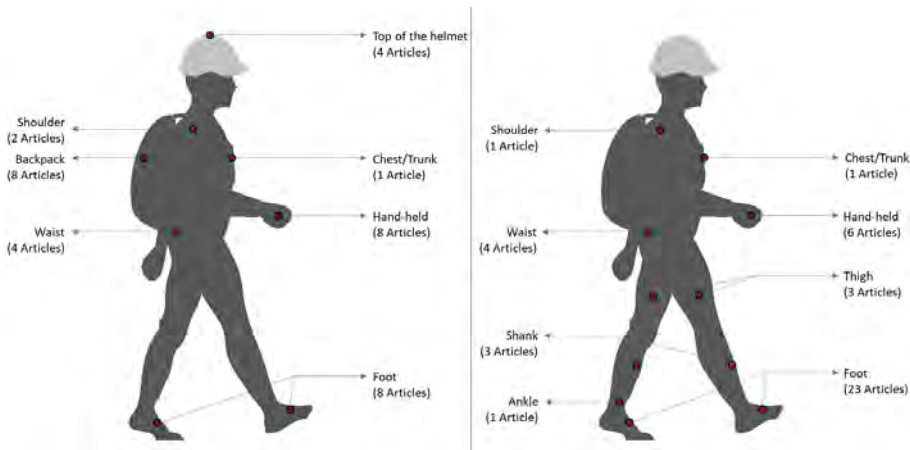


Figure 2.5: UWB sensor placement (left) and MIMU sensor placement (right) locations on the human subject in the reviewed articles along with the number of corresponding articles for each location.

For MIMU sensors, the most widely used placement location was the foot [57,60,76,77,83,85,87-89,91,92,96-99,103,104,106-108] and it comprised 20 articles. Among them, one article [85] had two sensors on both feet, while others had a single MIMU on one of the feet. The other placement locations were ankles [80], waist [81], shoulders [102], chest/trunk [105], or held in hand [86,90,93,100,101,110]. Three articles [68,82,84] had a set of seven MIMUs placed such that there was one on the waist, and pairs of two on the upper legs, lower legs, and feet. These additional MIMUs were used to estimate the body kinematics, such as angles and pose, in

addition to the general body position estimation. For four articles, no placement information was available [78,94,95,109]. The placement locations of MIMUs on the body for all the articles are illustrated in Figure 2.5 (right).

Position Estimation Methods Combining UWB/MIMU Data

The key objective of the data fusion approach in the examined papers was to achieve a better position estimate than what can be achieved with only MIMU-based methods or only UWB-based methods by combining the strengths of both and, with that, overcoming their weaknesses. The data fusion approaches used in the reviewed articles can be widely classified as loosely coupled and tightly coupled approaches, based on the way the data were used for the UWB/MIMU fusion. The loosely coupled approach uses the raw time of UWB transmissions between the nodes (distance estimates), while the tightly coupled approach uses the triangulated position estimates of the UWB for the data fusion. All the algorithms/methods identified are listed in Table 2.1, along with the update parameter which directly indicates if it is a loosely or tightly coupled approach.

Summarizing the methods in the articles reviewed, the general data fusion pipeline generally contained two stages, which were a data preprocessing and a data fusion stage. Data preprocessing stages included activities like setting the start position, a priori estimation of the error characteristics of the sensor output, and detection of zero velocity instants. The data fusion stage had two phases. In the first phase (prediction), the position of the sensor (in loosely coupled methods) or distances between sensors (in tightly coupled methods) were estimated based on information from one of the two sensors used in the experiment, using the algorithms described in “UWB Sensor System Configuration and Measurement” or “MIMU Sensor System Configuration and Measurement”. In the second phase (update), the additional redundant information, here the second type of data, was merged with the predicted/priori estimates to achieve a more accurate estimate.

All the articles reviewed except [93] used MIMU sensor information in the prediction phase and UWB in the update phase, probably due to the typically higher sampling rate of the MIMUs and since quantifying error characteristics was easier for UWB data. The one paper that used UWB data in the prediction phase [93] used MIMU in

the update phase only to get the relative orientation of the two ranging UWB. This was subsequently used to correct the UWB ranging error previously characterized in this article based on the orientation of the ranging operation. All the listed articles with the direct strapdown integration method used that approach during their prediction phase, while the articles listed under PDR utilized the PDR algorithm for estimating positions in the prediction phase. In the update phase, articles listed under the loosely coupled approach used positions as the UWB observation, while the ones under the tightly coupled approach used distances as the UWB observation.

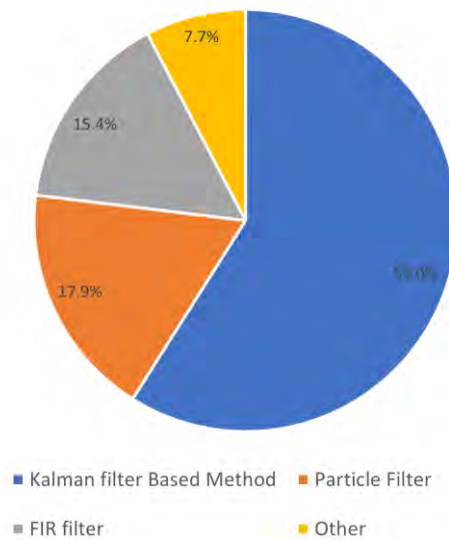


Figure 2.6: Distribution of data fusion methods for position estimation.

The reviewed papers most commonly used Kalman Filter (KF)- or Particle Filter (PF)-based methods for data fusion (Figure 2.6). Almost 59% of the articles reviewed utilized the KF-based data fusion methods [68,76-78,80-82,84-86,91,94-97,102,104-109]. Among the Kalman Filter-based articles, thirteen articles used a loosely coupled approach [68,76,77,80-82,84,94,95,97,105,108,109], while nine articles used the tightly coupled approach [78,85,86,91,96,102,104,106,107]. All articles using KF follow the general data fusion pipeline as mentioned above, which optimally combines the position estimates from MIMU and UWB by calculating a weighted average of the predicted state and the updated measurement considering their uncertainties. The main variations seen among them are based on the use of multiple

layers of KF namely the cascaded KF [68,81,82,84], or a different tuning approach of the KF covariance or error parameters. The multiple layered or cascaded KF consisted of independent KFs, where each KF was performing a data fusion for estimating orientation, position, and heading, which were performed in order. Additionally, some articles use an EKF [78,80,86,94-97,104,106,108] or an Unscented Kalman Filter (UKF) [78,85] for dealing with non-linear models.

Approximately 18% of the articles relied on the particle-filtering approach for the fusion of the two systems [57,60,90,93,100,101,110]. Articles using the PF method represent the position estimates from MIMU as a set of particles, except for [93], which uses UWB distances (as described previously). These particles were propagated using dynamic models based on the UWB update measurements and their weights were updated based on their closeness to observations from UWB. The particles were then converged by resampling the particles with higher weights. The PF method is reported to be better in handling non-linear and non-Gaussian systems in the reviewed articles. Among the PF-based articles, two articles used a loosely coupled approach [57,60] while five articles used a tightly coupled approach [90,93,100,101,110].

The Finite Impulse Response (FIR) filtering-based approach was utilized for approximately 15% of the reviewed articles and they were all from the same author or research group [88,89,92,98,99,103]. FIR filter-based approaches combine the information from UWB and MIMU by convolving their measurements with specific filter coefficients which are based on the sensor measurement characteristics. They all exploit the temporal properties of the FIR filter. The FIR filters in the reviewed articles either used Extended Finite Impulse Response (EFIR) filter [88,98,103] or Unbiased Finite Impulse Response (UFIR) filter [89,92,99] based approaches. Where the EFIR method mitigates the errors by assigning appropriate weights to the measurements from both sensors, the UFIR considers the characteristics of both the sensors and constructs multiple FIR filters that effectively eliminate the errors.

Three other methods were also found, namely graph optimization-based fusion [87], Maximum a Posteriori (MAP) estimation algorithm [83], and a combination filter with KF and PF [57]. The graph optimization approach represents the sensor measurements and their relations as a graph. In the reviewed article using graph

optimization [87], the UWB anchors are represented as vertexes of the graph and the information from UWB and MIMU measurements are used to represent the constraints on each vertex. An optimization is performed on this graph minimizing the cost function. Finally, this method determines the confidence level for both the sensor observations based on the optimization results and the combined measurement errors. In the article on the MAP algorithm [83], both sensors provide a likelihood function that informs how likely the target states are given and is used to model the measurement model. The MAP algorithm finds the state that maximizes the probability of the posterior by performing an optimization that considers the sensor measurement model and prior information. The combined KF and PF filter approach article [57] uses an EKF for estimating position from MIMU and then used these position estimates for a PF approach.

Non-Line of Sight (NLOS) Mitigation Strategies

In the reviewed articles, 14 articles [77,86,93-97,102,104-106,108-110] had some NLOS mitigation strategies in their algorithm. In all articles, the NLOS mitigation strategy first involved the identification of the NLOS situation, followed by the NLOS error elimination. The NLOS identification methods used can be mainly classified into two types. The first class of detection methods was based on communication channel characteristics [94,102,104,105,109,110]. Here, all of the methods relied on the fact that the Received Signal Strength (RSS) of the multi-path is smaller than the RSS of the direct path. The articles using this principle then used a threshold for this difference between the two RSS to classify the measurement as LOS or NLOS except for [109], which used a state vector machine for classification based on the channel characteristic information.

The second class of methods for detecting NLOS situations was based on the ranging estimation inconsistencies [86,95-97,106,108]. Here, the ranging estimations were used to either obtain the Mahalanobis distance for estimating outliers [86,96], the likelihood ratio test [95,97], or residual errors between the ranging estimate and MIMU estimates for each instance to identify outliers or NLOS [106,108]. In addition to the two methods mentioned above, two articles used different approaches, where one of them [77] used distance estimates from the anchors only in front of the subject carrying the sensor with LOS. Meanwhile, the other [93] used MIMU to find

the orientation of the UWB tag to anchor and used a predefined error model based on the facing orientation between the tag and anchor. The NLOS error elimination in all these identified articles was performed by adjusting the error covariances for the data fusion update, except for four articles [77,94,105,109]. For these articles, the error elimination was performed by dismissing the updates that were detected to be acquired under NLOS.

2.3.3 Accuracy and Stability of Position Estimates

The position estimation errors are mostly reported as either mean (absolute) error MAE or RMSE, sometimes along with additional information like minimum error, maximum error, and error standard deviations. Some articles only provided error graphs (showing RMSE, MAE, or a cumulative error distribution function graph). Two articles reported the errors in MSE, which were converted to RMSE before listing them in Table 2.2. Among the articles reviewed, the smallest position estimation error based on MAE error was 0.04 m [81] and 0.076 m [76], respectively, while for RMSE the lowest reported position estimation error was 0.048 m [83], 0.066 m [68] and 0.068 m [82], respectively. Apart from this, the majority of reported errors were in the range between 0.1 m to 0.8 m, while four articles reported errors above 1 m of up to almost 2.5 m.

Most of the position estimation errors for the KF based-method were within 40 cm (nine out of seventeen articles) except for six articles [80,86,95,96,106,107] that had errors between 40 cm and 75 cm, and one article with errors as high as 2 m [94]. For the PF-based approach, only one article had an error below 15 cm which is 0.12/0.16 m [93]. For all the other PF-based articles, the errors were larger than 50 cm. The FIR-based articles had errors above 0.20 m and up to 0.78 m. For the graph optimization and combined KF/PF methods, the accuracies were above 0.4 m and above 0.5 m, respectively. Very few articles reported error standard deviation (SD). An overview of the position estimation accuracy along with the experiment details for all the reviewed articles is provided in Table 2.2. The reader may compare RMSE and MAE values under the assumption of a normally distributed error using their statistical relationship as explained in the Section 2.2 ($RMSE = \sim 1.5$ times MAE).

Table 2.2: Accuracy of position estimates and stability parameters.

Author and Year	2D/3D	LOS/NLOS	Exp. Activities	Integrated Accuracy [m]			Errors Around Each Axis [m]	Test Time [s]
				RMSE	MAE	Max Error		
Youssef, Denis et al. 2012 [80]	2D	Combined LOS and NLOS	Walking	-	0.4	-	-	~240
Zihajezadeh, Yoon et al. 2015 [81]	2D	LOS	Jumping task	-	<0.04	-	<0.04 in x and y axis	90
Zihajezadeh, Yoon et al. 2015 [82]	3D	LOS	Walking and Jumping	Walking: 0.068 * Jumping: 0.073 *	-	-	Walking: X-0.039 ± 0.016; Y-0.036 ± 0.015; Z-0.043 ± 0.017 Jumping: X-0.042 ± 0.019; Y-0.036 ± 0.015; Z-0.049 ± 0.023	~120
Kok, Hol et al. 2015 [83]	3D	LOS	Walking	0.048 *	-	-	X-0.03; Y-0.03; Z-0.023	24
Zihajezadeh and Park 2017 [68]	3D	LOS	Walking and Jumping	Waist: 0.075 * Feet: 0.067 *	-	-	Waist: X-0.043; Y-0.048; Z-0.038; Feet: X-0.039; Y-0.041; Z-0.035	100
Yoon, Zihajezadeh et al. 2017 [84]	3D	LOS	Walking and Dynamic (combining Running and Jumping)	Overall: 0.108 Walking: 0.092 Dynamic: 0.129	-	-	Overall: X-0.074; Y-0.072; Z-0.030; Walking: X-0.063; Y-0.062; Z-0.026; Dynamic: X-0.086; Y-0.086; Z-0.04	75
Chen, Kuang et al. 2017 [85]	2D	LOS	Walking at different speeds from 1–3 m/s	-	Overall: 0.15 Speed 1 m/s: 0.129 Speed 2 m/s: 0.155 Speed 3 m/s: 0.195	0.05	0.35	30

Table 2.2: Continued.

Author and Year	2D/3D	LOS/NLOS	Exp. Activities	Integrated Accuracy [m]			Errors Around Each Axis [m]	Test Time [s]
				RMSE	MAE	Min Error		
Wang and Li, 2017 [60]	2D	Separate LOS and NLOS	Walking	-	LOS: 0.708 ± 0.660 NLOS: 0.726 ± 0.661	-	-	~24 to 58
Li, Wang et al. 2018 [86]	2D	Combined LOS and NLOS	Walking along two different routes	Route 1 (Less NLOS): 0.35 Route 2 (More NLOS): 0.45	-	-	-	-
Li, Wang et al. 2018 [57]	2D	Separate LOS and NLOS	Walking along two different routes	-	LOS Route 1: 0.637 Route 2: 0.531 NLOS Route 1: 0.735 Route 2: 0.571	LOS Route 1: 0.001 Route 2: 0.001 NLOS Route 1: 0.003 Route 2: 0.007	LOS Route 1: 2.087 Route 2: 1.462 NLOS Route 1: 2.896 Route 2: 1.816	~390 to 420
Wang and Li, 2018 [87]	2D	Combined LOS and NLOS	Walking along three different routes	-	LOS Route 1: 0.685 Route 2: 0.505 NLOS Route 1: 0.624 Route 2: 0.527	LOS Route 1: 0.003 Route 2: 0.009 NLOS Route 1: 0.003 Route 2: 0.008	LOS Route 1: 2.576 Route 2: 1.356 NLOS Route 1: 2.576 Route 2: 1.524	~100 to 180
Xu, Tian et al. 2018 [88]	2D	LOS	Walking	0.576 *	-	-	X-0.36; Y-0.45	45
Xu, Ahn et al. 2018 [89]	2D	LOS	Walking	0.297 *	-	-	X-0.2; Y-0.22	60

Table 2.2: Continued.

Tian, Wang et al. 2019 [90]	2D	LOS	Walking along two different routes	-	Route 1: 0.60 Route 2: 0.58	-	-	258.8 & 391.8
Xu, Shen et al. 2019 [91]	2D	LOS	Walking	0.299 *	-	-	X-0.173 **, Y-0.245 **	30
Xu, Ahn et al. 2019 [92]	2D	LOS	Walking along three different routes	Route 1: 0.391 * Route 2: 0.355 * Route 3: 0.700 *	-	-	Route 1: X-1.03; Y-1.21 Route 2: X-0.44; Y-1.20 Route 3: X-2.28; Y-2.20	25
Tian, Wang et al. 2019 [93]	2D	Combined LOS and NLOS	Walking along two different routes	-	Route 1: 0.125 ± 0.059 Route 2: 0.164 ± 0.084	-	-	50 & 100
Ferreira, Fernandes et al. 2019 [94]	2D	Separate LOS and NLOS	Walking	-	LOS: less than 1.5 m for 99th percentile; NLOS: Less than 2 m for the 99th percentile	-	-	-
Li, Hao et al. 2019 [95]	2D	Combined LOS and NLOS	NA	-	~0.4	0.05	-	-
Wang, Li et al. 2019 [96]	2D	Combined LOS and NLOS	Walking along two different routes	-	Route 1: 7-anchor: 0.58 ± 0.22 3-anchor: 0.62 ± 0.33 2-anchor: 0.63 ± 0.34	-	NA	180 & 585

Table 2.2: Continued.

Author and Year	2D/3D	LOS/NLOS	Exp. Activities	Integrated Accuracy [m]			Errors Around Each Axis [m]	Test Time [s]
				RMSE	MAE	Max Error		
Wang, Li et al. 2019 [96]	2D	Combined LOS and NLOS	Walking along two different routes	-	Route 2: 7-anchor: 0.59 ± 0.27 3-anchor: 0.66 ± 0.32 2-anchor: 0.96 ± 0.47	NA	180 & 585	
Zhang, Zhang et al. 2020 [76]	2D	LOS	Walking	-	0.076	-	X-0.051; Y-0.055 ~20 to 25	
Zhang, Tan et al. 2020 [97]	2D	Separate LOS and NLOS	Walking	-	LOS: 0.24 ± 0.26 NLOS: 0.35 ± 0.35	LOS: 1.52 NLOS: 1.02	LOS: X-0.30; Y-0.18 NLOS: X-0.43; Y-0.23 ~20 to 40	
Xu, Shmaliy et al. 2020 [98]	2D	LOS	Walking	0.788 *	-	-	X-0.364; Y-0.699 ~20 to 25	
Xu, Li et al. 2020 [99]	2D	LOS	Walking	0.264 *	-	-	X-0.173 **, Y-0.200 ** ~270	
Tian, Wang et al. 2020 [100]	2D	Combined LOS and NLOS	Walking along two different routes	-	Route 1: 0.87 ± 0.52 Route 2: 0.81 ± 0.39	-	323 & 447	
Tian, Wang et al. 2020 [101]	2D	Combined LOS and NLOS	Walking	-	2.09 ± 1.33	-	~479	

Table 2.2: Continued.

Tian, Wang et al. 2020 [100]	2D	LOS	Walking	-	2.48	-	-	-	334.1 & 329.9
Feng, Wang et al. 2020 [78]	2D	LOS	NA	< 0.2 <0.16	-	-	-	-	NA
Wen, Yu et al. 2020 [77]	2D	LOS	Walking	0.132	-	-	-	-	~550
Guo, Zhang et al. 2020 [102]	2D	Combined LOS and NLOS	Walking	-	0.157	-	0.601	-	~50
Xu, Shmaliy et al. 2021 [103]	2D	LOS	Walking	0.305 *	-	-	-	X-0.20; Y-0.23	90
Ali, Liu et al. 2021 [104]	3D	LOS	Walking	-	50% of the time below 0.39	-	-	-	325
Kim and Pyun 2021 [105]	2D	Combined LOS and NLOS	Walking along six different routes	Less NLOS Route 1: 0.234; Route 2: 0.39; Route 3: 0.556 More NLOS Route 4: 0.314; Route 5: 0.492; Route 6: 0.473 Average: 0.4266	-	-	-	-	~15 to 30

Table 2.2: Continued.

Author and Year	2D/3D	LOS/NLOS	Exp. Activities	Integrated Accuracy [m]			Errors Around Each Axis [m]	Test Time [s]	
				RMSE	MAE	Max Error			
Wang and Li 2021 [106]	2D	Combined LOS and NLOS	Walking along two different routes	Route 1: 0.48 ± 0.37	Route 2: 0.62	-	-	250	
				Reduced no of Anchors: 4Anc: 0.36 ± 0.24; 3Anc: 0.51 ± 0.24 (Best comb)			-		-
Xu, Cao et al. 2021 [107]	2D	LOS	Walking along two different routes	Route 1: 0.61 Route 2: 0.53	-	-	-	460	
Naheem and Kim 2022 [108]	2D	Combined LOS and NLOS	Walking along two different routes	Route 1: 0.24	Route 2: 0.29	Route 1: 0.47	Route 2: 0.66	Route 1: X-0.18; Y-0.15 Route 2: X-0.18; Y-0.24	~10 to 20
				-	-	-	-	-	
Liu, Zhang et al. 2023 [109]	2D	Separate LOS and NLOS	Walking along two different routes	NLOS: 0.128 LOS: 0.099	-	-	-	~5 to 10	

* Estimated position RMSE from the corresponding RMSE errors around each axis; ** RMSE computed from provided MAE values.

2.4 Discussion

2.4.1 General

Examining the number of records published over time, it appears that since 2014, there has been an upward trend in the number of publications fulfilling the search criteria for this study until the year 2020, with the years 2021 and 2022 being a major exception, and this result is possibly pandemic-related. However, there were still conference publications in these two years indicating that further research into this topic is happening that could still result in more publications in the near future.

This review's main goal is to identify the possibilities and limitations of methods integrating UWB and MIMU sensor systems to provide accurate position estimates. To achieve this, four objectives were formulated in the Introduction. They were satisfied as follows: A summary of the current state-of-the-art UWB/MIMU integrated sensing for position estimation is provided along with a detailed description in Section 2.3 of this paper, addressing objectives 1 and 2 (Section 2.3.2). Also, the achieved accuracies and stabilities reported in the reviewed articles were extracted and summarized addressing objective 3 (Section 2.3.3). This Discussion addresses the strengths and limitations of these methods in the context of the application of 3D analysis of human movement, addressing objective 4.

2.4.2 Position Estimation Accuracy and Stability

Among the reviewed articles, 20 articles (54%) have validated their position estimation accuracy only in clear LOS situations, while 12 articles (32%) validated their position estimation accuracy in a combination of LOS/NLOS situations. Only five articles (14%) validated their position estimation accuracies in both LOS and NLOS situations separately. In LOS situations, only approximately seven articles (19%) of the total reviewed articles report errors of approximately 10 cm or less than 10 cm (Table 2). This is also only 26% of all the articles validated in the LOS situation. The highest accuracy results reported were an average position estimation error of 0.04 m in 2D position estimation [81] and an error of 0.048 m in 3D position estimation [83]. In addition to this, only two articles [68,82] reported 3D position estimate errors close to 0.05 m and less than 0.07 m, respectively. These four articles with the highest accuracies were all published between the years 2015 and the end

of 2017. Apart from these, only three articles reported errors of approximately 0.1 m or less than 0.1 m, of which one was for 3D position estimate [84] while the other two were for 2D position estimates [76,109]. All other articles validated in LOS had errors higher than 0.13 m.

Amidst the seven articles reporting high accuracy, four articles were from the same author or research group (Zihajehzadeh et al.), who used information from an additional biomechanical model in their data fusion for the MIMUs alone, which could have helped in achieving better accuracy. The position error of article [83], with the lowest RMSE of 0.048 m, as well as the articles [49,62], was based on the validations in a slow activity with a very short measurement duration (i.e., 24 s and 10 s, respectively). How this method performs in longer recordings of more dynamic movements is not reported. Another author, Yoon et al., expressed doubts about the stability of these methods over longer periods [84].

The comparison of the results of the articles that validated the position estimation in NLOS situations is difficult since these errors very much depend on the type and dimensions of the obstruction, while these details are mostly unavailable in the articles reviewed. In general NLOS conditions, there is always an increased ranging estimate error that deteriorates the subsequent position estimation. None of the articles in NLOS had errors less than 10 cm. The highest accuracy reported in their specific NLOS situation was 0.128 m [109], 0.157 m [102], and 0.12/0.16 m (two different paths) [93], while all the other articles reported errors higher than 0.20 m for their own specific NLOS situations. Also, for article [109], the test duration was much shorter (approximately 10 s), which generates doubts about performance over a longer duration. Overall, the reported accuracies of the NLOS position estimate were widely varying, which is expected due to the varying NLOS conditions. Very little information was gathered from the reviewed studies on specific effects of NLOS situations as all obstructions were either environmental objects like pillars, etc., or bodies of accidental passers-by in a corridor experiment. Only one study tried to calibrate for NLOS errors [93] based on the assumption that there is a fixed relationship between pose and error. This suggests a model for calibrating the structural component (systematic errors) of the NLOS-related error.

As systematic error components could possibly be mitigated by some sort of calibration method, it is important to distinguish between random and systematic components in the estimation errors. None of the other articles indicate the systematic or random components for the reported errors. All authors reported accuracies in terms of estimation errors, either expressed in RMSE or MAE. Only eight articles reported the estimation error standard deviation, representing the random component in the estimation error [60,82,93,96,97,101,106,110]. Still, the value of the systematic component (bias) in the estimation error is not clear in any of these articles, as the average of the position errors was not explicitly mentioned. Also, it cannot be derived easily from reported RMSE and SD values, which is the average error, as in all cases there seem to be both positive and negative error values.

For the successful application of this technology in the 3D analysis of human movement, the key criterion is the level of confidence that clinicians can have in this system. This level of confidence or trustworthiness can be related to the validity and reliability of the sensor system [113]. The validity can be linked to the accuracy of the system. Meanwhile, the capability of the UWB/MIMU data fusion estimation methods to maintain the reported accuracy over longer recordings (consistency) can be related to the reliability of the system. From the observations of the reviewed articles, it can be concluded that the accuracy achieved so far is not close enough to the required targeted value of approximately 1 cm as stated in the Introduction (Section 2.1). Therefore, further improvements in accuracy are required for this integrated system to be useful for 3D analysis of human movement. The reliability parameter is supposed to be one of the major possible improvements of the integrated UWB/MIMU sensor system over MIMU-based methods. However, this accuracy over prolonged recordings (reliability) is not addressed or reported in any of the articles reviewed.

2.4.3 Effect on Position Estimation Accuracy Based on Sensor Configuration and Sensor Placement

Based on the sensor's physical hardware integration, the situation with both the UWB and MIMU physically integrated into single hardware is called the 'Integrated Hardware' (IH) sensor, while when they were separate hardware systems it is called the 'Non-integrated Hardware' (NIH) sensor for this paper. The reviewed papers

that use IH sensors in general report lower errors than 20 cm except for [104]. Among the articles using NIH sensors, the articles that used physically tied NIH sensors (placed in the same location with the two sensor systems synchronized) had more number of articles with position estimation errors lower than 20 cm (6 out of 15). Meanwhile, only two out of fifteen articles that used NIH sensors that are not physically tied to each other had errors lower than 20cm. Although there are some exceptions, it seems that with IH sensors, it is easier to achieve a higher accuracy, probably because their physical integration ties them together to a single location, which makes them experience the same kinematics and facilitates tightly synchronized data acquisition.

The number of anchors has a notable influence on the accuracy of UWB-based position estimation, which is shown by varying the number of anchors in a few studies [96,106]. Specifically, increasing the number of anchors generally improves localization performance, particularly under non-line-of-sight (NLOS) conditions, by enhancing geometric coverage and providing measurement redundancy. Most reviewed studies used 3 to 5 anchors, which seems sufficient for reliable 3D position estimation. Studies employing a larger number of anchors (≥ 7) reported improved accuracy, whereas configurations with fewer than three anchors exhibited reduced accuracy. However, while a higher number of anchors can increase accuracy and enable optimization-based estimation techniques, it also requires a more complex and costly infrastructure [114]. Furthermore, some studies have reported that an excessive number of anchors can introduce additional measurement noise and uncertainties, potentially leading to estimation instability [115,116]. The number of tags was mostly limited to one as the application scenarios in the reviewed articles were for pedestrian localization or tracking.

Examining the accuracy as a function of the placement of the sensor on the body, the lowest errors were reported when using waist-mounted attachments, for which all four articles reported errors of less than 11 cm. Followed by this, the two articles with shoulder placement reported errors of less than 16 cm. Among the more widely used locations (feet, shoulder bag, and hand), the feet had the highest accuracy with errors lower than 30 cm for most of the articles, i.e., four out of seven articles.

Only one article mentioned the possibility of an effect on the estimation accuracy of the sensor location on the body in its discussion [76]. No article reported on the effects on estimation accuracy caused by placement in different locations on the body. Outside the selected articles for this review, two articles by Otim et al. [71,72] studied the effect of the placement of a UWB sensor (without MIMUs) in multiple different locations on-body. These studies consist of UWB anchors placed around the test area (13 m \times 6 m) and the UWB tags on different locations on the body. The distances measured are between the anchor and each tag on the body, while the positions of each tag on the body were estimated based on trilateration. In these two articles, they have studied the accuracies of the ranging and position for the following on-body locations namely forehead, hand, ankle, wrist, thigh, arm, and chest. From this study, the forehead is identified to be the location with the highest accuracy with average position errors of approximately 0.2 m and the chest is the location with worst accuracy with average position errors of approximately 2.46 m. The other locations between the forehead and chest in the descending order of accuracy were hands, ankle, wrist, thigh, and arm.

Direct comparison between these studies on locations [117,118] and the reviewed articles is not possible as the reviewed articles are the results of data fusion between the UWB and MIMU while the study of locations was performed only using the UWB sensors. However, if compared against the reviewed articles, assuming that the errors of UWB stay even after data fusion, the feet-mounted sensors had errors closer to the ankle-mounted situation and also for the hand-mounted situation it seems to be close enough. However, for the chest, in contrast to the findings of [117,118], the accuracy in reviewed articles was much lower and in the range between 0.23 m to 0.55 m.

2.4.4 Effect on Position Estimation Accuracy Based on the Data Fusion Algorithm/Methods

Out of the two data fusion approaches reported, the loosely coupled data fusion approach is claimed to be easier in implementation with less required computation time [80,81], and is used by approximately 49% of the articles reviewed and approximately 51% used the tightly coupled method. Loosely coupled approaches are stated to be susceptible to errors due to loss of information during the estimation

of position from the measured UWB distances. The data fusion algorithm then has only these position estimates available in the update and possibly misses out on details that were present in the underlying UWB-based distance estimates. The tightly coupled approach is claimed to be beneficial over the loosely coupled approach since they utilize unprocessed distance estimates from the UWB for the data fusion algorithm [83]. However, of the seven articles reporting the highest accuracy, all except [83] used the loosely coupled approach. Also, analyzing the entire set of articles, similar accuracies are reported for both approaches. So, no evidence was found in the papers reviewed for the claims of possible higher achievable accuracy when using tightly coupled approaches. *This suggests that, based on currently published results, there indeed is no performance advantage of the tightly coupled approach, and therefore the loosely coupled approach seems preferable as it has the advantage of easier implementation and a lower computational cost.*

All seven articles with the highest reported accuracy used the KF-based method except [83], which used the MAP estimation algorithm (also the only article to use that method in very limited conditions). Other methods performed less well than the best six KF-based methods, which were also applied in more than 50% of the articles, *so based on this review, KF appears most frequently and performs well under the reported conditions, thereby it appears to be the best candidate for achieving the high accuracy required for the analysis of human movement.*

All three articles [93,102,109] that reported the highest accuracies in NLOS conditions have used some form of explicit NLOS mitigation method in their algorithm. For the NLOS detection algorithm, both the methods based on communication channel characteristics and based on the ranging estimation inconsistencies are seen to be equally efficient in recognizing or identifying the NLOS situations. However, for the NLOS error-elimination methods, it is difficult to identify which error-elimination method is the best between the covariance-adjustment method and the method dismissing the NLOS updates. This is mainly attributed to the inconsistency in the accuracies reported for these methods, that is, both methods performed better in a few articles while having a lower accuracy in others. *Among the two methods for mitigating the NLOS error, the covariance*

adaptation method seems to be a better strategy since it does not discard all the updates under NLOS conditions.

2.4.5 General Recommendations

For integrated UWB/MIMU position estimation to be valuable for 3D analysis of human movement, achieving a high enough structural accuracy is the most important prerequisite. However, none of the studies reviewed reported an accuracy below, or close to, the targeted value of approximately 1 cm. Also, none of the studies explicitly reports the actual magnitude of systematic and random components in the errors. This is important as for both types of error components possible opportunities for improvement are very different in nature (e.g., systematic components might be improved upon by improved calibration procedures and random components might be improved upon by increased redundancy in the number of ranging paths). Also, very little is reported about the stability of performance over longer recordings, which is important to understand their possible scope of application, especially as the main source of error in MIMU-only applications lies in time-variant integration drift errors, of which the magnitude is even depending on speed and type of movement performed. Therefore, future studies should separately examine and report systematic and random errors, both as a function of recording duration and studied in all relevant movement scenarios. Also, none of the papers reported on the stability of the ranging accuracy over longer recordings and this should be further investigated.

The accuracy of the data fusion benefits from improved accuracy of UWB ranging, as the UWB-based distance estimates (or the derived position estimates) are serving as absolute time-invariant updates for the UWB/MIMU data fusion. Therefore, any further improvement of the UWB ranging estimates themselves will be beneficial for any future UWB/MIMU data fusion application. Most studies reviewed used the same UWB sensors from the same manufacturer 'as is'. There was no mention of developing or performing custom calibration procedures to optimize the ranging performance of the UWB sensors used. As no, or very little, attention to these details is reported, it is not clear whether the optimal ranging performance is already achieved in any of the methods presented. This suggests that possibly UWB ranging performance improvement can be achieved by further investigation and optimizing

the ranging estimate methods themselves including their calibration methods. As NLOS situations would typically occur frequently in any 3D analysis of human movement application also studying their effects on ranging accuracy and ways of mitigation seems relevant.

2.5 Conclusions

This review provides a comprehensive analysis of the methods combining data from UWB and MIMU sensors mounted on a human subject for estimation of position. None of the articles reviewed reported an accuracy close to the desired 1 cm, which was stated to be required for successful application in the 3D analysis of human movement. The highest accuracies achieved in the LOS situation were reported in two articles to have an MAE of 0.04 m and an RMSE of 0.048 m, respectively, and both were achieved in rather limited conditions. All other articles reviewed reported substantially larger errors. The papers reviewed provided very little information on how large the contributions of systematic and random components are to the estimation errors. This severely limits the possibilities of identifying possible opportunities for achieving the accuracies required for applications in the 3D analysis of human movement. For the different NLOS situations, the lowest errors reported were found to be approximately 0.12 m for both MAE and RMSE. NLOS conditions were clearly influencing the UWB ranging estimation performance. Still, reviewed articles revealed very little information on the nature and predictability of the extra errors of NLOS situations, which are especially relevant for application in the analysis of human movement. The effect of the mere presence of the human body on the accuracy of the position estimates is not reported or addressed, though some studies suggested there is a possible effect. This indicates a need for addressing the effect of these error sources in future research. Overall, this technical review intends to be a comprehensive resource offering insights into the current advancements and prospects of integrating UWB and MIMU sensors for accurate position estimation, especially for applications in the field of 3D analysis of human movement.

Chapter 3

UWB Distance Estimation Errors in (Non-)Line of Sight Situations within the Context of 3D Analysis of Human Movement

This chapter is published as:

Yogesh, V.; Rook, J.W.A.; Keizers, T.; Voort, C.; Buurke, J.H.; Velink, P.H.; Baten, C.T.M. UWB distance estimation errors in (non-)line of sight situations within the context of 3D analysis of human movement. *Engineering Research Express* 2024, 6, doi:10.1088/2631-8695/ad7e7e.

Abstract

Integrated Ultrawideband (UWB) and Magnetic Inertial Measurement Unit (MIMU) sensors are becoming popular for indoor localization applications, as a higher accuracy can be achieved than with just MIMU sensors. These integrated sensors could extend stability and accuracy in the field of 3D analysis of human movement (3D AHM) if they can deliver position estimates with an accuracy close to 1 cm. Achieving this high accuracy of 1 cm remains challenging, with most studies reporting position estimation errors around 5 cm, often due to Non-Line of Sight (NLOS) conditions and systematic UWB sensor distance estimation errors. Studying the distance error characteristic of UWB in situations of 3D AHM is essential to deal with these errors. While research on UWB distance errors in Line of Sight (LOS) and NLOS situations exists, few studies focus on the NLOS errors caused by the human body and were not in the relevant scenarios of 3D AHM. Therefore, this article examines UWB sensor performance and distance error characteristics in LOS and NLOS situations typical for the 3D AHM. Both the LOS and NLOS situations were studied in the typical 3D AHM distance range of 0.2 m to 2 m. The NLOS situations were studied first with a human subject as the NLOS causing object and then with simulated human body segments (PVC pipes filled with water) of varying diameters. In LOS situations, consistent systematic bias errors were observed, along with incidental errors at specific positions in the room. In NLOS scenarios caused by the human and simulated body segments, a consistent and reproducible overestimation of distances was found. The reproducibility of these errors based on relative node and object positions suggests that systematic mitigation methods could significantly reduce errors, enabling more accurate and reproducible 3D human movement analysis.

3.1 Introduction

Integrated Ultrawideband (UWB) and Magnetic Inertial Measurement Unit (MIMU) sensors have become popular in the estimation of accurate positions for localization and pedestrian navigation applications. This is mainly due to their complementary error characteristics, which can be exploited in data fusion approaches to achieve better accuracy than from the use of these sensors independently [65,78]. Specifically, kinematics estimation algorithms driven by MIMU sensor data are affected by integration drift errors [42,43] for both position and orientation estimates, but are not affected by Non-Line of Sight (NLOS) situations. While the UWB sensors are capable of delivering drift-free position estimates driven by absolute distance measurements, they are strongly affected by NLOS situations [57,65]. The UWB technology stabilizes the integration drift in position estimation, which typically occurs in solutions using only MIMUs, by offering directly measured distance or (relative) position updates to a data fusion-based estimator. Additionally, UWB technology is a cost-effective solution that operates across a wide frequency spectrum (3.1 GHz to 10.6 GHz) and offers significantly higher accuracy in indoor positioning compared to other wireless systems like Bluetooth, LiDAR, and GPS [119,120]. To achieve good UWB/MIMU data fusion results, the UWB distance estimates have to possess very low or no systematic errors. Therefore, the accuracy with which the UWB system can deliver these updates is very relevant to the accuracy that can be achieved by the data fusion-based position estimator.

The integrated UWB/MIMU sensor systems could bring a great improvement to the ambulatory 3D analysis of human movement (3D AHM) if they can achieve accuracies in position estimation similar to the vision-based measurement systems such as Vicon [119]. This is attributed to the fact that the vision-based measurement system is considered to be the ‘gold standard’ and is deemed clinically relevant for 3D AHM, with position estimation errors less than 1 cm [46,71]. Therefore, a systematic error of 1 cm or less in position estimation is targeted. However, the smallest errors in position estimation reported so far by these integrated UWB/MIMU sensor systems are around 4 cm [81,83], which is not sufficient for the 3D AHM application. Also, these were achieved in most ideal conditions, i.e., in clear Line of Sight (LOS) situations [119]. For the NLOS situation (a typical 3D AHM situation), almost all studies on the integrated UWB/MIMU sensors reported

position estimate errors greater than 10 cm [119,121,122]. Most of these studies indicate that the high errors in the UWB distance estimates as the main cause for these position estimate errors in UWB/MIMU data fusion [119]. This again suggests that improvement of the UWB distance estimates could potentially improve the accuracy of position estimation through UWB/MIMU data fusion to accuracies required in 3D AHM applications.

UWB systems are reported to deliver distance estimates with sub-centimeter-level accuracy in ideal controlled environments such as an anechoic chamber [108,120]. However, in real-life applications, this high accuracy can only be achieved in LOS situations, like in unobstructed free (outdoor) space [123]. In indoor environments, the accuracy of UWB typically tends to drop significantly because of the presence of complex varying obstacles such as furniture, human bodies, and building infrastructure (walls, floors, furniture, and pillars) that disturb the UWB ranging accuracy by causing NLOS situations and additional disturbances by reflections [124]. For application in 3D AHM, multiple UWB nodes would be mounted on the human skin or body surface, which would perform distance-ranging measurements between each other and sometimes also with external sensor nodes. In this application, NLOS situations caused by human body segments will occur regularly [120]. As a result, overestimation of distances would occur to an extent that suggests that the distance of the shortest pathway around the obstruction is measured [125].

There are multiple research on the mitigation of errors occurring due to NLOS situations and are all described in these comprehensive review articles [126,127]. However, only a limited number of research among them are aimed towards mitigating the effects of NLOS caused by human body [93,120,128-133], a typical NLOS situation of 3D AHM application. The lowest position estimation errors after utilizing these mitigation strategies were reported to be around 12cm [93], with all other methods higher than 20cm and these are still not suitable for the application of 3D AHM. A comprehensive study of UWB distance estimation error characteristics and behaviour in scenarios specific to 3D AHM is crucial for advancing research on developing targeted mitigation strategies tailored to this application.

The typical 3D AHM application scenario consists of distance measurements between on-body UWB sensor nodes and possibly a few external UWB nodes, all within the distance range of 0.2 m to 1.8 m. Besides, all the NLOS-induced errors are caused by human body segments being present either between on-body nodes or between an on-body and an external node. The UWB distance or ranging error characteristics found in the literature are mostly reported for LOS situations and NLOS situations caused by infrastructures in the measurement environment [127]. There are no studies on LOS situations within short distance ranges relevant to 3D AHM scenarios and only a few studies report on NLOS effects caused by human body segments [93,123,133-136]. All these reported studies on NLOS effects caused by human body, examined situations with the inter-node distances being 1 m or (much) larger, while typical 3D AHM situations would have distances around 1.5 m and smaller. Also, all of these reports only considered scenarios with a human subject present in between two ranging nodes at some distance, while this was not studied for two or more on-body sensors. The study by Jie et al. [123] and Tian et al. [93] were the only reported NLOS experiments among the identified literature that measured the distance between a single on-body sensor node and one fixed anchor node at some distance.

To the best of the authors' knowledge, there are no studies that study the errors of UWB in short ranges relevant for 3D AHM scenarios in both the LOS and for NLOS due to human interference, as well as no studies on errors in distance between on-body sensors. Also, there is very limited research and information on the behavior of UWB sensors in NLOS situations caused by the human body. Therefore, this article aims to study the UWB distance estimation performance and error characteristics under conditions typically occurring in the 3D AHM application, with the purpose of identifying the possibilities to maximize future mitigation of these errors in the intended application. The novelty introduced by this article lies in the examination of specific conditions for 3D AHM that have not been previously explored:

1. Distance errors in LOS situations for short ranges (0.2 m and 1.8 m) relevant to 3D AHM.

2. Distance errors in NLOS situations caused by the human body, both when both UWB sensors are on the body and when one sensor is on the body with the other off the body.
3. Distance errors in NLOS situations caused by varying thicknesses of the human body, achieved using simulated human body segments of different diameters, all within the distance ranges relevant to 3D AHM.

The remainder of the article is organized as follows: Section 3.2 outlines the detailed methodology for error characterization, including a description of the UWB measurement system used in this study and the experimental setup. Further, describes the experimental scenarios designed for error characterization. Section 3.3 presents the observed error characteristics across the various tested scenarios. Finally, Section 3.4 offers an in-depth discussion of the observed error characteristics and analyzes their implications for the intended application of 3D AHM.

3.2 Methods

3.2.1 UWB measurement system

The UWB sensors or measurement system used in this research was a customized fully integrated UWB/MIMU sensor hardware platform developed in-house, named ‘UMIMU’ sensor system (Ultra-wideband Magnetic Inertial Measurement Unit sensor system; Figure 3.1(a)). The UMIMU sensors included a UWB transceiver module DWM1000 (Qorvo Inc., Greensboro, USA) combined with a 9-axis MTi-3 MIMU (Xsens Technologies, Enschede, Netherlands). The DWM1000 UWB module used in this paper was operated in channel 2 with a center frequency of 3.9 GHz (bandwidth of 3.7 GHz to 4.2 GHz), utilizes Binary Phase Modulation (BPM) combined with Binary Phase Shift Keying (BPSK) for signal modulation and supports a theoretical range of up to 300 m. An STM32F722R microcontroller (STMicroelectronics, Geneva, Switzerland) controlled the node configurations, the node role attribution and the effective swarm topology and ranging in a round-robin scheme optimized for minimal (and known) time between individual ranging actions between node pairs within each update. Additionally, it also controlled the data transport of UWB distance measures as well as the full 3D MIMU kinematics data

from UMIMU nodes to the PC. All UMIMU nodes were identical in hardware configuration and were calibrated for antenna delay following manufacturer specifications, ensuring that any hardware-induced bias remained consistent across all measurements. The UMIMU was also equipped with a USB port for charging, configuration, and data communication.

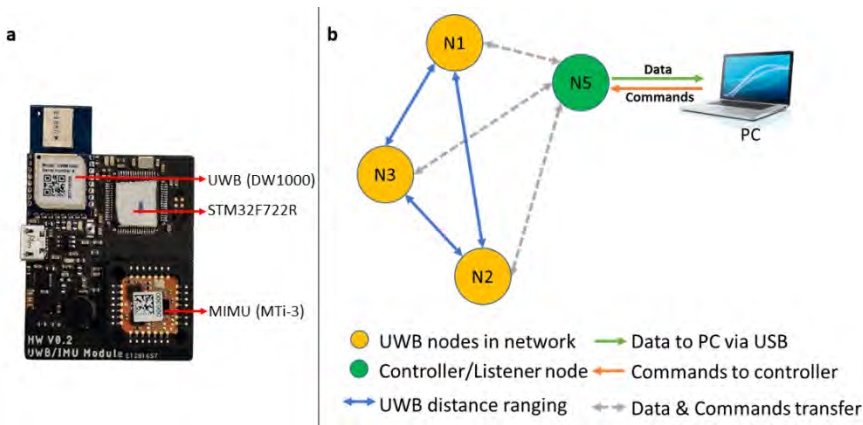


Figure 3.1: (a) UMIMU sensor hardware; (b) Typical UMIMU sensor system configuration with swarm topology and their functioning.

This paper examines the performance of the UWB sensors in the UMIMU modules under (N)LOS situations. Therefore, for reasons of readability, in the rest of the paper we refer to the UWB sensors in the UMIMU modules simply as ‘UWB nodes’. The UWB nodes estimate the distance between two ranging nodes by the Alternative Double-Sided-Two-Way Ranging (AltDS-TWR) method as described in Neirynek et al., 2016 [137]. Also, all the UWB nodes used in this study were (re-)calibrated for the antenna delay settings to minimize ranging errors as per the manufacturer’s manual [138]. The UWB data were recorded at an update rate of 27.73 or 36 samples per second for a set of 3 or 2 ranging UWB nodes in the network, respectively. The data of the MIMU sensors in the UMIMUs was recorded, but was only used to synchronize the UWB ranging data with the data of the vision-based reference system. The MIMUs delivered 100 samples per second, comprising 3D orientation, acceleration, and angular velocity.

The UMIMU sensors were specifically developed for the intended use in a typical 3D AHM application with only on-body UMIMUs in a swarm topology. In this topology, ranging operations are performed between all possible UWB node pairs

in the swarm. The physical configuration of the UWB sensor system comprises three or more nodes (which are all physically the same), of which one node assumes the role of ‘controller node’ and the remaining nodes assume roles of ranging initiator or ranging responder (Figure 3.1 (b)). The controller node always remains connected to a PC via a USB connection and is used to configure and control the node roles, ranging operation, and collecting all the distance estimates between the ranging UWB nodes for the PC. Also, the MIMU data is transported from all ranging nodes through the controller node to the PC, where it is stored along with the ranging data for further processing (in this case, only for synchronization purposes).

3.2.2 Distance estimation error definition

The true distance between two ranging UWB nodes (sensor i and j) is defined as $D_{true\ i,j}$ and the estimated distance between the ranging UWB nodes is defined as $D_{uwb\ i,j}$. The distance estimation error $D_{error\ i,j}$ is defined as the difference between the estimated distance and the true distance:

$$D_{error\ i,j} = D_{uwb\ i,j} - D_{true\ i,j} \quad 3.1$$

3.2.3 Error characterization experiment setup

The true distance between the UWB nodes, $D_{true\ i,j}$ was estimated using a vision-based motion analysis system (Vicon Motion Systems Ltd, Oxford, UK), which for this study is regarded as ‘gold-standard’, as this system is capable of sub-centimetre level accuracy in estimating marker positions and distances (Figure 3.2 (a)). The UWB node position was defined as being located at the centre of the physical UWB antenna. As placing a physical reflective marker on the UWB antenna would very likely influence the ranging process, each UWB nodes were placed on a sensor-holding rig with 3 Vicon markers attached at some fixed distances away from the UWB antenna (Figure 3.2 (b)). The reflective markers on the sensor-holding rig were labelled M1 to M3 (Figure 3.2 (b)). To estimate the position of the UWB node with respect to the rig an initial rig calibration procedure was performed, where the fixed relation between the UWB node antenna and the rig markers was derived. This was achieved through a static measurement of the rig markers with the Vicon system, with an additional temporary marker placed on the UWB antenna. This rig

calibration measurement was then used to estimate the position of the UWB node during the experiment by utilizing the derived relation between the rig frame and sensor frame. Also, the UMIMU orientations were derived from the rig orientation.

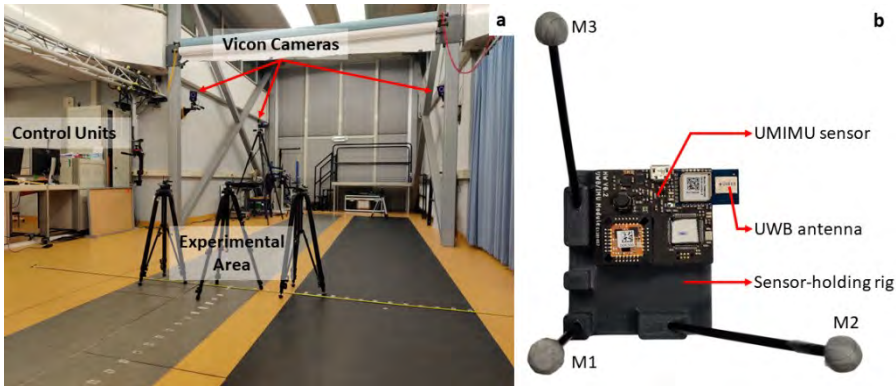


Figure 3.2: (a) Vicon optical motion tracking and analysis system; (b) Rig with the UMIMU sensor and the Vicon optical markers M1 to M3 on sticks at some distances of the UWB antenna.

3.2.4 Error characterization pipeline

The error characterization process involved multiple steps that were clustered into four phases: the preparation phase, the data collection phase, the data processing phase, and the error estimation phase (Figure 3.3). The preparation phase involved setting up both the Vicon measurement system and the UWB nodes. This phase comprised the calibration of the Vicon system, followed by the UWB node antenna delay calibration and the rig calibration procedure as explained in Section 3.2.3. The data collection phase involved the collection and storage of all the data from all 3 (or 2) UWB nodes and the Vicon system in all the experiments. The data processing phase consisted of estimating true distances from Vicon, processing measurements of the UMIMU sensors, synchronizing both the UMIMU and Vicon measurement systems, and preparing them for error computation. First, the true distances between the sensor nodes $D_{true\ i,j}$, were computed using the Euclidean distance method based on the marker positions measured by the Vicon system. Additionally, node accelerations, \mathbf{a}_i^{vicon} were obtained by double differentiation of these positions. The accelerations from the MIMU sensors of the UMIMU sensor system, \mathbf{a}_i^{uwb} were interpolated if there are any missing samples, and distances measured by the UWB nodes, $D_{uwb\ i,j}$ were parsed into readable arrays. Synchronization of the UMIMU

and Vicon systems was then achieved through cross-correlation of acceleration magnitudes derived from both systems, sampled at 100 samples per second (i.e., the norm of a_i^{vicon} and a_i^{uwb}).

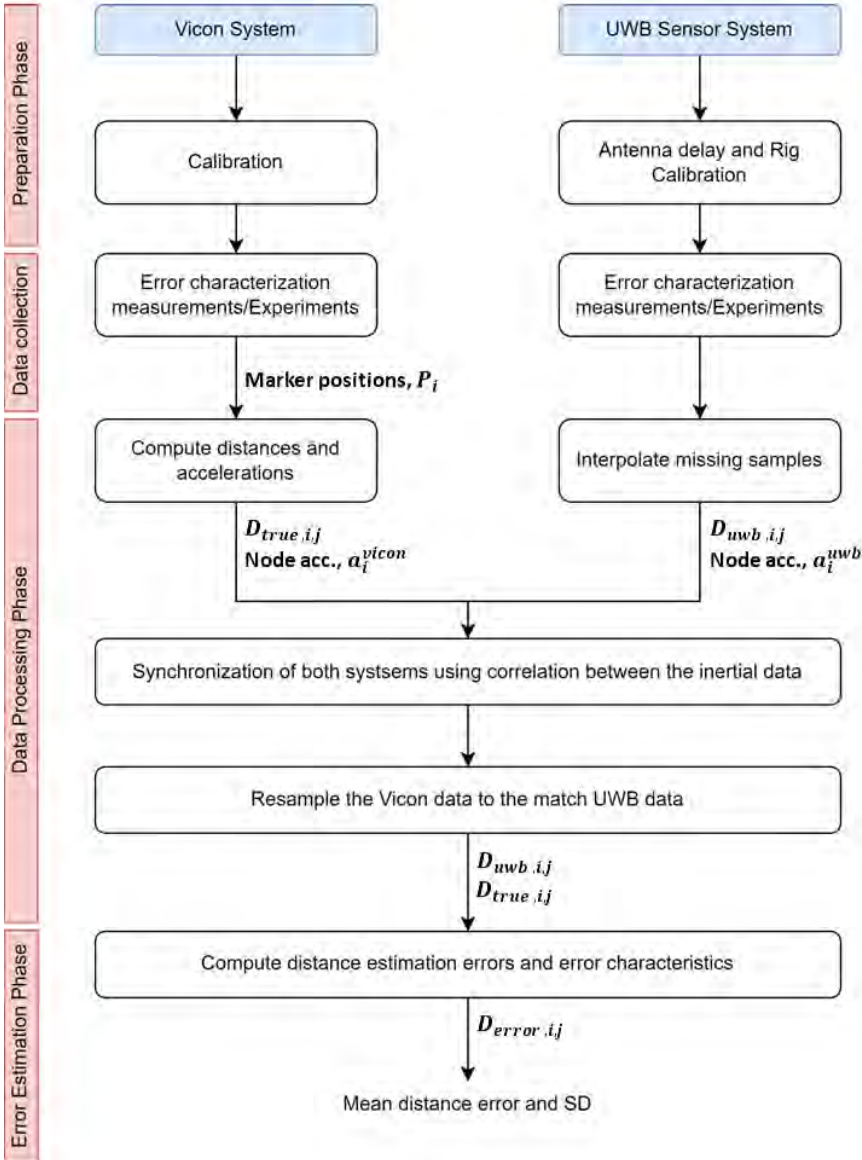


Figure 3.3: Illustration of the UWB error characterization pipeline.

Subsequently, after the synchronization between both systems, the Vicon data was resampled to match the UWB update rates and instances using spline interpolation.

Finally, for the error estimation phase, the errors in the distance estimates $D_{error\ i,j}$ were estimated by applying equation 3.1 for the resampled and synchronized distances from the UWB, $D_{uwb\ i,j}$ and the distances from Vicon measurement system, $D_{true\ i,j}$.

3.2.5 Experimental scenarios

The experimental scenarios were designed to consider the relevant situation of the 3D AHM. For both the LOS and NLOS conditions, several scenarios were tested. This includes examining the effects of relative sensor position and relative sensor orientations in LOS conditions relevant to 3D AHM. Followed by the examination of the effects of NLOS caused by a subject's thorax and simulated human body segments, specifically PVC pipes filled with water with varying diameters as physical models of human limbs.

LOS in a static measurement scenario (Scenario 1)

In the static LOS measurement scenario, inter-UWB distances were measured with the sensor nodes positioned in multiple fixed positions and orientations, maximally securing LOS situations at all times. The objective of these measurements was to study the effect of antenna orientation and inter-node distances on their distance estimation accuracy. The experimental scenario comprised a 'central node', CN positioned on a tripod in a central location M and two 'free nodes' FN1 and FN2 mounted on tripods. The UWB nodes were always positioned in the same horizontal plane (xy-plane) of 0.84 m above the floor more or less in the center of a relatively large movement lab space (Figure 3.4 (a)). The central node was kept in the same position and orientation during the complete session, while the tripods of the two free nodes were moved to different positions for each measurement. A nomenclature was defined to describe the positions of the UWB nodes in the lab space and the horizontal direction of the two nodes with respect to each other. The 'ranging heading' was defined as the angle between the central node and one of the free nodes, with the global x-axis of the Vicon system reference frame chosen as a heading of 0°. The 'antenna heading' was defined as the direction in which the antenna of a node is facing using the same angles as used in the ranging heading. Since, DWM1000 antenna has a non-isotropic radiation pattern, antenna orientation

can influence ranging accuracy. Specifically, on-body sensor orientation changes during movement, and therefore testing different antenna headings helps identify and mitigate orientation-related bias in 3DAHM applications. An example of the central node with an antenna heading of 0° , and two free nodes at ranging heading 315° and 135° with respect to the central node is depicted in Figure 3.4 (b).

In four different LOS protocols, distance estimates were collected in different combinations of free node distance to M, ranging heading, central node heading, and with free nodes elevated. In LOS-Protocol 1, the central and free nodes were placed at a height of 0.83 m above the floor. The free nodes were positioned on opposite sides of the central node and the distance estimates between the central node and the two free nodes were recorded for 30 seconds in each position. For each ranging heading the distance from the central node was increased in steps of 0.1 m after every 30 seconds of measurement, starting from a distance of 0.2 m up to a distance of 2 m. These measurements were repeated in all the 8 different ranging headings (Figure 3.4 (a)).

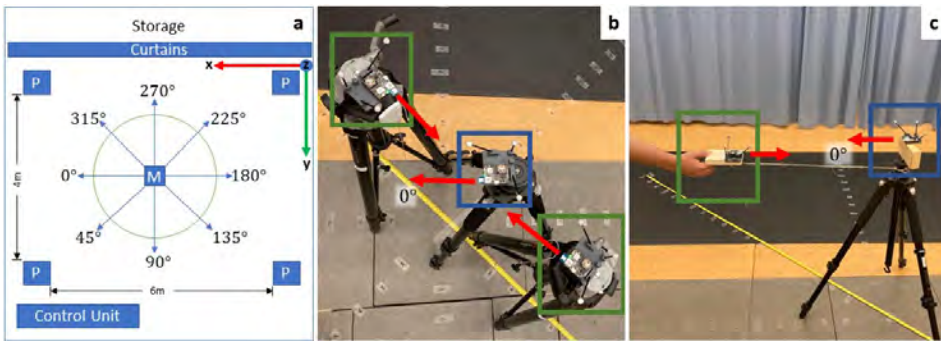


Figure 3.4: Overview of the LOS measurement scenario. (a) Schematic map of the room (not to scale), where P are metallic poles, and M is the position of the central node. The eight blue arrows indicate the eight different directions in which the two free nodes were moved. (b) Top view of the LOS static measurement with one central node (blue square) and two free nodes (green squares). The free node in the top left and bottom left is positioned in ranging headings 315° and 135° , respectively. (c) Overview of LOS dynamic measurement with central node (blue square) and one handheld free node on a wooden block (green square), at a fixed radius from the central node. (Red arrows in the figure indicate the antenna heading)

In LOS-Protocol 2, the same procedure as LOS-Protocol 1 was repeated for the ranging headings 90° and 270° , while keeping the antenna headings of the free nodes also at 0° (in the same antenna heading as the central node). This ensured all

antennas of the ranging UWB nodes were parallel to each other. In LOS-Protocol 3, the same LOS-Protocol 1 was repeated, but with the antenna heading of the central node inverted, i.e., having an antenna heading the ranging direction of 180° . Also, this measurement was only performed with the free nodes for the four ranging headings of 0° , 135° , 180° and 315° respectively. In LOS-Protocol 4, LOS-Protocol 1 was repeated, but with the antenna heading of the free nodes turned upwards and the heights of the free nodes now being increased to 125.5 cm above the floor. The central node stayed at a height of 0.83 m and this setting creates a perpendicular antenna heading between the ranging nodes. This LOS-Protocol 4 was performed for the ranging headings of 0° , 135° , 180° and 315° respectively.

LOS in a dynamic measurement scenario (Scenario 2)

In the dynamic experiment scenario of the LOS situation (LOS-Protocol 5), the UWB distance measures were acquired during a continuous change in position of the free node, with the central node remaining at its fixed position in location M at all times as seen in the static protocols. The moving free node was placed on a wooden block that was kept at a fixed distance from the central node by keeping a rope attached to the central tripod fully stretched (Figure 3.4 (c)). The wooden block was handheld by the researcher with a stretched arm to keep his body at a maximal distance to minimize the effects of body proximity to the ranging node (Figure 3.4 (c)). During the measurement, the researcher walked three circles around the static tripod, keeping the distance between the two ranging nodes fixed by keeping the rope fully stretched at all times. In total eight measurements with radius of 0.5 m, 1 m, 1.5 m, and 2 m were conducted for each of the two free nodes that were also used in the static trials.

Pilot experiment NLOS introduced by human body (Scenario 3)

In the NLOS situation introduced by the human body, static measurements were performed with a human torso as LOS blocking element. In this experiment, the central node was placed on a tripod at location M and the two free nodes were placed on the body of the human test subject (Figure 3.5 (a)). One of the free nodes was placed at the frontal side of the subject on the sternum (1.2 m above the floor) and was called the ‘ventral node’, VN (Figure 3.5 (b)). The second free node also named

the ‘dorsal node’, DN was placed on the dorsal side of the subject at the same height as the ventral node (Figure 3.5 (c)). The subject was facing the central node at all times, thereby ensuring an NLOS situation between the dorsal node and ventral node, and also between the dorsal node and central node. Additionally, the distance between the ventral node and the central node was also measured. Though this specific distance measurement was in an LOS situation, it was still measured to study the effects on distance estimate due to close contact of the sensor with human body in LOS situations. The measurement protocol was similar to the one of LOS-Protocol 1, with the distance between the frontal node and central node increasing from 0.2 m by approximately 0.1 m every 30 seconds up to 2 m and in all the 8 ranging headings. The dorsal node remained at a fixed distance from the frontal node, while the distance with the central node was increased in steps of 0.1 m as moved along with the frontal node. Due to the limited field of view of the Vicon system, the true position of the dorsal node could not be estimated for distances larger than 1.3 m for the ranging headings 45° , 90° , 270° and 315° . Therefore, these were excluded from the analysis.

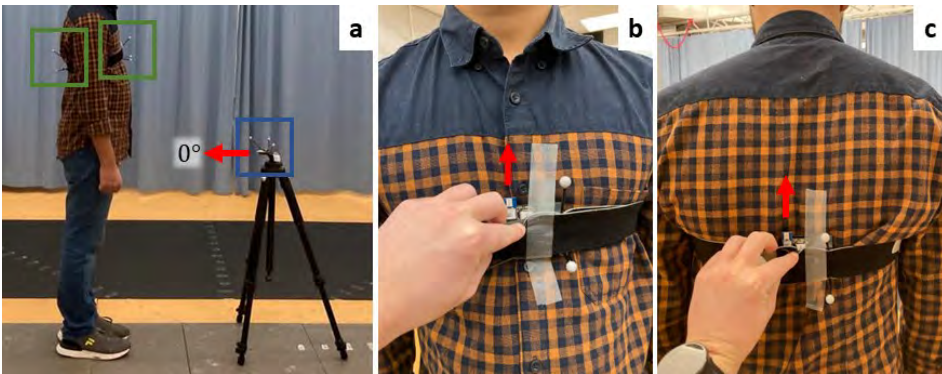


Figure 3.5: (a) Overview of the measurement setup with central node mounted on a tripod (blue square), and two nodes mounted on-body (green square), where human body acts as an NLOS obstacle between the DN and VN, as well as DN and CN. The red arrows indicate the antenna headings of the tripod node and respectively (b) the dorsal and (c) frontal body-worn nodes in more detail.

NLOS introduced by defined structures (Scenario 4)

For the experiments in scenario 4, the NLOS situations occurring when UWB nodes are used on a human body were emulated by using water-filled PVC pipes with

varying diameters as a model for the human body. PVC was chosen to be the material of the container because of its relative permeance to electromagnetic fields causing minimal additional signal disturbance. Three PVC cylinders with diameters 4, 8, and 12.5 cm and a length of 80 cm were filled to the brim with water and subsequently sealed to ensure the safety of the measurement equipment and lab space. The selected diameters were chosen to represent a range of human limb and lower-torso segment sizes while maintaining a controlled and reproducible setup, with the primary intention to examine the systematic influence of obstacle diameter on ranging errors.

A custom wooden measurement platform was constructed that holds the pipes in an upright orientation and allows accurate and quick (re)positioning of the ranging UWB nodes at any position (Figure 3.6). The platform consists of a wooden base (1 m x 0.5 m plywood base) with guide rails on both the horizontal and vertical axis. It also consisted of two vertical sensor holders that can be moved in the horizontal plane along the guide rails (Figure 3.6 (a)). Rulers were attached along the guide rails to allow free and accurate placement of vertical sensor holders in a horizontal area of 0.8 m to 0.5 m. The platform was leveled through adjustable legs at its four corners and the UWB nodes were mounted at a height that was half of the length of the pipes. The center point of the platform was defined as the origin of the xy-reference frame. The PVC cylinder (simulated human body NLOS obstacle) was positioned at the center of the measurement platform in an upright position (Figure 3.6 (b)) with the two UWB nodes on each side of the obstacle. The true distances $D_{true\ i,j}$ between the UWB nodes were derived from the measured position of Vicon markers placed on the sensor holders. The true position of the UWB node antennas on the vertical sensor holders was calibrated with respect to the markers on the base of the sticks by performing an extra Vicon measurement with an extra marker positioned on the UWB antennas.

Two NLOS protocols were performed. In NLOS-Protocol 1, the pipe was placed in the origin and two UWB nodes were placed on opposite sides of the pipe on the X-axis. The UWB node on the left side of the pipe ‘node 1’ (Figure 3.6 (a)) was kept fixed at a set distance x_1 from the pipe (NLOS obstacle). The UWB node on the right side ‘node 2’ (Figure 3.6 (a)) was positioned along the x-axis in steps of 1 cm starting from the closest point on the surface of the pipe to 0.3 m away from the

central pipe, indicated by x_2 . This was repeated for multiple fixed distances x_1 in increments of 1 cm. For each combination of positions x_1 and x_2 data was recorded with both the UWB and Vicon sensor system simultaneously for 10 seconds after the researcher had moved away from the platform. Before performing the NLOS-Protocols, a baseline measurement was obtained by performing the same protocol without the NLOS obstacle (PVC pipe), to identify and eliminate the additional errors caused by the measurement setup.

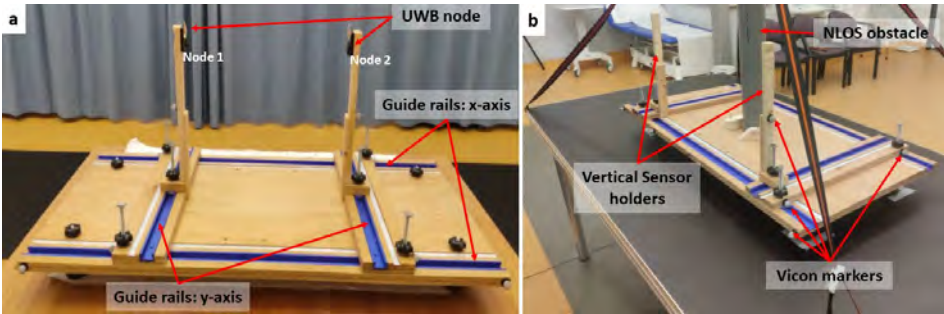


Figure 3.6: (a) Specialized platform for the NLOS experimental scenario; (b) A typical scenario during an experiment with the NLOS situation introduced with a PVC pipe in between ranging sensors on the setup.

In NLOS-Protocol 2, data was gathered in different situations of the pipe (partially) eclipsing the line-of-sight between the two sensors. The pipe was kept fixed in the origin and both the UWB nodes were kept fixed along the x-axis with the distance between the pipe and each UWB node same (i.e., $x_1 = -x_2$, where x_1 and x_2 are the positions of node 1 and 2 in x-axis respectively). Both the UWB nodes were moved in parallel along the entire y-axis (so always $y_1 = y_2$) in step sizes of 1 cm and 0.5 cm depending on the diameter of the pipe. For the pipe with a diameter of 12.5 cm, the step interval was 1 cm, while for the pipes with diameters of 8 and 4 cm, the step sizes were 0.5 cm. This was repeated for five different fixed distances along the x-axis, where x_1 being respectively 17 cm, 27 cm, 37 cm, 47 cm, and 57 cm.

3.2.6 Data analysis

The main error metrics used in this study are mean of the distance measurement errors, $D_{error\ i,j}$ and their standard deviations (SD) for a particular position and orientation used in the experimental scenarios. For all static experiments of LOS situations in Scenario 1 the mean of distance measurement errors along with their

SD were computed for each ranging heading and distance from a set of around 500 distance measurements (30 seconds at approximately 20 samples per second) at their respective positions. For the dynamic LOS experiments of Scenario 2, the mean of the distance measurement errors for each orientation was computed from the three circular movements made. For scenario 3, the mean and SD of distance measurement errors between the central node and ventral node on the body were computed for each ranging heading and distance from a set of around 500 measurements (30 seconds at approximately 20 samples per second) at their respective positions. Also, the mean and SD of distance measurement errors between both on-body sensors (ventral and dorsal node) were examined. For the NLOS experiments with the pipes of Scenario 4, again the mean distance errors along with their SD over each position with varying distances were computed.

3.3 Results

3.3.1 Ranging quality for LOS in a static measurement scenario

In all experiments of LOS-Protocol 1, the measurement error in the distance between the two free nodes and the central node, namely FN1-CN and FN2-CN were comparable and similar to each other in most measurement positions (Figure 3.7). For the ranging headings 90° , 180° , 225° and 270° , all the mean distance measurement errors for FN1-CN and FN2-CN were below 10 cm for almost all measurement positions. Also, the mean distance error for each of these ranging headings was below 7 cm (Figure 3.7). Conversely, for the ranging headings 0° , 45° , 135° , and 315° , the errors vary (mostly increase) with increasing distance between the ranging UWB nodes, also with mean distance errors higher than 10 cm for all ranging headings. The SD of the distance measurement was consistent and small (≈ 0.02 m) for almost all the ranging headings over all the varying distances. An exception was formed for some specific positions, where the SD was very high for ranging headings of 45° (for a distance of 2m) and 315° (for distances of 1.5 m, 1.6 m and 2 m).

For LOS-Protocol 2, with the antenna headings in parallel orientation, the mean distance measurement errors for both the ranging headings were equal to or lower than 10 cm for most of the distances (Figure 3.8). However, for a few measurements

in the ranging heading 90° the errors were greater than 10 cm, specifically for distances above 1.3m. The mean distance error for the two ranging headings 90° and 270° were $0.08 \pm 0.03\text{m}$ and $0.04 \pm 0.02\text{m}$ respectively. Similar to LOS-Protocol 1, the SD of the distance estimation was consistent and small ($\approx 0.02\text{m}$) for both ranging headings over all the varying distances.

Experimental results of LOS-Protocol 3, with the antenna heading of the central UWB node reversed (antenna heading: 180°) had comparable and similar distance measurement error for the node combination FN1-CN and FN2-CN, except for ranging heading 315° (Figure 3.9).

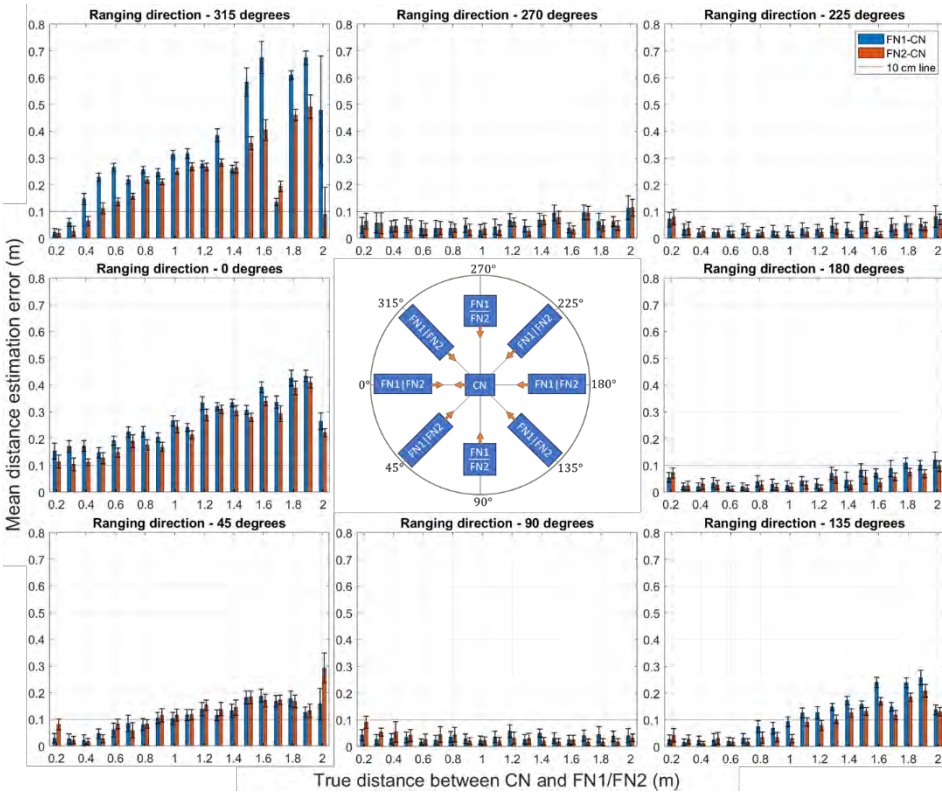


Figure 3.7: The mean distance measurement error and SD for the two ranging sensor pairs (FN1-CN and FN2-CN) in LOS-Protocol1 in all the eight antenna heading directions as well as multiple distances between 0.2m to 2m. The central figure is to represent the orientation of the sensors in this protocol, where the orange arrows indicate the antenna heading of the nodes.

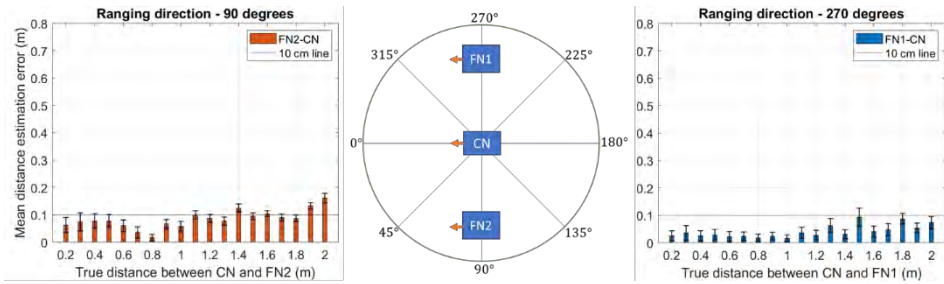


Figure 3.8: The mean distance measurement error and SD for the two ranging sensor pairs in the LOS scenario, with the antenna heading parallel to each other (LOS-Protocol2).

The mean distance measurement errors for the ranging heading 0° were lower than those of the LOS-Protocol 1, for both ranging node combinations. The errors in all measurements appear to increase with increasing distance. For the ranging heading 315° , the node combination of FN1-CN still exhibits high errors as the distance increases also with a high SD similar to LOS-Protocol 1. For the ranging heading of 90° , the node combination FN2-CN demonstrates errors mostly below 10 cm up to a distance of 1.8m. The SD of the distance estimation was consistent and small ($\approx 0.02\text{m}$) for almost all the ranging headings over all the varying distances, except for ranging heading 315° where SD was high with values up to 0.2m.

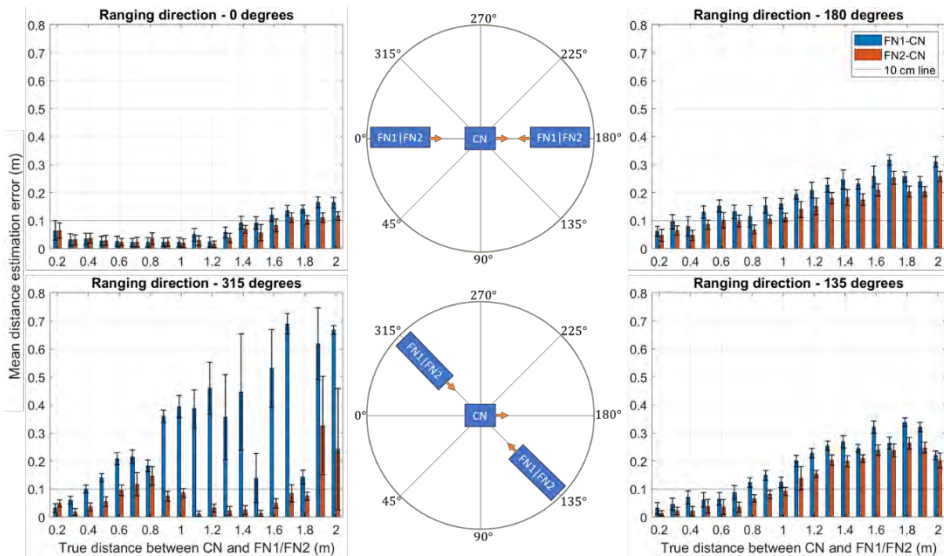


Figure 3.9: The mean distance measurement error and SD for the two ranging sensor pairs in LOS-Protocol 3 with the antenna heading direction of the central UWB node reversed.

For LOS-Protocol 4, the mean distance measurement errors were mostly below 10 cm and were also lower than the UWB-ranging situation in all the previous LOS protocols (Figure 3.10). For directions 0° and 315° , there is a trend toward smaller errors as the distance between the nodes increases. In contrast, for 180° , the mean errors increase as the distance between the nodes increases. In this protocol, the SD of errors over all ranging headings and distances was consistent and small (≈ 0.02 m). The mean distance error from the two sensor combinations for all 4 ranging headings of LOS-Protocol 4 was always lower than 6 cm.

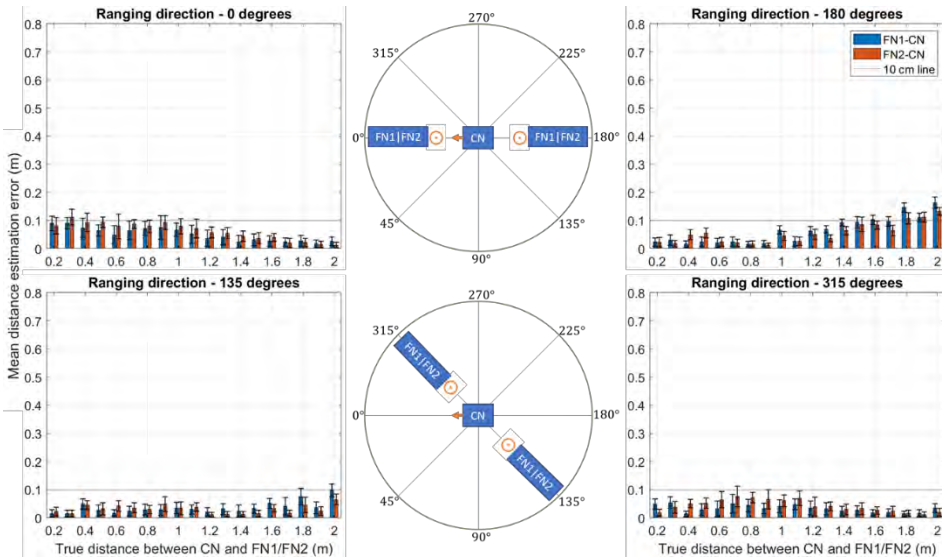


Figure 3.10: The mean distance measurement error and SD for the two ranging sensor pairs in LOS-Protocol 4 with increased height from the floor. The orange arrow and circles indicate the antenna headings, where the circle is to represent the antenna heading upwards.

3.3.2 Ranging quality for LOS in a dynamic measurement scenario

For all four radii in the dynamic LOS measurement scenario, an increased error (peaks) around the antenna heading direction of 315° was observed (Figure 3.11). Also, for a higher radius of 1.5 m and 2 m, there is an increase in error around the antenna heading direction of 135° . The pattern of error is similar for all the radii, however, there is a slight increase in the overall error with an increase in distance of 1.5 m and above. The SD of errors was highly consistently below 3 cm, except for

the errors around the ranging heading 315° and around 150° for radii higher than 1.5 m. Both the mean distance measurement errors and SD were similar to the static LOS protocols for all ranging headings.

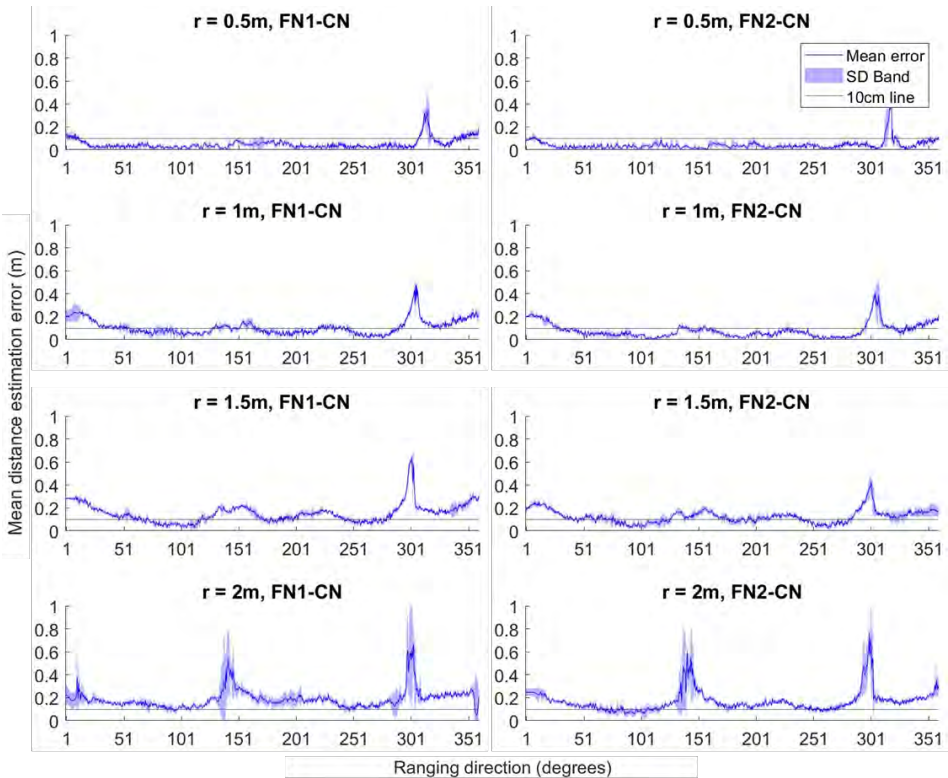


Figure 3.11: The mean distance measurement error and SD for the two ranging sensor pairs in the LOS dynamic scenario for all the ranging heading directions between 0° to 360° .

3.3.3 Ranging quality for NLOS introduced by human body

The NLOS situations introduced by the human body have a significant effect on distance estimation with higher errors than the LOS situation (Figure 3.12). The mean distance estimation errors between the UWB sensors on the back and sternum of the human subject (DN-VN) had a highly consistent error of around 0.53 m and a very low variability over varying ranging headings and distances ($SD < 0.01$ m). For the sensor node combination between the dorsal and ventral node, DN-CN shows very consistent mean distance estimation errors of approximately 35 cm. The ranging between the ventral node, VN and the central node, CN was in LOS

situations and the results indicate very similar distance estimation errors as seen in the LOS static scenario protocols. The mean distance estimation error from the three sensor combinations for all ranging headings was consistent with a small SD (Figure 3.12).

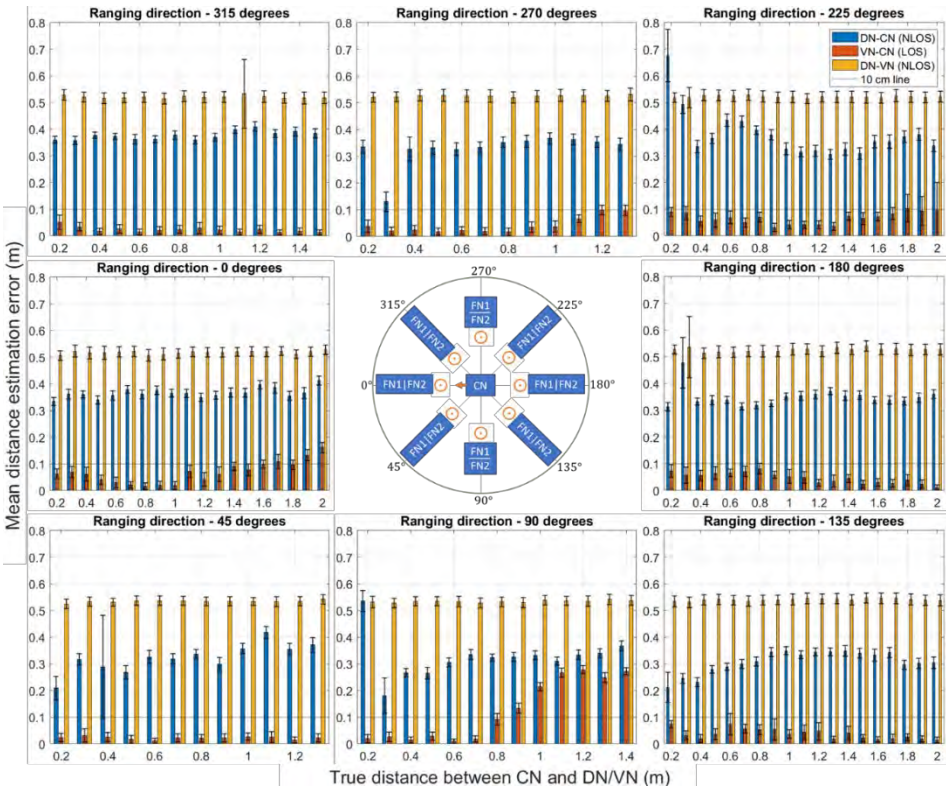


Figure 3.12: The mean distance measurement error and SD for the ranging sensor pair for NLOS scenario by human body in all the eight antenna heading directions as well as multiple distances between 0.2m to 2m. The central figure represents the orientation of the sensors in this protocol, where the orange arrow and circles indicate the antenna heading of the nodes. (the circle is to represent the antenna heading upwards).

3.3.4 Ranging quality for NLOS introduced by defined structures

The baseline distance measurements with the NLOS experimental setup show an effect of the setup on the distance measures between the UWB nodes (Figure 3.13). After the correction of the distance measure by the estimated baseline correction values the UWB distance measures show a stable measurement with minimal errors around zero (Figure 3.13).

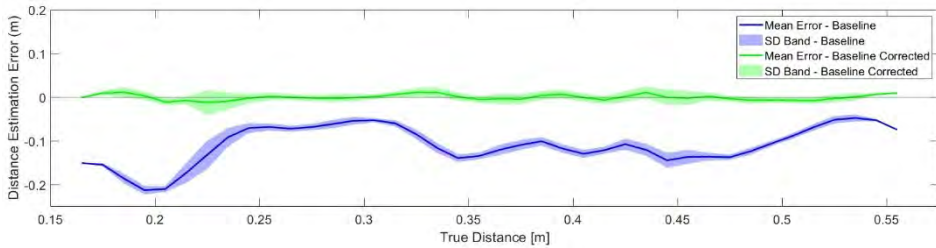


Figure 3.13: Baseline UWB ranging error as a function of the distance between sensors with no NLOS situation (blue) and baseline measurements after correction with the baseline error function (green).

Experimental results of NLOS-Protocol 1 showed mean distance errors that increased with the increasing diameter of the obstructing pipes (Figure 3.14). The mean distance measurement errors of NLOS situation by 4 cm pipe was always within 10 cm for most of the distance points. For the NLOS caused by 8 cm and 12 cm pipes, the errors increased with higher errors of 20 cm and above when UWB nodes were closer to the pipe. The SD for the baseline corrected mean distance errors are also provided in the graphs. The SD varied between 0.05 cm to 2.52 cm in NLOS with 4 cm pipe, while it was between 0.56 cm to 4.18 cm in NLOS with 8 cm pipe and the SD was between 0.06 cm to 3.30 cm in NLOS with 12 cm pipe.

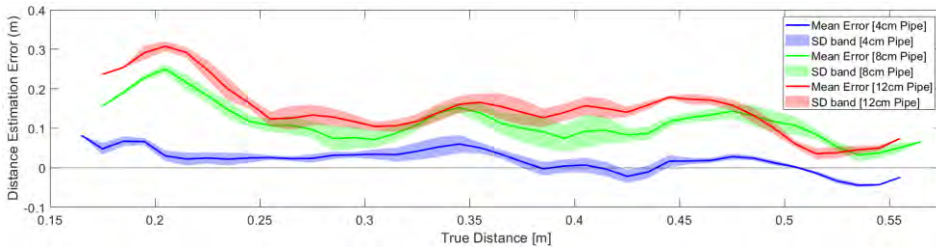


Figure 3.14: The mean distance measurement error (along with SD band) as a function of the distance between the ranging sensors from NLOS-Protocol 1, for the simulated NLOS situation with water-filled pipes of diameter 4 cm (blue), 8 cm (green) and 12.5 cm (red) respectively.

For the NLOS-Protocol 2, the mean distance estimation errors were minimal for the NLOS situation with a 4 cm pipe, and only a slightly higher error was found close to the pipe (Figure 3.15). For the other two NLOS obstacles, the position of the pipe is distinguishable from the ranging error as it increases when closer to the pipe. The errors always increased when closer to the pipe and dropped around the center of the pipe for all the NLOS situations of pipe with 8 cm and 12 cm.

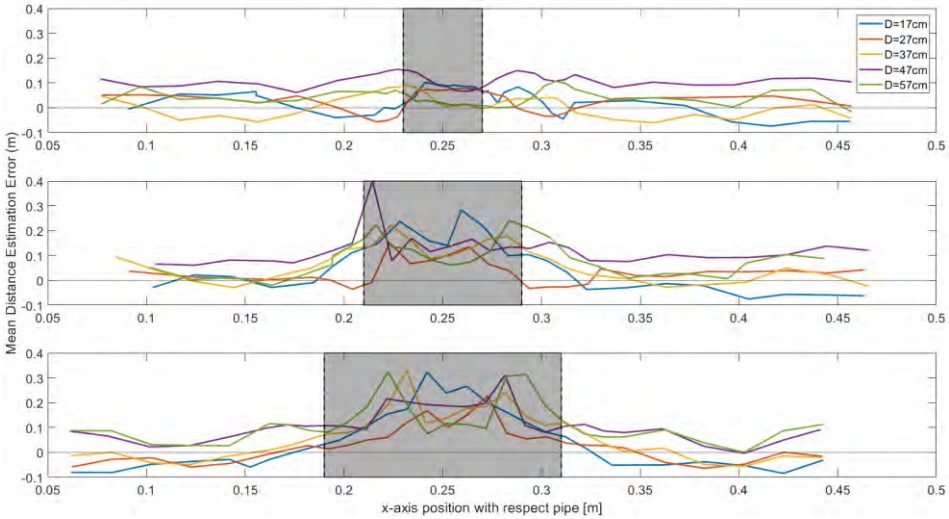


Figure 3.15: The mean distance measurement error as a function of position on the measurement table between the ranging sensors from NLOS-Protocol 2, for the simulated NLOS situation with a water-filled pipe diameter of 4 cm (top), 8 cm (middle) and 12.5 cm (bottom) respectively. The grey-shaded region indicates the position of the pipe.

3.4 Discussion

This study collected a comprehensive set of experimental data to examine the behavior of UWB node distance estimation errors under conditions relevant to the intended application scenario of 3D AHM. Different combinations of relevant ranging distances and sensor node orientations were examined in both LOS and NLOS situations. Firstly, the study provided a comprehensive distance estimation error analysis in static and dynamic LOS situations for the typical range of 3D AHM applications (0.2 m to 2 m). Secondly, a similar analysis was performed for the NLOS situation with two sensors mounted on opposite sides of the human thorax plus an external sensor at some distance. Following this, a more controlled NLOS situation, using water-filled PVC pipes simulating NLOS situations as they would be caused by human body segments, was studied. Inferences from the observed distance estimation error behaviour and its relevance to 3D AHM are further discussed in this section.

3.4.1 Distance measurement in LOS situations

The extensive study of the UWB distance measurement error in LOS situations was performed for two sensor node combinations (FN1-CN and FN2-CN). The resulting distance measurement errors from both sensor sets indicate that their performance was highly consistent, exhibiting very similar error values in almost all the experimental protocols. This indicates that the individual UWB nodes showed a consistent performance and provided confidence in the reliability of the measurement from the UWB sensor system being used. This also implies that sufficient care was taken to not influence the experiments by the presence of the human body (researcher) or other elements of the experimental set-up.

The results of LOS-Protocol 1 showed mean distance estimation errors below 6 cm for ranging headings 90° , 180° , 225° and 270° . They were slightly higher (between 8 to 12 cm) for ranging headings 45° and 135° , and very high (>20 cm) for ranging headings 0° and 315° (Figure 3.7). In LOS-Protocol 3, the antenna heading of the central node was rotated to 180° and the mean distance errors of ranging headings 0° and 180° were reversed compared to LOS-Protocol 1 (Figure 3.9). This indicates that the increased error in the ranging heading of 0° is related to reduced signal strength between two ranging nodes that typically occurs when their antennas are facing each other [139].

For all the other ranging directions with higher errors, like the ranging heading 315° , 45° and 135° , the asymmetry in the distance error graphs in Figure 3.7 suggests that this is not caused by ranging headings but by some unrelated cause. For example, the errors in the ranging direction 315° do not match the error from the ranging heading 45° . Also, unlike the case of headings 0° and 180° , in LOS-Protocol 3 the mean distance errors of ranging heading 315° remained similar to the previous condition but were not reversed, thus confirming that these errors were not an effect of ranging heading.

From the results of LOS-Protocols 1, 2 and 4, there is an effect of antenna heading found. In the LOS-Protocol 4, with the antenna headings of both nodes perpendicular to each other, the mean distance errors were always lower than 7 cm, suggesting it to be the best-relative antenna heading compared to others (Figure 3.10). The LOS-Protocols 2 with the antenna headings parallel to each other, were

the next antenna heading with lower errors than 8 cm. The antenna heading-dependent errors observed could possibly be attributed to the non-isotropic radiation pattern of the DWM1000 antenna [139]. However, from the LOS-Protocol 1, it is clear that the antenna headings when facing each other have different errors over varying ranging headings and distances as described previously. This suggests that for these specific antenna heading configurations there is an error caused by a parameter that is not ranging heading or distance alone.

The observations from all these LOS static protocols as mentioned above clearly indicate the presence of an additional error, which is not relevant to the antenna heading or ranging heading. Also, there was an increase in the mean distance errors above 1.5 m in most of the ranging headings suggesting that within the range of 0.2 m to 1.5 m, errors are small and consistent. These inferences from the LOS static protocols thus suggest that the effect is a function of UWB node position in the room (3D space) as it is a combination of the ranging heading and distance from the central node with fixed position. This was again confirmed by the LOS dynamic experiments, where the distance errors become very high at around the ranging headings 135° and 315° as observed in the LOS static protocols (Figure 3.11). In the dynamic experiments, this position-bound error manifests itself as a transient error occurring each time when the moving node passes specific positions, formed by specific combinations of ranging headings and distances. Also, these transient errors were clearly identified by very high variance (higher SD) in the distance estimates, which was otherwise very low and stable (≈ 2 cm).

When neglecting position-based disturbances, there are only systematic offset errors of around 6 cm. These systematic errors were very consistent and repeatable, as was indicated by the very small SD values of the distance estimates. This was also confirmed by Schmid et al. [140], where the errors were highly consistent and systematic offset of around 7 cm. Another study by Jimenez et al. [75] reported mean errors as small as 12 cm and an SD value of 13 cm for an indoor environment with ranging distances between 0 and 5 m. However, this study by Jimenez et al. was performed in a very dynamic measurement environment with strongly varying LOS and NLOS situation combinations. Though there were other studies in the literature, comparison of the results of this study against other studies was difficult due to varying measurement conditions. Most studies focus on ranges higher than 1 m (up

to 20 meters or more) [123,134-136], while this study focuses on ranges relevant to 3D AHM application (up to 2 m), providing a unique knowledge that has not been studied before.

3.4.2 Distance measurement in NLOS situations by human body

The UWB distance measurement errors in NLOS situations were studied through a pilot experiment with a (blocking) human body and under more controlled conditions with artificial obstacles with properties close to human body segments (water-filled PVC pipes). All the experiments in NLOS situations used parallel and perpendicular antenna heading configurations, as these had shown the best results in LOS situations. Additional distance estimation errors were observed for the situation of ranging between nodes on the platform without a pipe present. It is assumed that these errors were caused by adverse effects of the complex mechanical platform. Under this assumption, an independent baseline measurement was performed and all data of the experiments in the NLOS situations were compensated by subtracting the baseline error. The fact that all compensation values for the same node distance were found to be very similar (SD <3 cm), regardless of the position of both nodes, suggests that the additional errors were a function of the distance between the nodes and not of the position of both nodes on the platform. All distance errors found after baseline compensation were consistently small (<1.3 cm) and similar to error magnitudes in the LOS experimental results (Figure 3.13), indicating a valid compensation.

The pilot experiments in NLOS situation with sensor nodes on the human body showed consistent, stable, and systematic overestimation errors in the distances between the UWB nodes. Experimental results showed a constant mean distance estimation error of approximately 0.53 m between the dorsal node and the ventral node (DN-VN), for all the subject positions in the experimental region (Figure 3.12). These distance error estimations were highly consistent, indicated by the very low SD (<1 cm for all measurements). The errors seen in the human body NLOS situation fit the model that assumes that the distance estimate reflects the shortest distance around the obstructing body segment [125] and also are similar in magnitude to errors reported in [117]. Similarly, there was a consistent distance estimation error between 31 cm to 38 cm for distance measures between the dorsal node and the

central node (VN-CN). This consistent effect remained the same throughout multiple ranging orientations and varying distances, except for the ranging orientation 90° . This was possibly due to the closeness of the subject to the electronic control unit of the Vicon measurement system in this specific position. Considering the inference from previous experiments in LOS situation, this effect would be a transient effect around that specific position.

Besides the effect of NLOS by direct obstruction of the human body, the UWB node combination VN-CN provides insights into the effect of being in close contact with human body in LOS situations. The closeness to the human body did not appear to have an additional effect on the distance estimation, which was evident from the errors between the ventral node and central node being similar to, and as small as, those in the LOS situations without body presence.

Experiments with NLOS situations by defined obstacles (the PVC pipes) showed a consistent overestimation of the distances between UWB nodes, similar to what was observed in the NLOS experiments with the human body. The distance estimation errors were more prominent and larger in amplitude with increasing PVC pipe diameters (Figure 3.14). This suggests a strong relationship between the geometry of the obstructing object and the observed ranging error. Specifically, the amplitude of the ranging error was shown to be strongly linked to the size of the object, with the errors of the pipe with a diameter of 0.04 m being minimal and close to those of a pure LOS situation while the errors are larger for increasing pipe diameter. The error pattern again matches the simple wrap-around model that assumes that the distance estimate reflects the shortest distance around the obstructing pipe [125]. Though the mean errors increased, the SD of the distance measures by the UWB remained lower than 3 cm and were similar to those in the LOS measurement situation, indicating a repeatable measurement.

Only a few studies on the NLOS effect through the human body were found [93,123,133-136]. All these studies with the human body between the UWB nodes were studying ranging performance at distances larger than 1m. In [136], distance estimation error was reported at around 0.18 m and 0.15 m for a fixed distance of 4 m and 7 m respectively between the UWB nodes with a human obstacle in the middle. Although a direct comparison of estimation errors of our study against [136]

is not possible due to the different distance ranges investigated, a similar trend can be observed, where increasing the distance between the UWB node and the NLOS obstacle resulted in reduced estimation error. This observation resonates similarly with the inference of this study that a higher distance from the obstacle will result in less error than being close to the obstacle. Jie et al. [123] and Qinglin et al., [93] studied the NLOS effect by placing UWB nodes on humans. However, only measurements were performed between the UWB sensor on the human body and an external UWB anchor more than 1 m away. Therefore, comparing [123] in ranges at 1 m and above confirms our observations that the ranging errors were higher (around 30 cm) when in NLOS by complete obstruction through the human body and errors were lower than 10 cm for on-body UWB in LOS with an external node. In addition to studying errors in the ranges relevant to 3D AHM, this study provides a very unique knowledge on measurements between on-body sensors both with human body and defined emulated human body segments.

3.4.3 Suitability for application in 3D AHM

The incidental higher errors observed in the LOS situation measurement appeared to occur as a function of absolute position in the room, as explained by the experimental static data (Section 3.4.1). As in typical 3D AHM applications subjects are moving through space, these errors will mostly manifest as transient errors, which was confirmed in the dynamic experiment data (Section 3.4.1). In situations when a subject holds a sensor in these specific positions for an extended period, the sensor data becomes invalid. However, since this issue can always be detected through different means using the redundant data set, this is not expected to be a critical problem. When these errors manifest as transients, multiple opportunities arise to mitigate these error components, e.g., in the data fusion process of MIMU and UWB measurements with the proposed UMIMU sensors. Additionally, the UWB distance measurement fails when the distance between the ranging nodes is below 15 cm. However, with the commonly used sensor node placement on the human body in clinical gait analysis/3D AHM, this situation rarely occurs and typically manifests as a transient in the human movement data, which may be mitigated with the data fusion process.

Despite the UWB nodes being calibrated before the measurements following the manufacturer's indications (antenna delay calibration), a systematic residual bias error of around 6 cm was found in all measurements. This error level is considerably larger than the level deemed required for successful application in 3D AHM. However, as for each UWB node combination a specific consistent error magnitude was found, and a further improvement of the estimation error level seems feasible. This suggests that an additional systematic mitigation process for these persistent bias errors is feasible and should be researched in future studies. The perpendicular and parallel antenna headings configurations showed the smallest distance estimation errors (as observed in the results of LOS-Protocols 2 and 4). In terms of angles between the antenna headings of ranging UWB nodes, the ranging heading angles of 90° , 180° , 225° and 270° consistently showed the smallest errors. This information can be used to optimize choices in sensor orientation and position in sensor mounting protocols in 3D AHM applications. Since the orientation of on-body sensors continuously changes during movement, such heading-dependent distance errors may propagate into position estimation. Identifying and compensating for these effects through calibration or fusion algorithms is therefore important to maintain higher accuracy in 3DAHM applications.

The findings of this study suggest that NLOS situations caused by simulated human body segments will always cause an overestimation of the node distance that seems related to the size of the simulated body segment causing the NLOS condition. This suggests that human body segments with smaller diameters such as the forearm and shank will have a smaller influence on the distance estimation, while the trunk and thighs will cause more substantial distance measurement errors. In our experiments, the effect of occlusion appeared consistent and repeatable. Therefore, these errors could possibly be mitigated through additional smart and automated systematic mitigation techniques to facilitate an accurate and stable application in 3D AHM.

3.5 Conclusion

This article provides a comprehensive analysis of the distance estimation errors between UWB node pairs, specifically for situations relevant to 3D AHM applications that have not been studied previously. The error analysis was performed for node distances in a range typically expected in 3D AHM applications (0.2 m to

2 m). Also, the effect of different node orientations was studied. Both static and dynamic LOS situations were examined, along with NLOS situations with human body and water-filled PVC pipes as physical models of human body segments. In LOS configurations, this study found errors of the consistent magnitude of around 6 cm for specific combinations of the relative position of nodes, (simulated) body and node orientation. This suggests the need for additional systematic error mitigation methods for UWB sensors. Small, consistent effects on the estimation error were found as a function of the relative ranging heading of the node antennas, providing valuable information for future on-body sensor placement. In both LOS and NLOS situations, no significant effect was observed on the closeness of the UWB nodes to the (simulated) human body. Large errors around 40 cm were found as a function of only the absolute position in the room, probably caused by reflection interference. In typical applications of 3D AHM (in which all sensors move most of the time), these errors will appear as transient errors in the data. This provides opportunities for error mitigation and appropriate independent detection of the presence of these transient errors. In NLOS situations, a typical, consistent overestimation of the distance between UWB nodes was found. The amplitude of the distance estimation error in NLOS situations was found to be a function of the object size as well as a function of the relative position to the object and appeared additive in nature. These observations made on the consistent character of UWB ranging errors within distance range and conditions relevant to 3D AHM will help to develop mitigating strategies for these errors in actual UMIMU data fusion-based applications in human movement analysis.

Chapter 4

Novel calibration method for improved UWB sensor distance measurement in the context of application for 3D analysis of human movement

This chapter is published as:

Yogesh, V.; Grevinga, L.; Voort, C.; Buurke, J.H.; Veltink, P.H.; Baten, C.T.M. Novel calibration method for improved UWB sensor distance measurement in the context of application for 3D analysis of human movement. *Engineering Science and Technology, an International Journal* 2024, 58, doi:10.1016/j.jestch.2024.101844.

Abstract

Integrated UWB and MIMU sensor systems have become popular for pedestrian tracking and indoor localization, since this facilitates data fusion that improves position estimation accuracy by exploiting the complementary nature of their error sources. Integrated UWB/MIMU sensors also have great potential in only on-body use for 3D analysis of human movement, as with MIMU sensors alone accurate direct estimation of (relative) body segment position is not possible. For this, a position estimation accuracy with errors smaller than 1 cm is deemed required. The lowest position estimating error with integrated UWB/MIMU systems, reported so far, is around 5 cm. The main accuracy limiting factors were found to be the systematic errors in the distance estimates from the UWB sensor. Multiple reported attempts to calibrate for these systematic errors failed to achieve the desired accuracy. This article presents a novel distance-bias calibration method that minimizes the residual systematic distance estimate errors using multiple sensors in a swarm configuration. Validation was performed against synthetic reference data and against reference data measured with an optical motion tracking system. Significantly reduced systematic distance estimate errors (≤ 0.5 cm) were found. These results promise to facilitate significantly better position estimates in future UWB/MIMU data fusion.

4.1 Introduction

In modern ambulatory 3D analysis of human movement, Magnetic Inertial Measurement Units (MIMUs) have gained popularity due to their low cost, ease of use, and portability [38,66]. MIMUs typically provide 3D orientation data in an (inertial) world frame with consistently high accuracy. This is achieved by exploiting redundancy in measured 3D kinematics, including 3D angular velocity, linear acceleration and, often, earth magnetic field data from respectively the three axial rate gyroscopes, linear accelerometers and magnetometers. This is typically done through applying data fusion methods [38-40,141]. Also, in limited use cases 3D sensor displacement (changes in sensor position over time) is often estimated from the recorded 3D linear acceleration combined with the already estimated 3D orientation [141]. With the starting position known, the 3D position can be estimated in an inertial world frame. However, the accuracy of the 3D displacement estimates, and thus also of the 3D position estimates, is relatively low. They typically suffer from strong estimation drift errors, as double integration of acceleration data is required [42,43]. The integration typically produces high errors as its input signal is already contaminated with accumulated additional errors from the preceding data preparation process on top of the existing inaccuracies in the acceleration signal itself. This makes the application of this approach ‘as is’ not feasible for relative on-body position estimation, except for short measurements.

Various studies have proposed multiple alternative methods for improved estimation of relative position in the 3D analysis of human movement. These were usually utilizing assumptions on aspects of the movement performed by the human. This involves e.g., applying an extra optimization with constraints to the joint kinematics derived from biomechanical models devised for human movement [45]. This requires biomechanical model constraints that sufficiently fit the subject evaluated and also requires enough excitation (subject movement) for optimization convergence. It is not trivial that this is sufficiently fulfilled in e.g., people with movement disorders. Another example is the Zero-Velocity-Update (ZUPT) algorithm, which detects instances of the foot in stance closest to zero velocity (and foot-flat pose) and restarts the integration process delivering 3D displacement, effectively resetting the integration drift to zero, often combined with first-order integration drift removal for the preceding step [44,69]. However, these methods are

limited to walking in specific subjects and situations in which this foot placement aspect of walking is taking place sufficiently consistent and detectable, which is specifically questionable in patients. Also, the ZUPT method cannot be used to minimize integration drift in position estimation of sensors on any other body parts than the feet.

An alternate approach to these methods is adding an additional sensing modality to the MIMU sensor hardware, that directly provides time-invariant position or distance estimates. Sensing modalities that were proposed to improve the positional estimates, and were already tested in integration with MIMUs, are distance estimation using miniature Ultrasound (US) [55] and infrared (IR) [56] technology. However, the contribution to the analysis of human movement applications of US is limited due to interference problems when more US tags are used simultaneously [63,64]. The possible application of IR is limited by the strict requirement of direct Line of Sight (LOS) conditions [63]. Other sensor modalities that were proposed to provide position or distance estimates are Wi-Fi, ZigBee, Bluetooth, Radio Frequency Identification (RFID) and Ultra-wideband (UWB) [49-53,74]. Among these, UWB is reported to be the most accurate with errors lower than 10 cm [57,112].

Therefore, the integrated UWB and MIMU sensors have become popular and have been utilized by many authors for position estimation applications in the last decade [119]. However, to the knowledge of the authors, no articles have been published that utilize this for estimating body segment kinematics in ambulatory 3D analysis of human movement applications with only on-body sensors. Instead, only applications of pedestrian navigation and indoor subject localization applications were reported [119]. For successful application in the 3D analysis of human movement, the technical accuracy of an integrated UWB/MIMU method (UMIMU method) should be similar or close to that of vision-based systems, which are regarded to be the current 'gold standard' in clinical movement analysis [46,47]. This suggests that the accuracies of the integrated UWB/MIMU system should have a position estimation accuracy of <1 cm [71,72].

Current accuracies reported for integrated or combined UWB/MIMU sensor approaches are still far from the desired accuracy for application in 3D analysis of

human movement [119]. A majority of the articles reported errors greater than 10 cm and also as high as 1m, even for optimal Line of Sight (LOS) conditions. The purpose of adding the UWB modality to the MIMU is to stabilize integration drift in displacement/position estimation, by offering time invariant distance/or (relative) position updates to a data fusion-based estimator. Therefore, the quality with which the UWB system can deliver these updates has a great influence on the possible accuracy that can be achieved by the data fusion-based position estimator. Most studies integrating MIMU and UWB sensing have used UWB sensors from one particular market-leading manufacturer (DMW1000 from Qorvo Inc, Greensboro, USA) ‘as is’ and none of them mentioned performing any quality improving or testing calibration procedures [119]. Also, none of these articles mentioned applying the antenna delay calibration that is recommended by the manufacturer. Still, almost all articles report errors that are systematic and that are much larger than what the producing company claims to be achievable (“ ± 5 cm distance error with 99% probability”). This clearly indicates the presence of systematic errors much larger than what is required for application in 3D analysis of human movement in the UWB distance estimates, an observation that was also confirmed in other studies [142,143].

Multiple attempts to develop methods for calibration or correction of systematic errors in UWB distance estimates were reported in the literature [138,142-146]. All these studies except [142] targeted specific aspects of UWB internal parameters e.g., the error introduced due to the skewness between the clocks of ranging UWB sensor nodes [143,145,146], and antenna delays [138,144]. One study estimated distance errors between each sensor combination from the received signal strength (RSS) and only tested this at the exact same location [142]. As RSS strongly depends on environmental factor details, this paper generated strong doubts about generalizability. Among all the other calibration methods, the lowest systematic error reported to have been achieved after the calibration was around 3 cm [145]. Also, in initial (own) pilot studies the authors of this paper found persistent residual errors greater than 4 cm in structural ranging components, even after performing the recommended antenna delay calibration by Qorvo [138].

Summarizing all results reported, the presence of persistent substantial systematic errors is the main factor preventing a position estimation accuracy through UWB/MIMU data fusion that is required for 3D analysis of human movement. This

article proposes a generalizable one-time calibration method for reducing the systematic UWB distance estimate errors to sub-centimeters and validates its performance against the gold standard method within the distance value range relevant to 3D analysis of human movement. As such, the article examines whether this method could facilitate the future development of MIMU/UWB data fusion methods for this application. The method utilizes data from a swarm of UWB sensor nodes. It applies an optimization procedure that exploits the redundancy in a set of UWB node distance estimates recorded during a ‘random’ movement within the relevant distance range. For this, it uses a simple distance bias error model. In this article, this method is referred to as the ‘distance-bias calibration method’.

4.2 Methods

4.2.1 UWB ranging method and configuration

The UWB sensors used in this research estimate distances between sensor nodes based on the Time of Flight (ToF) information, which is also the most popular and commonly used technique for distance measurement using these sensors [147]. The distances were estimated using the available information on ToF and the known speed of the UWB transmission. For the ToF estimation, the method/algorithm implemented was the Alternative Double Sided-TWR (AltDS-TWR) [137]. The AltDS-TWR method is the most robust and popular approach used to deal with the internal clock drift between unsynchronized UWB nodes in ToF measurements [111]. This AltDS-TWR is also the current state-of-the-art approach used in most of the commercial UWB sensors such as the DW1000. In addition, the antenna delay calibration was applied, as recommended by Qorvo [138], for all the UWB sensor nodes that were used for this research.

Since the targeted use case application in this research is full body 3D analysis of human movement, a swarm topology is used for the UWB ranging, as opposed to the star topology typically used in tracking applications. The swarm topology uses a fully connected network that performs the UWB distance-ranging operation between all pairs of UWB sensor nodes present in the network. This typically delivers redundant data for estimating node relative positions applying e.g., an optimization approach. This swarm topology implementation is illustrated in Figure

4.1. In this implementation, one additional sensor node, not participating in the ranging, assumed the role of a controller and listener (green node in Figure 4.1). This ‘controller node’ was connected to a PC with a user interface for configuring and operating the sensor system. This node controlled the overall timing of the ranging protocol and relayed any operational command to the ranging sensors. It also acted as a listener device and collected all distance estimates from all nodes in the network along with the MIMU data and uploaded this data to a PC via USB for processing. This swarm configuration yields $(n-1)!$ distance estimates for a set of n UWB sensor nodes per update in a fully connected swarm of n sensors.

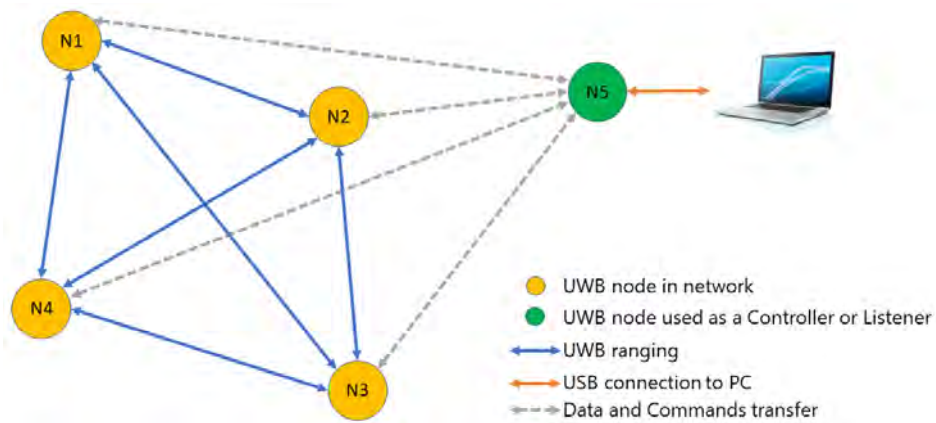


Figure 4.1: Configuration and swarm topology of identical UWB nodes. The nodes taking part in the ranging process (yellow) switch roles between the ranging initiator and ranging responder following a fixed round-robin scheme installed in all of them by the controller/listener node (green).

4.2.2 Proposed distance-bias calibration

Error model

The distance-bias calibration error estimation model in this research was built for multiple swarms of three UWB sensor nodes (the minimum required to form a swarm), also for reasons of optimizing computational load (Figure 4.2). The UWB sensor nodes participating in the ranging are identified as ‘Node i ’ where i corresponds to the sensor number with $i \in N$. A priori unknown position within the sensor node casings between which the distance was actually measured was named the UWB center point, C_i (blue dots in Figure 4.2). UWB center points, C_i

were assumed to be on or close to the antenna of the UWB unit inside the sensor casing. The distances measured between the C_i points in a pair of sensor nodes i and j were defined as $D_{uwb\ i,j}$ and the distance between the sensors $D_{i,j}$ is indicated with blue lines in the figure. A physical reference point on the sensor casing that can be measured using any external reference system is defined as the UWB casing frame origin, P_i . The position of P_i with respect to the global reference frame was represented as \vec{P}_i (yellow vectors). The position of UWB center point, C_i with respect to the UWB casing frame origin, P_i was represented as UWB center point vector, $\vec{C}_{g,i}$ in the global frame. Since all the UWB nodes were physically identical in hardware and ran the same embedded software, it was assumed that all the vectors $\vec{C}_{g,i}$ (orange vectors) are identical for all the sensor nodes in the sensor frame and will be always represented as \vec{C}_s . The position of UWB center point C_i relative to the origin of the global reference frame is indicated by $\vec{K}_{g,i}$ (green vectors).

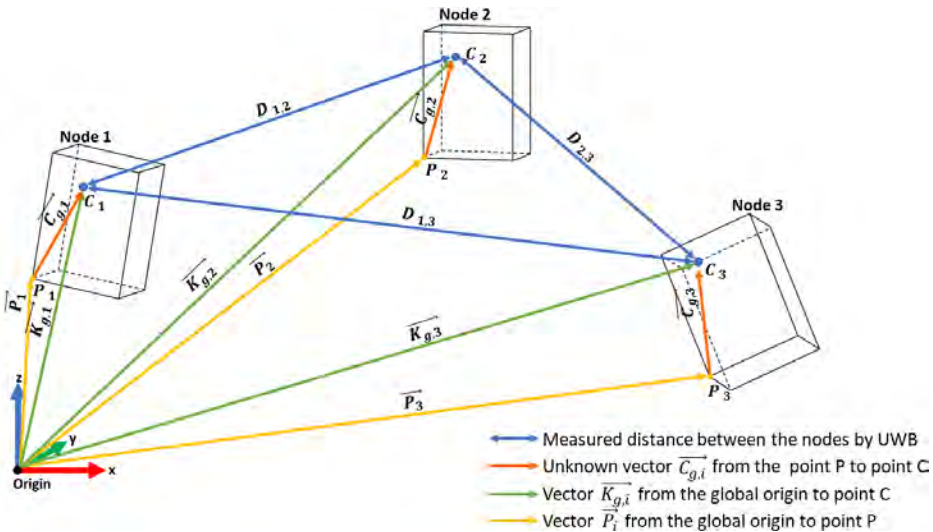


Figure 4.2: Illustration of the swarm measurement model. Note that the externally observable distances P_i (e.g. by a reference system) are different from the measured distances C_i in any situation except the situation in which the 3D orientation of all sensor nodes is exactly equal.

The error model was built based on the assumption that both the UWB nodes participating in a ranging operation contribute individually to the bias error in the distance estimated with a fixed contribution. It is assumed that the main errors in determining the ToF and distance are formed by systematic, but unknown, time

delays, that are caused by delays inside sensor hardware and software and which therefore are not related to the distance between the sensors. All these probable error causes are assumed to occur to the same extent in each ranging operation. Besides this, these errors can be generalized as a single error corresponding to each sensor irrespective of the source of error being attributed to transmission and reception errors, since the AltDS-TWR ranging protocol ensures that both operations occur twice in each sensor. Consequentially they are modeled as sensor-specific bias errors. Earlier studies into ranging errors within the relevance of human tracking did not report an effect of the distance between the ranging UWB nodes on the reported distance estimation [119]. This suggests that the observed non-random estimation error components were mainly pure bias errors and did not contain gain effects. This was again confirmed by an initial extensive error evaluation of all pairs of two UWB sensor nodes within the distances relevant for 3D analysis of human movement. Therefore, in this study estimation errors were modeled as pure bias errors. This allowed for the distance estimation bias errors to be modeled as the sum of the two bias error contributions eb_i and eb_j of both involved UWB sensor nodes i and j . Then the estimated distance between them, $D_{uwb\ i,j}$, can be written as

$$D_{uwb\ i,j} = D_{true\ i,j} + eb_i + eb_j \quad 4.1$$

Here, $D_{true\ i,j}$ is the true distance between the two UWB Center points C_i and C_j . Considering the ranging operation between two UWB sensor nodes i and j in a swarm of n sensor nodes, the true distances between the nodes i and j , $D_{true\ i,j}$ can be also defined in terms of the global coordinate vector to the UWB center point, \vec{K}_g and is given as

$$D_{true\ i,j} = |\vec{K}_{g,i} - \vec{K}_{g,j}| \quad for\ i,j \in [1, n] \quad 4.2$$

combining equations 4.1 and 4.2, and defining them in terms of the true distance $D_{true\ i,j}$ gives

$$D_{true\ i,j} = |\vec{K}_{g,i} - \vec{K}_{g,j}| = D_{uwb\ i,j} - eb_i - eb_j \quad for\ i < j \quad 4.3$$

The position of C_i relative to the origin of the global reference frame, $\overrightarrow{K_{g,i}}$ can be derived based on the geometric relations as seen in Figure 4.2 through vector addition. With this considered, the following relation can be derived for the global coordinate vector to the UWB center point, $\overrightarrow{K_g}$ from the UWB casing frame origin, P_i and center point vector, $\overrightarrow{C_{g,i}}$:

$$\overrightarrow{K_{g,i}} = \overrightarrow{C_{g,i}} + \overrightarrow{P_i} \quad \text{for } i \in [1, n] \quad 4.4$$

As previously mentioned, all the vectors $\overrightarrow{C_{g,i}}$ were assumed identical for all the sensor nodes in the sensor frame. This implies that the vectors $\overrightarrow{C_{g,i}}$ are the vector in the sensor frame, $\overrightarrow{C_s}$ rotated to the global frame. Therefore, with a known orientation of the sensor node the $\overrightarrow{C_{g,i}}$ can be estimated as:

$$\overrightarrow{C_{g,i}} = q_i^* \overrightarrow{C_s} q_i \quad \text{for } i \in [1, n] \quad 4.5$$

Where q_i is the orientation of sensor node i expressed as unit quaternion in the global reference frame, while q_i^* is the conjugate of the quaternion q_i . Substituting equation 4.5 in 4.4:

$$\overrightarrow{K_{g,i}} = q_i^* \overrightarrow{C_s} q_i + \overrightarrow{P_i} \quad \text{for } i \in [1, n] \quad 4.6$$

Substituting equation 4.6 in 4.3 provides the final model which then can be used to estimate the unknown parameters eb_i and $\overrightarrow{C_s}$ by optimization. Thus, the model is defined as:

$$\| (q_i^* \overrightarrow{C_s} q_i + \overrightarrow{P_i}) - (q_j^* \overrightarrow{C_s} q_j + \overrightarrow{P_j}) \| = D_{uwb,i,j} - eb_i - eb_j \quad 4.7$$

In this equation the measured distance between each node $D_{uwb,i,j}$, the position of the node casing $\overrightarrow{P_i}$ and the node orientations q_i are the known variables that were measured. The UWB center point vector, $\overrightarrow{C_s}$ and the bias errors eb_i and eb_j are the unknown variables. When expanding these equations to a form suitable for numerical evaluation, some of the unknown variables appear in quadratic terms. This means that evaluation requires a non-linear optimization method.

For three UWB nodes, this expansion yields 3 equations with 6 unknowns. For n nodes, this yields $n-1$ triangular number of equations:

$$\text{no. of equations} = 1 + 2 + \dots + (n - 1) \text{ for } n \in N \quad 4.8$$

Also, this yields a total of $n+3$ unknowns. This makes this set of equations an underdetermined ($n<5$) or overdetermined ($n\geq 5$) system suggesting the application of an optimization approach to a set of multiple samples at different distance combinations to solve for the unknown bias errors eb_i and UWB center point vector, \vec{C}_s .

Optimization approach

A multi-objective constrained non-linear optimization method was applied to estimate the unknown bias errors eb_i and \vec{C}_s by minimizing the differences between D_{true} and $D_{uwb} - eb_i - eb_j$, utilizing the model defined in equation 4.7.

$$\begin{aligned} \text{Min} \left(\left\| (q_i^* \vec{C}_s q_i + \vec{P}_i) - (q_j^* \vec{C}_s q_j + \vec{P}_j) \right\| \right. \\ \left. - (D_{uwb,i,j} - eb_i - eb_j) \right) \text{ for } i, j \in N \end{aligned} \quad 4.9$$

This was done by applying the non-linear optimization method of Nelder-Mead (NMinimize function implemented in Wolfram Mathematica version 12.1). Two constraints are included to improve the chances and speed/computational load of convergence to the global best solution. The first constraint limits the solution space of the UWB center point, C_i to a volume derived from the UMIMU sensor's physical dimensions assuming that C_i is on, or very near, the antenna surface and inside the sensor casing. As a consequence, \vec{C}_s was limited to positive values with maximum coordinate values chosen equal to the dimensions of the sensor node casing. The second constraint limits the bias error estimates to be always positive, which were based on reasoning confirmed in all pilot test results, that the ranging errors are caused by an apparent overestimation of ToF values. The bias error upper limits were constrained to a worst-case maximum of 15 cm, also based on results of pilot experiments yielding distance estimate errors never greater than 15 cm.

4.2.3 Validation with synthetic data

Synthetically generated distance estimates with predefined bias error values eb_i and UWB center point values C_i were used for directly validating the performance of the calibration algorithm. Additionally, to evaluate the convergence of the optimization requires the synthetic data in which the true values of eb_i and C_i are known as opposed to them not being known in experimental data. The data were generated with a custom-built data generator, mimicking a physically realistic movement (speed of movement and change in orientations limited to a normal human movement scenario) for a set of three sensors named S1, S2 and S3 respectively. The resulting distances between all three sensor pairs were provided as an output of the data generator, with the distance combinations between the sensors being labeled with their number assigned to them (For example: the distance between S1 and S2 sensors was labeled as $D_{uwb\ 1,2}$). The distance update rate of the generated data was set to 10 samples per second, which was close to the general update rate of commercial UWB sensors. To achieve realistic translation and rotation of the sensor's data for each timestep, these were randomly drawn from a uniform distribution with a minimum of 1 degree and maximum of 5 degrees for the change in rotation of the sensor and with a minimum of 5 cm and a maximum of 20 cm for the change in sensor position. In addition to this, white noise with an SD of 2.5 cm was added to the generated distance data. Noise SD values were based on the experimental evaluation of UWB ranging. A total of 30 data sets were generated with varying values for \vec{C}_s and eb_i randomly drawn from uniform distributions ($0 < C_x < 5$, $0 < C_y < 4$, $0 < C_z < 0.8$, $-15 < eb_n < 15$) and the resulting sensor distances were fed as inputs into the optimization algorithm. For each of the 30 generated data sets, the optimization procedure was repeated 30 times, each time with a different random permutation of the input data and different initial vector values randomly drawn from uniform distribution within the given constraints. The estimated values of \vec{C}_s and eb_i with the lowest residual error in a set of 30 optimizations were considered as the final estimates. The resulting parameter estimates for \vec{C}_s and eb_i were compared against the ground truth values used in the synthetic data generation. Additionally, the errors of the calibrated distances were compared against the distance errors before the calibration of the distance estimates.

4.2.4 Validation with experimental data

UWB sensor hardware and calibration setup

A custom fully integrated UWB/MIMU sensor hardware platform was developed in-house, the sensors of which were named ‘UMIMU’ sensors (Ultra-wideband Magnetic Inertial Measurement Unit sensors) and were used in this research. UMIMU sensors consist of a UWB transceiver module DW1000, a 9-axis MTi-3 MIMU (Xsens Technologies, Enschede, Netherlands), an STM32F722RE microcontroller (STMicroelectronics, Geneva, Switzerland), USB communication for charging, configuration and programming combined on a custom PCB (Figure 4.3a). The UWB sensor nodes estimate the distance between them by the AltDS-TWR method as described in Section 4.2.1. The onboard MIMU is sampling independently using the MIMU chip clock at 100 samples per second to deliver 3D orientation, acceleration and angular velocity. The UWB onboard the UMIMU sensor platform is controlled by the clock of the microcontroller of the sensor platform. The UWB update rate depends on the number of rangings requested within one update and was recorded at an update rate of 15 samples per second (with 4 UMIMUs in a fully connected swarm). Each UWB update is attributed to the same time instant as the last MIMU update. This yields a synchronization uncertainty of ± 0.0099 s between the UWB data and the MIMU data. This paper only utilizes the UWB sensors in the UMIMU modules, while the MIMUs on-board are only used for synchronization between the UWB and camera-based motion analysis system.

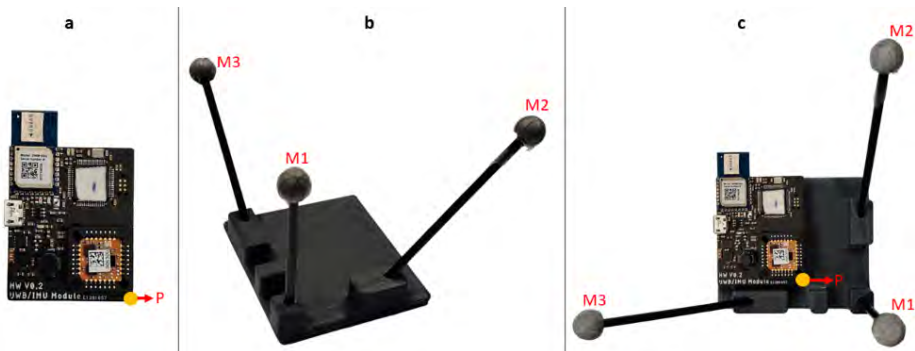


Figure 4.3: a) UMIMU sensor module; b) Sensor holding rig with reflective markers; c) Experimental setup with UMIMU sensor fixed to the rig.

For the purpose of validation and for obtaining data necessary for the calibration algorithm such as \vec{P}_i and q_i , a camera-based motion analysis system Vicon (Vicon Motion Systems Ltd, Oxford, UK) was used due to its capability of sub-centimeter level accuracy for marker position estimation. A special sensor-holding rig with reflective markers (Figure 4.3b) was designed to aid the estimation of the necessary parameters. The rig had three reflective markers (labeled M1 to M3) mounted on sticks (Figure 4.3b and 3c). A local right-handed reference frame was derived for each rig from the three markers. The UWB casing frame origin, P_i was defined as being located at the right-bottom corner of the sensor PCB (yellow dot, Figure 4.3a). The casing reference frame X-axis and Y-axis were defined parallel to the ribs of the PCB and the Z-axis was defined perpendicular to the rig base plate. For consistent estimation of the sensor orientation q_i and position P_i , the sensors are always aligned to the two sides of the rig base as seen in Figure 4.3c. This is followed by an initial rig calibration procedure performed before the start of the distance-bias calibration protocol. The rig calibration procedure was a static measurement of the rig markers along with the UMIMU sensor mounted with an additional temporary marker placed on the position P_i . This static measurement was used for deriving the relation (translation and rotation) between the rig reference frame and the sensor frame. This then would be applied for the calibration measurement with the marker on P_i removed to avoid possible interference of the marker on P_i with the UWB antenna function. The orientation of the sensor rig q_i was defined as the orientation of this local rig reference frame with respect to the global reference frame (defined by the global Vicon system reference frame).

Calibration experiment/protocol

The distance-bias calibration algorithm requires an input dataset that consists of a wide range of sensor distances and different sensor orientations to facilitate the convergence of the optimization process across different scenarios and conditions. Therefore, in each calibration session, a series of sensor node movements were chosen to contain sufficient variations in node distances and orientations in a volume of interest for the intended application of analysis of human movement.

The experimental validation was performed with the UMIMU sensor system, and a reference optical motion capture system as described in Section 4.2.4. The

calibration was performed by two persons moving two wooden sticks, with a sensor-holding rig with a sensor attached to the end of each stick (Figure 4.4, right). Maximal care was taken to prevent any interference or NLOS situation through the bodies of the 2 persons performing the calibration protocol. Two sets of 4 sensors were used for the experimental validation, and they were named Set-A (sensors 1, 2, 3 and 4) and Set-B (6,7, 8 and 9). Sensor 5 was assigned to be the controller/listener for both sets.

Two calibration movement protocols, differing in the movements made were performed to test the optimization performance. In protocol 1, two persons held a calibration stick with a rig and sensor in each hand, while facing each other, (Figure 4.4-left) and made random free-arm movements while the persons remained in the same position for the duration of the protocol. In protocol 2 the two persons start in the same position and pose again facing each other while making random free-arm movements. In addition, they moved slowly in circles of about 1.5m in diameter, while keeping the same distance, facing each other and keeping the sticks in between them, again maximally avoiding any NLOS situation. Both protocols were performed for both set A and set B. All measurements lasted approximately 3 minutes and were repeated twice, yielding ‘trial 1’ and ‘trial 2’ for each protocol.

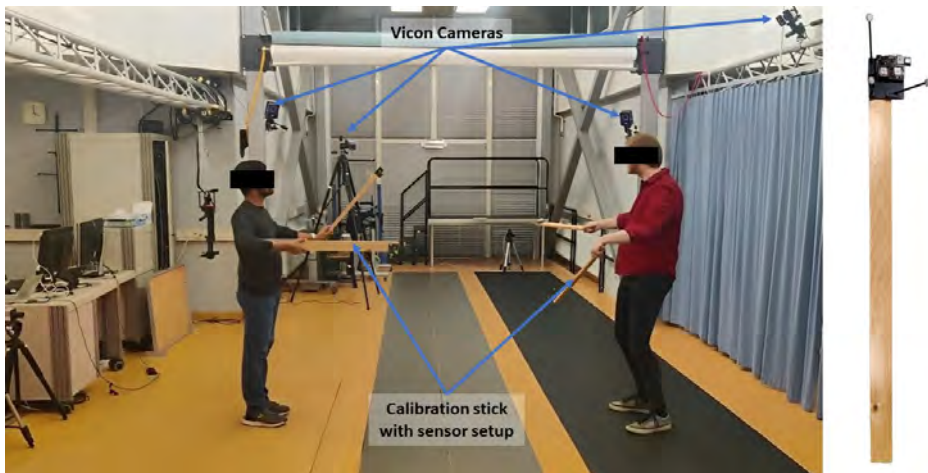


Figure 4.4: Calibration protocol situation with four UWB nodes labeled N1 to N4 along with the reference VICON system cameras (left) and the calibration stick with the sensor setup (right).

For each protocol, only the first 800 samples of the data from trial 1 (the ‘training set’) were fed into the calibration optimization process. Since the optimization algorithm was developed for sets of three sensors, this procedure was repeated for all four possible subsets of both set A and set B. For set 1, the four subsets were named set-123, set-234, set-341 and set-412. Similar naming was given to the subsets of set B. The optimization was then repeated 30 times for each of these combinations. The estimated values of \vec{C}_s and eb_i with the lowest residual error in a set of 30 optimizations were considered as the final estimates. As the results of all four subsets yielded more than one estimate, the final estimates for the values of eb_i and \vec{C}_s were computed by averaging the resulting values for eb_i (2 for each sensor) and \vec{C}_s (4 estimates) respectively.

In the experimental validation, it is not possible to directly compare the estimated distances after calibration against its ground truth values, because the gold standard reference system does not deliver ground truth values for $\vec{K}_{g,t}$ and therefore not for $D_{i,j}$. Instead, it only delivers ground truth values for \vec{P}_i . Therefore, estimated distances after calibration were validated against a virtual ground truth value for $D_{i,j}$, named $D_{ref\ i,j}$, being the distance between the virtual $\vec{K}_{g,t}$ values that were estimated from known values of \vec{P}_i and q_i from Vicon and the estimated values \vec{C}_s from the optimization results. First, validation was performed for the values from the training set. Then a validation was performed for a ‘validation set’ containing the remaining values of trial 1 and trial 2 for each protocol.

Calibration process pipeline

In the swarm calibration process pipeline (Figure 4.5), first the positions of the markers attached to the sensor node rig were estimated through the Vicon system. Secondly, the UMIMU sensor nodes provided the distance estimates, $D_{uwb\ i,j}$ (as well as all 3D orientation, angular velocity and acceleration estimates, for future studies) of each node in the network. The position estimates of the Vicon system were used to obtain the orientation q_i and the vector to the UWB casing point, \vec{P}_i . This information was also used to estimate the distance between the sensor nodes D_{true} which then was later used for estimating the accuracy of the UWB distance

estimates D_{uwb} . Synchronization of the UMIMU and Vicon systems was done by lining up the acceleration magnitude estimates of both systems for the same node/rig (applying a cross-correlation approach) measured at 100 samples per second.

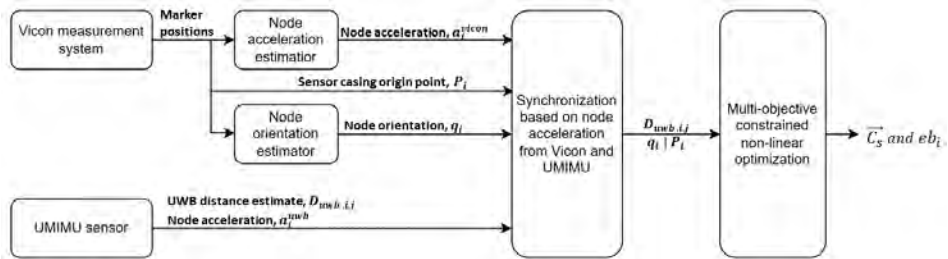


Figure 4.5: Schematic of the distance-bias calibration process pipeline.

4.2.5 Data analysis

For both validation with simulated synthetic data and with experimental data the accuracy of the swarm calibration method was computed for each condition through estimated confidence intervals and correlation coefficients between UWB-based and ground-truth reference estimates. Additionally for the synthetic data, the accuracy of estimation of the values of \vec{C}_s and eb_i were computed based on a direct comparison between the values used as input for data generation and the values of \vec{C}_s and eb_i estimated by the swarm calibration method. Reproducibility and consistency of the distance-bias calibration method were evaluated for both the generated and synthetic data sets through statistical moments of the distributions of the 30 calibration results per set and summarized over all the generated sets.

4.3 Results

4.3.1 Validation results with synthetic data

For the synthetic data, the distance estimates after calibration were clearly more accurate than the ones before and very closely followed the ground truth distance measures, as illustrated in a typical example (Figure 4.6).

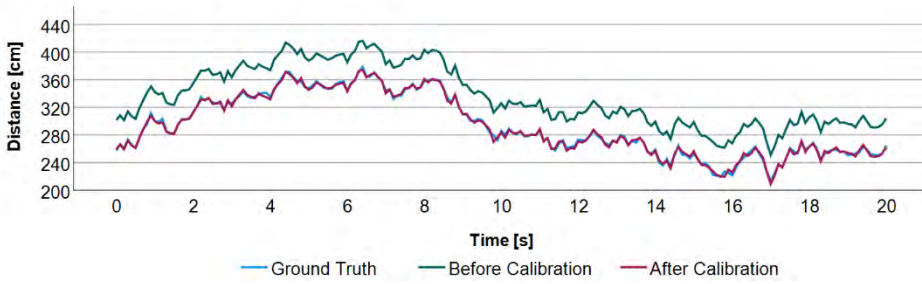


Figure 4.6: Typical example of distance estimates before (green) and after calibration (red) along with their reference distance (blue) for the synthetic data set.

The distance-bias calibration has successfully removed the systematic bias component in the distance estimates, which have significantly reduced from around 35 cm to around -0.4 cm. The mean distance error before the calibration varied widely between the data sets generated, as they were based on the input values of \vec{C}_S and eb_i (Figure 4.7). The mean distance errors before calibration over all the 30 data sets were 35.1 ± 11.1 cm, 35.5 ± 11.0 cm and 36.0 ± 12.3 cm for the ranging sensor pairs 12, 13 and 23 respectively (Figure 7-Top).

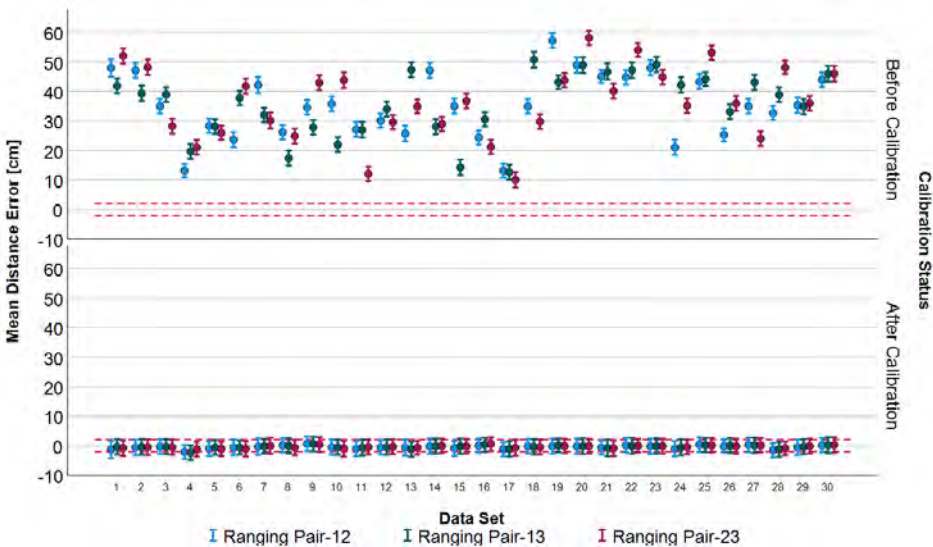


Figure 4.7: Mean and standard deviation (whiskers) of distance errors before (top) and after the calibration (bottom) for all the 30 synthetic data sets generated of the three ranging sensor pairs. The dotted red lines are 2 cm away from the graph's origin line on both the positive and negative axes.

The standard deviation (SD) values of these errors before calibration were a direct result of the noise parameters set for the synthetic data generator (Section 4.2.3) and were around 2.5 cm. The average distance errors after calibration over all the 30 data sets with unique \vec{C}_s and eb_i values were -0.46 ± 2.58 cm, -0.35 ± 2.60 cm, -0.35 ± 2.53 cm for the ranging sensor pairs 12, 13 and 23 respectively. The SD values of the errors after calibration were again around 2.5 cm (Figure 4.7-Bottom).

For all three simulated sensors, the mean absolute errors (MAE) of the estimated bias values eb_i were always less than 1 cm for almost all the 30 different data sets (Figure 4.8-Top), with one outlier in synthetic data set-4 (MAE of 1.70 cm for eb_1). For all the 30 data sets, the average of the MAE in bias estimation was 0.33 ± 0.34 cm, 0.31 ± 0.22 cm and 0.30 ± 0.24 cm for eb_1 , eb_2 and eb_3 respectively. The MAE of the estimated UWB center point, C_s was always less than 0.75 cm for almost all the 30 different data sets (Figure 4.8-bottom), except for one of the three coordinates for three data sets (MAE of 1.1 cm for C_x in data set-11; MAE of 1.31 cm and 1.14 cm for C_y in data set-13 and 19 respectively). For all the 30 data sets, the average of the MAE in UWB center point estimation was 0.37 ± 0.32 cm, 0.38 ± 0.24 cm and 0.21 ± 0.09 cm for C_x , C_y and C_z respectively.

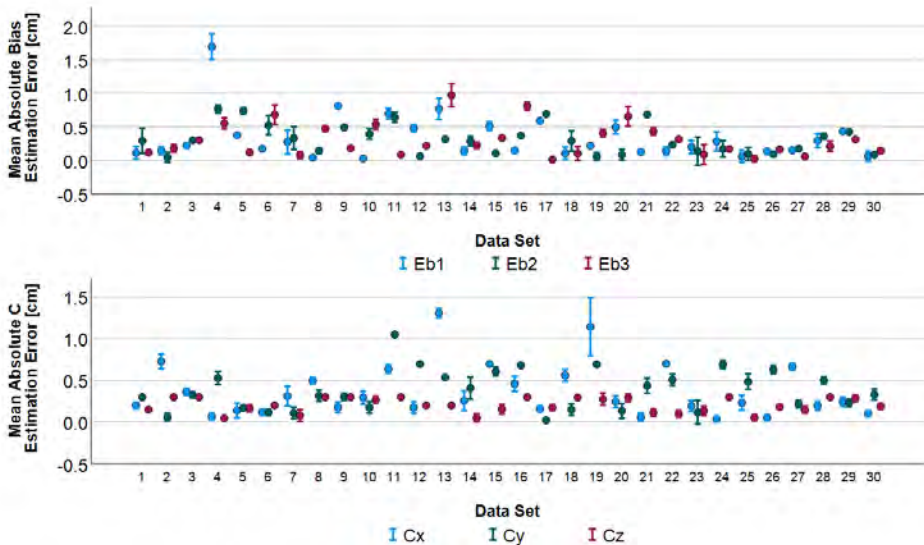


Figure 4.8: Bias estimation errors for all three sensors (Top) and the UWB center point estimation errors (Bottom) for the synthetic data set.

The repeatability of the optimization is indicated by the residual error of the optimization procedure for iteration within a specific data set and is found to be very consistent over the 30 data sets (Figure 4.9). The average error of the mean residual errors over all the data sets was estimated to be 2.2 cm with an SD of 0.1 cm.

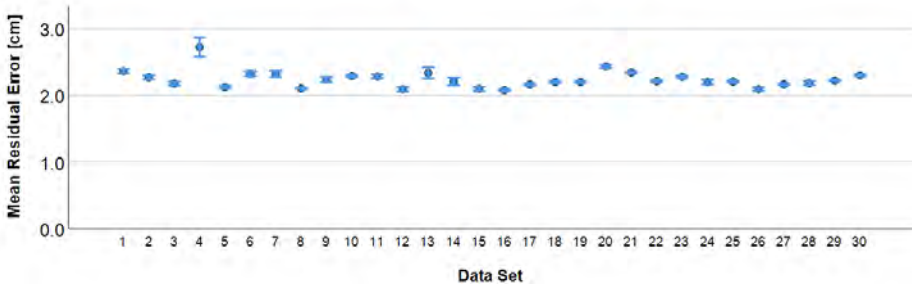


Figure 4.9: The residual error of the optimization procedure for all the 30 data sets in the synthetic data set.

4.3.2 Validation results with experimental data

Similar to the synthetic data set, the distance estimates after the calibration for the experimental data were clearly found to be more accurate than those before and closely followed the ground truth distance values. This is illustrated in a typical example of the distances measured between two nodes in an experiment (Figure 4.10).

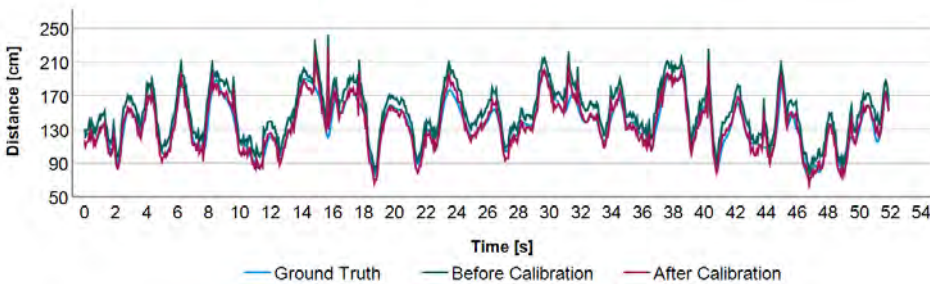


Figure 4.10: Typical example of distance estimates from UWB sensors before calibration (green) and after calibration (red) along with their reference distance (blue) from the Vicon optical system concerning the experimental data.

For the experimental training data set, the distance-bias calibration has removed the systematic bias component in the distance estimates, which have reduced from around 3.7 cm and 2.1 cm to around 0.5 cm and -0.5 cm in protocol 1 and protocol

2 respectively (Figure 4.11). The random distance errors before calibration for each of the 12 ranging combinations were around 11.0 cm and 12.0 cm in protocols 1 and 2 respectively. After applying calibration these only improved marginally to 9.7 cm and 10.6 cm in protocol 1 and 2 respectively, though the distance-bias calibration is not intended for dealing with the random errors. The mean distance errors after the calibration for almost all individual ranging combinations improved in both protocols applied, except for a single ranging sensor pair 89 in protocol 2. This specific pair had a higher mean error of -7.3 cm (Figure 4.11).

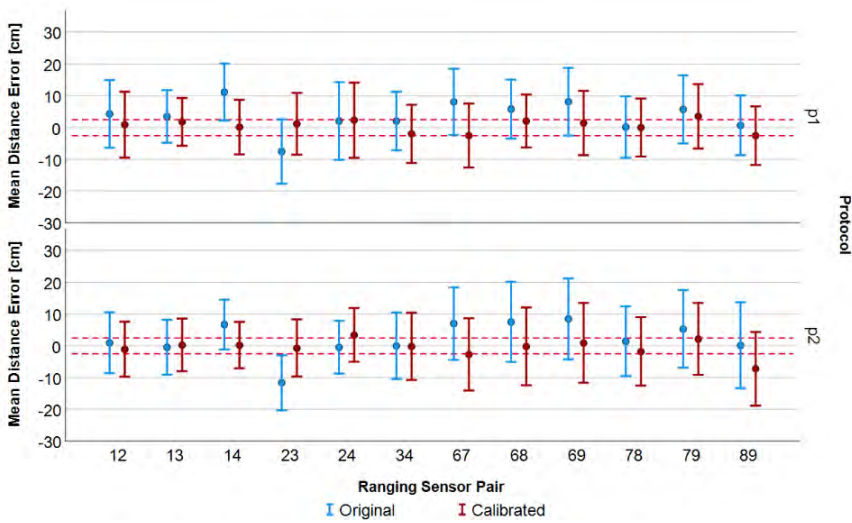


Figure 4.11: Mean distance estimation error before (blue) and after (red) distance-bias calibration for each ranging combination for both the protocols validated for the experimental training data set. Dots represent the systematic distance estimation errors, and the whiskers indicate the distance estimation error SD, that is random error component. The dotted red lines are 2.5 cm away from the graph’s origin line on both the positive and negative axes.

For the experimental validation data set, similar to the previous results distance-bias calibration has removed the systematic bias component in the distance estimates. The systematic errors have reduced from around 2.5 cm and 2.6 cm to around -0.3 cm and -0.5 cm in protocol 1 and protocol 2 respectively (Figure 4.12). The random distance errors before calibration for each of the 12 ranging combinations were around 11.4 cm and 11.5 cm in protocol 1 and 2 respectively. After applying calibration these only improved marginally to 10.2 cm and 10.5 cm in protocol 1 and 2 respectively. Similar to the training data set, mean distance errors after the

calibration for almost all individual ranging combinations improved in both protocols applied, except for a single ranging sensor pair 89 in protocol 2. This specific pair had a higher mean error of -7.7 cm (Figure 4.12). In addition, the mean systematic errors before the calibration for all the sensor ranging combinations when compared against the distance between the \vec{P}_i (without considering the orientation of the sensor, i.e., estimated \vec{C}_i), were -4.5 cm and 4.6 cm in protocol 1 and 2 respectively. For all the optimization combinations the mean residual error at solution convergence was always around 5 cm. Also, the mean residual value of all the iterations is 5.91 cm with an SD of 2.51 cm.

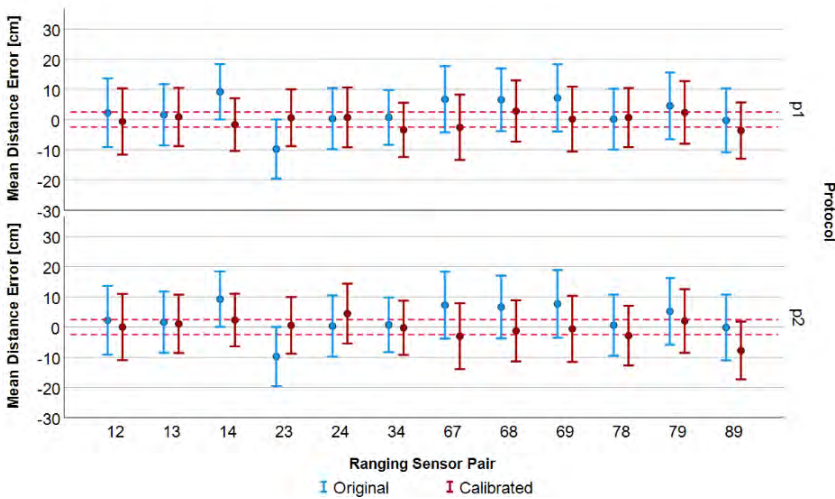


Figure 4.12: Mean distance estimation error before (blue) and after (red) distance-bias calibration for each ranging combination for both the protocols validated for the experimental validation data set. Dots represent the systematic distance estimation errors, and the whiskers indicate the distance estimation error SD, that is random error component. The dotted red lines are 2.5 cm away from the graph’s origin line on both the positive and negative axes.

4.4 Discussion

Over all tested situations the distance estimates were found to be substantially closer to the true distance values after applying the proposed distance-bias calibration method. For both the validations with synthetic data and experimental data, the estimates for distance $D_{i,j}$ consistently showed a higher accuracy with the distance-bias calibration procedure applied than without (Figure 4.6 and Figure 4.10). After

calibration, systematic estimate errors were consistently around or below 0.5 cm for both validations. The non-linear optimization procedure did consistently converge over multiple repetitions for each condition.

For the synthetic data, the systematic errors of the full procedure reduced significantly from around 35 cm to -0.4 cm, and the distance error magnitude was consistently lower than 2 cm for all the 30 underlying unique data sets used. The accuracy of the distance-bias calibration method in estimating the values of the unknown UWB center point vector, \vec{C}_s and the ranging bias errors eb_i was only directly validated with the synthetic data set, since it is not possible to assess their true values directly in the experiments. The estimation errors in these parameters were consistently found to be at a sub-centimeter level over all 30 different synthetic data sets (Figure 8). All validation results for the synthetic data support the conclusion that the distance-bias calibration procedure seems capable of consistently improving distance estimates to the desired level by accurately estimating of \vec{C}_s and eb_i .

For the experimental data, a very similar consistent improvement of applying the distance-bias calibration was found as for the synthetic data. Distance-bias calibration performed almost equally for both the protocols tested with the residual systematic bias being -0.3 cm and -0.5 cm in protocol 1 and protocol 2 respectively. Although the difference in performance was very small between the two protocols overall performance of protocol 1 is better than the other. This could be due to the nature of movement in protocol 1 where the subjects performing the calibration were standing still and probably had minimal chances of introducing accidental NLOS, which can occur when subjects are moving as in protocol 2. It can be observed that the reduction in the total distance error magnitude after calibration was mainly due to the removal of the systematic bias component, while the random error component remained largely unaffected. This is consistent with the intended purpose of the proposed calibration, which addresses deterministic sensor-specific biases rather than stochastic measurement noise. The sub-centimeter reduction in systematic error therefore represents an improvement in accuracy within the context of 3D human-movement analysis, even though the overall error variation (SD) changed only slightly. The random component of the distance error (SD) was

comparatively larger than the ones found for the synthetic data set. For the experimental data, the estimation accuracy of \vec{C}_s and eb_i were not validated directly as they cannot be measured with a reference method. However, the estimates for the effective UWB center point C_i position was found to be close to the position of the antenna center position within the casing.

The proposed calibration algorithm delivered very reproducible distance estimation accuracy results as illustrated by consistent SD values of the low residual errors achieved (Figure 9). For the synthetic data set these were consistently close to each other over 30 permutations within each combination of input parameters \vec{C}_s and eb_i with SD values always lower than 0.1 cm. Also, the estimates of the unknown parameters \vec{C}_s and eb_i were consistently close to the true value for all tests with synthetic data. The residual errors for the experimental data also showed good reproducibility (SD 2.5 cm). For the experimental data, the results for distance estimation resembled the ones for the simulated synthetic data set in their consistent strong improvement of accuracy in the estimation of distance $D_{i,j}$. This suggests that for the experimental data, the values for eb_i (as well as \vec{C}_s) were also estimated with similar accuracy as for the synthetic data.

All other calibration methods proposed in the literature calibrate parameters at the hardware level, in attempts to directly correct for sources of the error [138,143-146]. They mainly address errors of clock drifts, and antenna delays directly. However, the distance-bias calibration method proposed in this paper is a more phenomenological approach directly addressing the observed errors. Therefore, a direct comparison against these other methods is not possible. Additionally, the proposed calibration was performed with the UWB sensors that were first calibrated at the hardware level (antenna calibration). Residual systematic errors of around 3cm were present even after the antenna calibration in the distance ranges (Figure 4.11 and Figure 4.12). Thus, the proposed calibration appears to reduce the systematic errors significantly over all of these other calibration methods at the hardware level [138,143-146], which report systematic errors of less than 3 cm [145], and around 6 cm [143], 7 cm [144], 5 cm [138] and 29 cm [146] respectively. Though [145] had achieved accuracies closer to our proposed method have only been validated in a controlled static measurement, while the validation in this study is during a more dynamic movement.

Also, the smaller systematic errors achieved with the proposed distance-bias method indicate that apparently, none of them tackles all error sources sufficiently.

Additionally, the effect of the orientation differences between UWB sensors for the ranging error is not considered in any of the research mentioned above. Though differences in the errors based on orientation between the ranging sensors were observed [142], it was still ignored for the calibration. In the proposed distance-bias calibration this orientation effect is considered by introducing the UWB center point vector, \vec{C}_s in the calibration model. The effect of neglecting the effect of relative orientation of both UWB sensors in a ranging operation was verified by the higher errors in the uncalibrated distance measures compared against the measured casing origin point vector when compared to the errors validated against the distances with the \vec{C}_s considered. Also, when the UWB modules used are bigger, then the errors will be bigger when the orientation effect is ignored. Therefore, the orientation effect has a significant contribution, and the proposed distance-bias method does compensate for this effectively.

The calibration algorithm in this article is only proposed for a swarm of three sensors, however, this could be further expanded based on the same equations and methods proposed. Expanding the equations for more sensors however increases the computation cost of the optimization, especially since an increase in each sensor node will lead to $n-1$ additive factorial number of equations (Equation 4.8). Thus, a practical approach would be to split the total sensor set available into sets of 3 for optimization. Whether repeating this process in other permutations of the sensor groupings and averaging results (like was done in this study for practical reasons) would improve overall calibration accuracy is subject to further studies. The same applies to investigating whether expanding the equation and performing optimization for larger sensor sets is possibly improving accuracy. Also, although attempts were made, the experiments in this study could possibly contain data samples from NLOS situations, which are expected to deteriorate the quality of the calibration outcome. Possibly the calibration procedure could be improved by avoiding NLOS situations 100% by design or by detection and removal of values from the calibration recordings that are affected by NLOS errors.

Proposed distance-bias calibration is considered to be a one-time calibration to be performed in clear LOS with no external interference, after performing the antenna calibration recommended by the manufacturer and before first use. However, the validity of the calibration over time is yet to be tested. Also, in terms of the infrastructure required for generating reference data for this calibration procedure complex systems such as the optical motion capture system could possibly be substituted with MIMU-based, or preferably UMIMU-based, reference data generating methods. Also, the manual performance of the calibration protocol movements could be possibly replaced by movements performed by a robotic system, especially in an in-factory calibration procedure.

The distance-bias calibration method appeared to be capable of consistently removing a large part of the observable systematic errors in the distance estimates. This supports the validity of the main underlying assumption that these errors can be attributed to individual sensors as additive errors, within the tested distance range, relevant for application in only on-body applications for 3D analysis of human movement. A practical consequence of the fact that the proposed distance-bias calibration method only acts on the observed distance estimates and sensor orientations is, that it can be applied to data acquired with any similar UWB ranging system without access to internal UWB sensor hard- or software settings. The distance-bias calibration deals only with the systematic errors and the UWB sensors could provide accurate distance estimates with a very low residual systematic error in clear LOS situations. However, additional errors due to the external interferences and NLOS are expected in the intended application scenario. Therefore, these errors due to the external interferences and NLOS situations should be further studied for the successful application in human movement analysis. It is expected that the improved accuracy in UWB distance estimation within the relevant distance range under LOS conditions facilitates future development of improved 3D position estimation through smart data fusion algorithms applied to data from a swarm of integrated UWB and MIMU sensors on the human body (UMIMU sensor system) in the intended application of ambulatory 3D analysis of human movement.

4.5 Conclusion

In this article, a novel distance-bias calibration algorithm was proposed for minimizing the apparent systematic UWB sensor distance estimate errors, assuming these are attributable to fixed contributions of individual UWB sensors in a swarm network. This is done by exploiting the redundancy in the distance estimates in a fully connected sensor swarm. The performance of the distance-bias calibration algorithm is validated with a synthetic data set and with an experimental data set on multiple swarms of 3 sensors. The validation with synthetic data confirmed the calibration algorithm's capability to reliably converge and estimate the systematic error parameters attributed to the different sensors with high and consistent accuracy. The validation with experimental data within a distance range relevant for future application in the 3D analysis of human movement further confirmed that the calibration protocol can reduce the systematic error component consistently to below or equal to 0.5 cm in magnitude, which is more accurate than any other methods reported in the literature. It was also shown that at these accuracy levels, it is also essential to represent the UWB sensor module position not by a reference point on the sensor casing, but by the actual effective positions within the casing of the 2 sensors that the UWB ranging hardware uses for distance estimation. This requires simultaneous observation during the calibration measurements of both the sensor casing positions (by the reference system) and their 3D orientations (by the MIMUs or the reference system). As a byproduct, the calibration procedure also delivers these effective positions with respect to the sensor casing reference frames consistently within the antenna surface of UWB nodes. The accuracy levels achieved with the proposed method promise to facilitate future development of improved 3D position estimation methods through a smart data fusion approach applied to a swarm of integrated UWB/MIMU sensors (UMIMU sensor swarm) with an accuracy required for clinically relevant applications in ambulatory 3D analysis of human movement.

Chapter 5

Position estimation based on UWB swarm optimization and comparison against traditional trilateration

This chapter is submitted for publication as:

Yogesh, V.; Beijnum, B.J.V.; Buurke, J.H.; Baten, C.T.M. Position estimation based on UWB swarm optimization and comparison against traditional trilateration.

Abstract

Ultra-wideband (UWB) is a promising technology for indoor position estimation for various localization applications of object swarms, such as in 3D analysis of human movement with multiple on-body sensors or a swarm of drones in an indoor environment. However, most UWB-only position estimation methods are based on a star topology, where the position of a mobile node is estimated using distances from several fixed anchors. These approaches ignore the valuable inter-node distance estimates, possible in a fully-connected ‘Swarm’ topology, which could provide more redundancy in the set of available distance estimates used for the position estimation. This would improve the accuracy and consistency of the position estimates. Also, published studies do not analyze how input measurement errors affect the final position estimates, which makes it difficult to assess the reliability under varying conditions. Therefore, this study first proposes a UWB swarm optimization-based position estimation method that utilizes all available internode distances to enhance accuracy and compare against the traditional trilateration method that utilizes the star configuration. All validations were done with synthetic UWB data, to enable testing all input error situations. The comprehensive error sensitivity analysis was conducted to evaluate its robustness under varying noise conditions. The proposed method consistently outperformed trilateration, with position estimation error around 5.7 cm for realistic UWB distance input estimates, while for higher noise conditions, the proposed method had errors around 6 cm lower than the trilateration method, which had position estimation errors around 19 cm. This study demonstrates the general potential of the Swarm optimization-based method for position estimation as a more accurate and consistent alternative to traditional star-based trilateration methods.

5.1 Introduction

Ultrawide-band (UWB) has emerged as one of the promising technologies for indoor localization and position estimation applications. This is mainly due to their relatively low cost, low power consumption, large bandwidth, and robust performance [148]. Besides, the UWB-based positioning currently offers the highest accuracy and can achieve sub-decimeter accuracy for indoor positioning among other wireless communication modalities used for positioning, such as Wi-Fi, ZigBee, Bluetooth, and radio frequency identification [149,150]. However, in practical applications, achieving higher accuracies is only feasible in clear line-of-sight (LOS) conditions, such as free unobstructed spaces [123]. In typical indoor environments, the UWB positioning accuracy is often degraded by the presence of various obstacles such as furniture, human bodies, and structural elements. These obstructions create non-line-of-sight (NLOS) conditions and introduce additional errors on top of the baseline noise and bias observed under LOS conditions, leading to inaccurate position estimations [124,151].

To improve positioning accuracy, UWB is often combined with other sensors such as Magnetic Inertial Measurement Unit (MIMU) [151,152], LiDAR [153], or vision-based systems [154] through data fusion techniques, such as (Extended-) Kalman filters. These multimodal data fusion-based approaches have significantly improved position estimation performance. Among these sensor combinations, the integrated UWB and MIMU sensors have shown immense potential and have been increasingly explored in recent research [65,78,152]. This is attributed to the complementary error characteristics between MIMU and UWB. Specifically, position estimation algorithms that rely on MIMU sensor data usually suffer from integration drift, leading to errors that increase over time [42,43]. However, they are generally unaffected by NLOS conditions as observed in UWB. In contrast, UWB sensors provide position data that is free from drift by using absolute distance measurements, while they are disrupted in NLOS environments [57,65]. Therefore, this specific combination of the UWB/MIMU achieves a higher accuracy than each of them used independently and is now widely utilized for positioning/localization applications such as pedestrian navigation, autonomous robotics, and drones.

Though the UWB/MIMU combination has been successfully applied for indoor localization, pedestrian navigation, and robotic applications, they have not yet been widely adopted for the 3D analysis of human movement (3D AHM) and clinical applications that demand very high-accuracy position estimates of multiple moving nodes on the human body [119]. In these high-accuracy applications, the position estimation errors are expected to be around 1 cm or lower [119], while the accuracy currently achieved by these integrated UWB/MIMU sensor systems is still not sufficient for such high-accuracy applications, with reported position estimation errors in pedestrian navigation around 10 cm or higher [119,148,155]. Studies suggest that the MIMU component in the widely adopted UWB/MIMU fusion approach has already been extensively optimized to achieve the current state-of-the-art accuracies [156]. As a result, to further enhance accuracy in such data fusion frameworks, it is required to improve UWB positioning accuracy itself. Enhancing UWB performance can be addressed in two aspects: (1) improving distance measurement of the UWB (UWB ranging) and (2) refining position estimation algorithms based on UWB distance measurements. Within the 1st aspect improvement, several studies have attempted to improve UWB ranging accuracy through calibration techniques and error modeling approaches [138,143-146,156], reducing distance estimation errors to a residual bias of approximately 0.5 cm [156], and with a random error component of around 5 cm [138]. This study focuses on accuracy enhancement on the 2nd aspect through using more effective computation strategies by developing and validating advanced algorithms to estimate position from distance measurements in a fully-connected UWB node Swarm.

Most UWB position estimation algorithms rely on distances measured between three or more fixed UWB sensor nodes at known positions, usually referred to as anchors, and mobile UWB nodes with unknown positions, referred to as mobile nodes, to estimate their positions. This configuration follows a star topology where distances are measured only between the fixed anchors and each mobile node in the network. The existing position estimation algorithms can be generally classified as linear positioning algorithms (non-iterative) and non-linear positioning algorithms (iterative/recursive) [157]. Linear algorithms, such as trilateration [158] and least squares approaches [159], estimate position based on geometric relationships. Non-linear or iterative algorithms, on the other hand, depend on advanced mathematical

frameworks, such as Taylor series approximations [160] or filtering techniques like an Extended Kalman Filter (EKF) [161] and Unscented Kalman Filter (UKF) [162], which incorporate motion models or data from additional sensors to refine position estimates. However, despite these advancements, most existing methods still struggle to provide the high accuracy required for applications such as clinical human movement analysis, where position estimation errors around 1 cm are sought [119]. Reported errors for only UWB-based positioning for most of the studies are around 10 cm [163-168], with the lowest achieved position estimation error being around 3 cm [168], achieved in a static LOS measurement scenario. These reported errors exceed the acceptable thresholds even in LOS conditions for applications demanding precise localization, making it necessary to explore alternative approaches to improve accuracy and robustness.

One of the key limitations of existing UWB positioning algorithms is their dependence on a star topology, where distances are measured only between anchors and one or more mobile tags in the network. This approach ignores the valuable internode distance information between all the mobile nodes connected in the network that could be exploited to enhance position estimates. Theoretically, a minimum of three anchors is required for 3D positioning with traditional star configuration [169], while a redundancy in star configuration can be achieved with having higher number of anchors [75,114]. This could potentially aid in improving accuracy through optimization-based techniques, however, this configuration with increased anchors requires a more sophisticated infrastructure and expensive setup [114]. In addition, studies have shown that though the increased anchors could provide redundancy to help improve position estimation, they also introduce more errors and uncertainty, thereby causing instability [115,116].

Therefore, to address these limitations while utilizing the minimal number of anchors (3 anchors), a swarm-based topology where all available internode distances (which also includes distances between all mobile nodes) are utilized for position estimation, was explored in this study. This could also help minimize the dependency on a large number of anchors and could make it possible to have redundant data with a minimum of three anchors and two or more mobile nodes. Additionally, while many existing UWB positioning algorithms have been validated, most studies do not specify the input distance measurement errors used during evaluation, and no

analysis of how input measurement errors affect final position estimates is conducted. Without this information, it is unclear under what conditions the reported accuracy can be reproduced, making it difficult to assess the method's performance in real-world scenarios. Therefore, it is important to explicitly evaluate how varying input error conditions in the distance estimates influence the resulting position estimation accuracy to ensure applicability in real-world scenarios.

To address these gaps, in this study, first, a non-linear optimization-based algorithm that utilizes the redundant internode distance measurements available in a swarm topology with a minimal anchor setup to improve localization accuracy is proposed, the 'swarm optimization algorithm'. The proposed method is validated with synthetically generated UWB distance data, created through controlled experiments where a high-precision optical motion capture system is used as ground truth for evaluating the estimated positions. To further validate the effectiveness of our approach, we compare its performance against the widely used trilateration method. Following this, an input error sensitivity analysis to evaluate the robustness of both methods under varying noise and bias conditions was conducted. The novelty of this work lies in introducing and evaluating a swarm-based optimization algorithm to identify its capability to enhance the accuracy and consistency of UWB positioning, as well as to present a comprehensive error sensitivity analysis providing valuable insights into how different input error conditions impact both our proposed method and trilateration.

5.2 Methods

5.2.1 UWB node swarm configuration

In this study the measurement system configuration (Figure 5.1) includes a total of n UWB nodes, where three nodes act as anchors which are placed at fixed, known positions within the measurement region (orange nodes in the figure), while the remaining $n - 3$ nodes are the mobile nodes (yellow nodes in the figure) that are attached to the subject/object being tracked. Within this study, UWB nodes are expected to determine inter-node distances based on Time of Flight (ToF) measurements, a commonly employed technique in commercial UWB systems [147]. Here, the ToF calculations are obtained using the Alternative Double-Sided Two-

Way Ranging (AltDS-TWR) method [137], which improves accuracy by mitigating clock drift errors between devices.

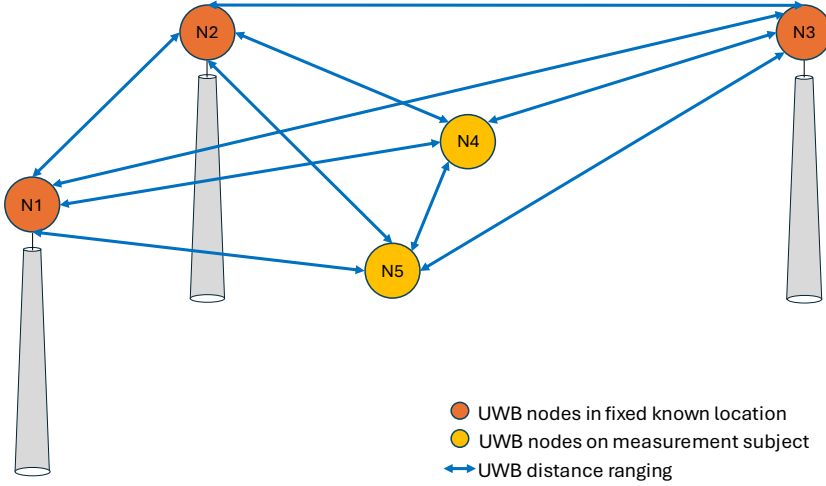


Figure 5.1: UWB measurement configuration and illustration of the swarm topology.

The UWB nodes operate in a swarm topology, where each node measures its distance to all other nodes in the system, forming a fully connected network (Figure 5.1). Given a total of n UWB nodes in the system, where $n = n_{anchor} + n_{tag}$, with n_{anchor} representing the number of fixed anchors and n_{tag} representing the number of mobile tags, the number of distance measurements differs based on the topology used. For a swarm topology configuration with n UWB nodes, the total number of distance measurements M_{swarm} generated for each measurement cycle correspond to the triangular number of pairwise rangings and is given by:

$$M_{swarm} = \frac{n(n-1)}{2} \quad 5.1$$

In comparison, the star topology configuration with the same n UWB nodes generates a total number of distance estimates M_{star} that is a product of the number of anchors and tags, and is given by:

$$M_{star} = n_{anchor} \times n_{tag} \quad 5.2$$

For example, if there is a UWB system with 3 anchors and 2 mobile tags (a total of 5 UWB nodes), the swarm topology will provide a total of 10 unique pairwise distance measurements, while the star topology will provide a total of 6 (2 times 3) pairwise distance measurements. Therefore, the swarm topology configuration utilized in this research provides more distance estimates, which are valuable for optimization-based relative position estimation.

5.2.2 Proposed swarm position estimation

An optimization-based estimation method was implemented in this study to determine the unknown positions of n_{tag} mobile sensor nodes in a swarm, based on all available inter-node UWB distance measurements, with n_{anchor} fixed anchors in a network of n UWB nodes ($n = n_{anchor} + n_{tag}$). The UWB distance data is initially filtered for eliminating noise, which is followed by a position estimation using a nonlinear constrained optimization approach (Figure 5.2). Additionally, an iterative refinement loop is included, which repeats the optimization until the RMSE of the measured distance and estimated distances from positions estimated via optimization is below a set threshold or has reached the maximum iteration count.

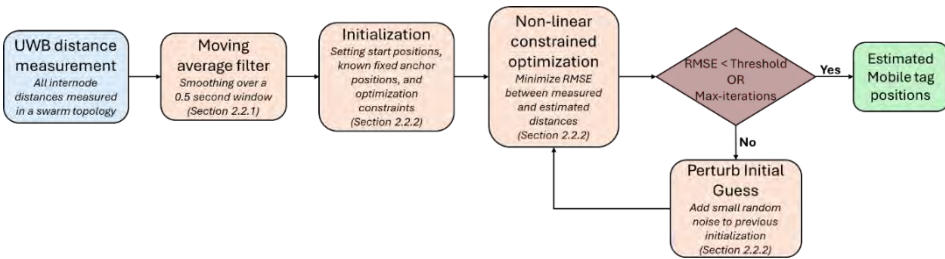


Figure 5.2: Proposed swarm position estimation pipeline

UWB measurement preprocessing

The UWB distance measures are initially filtered using a moving average filter to reduce the influence of high-frequency noise in UWB distance measurements. To preserve the responsiveness to actual movement, a moving average filter with a window length equivalent to 0.5 seconds was selected for smoothing. This means that for a UWB measurement system measuring at 4 samples per second, a window of 2 samples is applied, while for a UWB measurement at 20 samples per second, a

window of 10 samples is applied. To eliminate phase lag, a forward and backward filtering approach was used, ensuring zero-phase distortion and accurate temporal alignment. This is equivalent to a low-pass 2nd-order filter with a Cutoff frequency of around 0.9 Hz, with zero delay or phase shift. The choice of a window of 0.5 seconds duration balances noise suppression and real-time performance, considering typical human movement velocities between 0.5 m/s to 2 m/s.

Swarm optimization-based position estimation

The position estimation of mobile UWB nodes from the distance measurements was implemented through a Sequential Quadratic Programming (SQP)-based nonlinear optimization approach (Constrained Nonlinear Optimization function, LabVIEW 2021), which was set up to find the optimal solution for the mobile sensor positions given the measured distances. For this, a set of equations was derived for the relationships between positions and distances, and an optimization criterion was defined.

The distance between any two sensor nodes i and j , can be estimated based on standard 3D Euclidean formula utilizing the position coordinates of the two sensor nodes i and j , and this estimated or reconstructed distance \hat{d}_{ij} is given as:

$$\hat{d}_{ij} = \sqrt{(x_i - x_j)^2 + (y_i - y_j)^2 + (z_i - z_j)^2} \quad 5.3$$

where \hat{d}_{ij} represents the estimated distance between sensor i and j , while (x_i, y_i, z_i) and (x_j, y_j, z_j) denote their respective 3D coordinates. This yielded a set of $n(n - 1)/2$ equations, for a set of n UWB nodes in the network.

The optimization objective was defined as finding the minimum of the root mean square differences between the measured and estimated positions of the mobile sensors (or the root mean square error (RMSE) in estimated position):

$$\min_{\mathbf{x}} f(\mathbf{x}) = \sqrt{\frac{1}{M} \sum_{(i,j) \in P} (d_{ij} - \hat{d}_{ij})^2} \quad 5.4$$

Where P is the set of all unique unordered sensor node pairs (i, j) and M is the number of sensor node pairs in a swarm configuration.

The measured distance values between all nodes d_{ij} are preprocessed (Section-UWB measurement preprocessing) and used as inputs for the optimization algorithm. Depending of whether i and j is anchor node or mobile node, their coordinates are taken either from the known anchor positions or the optimization variable \mathbf{x} . This reconstruction of distances using the Euclidean formula results in a system of $n(n - 1)/2$ nonlinear equations with $3(n - 3)$ unknowns (as three fixed sensor positions are known in 3D space). In this study in a system with 9 UWB nodes, there are 36 distance measurements, leading to 36 equations and 18 unknowns. This results in an overdetermined system with more equations than the number of unknowns and is solved through optimization.

The UWB swarm topology provides $n(n - 1)/2$ unique pairwise distance measurements per update cycle for a set of n UWB nodes (section 5.2.1). As three UWB nodes were placed at fixed, known positions (in order to accommodate both star and swarm approaches), their position values were filled out in the equations as given constants. Only the positions of the remaining $n - 3$ mobile sensor nodes needed to be estimated. The unknown 3D positions of these $n - 3$ mobile UWB nodes were concatenated into the optimization vector:

$$\mathbf{x} = [x_1, y_1, z_1, x_2, y_2, z_2, \dots, x_{n-3}, y_{n-3}, z_{n-3}]^T \in \mathbb{R}^{3(n-3)} \quad 5.5$$

The formulated optimization problem was solved using the Sequential Quadratic Programming (SQP) method [170], a widely used iterative technique for constrained nonlinear problems, where each step involves solving a Quadratic Programming (QP) subproblem that locally approximates the original nonlinear objective and constraint functions. At each iteration, the QP linearizes the constraints and approximates the objective using a second-order Taylor expansion. Following this, a line search is applied for merit functions to update the estimates, and the solution is iteratively refined until convergence is achieved. This SQP method was chosen due to its effectiveness in minimizing nonlinear least-squares problems, its ability to enforce physical constraints such as the UWB node positions bounded within a

defined measurement region, and its high accuracy and convergence properties in moderately sized problems like 6 unknown mobile tag positions in our tested case.

The optimization method was initialized with well-defined initial start position estimates at the first update cycle, where the start position was set at approximate sensor node locations that were determined using prior knowledge of their expected placement relative to the fixed sensor nodes. For subsequent time steps, the estimated positions from the previous time step were used as the initialization for optimization. For the experiments in this study, the search space was constrained to the actual measurement region with the minimum and maximum bounds set at $[-2\text{m}, 2\text{m}]$ in the X and Y dimensions and at $[0\text{m}, 2\text{m}]$ in the Z dimension.

An additional iterative refinement loop was introduced to improve robustness and avoid convergence to local minima. After each optimization cycle, the estimated positions were used to compute the reconstructed distances. If the distance estimation error exceeded a predefined threshold equal to the standard deviation of the random error component of the UWB distance measurement, the optimization was re-run with adjusted initial values. These adjustments involved adding small random perturbations (± 1 cm) to the previous initialization to explore alternate solutions. This process was repeated until either the estimated distances closely matched the measured distances (i.e., RMSE fell below the threshold) or a maximum of 10 iterations was reached. If the threshold was not met within the allowed iterations, the solution with the lowest RMSE was selected as the final position estimate.

5.2.3 Trilateration-based position estimation

The standard trilateration-based approach [158] based on geometric technique was implemented for UWB position estimation, considering distance estimates that correspond to the star configuration. The UWB distance measures were initially filtered as mentioned in Section-UWB measurement preprocessing, to have the same input quality as used for the proposed Swarm method. In this method, the positions of each of the mobile UWB nodes were determined using their measured distances with all of the fixed sensor nodes and the known locations of the three fixed UWB nodes in the network. Since each known distance represents a sphere of possible mobile sensor positions centered at the corresponding fixed sensor node, the best

estimate of the position of the intersection of these spheres in a 3D space is taken as the position estimate for the mobile sensor node. This results in a set of three Euclidean distance equation (equation 5.3) between each mobile node and the three known fixed sensor nodes. Solving for this set of equations provides two intersection points. Due to the positioning of the fixed nodes, only one of the two possible solutions can be identified as being inside the measurement area is taken as an estimate for the position of the mobile node.

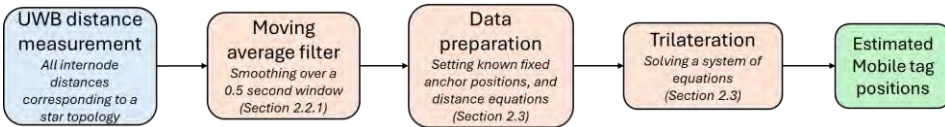


Figure 5.3: Trilateration-based position estimation process pipeline

5.2.4 Experimental validation

Sensitivity analysis with synthetic UWB distance estimates

The experiments were carried out in a motion capture laboratory to facilitate validation against a gold standard optical marker-based motion capture system for clinical applications (Vicon Motion Systems Ltd, Oxford, UK, 8 cameras). The optical motion capture system measures the positions of auto-reflective markers at a rate of 100 samples per second. To enable a controlled sensitivity analysis for the effect of varying levels of UWB distance measures bias and random errors, in this study the distance measurements were synthetically generated by combining the Euclidian distances between recorded position data for pairs of auto-reflective markers (simulated synthetic node positions) with synthetic bias and uniformly distributed random errors, simulating realistic distance estimates recorded through UWB nodes for different amounts of bias and random errors. Value ranges for distance estimate bias error and random error standard deviation were based on actual experiments with UWB nodes [156,171].

Validation Protocol

A total of nine synthetic sensor nodes were used, with three sensor nodes on fixed known locations (‘anchor nodes’) and the remaining six synthetic sensor nodes (‘mobile nodes’) were moved around. Each of the six synthetic nodes was mounted

on a wooden stick, held by three persons performing varying movements. Three trials with varying free movements were performed with node distances typical for 3DAHM (0.2 to 2m), delivering position estimates of 6 mobile nodes. All measurements with the optical motion capture system were down-sampled from 100 samples per second to 4 samples per second, as this is a typical UWB update rate for a swarm of 9 nodes [119] and also delivers statistically independent samples (based on autocorrelation analysis of the position data). All the trials lasted around 5 minutes, resulting in around 1,200 position estimates per sensor per trial (12,600 position estimates for all trials). All inter-node distances for the swarm of 9 nodes were computed from the measured positions.

A sensitivity analysis was performed for position estimation performance for both the trilateration and the proposed Swarm optimization methods by comparing their estimates against the position estimates of the optical motion capture system considered being the ground-truth. This sensitivity analysis was done by repeatedly applying both methods to the synthetic node distance data with various amounts of added bias and random errors. The values for bias errors and random error standard deviation in the synthetic distance estimates were chosen based on previous experiments in which UWB node distance estimation performance was iteratively optimized and tested against the optical motion capture system [138,156]. The best performance achieved was a bias error of 0.5 cm and a random error SD of 5 cm (referred to henceforth as ‘Realistic UWB distance error level’). Therefore, the sensitivity analysis was performed for this combination of error values and multiple combinations with higher and lower error values around this standard error level. Specifically, the bias in the synthetic UWB distance measurement was chosen to be discrete steps from 0 cm, 0.5 cm, 1 cm, and 2 cm. For each bias level, the standard deviation of the normally-distributed random error was progressively increased from 0 cm to 12 cm in 2 cm steps, with additional tests performed for values of 0.5 cm, 1 cm, and 5 cm. In the results section, special attention was given to the validation with the Realistic UWB distance error level.

5.2.5 Data analysis

To evaluate the accuracy of both position estimation methods, the position estimation error was calculated as the Euclidean distance between the positions

estimated with these methods and those directly measured with the optical motion capture system-based positions. Mean position estimation error and its standard deviation (SD) were analyzed across various test conditions. Axis-specific accuracy was examined by analyzing the absolute mean errors and their SD in X, Y, and Z directions separately. Additionally, the statistical significance of the error reduction achieved by the swarm optimization method over trilateration in Realistic UWB distance error level conditions was tested using IBM SPSS Statistics (Version 28.0.1.0). The choice of test was determined based on the distribution of the error, where a standard paired t-test would be performed if the errors are normally distributed, or a Wilcoxon test would be performed otherwise.

5.3 Results

5.3.1 Outcome data distribution

The position estimation error based on both the proposed method and trilateration was found not to be normally distributed, therefore, a paired Wilcoxon tests were used to assess the statistical significance of the found difference in performance between both methods. The position estimation for the individual axis was normally distributed across the X and Y axes, while it was non-normal for the Z-axis. Therefore, a paired t-test was performed for the X and Y, and a Wilcoxon test for the Z-axis errors.

5.3.2 Realistic UWB distance error level validation results

The estimated positions obtained from both the proposed swarm optimization and trilateration methods for Realistic UWB distance error level (bias- 0.5 cm and random error- 5 cm) in the synthetic distance estimates from one of the trials are plotted for each coordinate axis alongside the actual ground truth positions (Figure 5.4). The mean 3D position estimation error for the swarm optimization method was 6.49 cm, whereas the trilateration method produced a higher mean error of 8.83 cm. Furthermore, the SD of position estimation error was also lower for swarm optimization at 5.77 cm compared to the trilateration SD of 6.54 cm ($p < 0.001$). The mean difference in error between the two methods was 2.33 cm, with a 95% confidence interval ranging from 2.26 cm to 2.39 cm.

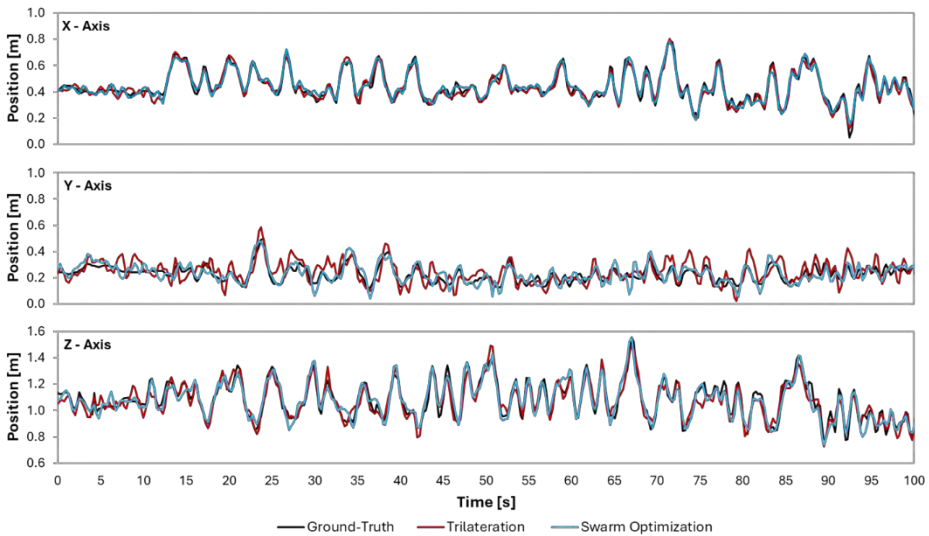


Figure 5.4: A zoomed-in typical example of the position estimated by the proposed swarm optimization (blue) and trilateration (red) methods, along with the ground-truth position estimates per coordinate axis.

In this study, x and y represent the horizontal directions (width and depth), while z represents the vertical direction. Accordingly, axis-specific position errors are reported as horizontal (x - y plane) and vertical (z -axis) errors. Examining the errors along individual axis coordinates, the absolute mean errors along the X , Y , and Z axes for swarm optimization were 1.9 ± 3.2 cm, 3.5 ± 2.9 cm, and 4.1 ± 4.9 cm, respectively. The trilateration method exhibited higher errors, with absolute mean errors of 2.1 ± 3.3 cm, 5.9 ± 4.6 cm, and 4.7 ± 5.3 cm, respectively. The significance testing of individual axes resulted in lower p -values ($p < 0.001$ for x and y axes; $p < 0.008$ for z -axis), indicating a significant improvement over trilateration.

5.3.3 Error sensitivity analysis results

The error sensitivity analysis under a no-bias situation shows that the mean position estimation errors of the swarm optimization method rise from 0.23 cm at 0 cm random error to 13.60 cm at 12 cm random error, while the trilateration method increases more significantly from 0.23 cm to 19.55 cm over the same noise levels (Figure 5.5). The SD of the position estimation error follows a similar trend, with the SDs being 5.23 cm at 0 cm random error for both methods and rising to 8.38 cm for swarm optimization and 11.45 cm for trilateration at 12 cm random error.

The position estimation based on the proposed swarm optimization method always showed a smaller error than the position estimates from the trilateration, except for the ideal scenario (No bias and no random error), where both had exactly the same accuracy (Figure 5.5). For both methods, the position estimation errors increase with the increasing random error and the bias error components in the UWB distance measurement.

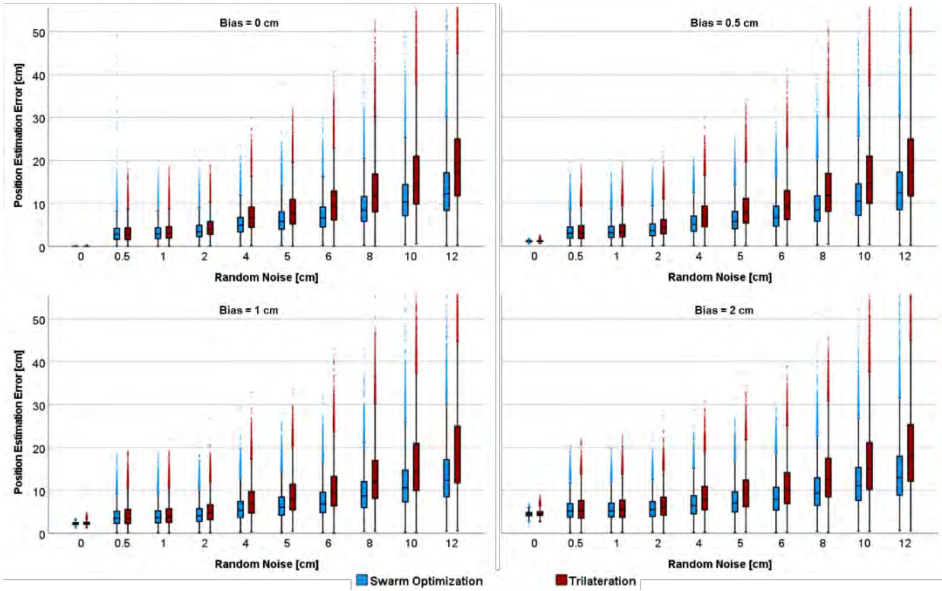


Figure 5.5: Boxplots of position estimation errors for Swarm Optimization and Trilateration methods across varying levels of input random error and bias conditions. The y-axis represents the position estimation error (cm), with the graph capped at 50 cm to improve visual clarity; outliers exceeding 50 cm are not shown but were retained in the statistical analysis.

For the swarm optimization method with no random error component in UWB distance measures, the mean position estimation errors increase from 0.23 cm at 0 cm bias to 4.66 cm at 2cm bias, while the trilateration method shows a larger increase from 0.23 cm to 4.85 cm under the same conditions. At the highest random error tested (12 cm), the error for the swarm method reaches 14.21 cm at 2 cm bias, whereas trilateration results in 19.465 cm. The significance testing indicated that for all the bias and random error cases, the improvement was always significant. Also, it can be again interpreted from the difference of the errors between the proposed swarm and trilateration method (Figure 5.6).

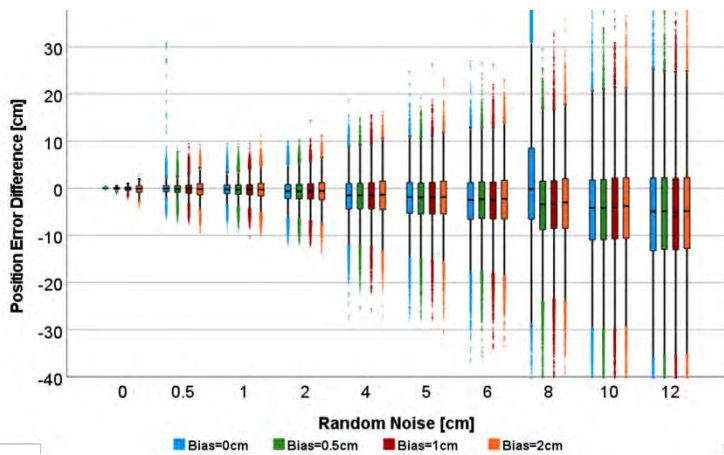


Figure 5.6: Boxplot showing the distribution of the differences in position estimation errors between Swarm Optimization and Trilateration (Swarm – Trilateration) across different combinations of bias and random error levels.

All processing time measurements were conducted on a system equipped with an Intel® Core™ i7-9700K CPU @ 3.60 GHz, with 16 GB RAM, running a 64-bit Windows 10 (Version 22H2) operating system. The positioning algorithms were implemented and executed in LabVIEW. The system was dedicated to running the positioning algorithms during the processing time measurements, with no significant background applications running. The average processing time of 21.27 ± 2.71 ms was observed for the swarm optimization method with noise combinations of no bias and low random error (None and 0.5 cm). While for all higher noise levels present in the UWB distance input, the average processing time of the swarm optimization method was 158.01 ± 57.46 ms, which was higher but very similar for all the varying noise levels. For trilateration, the average processing time per position estimate was almost the same irrespective of the input noise levels, with the mean estimation time being 0.52 ± 0.58 ms for no noise settings and 0.61 ± 0.52 ms for the highest input noise setting.

5.4 Discussion

The results of this study demonstrate that the proposed swarm optimization-based method significantly enhances position estimation accuracy compared to the conventional trilateration method. The swarm optimization-based approach method showed position estimation errors of around 6.5 cm for the Realistic UWB distance

error levels in the input measurement, which is significantly lower than the trilateration method with errors of around 9 cm ($p < 0.001$). This suggests that the proposed method is a reliable alternative for UWB-based position estimation. Additionally, the SD of position estimates was always lower for the swarm-based method compared to trilateration, indicating the method has a greater consistency in its achieved accuracy.

The comprehensive error sensitivity analysis conducted in this study provides a practical understanding of the input error conditions required to achieve a desired level of position estimation accuracy. This study establishes a reference for real-world deployment of UWB-based localization methods. Error sensitivity analysis results indicate that the proposed swarm optimization method outperforms the trilateration methods in all input error conditions (Figure 5.5), except the zero input error scenario, where both methods performed similarly. The trilateration's performance deteriorates more rapidly as noise and bias increase, making it less reliable for higher input errors in UWB distance measures. When random error present in the UWB distance measurements is below 4 cm, trilateration performs comparably to the proposed swarm optimization method (<1 cm difference in position errors), making it a suitable solution if the required accuracy and consistency are achieved. However, for a higher noise level of 4 cm or higher, the swarm optimization method significantly outperforms trilateration by reducing errors by more than 20%, and with up to 6 cm lower error than trilateration at the highest tested noise level (i.e., around 40% reduced errors). This suggests that the proposed swarm optimization-based approach provides an overall more reliable position estimate, making it beneficial for real-world scenarios where measurement noise can be higher.

The performance demonstrated by the proposed swarm optimization-based method is comparable to a few of the more complex state-of-the-art UWB positioning algorithms [157,172,173], while better than most of the reported accuracies [163,164,166-168], tested under similar LOS conditions. For instance, [157] conducted a comparative study of multiple position estimation algorithms, where the best accuracy achieved was 5.51 cm using a Kalman filter with the least square-based position estimates utilized as an update. While all other methods tested in the study of Sang et.al., 2019, under similar conditions resulted in position estimation errors

of around 8 cm [157]. Only a few cutting-edge methods push the error down to the single-digit centimeter level, specifically Guo et al., 2024 attained around 2 cm error by aggressively mitigating NLOS multipath [172], and Huang et al., 2024 achieved around 5 cm error by robust filtering (MCC-UKF fusion) in controlled settings [173]. In contrast, most real-world UWB deployments (with no sensor fusion) and based on conventional multilateration methods achieved position estimation errors in the range of 10 to 30 cm, under LOS conditions [163,164,166-168]. In essence, the proposed swarm optimization-based approach could match the best reported accuracies and exceed other conventional methods without the need for heavy infrastructure (minimal anchors) and without any complex algorithms such as sensor fusion.

In terms of computational efficiency, the trilateration method demonstrated a significantly lower computational cost, with an average processing time of less than 1 ms for each position estimate. This reflects the inherent simplicity of trilateration, which relies on direct geometric solutions without iterative computations. In contrast, the proposed swarm optimization involves solving a non-linear optimization problem with multiple variables, making it computationally more intensive by design. The proposed Swarm optimization approach exhibited an average processing time of around 158 ms per estimate. Only in the virtual absence of random error did the computational time go down substantially. Thus, while trilateration offers superior computational efficiency, the swarm optimization approach provides improved accuracy, particularly in noisy conditions, at the cost of greater algorithmic complexity and processing demands. The trade-off between accuracy and computational efficiency suggests that trilateration remains preferable in low-noise conditions, while swarm optimization is more beneficial when accuracy is a priority in noisy environments.

Across all tested conditions, the Swarm Optimization method consistently produced lower standard deviation values in the position estimation errors compared to the Trilateration method, indicating higher consistency (i.e., reduced fluctuation in the position estimates). This higher consistency of the proposed method under high-noise conditions highlights its potential for applications that require highly consistent estimates, such as clinical rehabilitation. Although the achieved accuracy is not yet sufficient for the direct use in the intended ambulatory 3D analysis of

human movement and clinical rehabilitation applications, which require an accuracy around 1 cm or lower [119], the proposed method's ability to provide more consistent position estimates than the raw input UWB distances makes it a strong candidate for integration with data fusion techniques. Specifically, to achieve even lower position estimate errors, typically the UWB position estimates are used as an update in data fusion with, e.g., MIMUs. As this study shows superior UWB-based position updates with the swarm optimization-based method, it is expected that also the position estimates of such data fusion methods should show lower errors than the current state of the art.

Though the extensive error sensitivity analysis provides insights into error propagation, guiding future application of this method, however, the real-life potential of the proposed method still has to be confirmed in experiments with actual UWB data. Especially, the errors caused by NLOS conditions and their mitigation should be studied in detail. Also, further improvements should focus on optimally exploiting the redundancy in the position estimates in a fully connected swarm to balance accuracy, mitigation of NLOS-related errors, update rate, and computational load.

5.5 Conclusion

This study introduces and evaluates a swarm optimization-based position estimation method that utilizes all available internode distances rather than restricting measurements to a star topology. The proposed swarm optimization approach was validated against an optical measurement system together with a well-established trilateration method, and their performance was compared. The swarm optimization method significantly improves the position estimation over the trilateration method, with position estimation errors around 6.5 cm. An extensive error sensitivity analysis provided a deeper understanding of how the error characteristics of UWB distance estimates influence position estimation quality. It is expected that using the improved position estimates in data fusion, e.g., with MIMUs, will improve the data fusion position estimation quality. Further research is required to achieve the lower error level required for the intended high-accuracy applications as 3D AHM. The increased accuracy in UWB-based position estimation seems generally beneficial for any application using a UWB swarm.

Chapter 6

Position Estimation with integrated UWB/MIMU sensors in relevance to 3D Analysis of Human Movement

This chapter is submitted for publication as:

Yogesh, V.; Beijnum, B.J.V.; Buurke, J.H.; Veltink, P.H.; Baten, C.T.M. Position Estimation with integrated UWB/MIMU sensors in relevance to 3D Analysis of Human Movement.

Abstract

The integration of Ultrawideband (UWB) and Magnetic Inertial Measurement Unit (MIMU) sensors offers a promising solution for accurate and consistent absolute position estimation in ambulatory 3D analysis of human movement (3D AHM). However, this integrated sensor system has not been utilized for 3D AHM, but has been widely used for pedestrian tracking applications. There is no specific data fusion tailored and validated for this application, and there is limited knowledge on the effect of errors in the UWB distance measures on the performance of the data fusion. This study proposes and evaluates a fusion algorithm, namely the UMIMU fusion algorithm, based on an Extended Kalman Filter (EKF) for fusing UWB and MIMU data to optimize position estimation in a 3D AHM setting. The proposed fusion algorithm's performance is systematically analyzed utilizing MIMU and synthetically generated UWB measurements (using an optical motion capture system) under varying UWB measurement errors and update frequencies. Results indicate that, with realistic UWB measurement updates, the UMIMU fusion algorithm achieves a position estimation error of approximately 6 cm for all the sensor nodes in the swarm. For UWB distance input with bias errors ≤ 1 cm and random errors ≤ 5 cm, results in position errors lower than the state-of-the-art accuracies already achieved, but degrade significantly beyond these thresholds. An update rate of 4 samples per second (sps) or more offers better accuracy. These findings provide crucial insights into improving UWB/MIMU sensor fusion, specifically guiding advancements in UWB technology, and facilitating their future adoption in clinical 3DAHM applications.

6.1 Introduction

Accurate 3D analysis of human movement (3D AHM) is essential in a wide range of applications, from clinical rehabilitation and performance assessment to biomechanical research and assistive technology design. In clinical settings, 3D AHM is traditionally performed in a laboratory-based optical-motion capture system and force plates that provide accurate measurements [174,175]. Although these systems are highly accurate, their practical use for clinical 3D AHM is limited by the need for a fixed laboratory setup, the complexity of use (manual post-processing of the measurement), the high cost of purchase and operation, and the lack of portability [16,175,176]. Wearable sensor technologies offer a promising alternative that enables ambulatory monitoring at a low cost with simple infrastructure, allowing human movement assessments to be conducted in any environment, such as clinics, homes, or sports fields. Magnetic Inertial Measurement Unit (MIMU) sensors are widely used wearable technology for ambulatory 3D AHM, due to their low cost, ease of use, and good accuracy [177,178]. MIMU sensors can provide accurate 3D orientation and rotational kinematics by exploiting the complementary information provided by accelerometers, gyroscopes, and magnetometers [179]. This high accuracy in rotational kinematics is typically achieved using sensor fusion techniques such as the Kalman Filter (KF) to integrate the data from the three sensor modalities [40,67,179]. However, their capability to estimate positions (displacement over time) accurately is limited due to the integration drift, especially since the positions are computed by double-integration of the accelerometer data [42,43].

Multiple methods have been explored to reduce position estimation errors through assumptions about the movement performed. The most commonly utilized method is Zero-Velocity-Update (ZUPT), which works by assuming that the foot is briefly stationary during the stance phase of walking [44,69]. Another approach utilizes biomechanical models that apply joint movement constraints to estimate motion more accurately [45]. While these methods can improve accuracy in specific tasks, they are often limited in clinical use because they rely on assumptions that may not always be valid for all people or situations. For example, patients often have irregular and unique movement styles (shuffling, toe-walking, or spasticity) that result in unclear phases of gait, thereby not matching the general biomechanical assumptions. Another strategy to limit drift is to constrain the analysis to short, cyclic movements

[3], however, this approach restricts the generalizability of position estimates across longer or more irregular movements.

A robust alternative solution is introducing additional sensor modalities to MIMU, which could provide independent position information to complement the MIMU data and create redundancy for 3D positional data. This would enable sensor fusion-based techniques to improve accuracy by combining information from these additional sensors, as this is the same mechanism already utilized to achieve higher accuracy for rotational kinematics. Among the available technologies, Ultrawideband (UWB) sensors are the most promising to be integrated with the MIMU sensors, especially due to their complementary error characteristics [57,119]. The UWB-based methods can provide absolute position estimates of a free-moving mobile UWB node within a local coordinate system defined by a fixed set of UWB anchors, using methods such as trilateration. These estimates are drift-free as they do not accumulate errors over time [57,65]. However, their accuracy is negatively affected by random ranging errors, distortion, and Non-line-of-sight (NLOS) situations [149,155]. MIMU sensor-based methods, on the other hand, provide 3D position estimates relative to their initial position by estimating sensor displacement over time by double integration of MIMU sensor acceleration with respect to a world frame. This approach typically causes large (integration drift) errors that accumulate over time [42,43], but are unaffected by NLOS situations. These complementary error characteristics of the UWB and MIMU position estimation methods facilitate combining them into an optimal estimate applying data fusion methods, to deliver an accuracy and consistency significantly better than each of the two methods can deliver on its own [65,78,105].

Despite the potential theoretical advantage and practical applicability for clinical 3D AHM, the integrated UWB/MIMU sensor system has not been adopted for applications of 3D AHM or in clinical rehabilitation [119]. To the best of the author's knowledge, no studies have utilized a swarm of these integrated sensors for estimating body segment position in ambulatory 3D AHM applications. Instead, they have only been widely used for human applications such as pedestrian navigation [180,181] and indoor localization [155,182], which have lower accuracy requirements compared to clinical scenarios [119]. In clinical 3D AHM, accurate and consistent position estimation is critical for assessing patient movement and

rehabilitation outcomes [29]. Currently, optical marker-based motion capture systems are considered the commonly accepted practical standard (current de facto gold standard) for clinical rehabilitation [174]. The current position estimation accuracy of these optical-motion capture systems is generally accepted as suitable for clinical 3D AHM applications [46,174], with an average marker position estimation error of these systems typically below 1 cm [46,71] with consistent, drift-free estimates. In addition to the accuracy, consistent position measurements are vital for ensuring reliable tracking during clinical evaluations or rehabilitation sessions [29]. Therefore, it is assumed that to achieve a similar clinical relevance, an integrated UWB/MIMU sensor system should deliver position estimates that are highly consistent and adequately accurate with non-cumulating position estimation errors lower than 1 cm.

The accuracy requirements for clinical 3D AHM are well understood, however, the actual performance of integrated UWB/MIMU systems in this domain remains largely untested [119], especially since there are no studies applying this in 3D AHM, as previously stated. Instead, these systems have only been used for applications of pedestrian navigation, and while the target applications differ, the reported accuracy metrics can offer useful insight into their current technical capabilities. In the context of other application areas such as pedestrian navigation, the lowest absolute position estimation errors reported are around 4 cm [81,83]. However, these were achieved in controlled settings with respect to fixed and clear Line-of-sight (LOS) situations [119]. In general, the majority of the studies reported a lower accuracy, with position estimation errors being around 10 cm or more [121,122]. Furthermore, the existing integrated UWB/MIMU sensor systems have not yet been systematically developed or validated for the demands of clinical 3D AHM applications, which require sub-centimeter accuracy, shorter movement ranges (0.2–2 m), mixed cyclic and random motions, and both LOS and NLOS conditions.

The quality and accuracy of the data fusion methods integrating the UWB and MIMU systems to estimate positions greatly rely on the accuracy of both sensors separately [183]. Previous research indicates that the MIMU sensors within the UWB/MIMU sensor systems have already been refined and tuned to reach the maximum obtainable accuracy by the integrated sensor system [48,156]. However, the current UWB sensor within the UWB/MIMU sensor systems does not

consistently meet these high accuracy requirements due to various sources of error, including measurement bias and random error, even after performing antenna calibrations and additional swarm calibrations [143-145,171]. Systematic bias and random error in UWB measurement updates can degrade the performance of the data fusion, even when the MIMU provides high-frequency position estimates (during the prediction phase of the data fusion). The accuracy that the data fusion-based position estimator can attain is highly correlated with the accuracy that the UWB system can provide these updates with [156,171]. Additionally, the update rate of integrating UWB position updates into the data fusion process, such as the Kalman filter, could also influence the final position estimation accuracy. So far, the influence of measurement update frequency has not been studied in detail.

In summary, despite the potential of integrated UWB/MIMU for clinical 3D AHM, they have not been tailored and validated for this application. Most prior research was on localization applications where accuracy demands were lower and conditions of measurement were different from 3D AHM settings. Typical 3D AHM demands sub-centimeter accuracy with high consistency, and the settings defined for the 3D AHM shorter distance ranges (0.2 m to 2 m), varying subject velocities, cyclic movements, and mixed LOS and NLOS conditions [171]. To enable UWB/MIMU fusion methods to reach comparable levels of clinical accuracy, it is also crucial to understand how UWB distance measurement errors and measurement update frequency affect the final fused position estimates. The impact of these UWB distance error characteristics, along with the update rate at which UWB-based position updates are incorporated into the fusion algorithm, remains insufficiently studied. Therefore, the goal of this article is to address this research gap by proposing a data fusion method based on an extended Kalman filter (EKF) combining the UWB and MIMU data specifically in 3D AHM settings, hereafter referred to as “UMIMU fusion algorithm”. Following this, the proposed UMIMU fusion algorithm is systematically evaluated and quantified for the effect of UWB distance measurement error on the position estimation accuracy, utilizing actual MIMU data and synthetically generated UWB data. The following objectives are designed to guide and address the goals and gaps:

1. Propose an EKF-based algorithm for estimating sensor positions by combining MIMU data and UWB position estimates in a 3D AHM setting and evaluate its accuracy and consistency.
2. Identify the effect of UWB distance measurement errors (bias and random error) on the final position estimation accuracy of the proposed algorithm through an error sensitivity analysis using synthetically generated UWB data.
3. Determine the optimal UWB measurement update frequency for the proposed algorithm, in terms of accuracy.

The novelty of this work lies in its focus on the 3D AHM application setting and its systematic exploration of how UWB distance error characteristics and update frequency influence fusion performance. The rest of the article is structured as follows: Section 2 provides a detailed description of the UWB/MIMU measurement configuration and the proposed UMIMU position estimation algorithm. Section 3 outlines the experimental setup, generation of synthetic UWB data, and procedures for evaluating the system's performance. Section 4 presents and discusses the results, including error analysis and update frequency effects. Finally, Section 5 concludes the article by summarizing the key findings, highlighting their clinical relevance, and suggesting directions for future research.

6.2 Methods

6.2.1 Integrated UWB/MIMU measurement configuration

The integrated UWB/MIMU sensor system used for this study is a single hardware platform that combines both the UWB and MIMU sensors and is referred to as the 'UMIMU' (Ultra-wideband Magnetic Inertial Measurement Unit) sensor system. The MIMU sensors (Xsens B.V., Enschede, The Netherlands) within the UMIMU system provide 3D acceleration, angular velocity, magnetic vector, and orientation data at 100 samples per second (sps) using an internal proprietary EKF algorithm for orientation estimation (XKF3 sensor fusion algorithm, Xsens B.V.). The UWB sensors in the UMIMU sensor system measure the distance between sensor nodes based on the Time of Flight (ToF) data [147]. The ToF estimates are derived using the Alternative Double-Sided-TWR (AltDS-TWR) algorithm [137], which estimates

the ToF by exchanging multiple timestamped messages between the ranging UWB nodes in both directions, compensating for the clock offsets.

The measurement configuration consists of a set of n UMIMU nodes, with three UMIMU nodes positioned at fixed, known positions within the measurement area, while the remaining $n - 3$ UMIMU nodes are attached to the measurement subject (Figure 6.1). An additional UMIMU node serves as the ‘controller node’, which coordinates UWB rangings, transmits operational commands, relays information to a PC via USB, and collects the UMIMU data for processing. The UWB distance measurements are performed using a swarm topology, a fully connected network where each UWB sensor node measures the distance to every other node in the system (Figure 6.1). This configuration ensures redundant distance estimates, which can be exploited for relative position estimation using optimization-based approaches. The swarm topology results in $n(n - 1)/2$ unique distance estimates per update cycle in a fully connected network of n sensors. The update rate for a complete set of distance estimates ranges from 1 to 20 sps, depending on the number of sensors used.

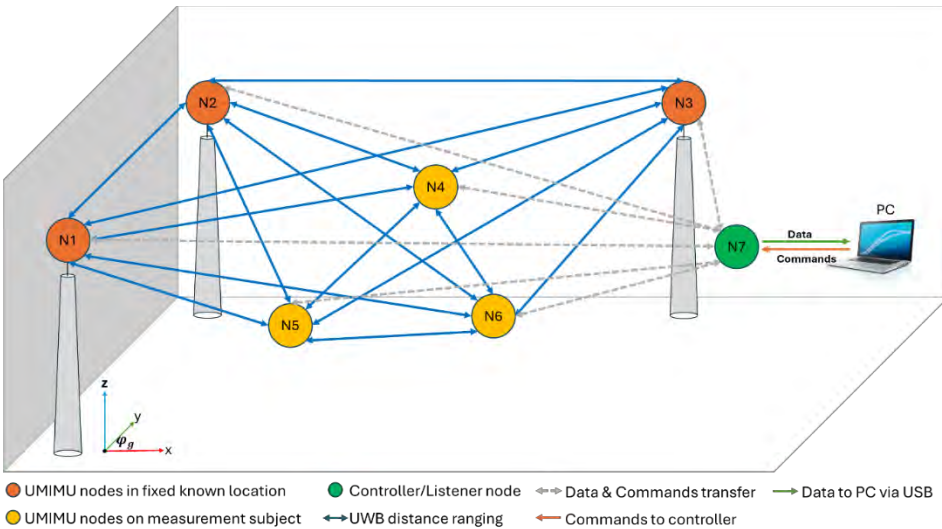


Figure 6.1: UMIMU sensor system measurement configuration and illustration of the swarm topology.

6.2.2 UMIMU fusion algorithm

The architecture of the proposed UMIMU fusion algorithm is based on a loosely coupled EKF-based sensor fusion approach (Figure 6.2). The loosely coupled framework utilizes the position estimates derived from the UWB distance measures as a measurement update in the EKF, and offers computational efficiency and flexibility while delivering performances comparable to the complex tightly coupled framework [119]. In this architecture, the EKF prediction step relies on the high-frequency MIMU data (sampled at 100 sps), which is used to propagate the state forward in time based on inertial measurements. UWB distance measurements are first preprocessed and then used in a swarm optimization algorithm to estimate absolute sensor positions. These positions serve as low-frequency measurement updates (1-20 sps) to the EKF. The EKF incorporates initialization routines, motion modeling, and a drift correction scheme that utilizes a polynomial and linear interpolation to minimize cumulative errors between measurement updates.

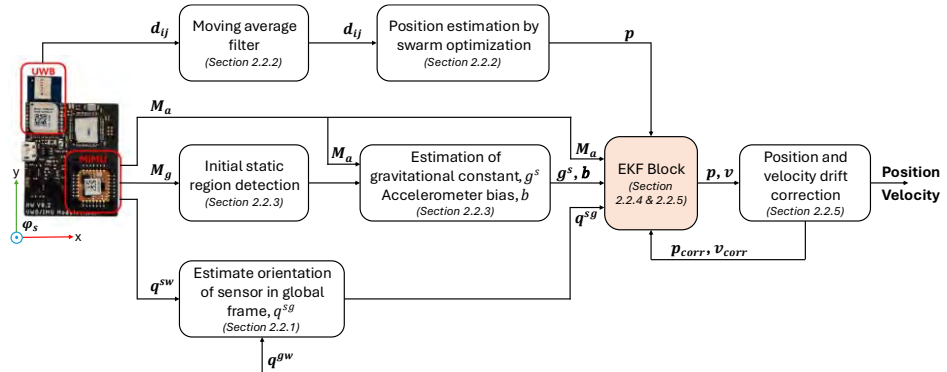


Figure 6.2: Architecture of the proposed UMIMU fusion algorithm combining the UWB and MIMU data based on the EKF.

Sensor measurement and models

The global coordinate frame φ_g is defined relative to the experimental setup (Figure 6.1), where the y-axis is aligned along the line connecting the two adjacent UWB anchor nodes, the x-axis is orthogonal to the y-axis in the horizontal plane and points towards the third UWB anchor, and the z-axis points vertically upwards. The sensor coordinate frame is defined by the MIMU sensor and represented with the physical layout of the sensor, where the x-axis runs along the narrow side of the sensor, the

y-axis along the wider side, and the z-axis perpendicularly upward from the sensor plane (Figure 6.2). While the world reference frame φ_w is the inertial navigation frame, where the x-axis points towards the Earth's magnetic north, the z-axis points upwards aligned with the gravity vector, and the y-axis completes the right-handed coordinate system. All orientations are represented as quaternions, q in this paper. In the proposed UIMMU fusion algorithm, the prediction phase of the EKF is specifically based on the accelerometer and orientation data measured by the MIMU sensors. The accelerometer signal M_a is described as the sum of the accelerations of the sensor a^s , gravitational acceleration g^s , accelerometer measurement bias b , and Gaussian noise e_a , all measured in the sensor coordinate frame φ_s , and is defined as

$$M_a = a^s + g^s + b + e_a \quad 6.1$$

The orientation provided by the MIMU sensor q^{sw} , measures the sensor orientation and expresses it as the rotation from the sensor coordinate frame φ_s to the world reference frame φ_w . The absolute position updates from the UWB distance measurements are expressed in the global coordinate frame φ_g , as defined by UWB anchor nodes. To ensure both data sources are represented in the same coordinate frame for fusion, the MIMU derived position estimates were transformed into the global coordinate frame φ_g . This is achieved by computing the relative orientation between the sensor and global frames q^{sg} , given by

$$q_t^{sg} = q_t^{sw} \cdot (q^{gw})^{-1} \quad 6.2$$

Here, q^{gw} is the quaternion representing the fixed rotational transformation from the global coordinate φ_g frame to the world reference frame φ_w and is treated as a constant during the fusion process. The subscript t in the quaternions represents the corresponding time step.

Position estimation from UWB

The absolute position estimates of the mobile sensor nodes in the global coordinate frame φ_g were computed from the swarm of UWB distance measurements through a previously developed swarm optimization-based position estimation approach

(Chapter 5). This approach estimates the 3D positions of mobile UWB sensor nodes by minimizing the root mean square error between all measured pairwise distances and those reconstructed from estimated coordinates, leveraging all available internode distances in a fully connected swarm topology. Before optimization, the raw UWB distance measurements were smoothed using a zero-phase moving average filter with a fixed window duration to reduce measurement noise without introducing temporal lag. Further details on the formulation, constraints, and preprocessing steps can be found in Chapter 5. The resulting UWB-based position estimates are used here as measurement updates in the proposed UMIMU fusion algorithm.

EKF state model and Initialization

The goal of the proposed UMIMU position estimation algorithm based on EKF is to estimate the state vector \mathbf{x} and its covariance P . The state vector consists of 3D position \mathbf{p} , velocity \mathbf{v} , and the accelerometer bias \mathbf{b} . For each UMIMU sensor, the state vector contains 9 states and is defined below:

$$\mathbf{x} = (p_{x,n} \quad p_{y,n} \quad p_{z,n} \quad v_{x,n} \quad v_{y,n} \quad v_{z,n} \quad b_{x,n} \quad b_{y,n} \quad b_{z,n})^T \quad 6.3$$

For n sensors, the total state dimension expands to $9n$ states.

In this article, a hat on a variable denotes an estimated value, while a superscript minus indicates an a priori estimate, meaning the value before incorporating measurement updates. The subscript t represents the corresponding filter time step.

The first step in the implementation of the UMIMU fusion algorithm is setting up all the initial ($t = 0$) state values of position, velocity, and accelerometer bias. The initial position of all the unknown mobile sensors was estimated through the swarm optimization of the UWB distance measures. All measurements start from a static position, therefore, the initial velocity is always set to zero. To identify the initial static region, the normalized gyroscope angular velocities were analyzed, and a threshold of 0.07 deg/s was applied. Within this detected static period, the accelerometer is assumed to measure only gravitational acceleration. Therefore, the gravity component was estimated by averaging the accelerometer norm over this static interval. With the gravity component determined, it was removed from each

accelerometer measurement within the same static region, and the residual values were averaged to estimate the accelerometer bias for each axis.

EKF State Prediction

Followed by the initialization, the prediction phase of the EKF estimates the positions of the unknown mobile sensors using MIMU data. For clarity and simplicity, the following mathematical formulation is described for a single mobile sensor (one MIMU and its corresponding UWB position update). In practice and during experimental validation in this study, the proposed UMIMU fusion algorithm is applied to multiple such sensors simultaneously. When scaling to a system with multiple mobile nodes, the same principles apply, and the corresponding matrices, such as the state vector, transition matrix, and covariance matrices, expand proportionally by stacking the individual sensor-specific blocks into a larger composite matrix.

The velocity and positions in the global coordinate frame are estimated based on Newton's equations of motion, as described below

$$\hat{v}_t^g = \hat{v}_{t-1}^g + \Delta T \hat{a}_{t-1}^g \quad 6.4$$

$$\hat{p}_t^g = \hat{p}_{t-1}^g + \Delta T \hat{v}_{t-1}^g + \frac{\Delta T^2}{2} \hat{a}_{t-1}^g \quad 6.5$$

The acceleration in the global coordinate frame \hat{a}^g , is required for all the computations. The measured acceleration in the sensor coordinate frame a^s , were translated to the global coordinate frame φ_g , with the previously estimated orientation of the sensor to the global coordinate frame q^{sg} . For ease of construction of matrices and computation, the final quaternion estimates q^{sg} were converted to rotation matrices R^{sg} and the translation of acceleration is defined as

$$\hat{a}_t^g = R_t^{sg} a_t^s \quad 6.6$$

Substituting the sensor model in Equation 6.1 into Equation 6.6 will result in

$$\hat{a}_t^g = R_t^{sg} M_a - g^g - \hat{b} \quad 6.7$$

The prediction of the state is performed with the equation as defined in [184] and is

$$\hat{\mathbf{x}}_t^- = A\hat{\mathbf{x}}_{t-1} + \mathbf{u}_{t-1} \quad 6.8$$

where the state transition matrix A and the input vector matrix \mathbf{u} are built from equations 6.4 to 6.7 and are defined as

$$A = \begin{bmatrix} I_3 & \Delta T & 0_3 \\ 0_3 & I_3 & \Delta T \\ 0_3 & 0_3 & I_3 \end{bmatrix} \quad 6.9$$

$$\mathbf{u} = \begin{bmatrix} \frac{\Delta T^2}{2} (R_t^{sg} M_a - g^g - \hat{\mathbf{b}}) \\ \Delta T (R_t^{sg} M_a - g^g - \hat{\mathbf{b}}) \\ 0_{3 \times 1} \end{bmatrix} \quad 6.10$$

The covariance matrix, which describes the uncertainty of the state vector, is updated as

$$P_t^- = AP_{t-1}A^T + Q \quad 6.11$$

where Q is the process noise covariance matrix constructed based on the error characteristic of the MIMU sensor used for the study.

To minimize integration drift in position and velocity predictions, a constraint is applied to the velocity and position estimates at the end of the prediction step. The rate of change between the predicted velocity and velocity estimates at the previous timestep is compared to the average velocity change per second observed in human movement. Based on biomechanical studies, human movement typically exhibits a maximum velocity change of approximately 1.5 m/s [185]. To ensure robustness, a slightly higher threshold of 2.0 m/s is applied. Given the EKF sampling rate of 100 Hz, this translates to a maximum velocity change of 0.02 m/s per time step. If the computed velocity change exceeds this threshold, it is capped at 0.02 m/s to prevent unrealistic acceleration spikes. The position estimates are then adjusted accordingly based on the corrected velocity.

EKF Measurement update and drift correction

The measurement update step is performed whenever there is a UWB measurement update. This update step refines the state estimates with the UWB positions estimated using the swarm optimization-based method as described earlier (Section 0), which computes positions from the inter-sensor UWB distance measurements. Each mobile node equipped with a MIMU sensor has a corresponding position estimate derived from UWB data, which serves as the measurement update for that specific node. These UWB-derived position estimates are integrated independently with the predicted positions from the MIMU-based state estimation for each node, thereby enabling node-specific data fusion within the EKF framework. The measurement updates are applied by the following equations as defined in [184], where the Kalman gain is given as

$$K_t = P_t^- H^T (H P_t^- H^T + R)^{-1} \quad 6.12$$

While the state estimate and covariance are updated as follows

$$\hat{x}_t = \hat{x}_t^- + K_t (z_t - H \hat{x}_t^-) \quad 6.13$$

$$P_t = (I - K_t H) P_t^- \quad 6.14$$

where R , is the measurement noise covariance, and H matrix is the state to measurement matrix, which in this specific case is defined as

$$H = [I_3 \quad 0_3 \quad 0_3] \quad 6.15$$

A drift correction method is applied to both position and velocity estimates after every UWB update to minimize drift errors between two UWB updates. Observations from experimental data (Appendix A) suggest that the position drift follows a second-order trend, with the position error at the midpoint between two UWB updates being approximately 20% of the final error at the update point (Appendix-Figure A2). To correct the drift in position estimates, a polynomial correction is applied. First, the accumulated position drift at each UWB update instance is computed by obtaining the difference between the EKF-predicted position and the corrected position obtained after the measurement update is

performed. Following this, a second-order polynomial is fitted using three points: zero error at the previous update, 20% drift at the midpoint, and the full error at the current update. This polynomial is then used to compensate position estimates at each intermediate time step, correcting for accumulated drift over time. For velocity drift, experimental observations indicated that the error follows almost a linear trend (Appendix B), which is also supported in various studies [44,69,186]. Thus, to compensate for this, a simple linear correction is applied to compensate for velocity errors. The velocity error at the previous UWB update is set to zero, and the error at the current update is determined from the difference between the predicted and final velocity estimates. This drift is then linearly interpolated across the interval to gradually adjust the velocity estimates at each intermediate timestep. This approach is conceptually similar to methods like Zero-Velocity Update (ZUPT), where drift is assumed to grow linearly in the absence of external corrections [44].

6.2.3 Experimental validation

To evaluate the position estimation performance of the proposed UMIMU fusion algorithm, a detailed experimental validation was conducted in an optical motion capture laboratory, where all the sensor movements were tested within the typical distance ranges of 3D AHM (i.e., 0.2 m to 2 m) and at speeds of typical human movement. The complete validation was performed with actual MIMU data and synthetic UWB distance data generated from the optical marker positions, specifically for controlling the UWB input error parameters for systematic evaluation.

Measurement system

The UMIMU sensors, with integrated UWB and MIMU sensors on a single board, were used in the experiments. The details of this UMIMU sensor system are provided in [171], and relevant information for this study is summarized here. The UMIMU sensor unit consists of a DW1000 UWB transceiver module (Qorvo Inc., Greensboro, USA), an MTi-3 9-axis MIMU (Xsens Technologies, Enschede, Netherlands), and an STM32F722RE microcontroller (STMicroelectronics, Geneva, Switzerland) mounted on a custom PCB. The MIMU provided 3D orientation,

acceleration, and angular velocity data in the sensor coordinate frame, sampled at 100 sps.

For this study, it is necessary to control and test the effect of different levels of errors in UWB distance measurements, while also evaluating the impact of varying UWB update frequencies. However, the built-in UWB module within the UMIMU sensor unit had a fixed error profile and predefined measurement frequency and hence was not used in this study. Instead, a Vicon optical motion capture system (Vicon Motion Systems Ltd, Oxford, UK) was utilized. The optical motion capture system provides precise position measurement and was utilized for ground-truth validation as well as to compute inter-node distances that mimic UWB distance measurements. This setup enabled simulating various UWB error conditions by introducing controlled levels of bias and random error into the distances. Therefore, in this study, we only use the synthetically generated UWB data from the optical motion capture system. The optical motion capture position data was measured at 100 sps and was down-sampled to the desired frequencies to be tested between 1-20 sps, to systematically evaluate the effect of different UWB update rates.

As placing reflective markers directly on the UMIMU sensor could interfere with the ranging and communication process, each UMIMU sensor was mounted on a sensor-holding rig with three fixed reflective markers positioned at known distances from the UWB antenna (Figure 6.3a). The UWB node position was then derived through an initial rig calibration step, where a temporary additional marker was placed on the UMIMU sensor, and a static measurement of the rig markers was recorded using Vicon. This calibration determined the fixed spatial relationship between the rig markers and the UMIMU sensor, enabling accurate estimation of the UMIMU node position throughout the experiment. In addition, the three markers also allowed the computation of the rig orientation in the optical system's global coordinate frame, which exactly matches the global coordinate frame φ_g defined before.

A total of ten UMIMU sensors were used in the study, with three sensors fixed at known positions on tripods, serving as reference points. A single UWB node acted as the controller/listener connected to the PC via USB, while the remaining six sensors were attached to moving objects (Figure 6.3c). Each of these six sensors was

mounted on a sensor-holding rig positioned at the end of a wooden stick (Figure 6.3b). Three participants, each holding two wooden sticks with the sensors (one in each hand), performed free-arm movements based on the validation protocol described in the next section.

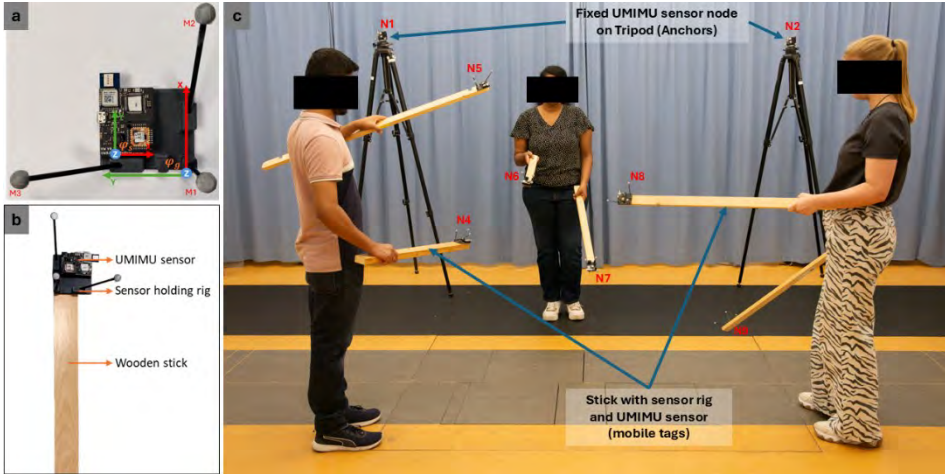


Figure 6.3: a) UMIMU sensor mounted on a sensor-holding rig with their respective coordinate systems; b) sensor holding rig with UMIMU sensor attached to a wooden stick; c) Experimental setup within a motion capture lab, with fixed known UMIMU sensors on a tripod (N1 to N3) and six unknown sensors held by three participants (N4 to N9). Note: Sensor nodes N3 (anchor), N10 (controller) are outside the view of the figure.

Establishing sensor orientation in the global frame

In this study, the fixed rotation quaternion q^{gw} was estimated through a calibration step using the optical motion capture system. The purpose of this calibration was to align the reference frames of the two systems to allow correct transformation of MIMU-derived position estimates into the global frame φ_g used by UWB. This transformation was assumed constant and used throughout all further computations to convert MIMU-derived data into the global coordinate frame used by UWB measurements. This calibration involved simultaneous measurement of both the MIMU and optical motion capture system, and utilizing the measured MIMU sensor orientation and computed rig sensor orientations for estimating the constant q^{gw} and is obtained as

$$q^{gw} = (q_t^{rg})^{-1} \cdot (q^{sr})^{-1} \cdot q_t^{sw} \quad 6.16$$

Where, q_t^{sw} is the sensor orientation expressed as the rotation from the sensor coordinate frame φ_s to the world reference frame φ_w , while, q^{sr} is the orientation of the sensor relative to the rig, and q^{rg} is the orientation of the rig in the global coordinate frame φ_g .

Experimental validation pipeline

The UMIMU sensors and the Vicon system record the movement data simultaneously at the rate of 100 sps. The measured data from both systems were synchronized by aligning the acceleration magnitude estimates from both systems using the cross-correlation technique (Figure 6.4). The synchronized Vicon data providing positions of each sensor unit were then used to estimate the inter-node Euclidean distances between all the UMIMU sensor units in the network, resulting in a set of 36 unique distances for 9 UMIMU sensor nodes used in the experiments. These estimated distances were then added with controlled levels of bias and random error to simulate UWB errors. After introducing these errors, the data was down-sampled to different rates between (1-20 sps) to match the update rates to be tested and then provided as measurement updates to the UMIMU fusion algorithm block. While the MIMU data were directly fed into the UMIMU fusion algorithm block.

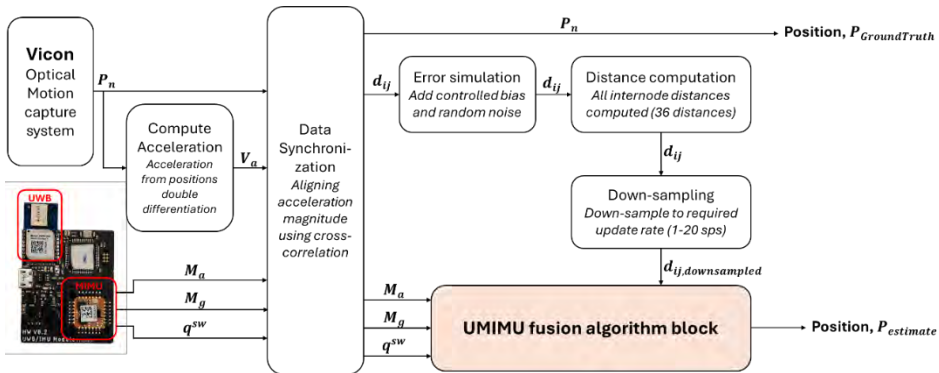


Figure 6.4: Schematic of experimental validation pipeline and implementation

6.2.4 Validation protocol

To evaluate the proposed UMIMU fusion algorithm under different motion conditions, the experiment included three distinct movement patterns. The first was cyclic movements, where controlled, repetitive motion patterns were executed. The second involved random movement, in which participants moved freely without any predetermined trajectory. The third was a combination of both, incorporating elements of cyclic and random motion. These different movement conditions were designed to assess the accuracy and consistency of the UMIMU fusion algorithm across various real-world application scenarios, particularly in LOS situations alone. All measurements for each type of movement were performed twice and recorded for a duration of around 5 minutes (~300 seconds), resulting in a total of six trials. Within each trial, the UMIMU fusion algorithm estimated the unknown positions of six sensors, providing a robust dataset for validation. To systematically assess the performance, three validation tests or evaluations were conducted, each focusing on a specific aspect of the proposed algorithm's accuracy and consistency.

Evaluation of UMIMU fusion algorithm under Realistic UWB conditions

The first validation test aimed to establish a baseline performance level for the UMIMU fusion algorithm under conditions that reflect the typical accuracy of state-of-the-art UWB measurements, hereafter referred to as 'Realistic UWB conditions'. From previous research, the Realistic UWB conditions are known to be a bias of 0.5 cm and a random error of 5 cm, with an update rate set at 4 sps, which is considered the best achievable UWB distance measurement accuracy and sampling rate [138,156]. These error settings and the update rate were applied to the synthetic UWB distances generated from all the experimental data sets. The sensor fusion framework was then applied across all the data sets (now with the error settings applied to synthetic UWB) for all three movement patterns to evaluate the UMIMU fusion algorithm's ability to accurately estimate sensor positions under these realistic error conditions.

Evaluation of the effect of UWB distance errors on UMIMU fusion algorithm accuracy

To assess the UMIMU fusion algorithm's sensitivity to increasing UWB measurement errors, a systematic error sensitivity analysis was performed. The update rate was kept constant at 4 sps while the bias of the simulated UWB distance measurement was varied in discrete steps from 0 cm to 2 cm in increments of 1 cm, with an additional test at 0.5 cm bias. For each bias level, the random error was incrementally increased from 0 cm to 12 cm in 2 cm steps, with additional tests conducted at 0.5 cm, 1 cm, and 5 cm. This validation was repeated for all movement scenarios to analyze how error levels influenced the proposed algorithm's accuracy.

Evaluation of the effect of UWB measurement update frequency on UMIMU fusion algorithm accuracy

The final validation test focused on identifying the effect of UWB update frequency on the proposed algorithm's position estimation accuracy. Update rates ranging from 1 sps to 20 sps were tested in steps of 4 sps to analyze the impact of measurement frequency on filter performance. Rather than testing all possible bias and error combinations, representative error levels were selected based on the findings from the error sensitivity analysis. Specifically, two conditions were tested: (i) an ideal scenario with no bias and no random error, and (ii) the Realistic UWB condition, i.e., 0.5 cm bias and 5 cm random error.

6.2.5 Data analysis

To quantify the UMIMU fusion algorithm's performance, the position estimation error was computed as the Euclidean norm of the positions along each axis between the proposed UMIMU fusion algorithm position estimates and the Vicon ground truth. This measure, referred to as the 'position estimation error', represents the overall discrepancy between the estimated and actual positions in three-dimensional space. The mean position estimation error was computed for each movement type and varying test conditions along with their standard deviations (SD). Additionally, the absolute mean errors for each axis (X, Y, and Z) were computed separately, along

with their respective SD, to provide further insight into axis-specific estimation accuracy.

6.3 Results

6.3.1 UMIMU fusion algorithm performance under Realistic UWB conditions

The position estimates from the proposed UMIMU fusion algorithm when utilizing the synthetic UWB distance update with Realistic UWB conditions (Bias 0.5 cm and Random error 5 cm), closely followed the ground truth position estimates from Vicon, as illustrated in a typical example (Figure 6.5). The mean position estimation error of the proposed UMIMU fusion algorithm across all three movement types in the realistic UWB measurement update conditions was 6.25 cm with an SD of 3.10 cm. It is observed that the UMIMU fusion algorithm without the drift compensation module typically exhibits higher position errors across all movement types, with the mean position estimation error approximately 2 cm greater than that of the full UMIMU fusion algorithm including drift compensation.

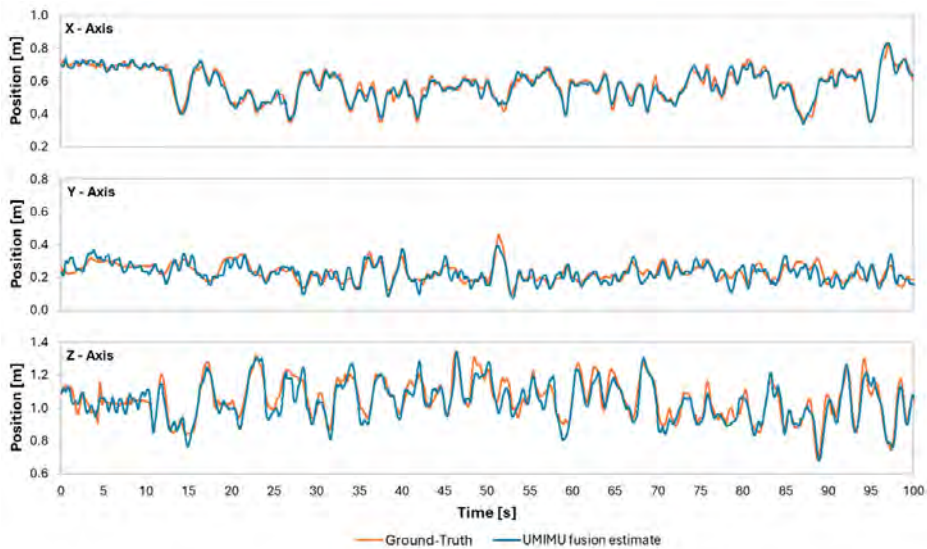


Figure 6.5: Typical example of position estimates from one of the experiment trials, where the position estimates of the UMIMU fusion algorithm (blue) are plotted along with their reference distance (orange) from the Vicon optical system.

The position estimation accuracy of the cyclic movement was the highest, with mean position estimation errors of 5.63 ± 2.70 cm (Table 6.1). Following the cyclic movement, both the random and mixed movements tested had very similar mean position estimation errors of 6.54 ± 3.18 cm and 6.63 ± 3.27 cm, respectively. The position estimation accuracy was highly consistent for all six sensor positions estimated for all experimental conditions (Table 6.1). The mean position estimation errors across each axis were 1.62 ± 1.23 cm, 3.19 ± 2.42 cm, and 3.42 ± 2.63 cm for the X, Y, and Z axes, respectively, for cyclic movement. Similarly, for the random movement, the mean position estimation errors across each axis were: 1.89 ± 1.46 cm, 3.52 ± 2.68 cm, 4.13 ± 3.25 cm, and for the mixed movement patterns: 1.95 ± 1.48 cm, 3.73 ± 2.92 cm, 3.99 ± 3.20 cm, respectively.

Table 6.1: Position estimation errors of every unknown sensor for each of the movement types tested

Sensor	Cyclic Movement		Random Movement		Mixed Movement	
	Position estimation error [cm]					
	Mean	SD	Mean	SD	Mean	SD
N1	5.72	2.68	5.99	2.78	6.88	3.38
N2	5.84	2.84	5.73	2.71	6.76	3.46
N3	5.33	2.48	7.47	3.60	6.67	3.28
N4	5.33	2.64	7.37	3.73	6.96	3.33
N5	5.72	2.76	6.40	2.84	6.41	3.07
N6	5.82	2.71	6.28	2.87	6.07	3.01
Overall	5.63	2.70	6.54	3.18	6.63	3.27

6.3.2 Effect of UWB distance errors on UMIMU fusion algorithm accuracy

The position estimation accuracy and the consistency of these estimates decreased with increasing UWB distance measurement errors (Figure 6.6). The cyclic movement pattern had the lowest estimation error, followed by both the random and mixed movement patterns. The variation in the position estimation errors was minimal with increasing biases. For example, in UWB distance measurement with random error of 5 cm, the mean position estimation errors were 6.25 ± 3.13 cm, 6.27 ± 3.09 cm, 6.53 ± 3.19 cm, and 7.50 ± 3.52 cm for the tested measurement biases of 0 cm, 0.5 cm, 1 cm, and 2 cm, respectively. While for increasing the random error component, there was significant variation in the final position estimation accuracy

of the UMIMU fusion algorithm. In Figure 6.6, the most achievable position estimation error as per the literature, which is around 10 cm is indicated in red dashed lines (---), while the baseline error achieved with the proposed UMIMU fusion algorithm, using the standard UWB error setting is 6.27 cm and is indicated as orange dashed lines (---). The desired position estimation error of 1 cm is indicated as green dashed lines (---) in the figure for better comparison.

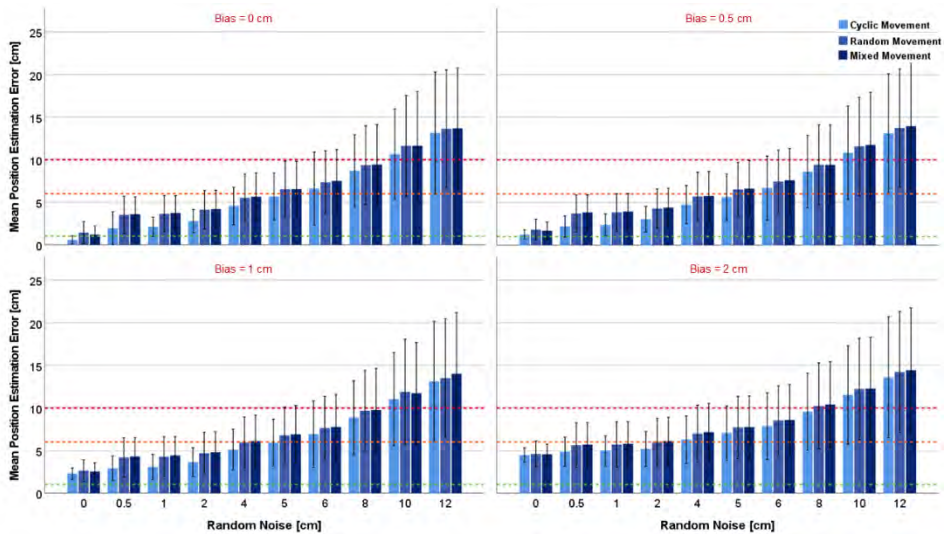


Figure 6.6: Results of error sensitivity analysis with mean position estimation errors for varying bias and random error in the UWB distance measurement at the typical UWB update rate of 4 sps.

6.3.3 Effect of UWB measurement update frequency on UMIMU fusion algorithm accuracy

The position estimation error decreased, and the consistency of the position estimation improved with an increase in the UWB measurement update frequency (Figure 6.7). The variation in position estimation errors across different movement patterns followed a consistent trend as observed in previous results, with the cyclic movement pattern with the lowest error, followed by random movement and mixed movement patterns for all the test cases. Similar to Figure 6.6, the reference lines defining the position estimation errors in literature (---), baseline error (---), and desired error (---) are also included in Figure 6.7, for comparison.

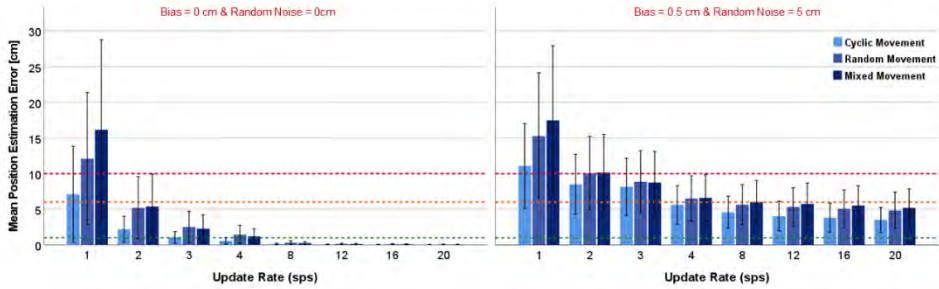


Figure 6.7: Mean position estimation errors for varying update rates of the UWB distance measurement, specifically for the ideal scenario with no errors in measurement (left) and for the standard UWB error setting scenario (right).

For the lowest update rates of UWB (1 sps), the position estimation error was very high, with mean errors of 11.78 ± 10.52 cm and 14.60 ± 9.03 cm for the ideal scenario and standard UWB setting scenario, respectively. For the standard update rate of 4 sps, the mean position estimation error was 1.07 ± 1.05 cm and 6.24 ± 3.08 cm for the ideal scenario and standard UWB setting scenario, respectively. In the ideal scenario, the mean position estimation errors and SD were less than 0.5 cm for update rates of 8 sps and higher, while for the standard UWB setting scenario, the errors were around 5 cm with an SD of around 2.5 cm for update rates above 4 sps (Figure 6.7).

6.4 Discussion

This study proposed and evaluated the UMIMU fusion algorithm, a data fusion method to estimate 3D position based on a loosely coupled EKF for combining the UWB and MIMU data, specifically for short distance ranges relevant for 3D AHM. The developed UMIMU fusion algorithm is then systematically evaluated in short distance ranges of 0.2 to 2 m with movement velocities and patterns relevant to the typical 3D AHM setting in LOS scenarios. Where MIMU-based position estimation typically shows large cumulating errors caused by integration drift, the position estimates produced by the UMIMU fusion algorithm showed no drift anymore. In all of the conditions tested, the proposed algorithm also consistently showed less error in position estimates than those derived from the UWB swarm directly.

Under realistic UWB conditions (distance error 0.5 ± 5 cm), the UMIMU fusion algorithm consistently estimated drift-free position with a mean error of around 6 cm, which is similar to the previously reported highest accuracy in applications of

pedestrian tracking [81,83]. However, they were both assessed only during slow movements and for short trials (24 s and 10 s, respectively), and specifically, the study of [81] was restricted to two-dimensional positioning. Overall, the achieved position estimation accuracy was better than all other studies, which reported position estimation errors greater than 10 cm [119]. The inclusion of the drift compensation mechanism in the proposed algorithm effectively suppresses drift accumulation between updates, which is reflected in the lower position estimation errors relative to the implementation without drift compensation. Additionally, examining the estimation error per movement axis, the errors were always lower and around 2 cm, 3 cm, and 4 cm for the x, y, and z axes, respectively. Also, the UMIMU fusion algorithm effectively reduced the measurement variability as evident from a lower SD in the position estimation (Table 6.1), leading to consistent position estimates with consistently lower random error.

The position estimation accuracy for the cyclic movement pattern was always higher than the random and mixed movement patterns. Since cyclic movement follows a repetitive, structured pattern, with smoother velocity and acceleration transitions compared to the other movements tested, it allows the EKF to adapt better to the motion dynamics over time. However, the difference in the performance was not very high, with the position estimation errors of cyclic movement always lower by a few millimeters (<1 cm), than the other two movement patterns.

The data fusion demonstrated consistent behavior, evident from the estimated positions for all six moving sensors, which showed a similar error across the different trials (Table 6.1). The error values remained close to each other with very small SD values of around 3 cm, indicating that the proposed UMIMU fusion algorithm provided a consistent performance regardless of the movement patterns tested in this study. The consistency was also well demonstrated with the long measurements of around 300 seconds, which is very critical for 3D AHM applications, where assessments often involve continuous and prolonged monitoring of movement patterns during full clinical tasks, such as gait cycles, functional movements, or rehabilitation exercises. In such scenarios, even small drifts or instabilities over time can lead to incorrect interpretation of movement quality or progress, reducing clinical reliability [29].

The position estimation accuracy in general was affected by the increasing UWB measurement noise (both bias and random errors). The bias errors in the UWB distance measurements had a limited impact on the position estimation when they remained at or below 1 cm. Specifically, the position estimation errors were nearly identical for the no bias and bias values of 0.5 cm, with the errors for the bias of 1 cm being only a few millimeters higher than the errors of the lower bias ranges. However, for bias errors exceeding 1 cm, the position estimation error increased even when the random error component was absent, which indicated that a higher bias introduces a systematic shift in position estimates. Though higher bias errors are a threat, it has been shown that these bias errors can be corrected already below 1 cm through proper calibrations [156].

The UMIMU fusion algorithm produced position estimates that consistently showed lower random errors than the position estimate updates derived from the UWB distances. This suggests that while the EKF filtering cannot fully eliminate large random errors, it provides a smoothing effect that enhances the consistency of the position estimates. Unlike the bias error, the random error in the UWB distance estimate had a strong (significant) effect on the accuracy of the UMIMU fusion algorithm's position estimates. For larger random error components, the position estimation errors were substantially larger. Random error components of 5 cm and below always resulted in position estimates with accuracies better than the already achieved accuracies in literature [119], as indicated by the orange dashed line in Figure 6.6.

The update rate of the UWB measurements had a significant impact, specifically at lower update rates. From a relatively large error at an update rate of 1 sps, the error decreases significantly with increasing update rate. Increasing the update rate to rates higher than 8 sps indicated that only a marginal gain can be achieved. This suggests that using double the update rate than the currently achievable update rate of 4 sps, with the UMIMU system with a swarm of 8 fully connected nodes (experiments in this paper), could take almost 2 cm of the systematic error. Besides, since the drift compensation mechanism in the algorithm effectively mitigates drift between updates, the necessity of further increasing the update rate becomes less critical.

The proposed UMIMU fusion algorithm demonstrates drift-free position estimation over longer measurement times with systematic and random errors lower than all previously reported methods, starting from UWB distance estimates with currently achievable accuracy [187]. This absence of drift is essential in rehabilitation settings, where precise motion tracking is needed to assess patient progress, guide therapy, and ensure accurate biomechanical analysis [29]. The errors in the position estimates delivered by the UMIMU fusion method appeared larger than what can be achieved with marker-based optical motion capture systems but they are similar to when using state of the art MIMU based systems [188]. The proposed method might be useful for specific scientific experiments, especially in semi-static situations and cyclical movements. However, for routine clinical application in 3D AHM, the position error still has to be brought down to lower values.

The results of the sensitivity study showed that bringing down the UWB position estimate random error will improve the UMIMU data fusion position estimates. Especially, reducing the random errors in the UWB distance estimates would have a large positive effect. Several options for improvement are currently under study, such as intelligently dealing with observable errors in distance estimation. Additionally, our results suggest that increasing the update rate to at least 8 sps will also bring the position errors down. Several options to achieve this, related to optimizing redundancy within the distance assessments, are under study.

In this paper, the UMIMU fusion algorithm performance was not evaluated using actual UWB ranging measurements. Instead, Vicon-derived inter-sensor distances were used with added controlled bias and random errors to simulate UWB measurements. The use of Vicon-derived distances with added synthetic errors for simulating the UWB measurement in this study, while beneficial for extensive systematic and controlled testing, may not fully replicate real-world UWB measurement errors, which can include errors caused by environmental factors such as multipath effects [171]. Future work should validate these findings using actual UWB measurements in typical 3D AHM activities with human subjects, and is being pursued as the next step of this study. Expanding the range of tested movements could provide a more comprehensive evaluation of the proposed UMIMU fusion algorithm's performance.

6.5 Conclusion

This study developed the UMIMU fusion algorithm, a method for the data fusion of UWB and MIMU sensors based on an EKF, and systematically evaluated the performance of the algorithm in a sensitivity study with synthetic data, focusing mainly on the effects of the UWB update measurement errors and update rates in situations of typical 3D AHM. Results demonstrated that the proposed UMIMU fusion algorithm provided drift-free position estimates with a mean error of around 6 cm. For UWB distance bias errors ≤ 1 cm and random errors around 5 cm (an estimation quality as achieved experimentally before, after applying a custom calibration procedure), the UMIMU fusion algorithm provided position estimates with accuracies better than any method reported before. For higher biases (>1 cm) and random error (>5 cm), the accuracy degraded significantly. The results also showed that increasing the update rate from 4 sps to 8 sps would decrease estimation errors significantly. This study provides significant insights into currently achievable accuracy with an integrated UWB/MIMU sensor system. Also, it provided detailed insights into error propagation, guiding research in further improvements towards a final goal of application in 3D AHM and clinical rehabilitation practices.

Chapter 7

General Discussion



This comprehensive PhD research investigated the feasibility and potential of an integrated Ultrawideband (UWB) and Magnetic Inertial Measurement Units (MIMUs) sensor system (referred to as the UMIMU system) for ambulatory 3D analysis of human movement (3D AHM). The core aim was to improve the accuracy and consistency of position estimation for clinical 3D AHM applications. A wearable prototype system integrating UWB and MIMU was developed, and a series of five interrelated studies was conducted to address key technical and methodological challenges:

1. A detailed literature review that identifies the gap between existing integrated UWB/MIMU research and the specific needs of clinical 3D AHM (Chapter 2).
2. The development of a custom integrated UWB/MIMU hardware platform and experimental characterization of UWB performance under conditions specific to 3D AHM, quantifying LOS and NLOS-related errors (Chapter 3).
3. A robust, generalizable swarm-based calibration method for mitigating the systematic distance bias errors in the UWB distance estimates (Chapter 4).
4. A swarm optimization-based UWB position estimation algorithm that exploits the inter-node distance estimates of a UWB swarm, validated using synthetic UWB data (Chapter 5).
5. A tailored UMIMU fusion algorithm based on the Extended Kalman Filter (EKF) that combines the MIMU data with synthetic UWB ranging data to achieve accurate and drift-free position estimation (Chapter 6).

Collectively, this thesis demonstrates a coherent progression from identifying fundamental limitations in current systems to developing and validating new calibration and estimation techniques specifically for 3D AHM applications. By addressing these challenges systematically, this research lays a strong foundation for future research and development towards application in clinical 3D AHM. This final chapter discusses the main findings, their implications for clinical human movement analysis and general technology, identifies the research limitations, proposes future research directions, and outlines a potential pathway toward clinical translation and real-world deployment of the proposed UMIMU system.

7.1 Main findings

7.1.1 Feasibility of the integrated UWB/MIMU sensor system for clinical 3D AHM

The primary objective of this PhD research was to evaluate the feasibility of the fully integrated UWB/MIMU sensor system for clinical 3D AHM, with a specific focus on the position estimation accuracy and consistency. The feasibility assessment was first initiated with a comprehensive systematic literature review (Chapter 2), which revealed that the integrated UWB/MIMU sensor system has been extensively studied and applied for localization and pedestrian tracking applications, while its application to clinical 3D AHM remains largely unexplored. These integrated sensor systems were typically developed for the localization and tracking applications in large-scale indoor environments such as warehouses, car parks, or open corridors with operational ranges extending up to 10 meters or more [105,106,108]. These conditions differ largely from those conditions/environments of the 3D AHM, where short ranges (20 cm up to 1 m to 2 m), and on-body positioning are targeted. In addition, the algorithms and methods developed in these earlier studies for position estimation were highly optimized and tailored for the application scenarios of tracking and localization. Several methodological gaps were identified in the literature that limit the clinical relevance of existing integrated UWB/MIMU sensor systems. Specifically, prior research on these integrated sensor systems was not well-characterized under conditions relevant to clinical 3D AHM. Additionally, only a few studies clearly report the systematic versus random error components in their systems, which limits our understanding of the systems' behavior under varying operational conditions and restricts their applicability for high-accuracy requiring applications in rehabilitation.

Based on the initial feasibility analysis and gap identification, a fully integrated UWB/MIMU sensor system, specifically optimized for on-body deployment and short-range use, was developed and validated in this research (Chapters 3 to 6). In Chapter 6, the technical feasibility of the system for clinical 3D AHM was demonstrated through a performance evaluation of the proposed UMIMU fusion algorithm under realistic UWB ranging error profiles. The developed integrated sensor system achieved a mean 3D position estimation error of 6.27 ± 3.10 cm (with

each coordinate axis error around 4 cm or lower) under realistic input UWB distance error levels across three distinct movement patterns observed in typical human movement (cyclic, random, mixed). These performance results are comparable to the only two highest accuracies reported for indoor UWB/MIMU fusion in localization and tracking applications [81,83]. However, one of these reports was limited to two-dimensional position estimation and relied on simplified biomechanical assumptions [81], while the other was validated only in slow-paced activity over very short recordings of around 24 seconds [83]. In general, the achieved accuracy with the proposed method in this research is higher than the average accuracy reported for pedestrian localization and tracking applications [121,122,155], which is position estimation errors around 10 cm or higher. In addition to the demonstrated accuracy, this thesis demonstrates the capability to produce consistent and drift-free position estimates. The consistently low and constant standard deviation (~ 3 cm) in position estimation across various movement types illustrates its temporal stability, a critical requirement for longitudinal assessments in clinical rehabilitation. While the proposed integrated UWB/MIMU sensor system does not yet meet the sub-centimeter precision of optical motion capture systems, its performance in position estimation exceeds most of the existing wearable movement analysis systems [178].

The proposed integrated UWB/MIMU sensor system, despite not matching the gold standard, provides a wireless, wearable, and more importantly, a drift-free solution that offers sufficient resolution for many clinical applications such as those involving segmental displacement and balance assessment [178,189,190]. For whole-body movements and balance tasks, a consistent and drift-free UWB/MIMU system offers adequate resolution to assess gross movement patterns and postural sway, bridging the gap between lab-grade analysis and real-world clinical needs. Unlike the MIMU sensors-only system, which suffers from rapid error accumulation in the absence of an external reference frame due to drift during integration [16,48], this integrated UWB/MIMU sensor system anchors inertial estimates to a global coordinate system through absolute UWB distance measurement updates. This prevents unbounded drift in position estimation and ensures consistency across time and tasks. This long-term stability (drift-free estimation) is important in extended monitoring scenarios where absolute spatial accuracy is required, such as

unsupervised rehabilitation, and home-based fall-risk assessment involving Center of Mass (CoM) displacement and foot clearance [189,191]. Besides, the comprehensive error sensitivity analysis presented in Chapters 5 and 6 indicates that the sensor system performance could be further improved by addressing the residual errors in the UWB ranging component. Specifically, implementing advanced non-line-of-sight (NLOS) detection and adaptive error compensation techniques may enhance the overall accuracy and robustness of the fusion algorithm.

In summary, the integrated UWB/MIMU sensor system developed in this thesis demonstrates strong feasibility for clinical 3D AHM applications. While further improvements are necessary to meet the sub-centimeter accuracy standards of traditional lab-based optical motion capture systems, the combination of portability, long-term stability (drift-free estimation), and consistent accuracy positions this sensor system as a viable and scalable solution for future real-world clinical deployment.

7.1.2 UWB error behaviour and accuracy enhancement in 3D AHM applications

A key finding and major advancement of this thesis is the identification and mitigation of performance limitations in UWB-based distance and position estimation when applied to short-range, on-body sensor configurations, typical to clinical 3D AHM (Chapters 3 to 5). While the MIMU sensors in the integrated UWB/MIMU sensor system were well studied and have been extensively validated for 3D AHM applications [16,187,192], the UWB sensors were not studied and characterized for the 3D AHM application environments [120]. Previous UWB positioning research has mainly focused on large-scale environments targeting pedestrian tracking applications with ranges of up to 10 meters or more [106,108], which differ significantly from the short-range (0.2 m to 2 m), on-body setups of 3D AHM, where body-induced NLOS conditions are more frequent. Though the human body is known to influence UWB distance estimation accuracy [120], there were only a few prior works [93,117,123] that provided partial insights into on-body usage of UWB, with limited validation under 3D AHM conditions.

In Chapter 3, controlled experiments revealed that standard factory-recommended antenna delay calibrations left residual systematic bias errors in UWB measurements up to 6 cm. This was also found to be the case in other UWB calibration research, where residual errors of 3 to 5 cm were reported in the distance measurement after applying their calibration techniques [143-145]. This study also revealed consistent and repeatable error patterns in both static and dynamic NLOS scenarios, highlighting the need for customized calibration and adaptive filtering techniques tailored for short-range, on-body applications. Chapter 4 addresses the identified residual systematic errors present in the UWB distance ranges through a novel generalizable calibration procedure that applies a nonlinear optimization to assign a unique bias value to each UWB sensor node being calibrated. This method accounts for both sensor-specific and network-level distance estimation biases, and the experimental validation demonstrated that this calibration procedure reduced systematic errors to sub-centimeter levels (≤ 0.5 cm), outperforming most reported UWB calibration strategies [144-146].

To transition from improved UWB distance estimates to position estimates suitable for integration with MIMU data, Chapter 5 applied an optimization-based position estimation algorithm for UWB-only position estimation. Unlike the conventional methods such as trilateration [158] or least square approaches [159], which typically rely on distances between a mobile tag and fixed anchors, this approach leveraged a swarm topology, where all inter-node distances within the wearable sensor network were used simultaneously. This redundancy enabled improved robustness and accuracy, specifically under noisy conditions typical of 3D AHM. The swarm-based position estimation algorithm consistently outperformed trilateration, achieving over 25% better accuracy in synthetic test scenarios with realistic noise levels. Beyond performance gains, the method is highly generalizable and does not depend on specific UWB hardware, and can be applied to other short-range ranging systems with similar architectural layouts. These advancements in the UWB distance and position estimation form a foundational step toward enabling effective fusion with MIMU data for clinical 3D AHM applications.

7.2 Clinical implications

Accurate and consistent (body segment) position estimation plays a key role in the clinical analysis of human movement [16,192]. Traditional gait analysis widely focuses on angular/orientation measurements such as joint angles and segment orientations, however, there are other important functional assessments in rehabilitation that depend on knowing how body segments move through space [192]. For example, spatial gait parameters like step length are derived from the 3D positions of the feet [193], and balance metrics rely on the trajectory of the body's center of mass (CoM) with respect to the base of support [194]. Position estimates in general provide the spatial relationship between limbs, joints, and the floor, enabling the rehabilitation clinicians to evaluate gait symmetry, balance, stability, and functional mobility with accurate objective measures.

The central challenge in current clinical rehabilitation is the lack of portable, affordable, objective tools for analyzing human movement with sufficient accuracy to guide diagnosis, treatment, and monitoring. In current practice, movement assessments are often based on visual observations. Although instrumented gait analysis based on optical marker-based systems and force plates is capable of providing highly accurate quantitative movement assessment, particularly for position estimation as focused in this study, they still remain primarily in use as research tools [12]. Their limited clinical adoption is primarily due to high costs, the need for dedicated laboratory space, lengthy manual post-processing of data, and the requirement for specialized personnel to operate the systems.

Wearable MIMU-based systems, on the other hand, offer a low-cost, flexible alternative, but they have other limitations. They can accurately capture angular kinematics [48], although observability limitations of the Earth's magnetic field (e.g., caused by vicinity of construction metal in floors or other building components) limit their application to short measurements, as the heading information derived from observation of the Earth's magnetic field causes a slow drift around the direction of the gravity vector [41]. Also, they struggle with large accumulating errors in position estimation due to the required double integration of free acceleration data [48,195]. While relative segment orientations are sufficient to derive many clinically relevant parameters, such as joint angles, the limited accuracy of these

sensors in estimating relative position constraints their ability to measure the spatial parameters. These spatial parameters, such as segmental position information, are essential for clinically relevant balance metrics that relate the position of the body's CoM to the position of the base of support (BoS) [189,196], and also for certain kinetics calculations such as load distribution across joints [197]. Therefore, this research addresses this clinical gap in position estimation accuracy by presenting a fully integrated UWB/MIMU wearable sensor system tailored to short-range, on-body use 3D AHM. Through custom hardware, a novel calibration approach, and data fusion algorithms, the system provides high-quality position estimates validated against VICON-derived ground truth. Importantly, the system is fully wearable, consistent, drift-free, and cost-effective, thereby bringing objective, quantitative movement analysis closer to routine clinical application.

7.2.1 Clinical use case of accurate and consistent position estimation

Modern MIMU fusion algorithms can track segment orientation with high accuracy [48], but obtaining segment and joint position from MIMUs remains challenging because MIMU measurements require double integration of free acceleration, which introduces an accumulating error, i.e., integration error [195]. In this thesis, this issue is addressed through an integration of the additional sensor modality UWB along with a minimal three fixed anchors. This framework supplies drift-free absolute position estimates in a sensor swarm, thereby providing redundancy in 3D positional data and enabling sensor fusion of UWB and MIMU data for accurate, drift-free, and consistent position estimation. The integrated UMIMU sensor platform introduced and developed in this research shows a more accurate and consistent position estimation than reported previously on integrated UWB/MIMU. Specifically, combining the improved position estimation with the already available accurate orientation estimation methods, made possible through this integrated sensor system, could potentially improve the overall kinematic measurement accuracy and consistency for clinical human movement analysis and help in the successful translation of this system for clinical rehabilitation.

Fall risk assessment in older adults and individuals with balance impairments is among the clinical applications most critically depending on accurate position

estimation. Functional balance and normal gait assessment rely on spatial parameters of gait such as the centre of mass (CoM) position relative to base of support (BoS), step width, foot placement variability, and vertical foot clearance [198-200]. These metrics are essential for detecting gait instability, predicting fall likelihood, and guiding interventions like strength training [199]. For example, reduced foot clearance or lateral pelvic sway during gait can increase the risk of tripping. Though angular kinematics provide valuable information regarding falls, the spatial parameters related to body segment positions provide more information regarding fall prevention, along with a direct approach to fall detection [201,202], and in addition, could help identify compensatory strategies employed when combined with the angular kinematics information. The integrated UMIMU sensor system developed in this research will allow tracking of (relative) 3D position and displacement of feet and pelvis, which are crucial for the assessment of fall risks. Since the current accuracy is still not as good as the current optical marker-based systems, this can act as an additional method to fall detection based on angular kinematics, mainly providing information on the fall mechanics and compensatory strategies used. The removal of drift in relative position estimation and its wearable and wireless design make it deployable in both clinical and home settings without complex infrastructure.

The clinical use of accurate position estimate further extends to various medical conditions that affect movement patterns, such as stroke [203,204], cerebral palsy [205], and Parkinson's [206], as well as post-operative and post-injury rehabilitation [8], where evaluation of recovery depends on a detailed understanding of movement quality. Especially, following a stroke (medical condition) or an ACL reconstruction surgery (post-operative), the rehabilitation clinicians could assess movement patterns and reaching patterns to determine the functional readiness and to coach the patient's recovery process through progressive loading [8,203]. These parameters are ideal to be assessed in order to decide on providing treatment adjustments in the case of medical conditions and to make return-to-activity decisions in the case of post-operative situations (e.g., ACL reconstruction surgery). While angular movement can be inferred accurately from MIMUs, the actual limb displacement relative to other body segments or to the task environment can provide a more functional and reasonable measure. Similar to the overall movement patterns, the

reach patterns are crucial for upper limb rehabilitation and tracking motor recovery in patients after stroke [203,207]. The developed integrated UWB/MIMU system, with its current capability to estimate inter-segment distances and 3D displacement with reasonably better accuracy and good consistency, could still enable accurate reconstruction of reach patterns and capabilities. This would support more detailed progress tracking and help in rehabilitation therapy across a broad spectrum of patients with medical conditions and post-surgical populations.

The ability to assess positions and displacement in mobility tasks such as sit-to-stand, bed transfer, or turning relies on tracking the position of CoM, BoS, body segments, and joints [208,209]. These parameters are important indicators of independence in daily activities and are linked to fall risk and functional capacity in aging or people with medical conditions. The integrated sensor system would enable clinicians to measure vertical displacement of the pelvis, trunk shift, and inter-limb coordination with greater accuracy and consistency. In particular, for patients with observed compensatory patterns, like forward lean, accurate and consistent position tracking would enable not just detection but quantification of compensation, thus enhancing both diagnostic precision and treatment plans. Overall, the system developed in this research does improve the position estimation over the already available MIMU-only based systems and would help reconstruct the spatial dimensions of human movement. From assessing fall risk and balance control to quantifying recovery post-surgery or post-injury, to capturing translational mobility tasks, accurate and consistent segmental position estimates are essential. This thesis delivers a wearable system and methods that could provide a consistent drift-free solution with reasonable accuracy, which can eventually help build the complete system that meets the above-mentioned needs, thereby enabling and bringing the technology closer to a future where real-world human movement analysis becomes a standard tool in clinical rehabilitation.

7.2.2 Continuous monitoring and tracking in daily life settings

Continuous gait and 3D AHM represent a powerful tool across a variety of clinical and real-world applications. Continuous measurement of how people move and walk in their daily lives provides significant insights that one-time tests cannot identify [201]. Besides, traditional gait measurements are performed in clinical or

laboratory settings, and they lack the ability to capture human movement parameters in real-world conditions. For example, studies on post-stroke rehabilitation have reported significant differences in the gait assessed in the laboratory compared to their walking in daily life [210,211]. In the rehabilitation of various medical conditions, such as stroke or after orthopaedic surgery, extended long-term human movement monitoring helps in tracking recovery trajectories, validating the effectiveness of therapy, and eventually improving patient outcomes [201]. In aging populations, long-term monitoring of gait enables fall-risk management by identifying relevant gait metrics and applying preventive interventions [212]. For chronic disease management, 3D AHM is an essential tool for understanding the patient's overall health status and for guiding personalized care that aims to maintain mobility and quality of life [202,213].

The availability of wearable human movement analysis tools based on MIMUs allows long-term gait analysis to be feasible in daily life settings. However, there is still a gap in using this technology widely for these purposes. For long-term gait analysis, both the spatial kinematics (position and displacement estimates) and angular kinematics are equally essential [201,202], because they directly relate to functional mobility and are feasible to monitor continuously outside the lab. As already discussed in the previous section (Section 7.2.1), spatial kinematics, such as the body segment and joint position, play a key role in human movement analysis. While the MIMU-based systems are accurate for angular kinematics, the major barrier to using wearable MIMU-based systems for extended monitoring is the accumulation of position errors over time [192], especially due to the integration errors, as already emphasized in this research. This limitation severely reduces their value in applications of continuous monitoring and tracking, especially as balance issues and fall risk are important topics in daily life activities.

The sensor system developed in this research addresses this gap through the integration of drift-free UWB distance measurements with data from MIMUs, anchoring position estimates to real-time UWB measurements, which do not accumulate errors over time. Though the current achieved accuracy does not yet reach the sub-centimeter level required to match the optical marker systems, they provide an accuracy better than most of the previously reported position estimation accuracy, as well as drift-free and consistent position estimates over time, as shown

through experimental validation with longer measurements in Chapter 6. In applications where continuous monitoring or long-duration assessments are essential, such as rehabilitation or daily-life mobility tracking, consistency and reproducibility of the estimates are often more critical than higher accuracy [214,215]. Therefore, the developed UMIMU system offers a wearable sensor system that can provide both spatial kinematics and angular kinematics with reasonable accuracy and good consistency over time. By using a comprehensive approach that values both spatial and angular kinematics data, clinicians and researchers can obtain a complete view of the patient's mobility over time. The ultimate benefit of the improved wearable system with accurate spatial and angular kinematics is in empowering individuals and clinicians with detailed knowledge of movement in everyday life, potentially leading to more responsive care and better outcomes in rehabilitation, fall prevention, and overall health maintenance.

7.2.3 Practical integration into clinical workflows

Wearable sensor systems intended for clinical rehabilitation practice must demonstrate accuracy as well as strong measurement consistency to ensure trust in their readings over time [216]. The current MIMU-based system is already accurate enough for the angular kinematics, still lacks sufficient accuracy with highly unstable spatial kinematics, as already emphasized in this research. The integrated UWB/MIMU sensor system developed and validated in this research significantly improved both the accuracy and consistency of the spatial kinematics, with an achieved mean position estimation error of around 6 cm with an SD of 3 cm. Though the achieved accuracy does not meet the sub-centimeter levels of optical motion capture systems, they have achieved a much higher stability and brought the accuracy closer to the required level (1 cm) in position estimation. A consistent drift-free measurement, even with a small constant bias, enables clinicians to reliably monitor patient changes, as any improvement or deterioration in their movement would be evident above the device's noise threshold [216]. In long-term rehabilitation monitoring (stroke, orthopedic recovery, or aging-related mobility decline), such consistency is what enables wearables to capture subtle changes in performance. For example, wearable sensors have been shown capable of detecting slight mobility changes that signal disease progression in Parkinson's and Huntington's disease [217], which would be missed by an unstable measurement

system. Importantly, this consistency means that clinicians could rely on the system not only for moment-in-time diagnostics but also for tracking subtle progression or recovery over time. While the next steps should focus on further improving the accuracy, the achieved accuracy with high consistency and reproducibility empowers wearable sensor systems to serve as sensitive trackers of mobility improvements or deteriorations over time, fulfilling a key requirement for their clinical translation [214,217].

For any wearable technology to succeed in clinical rehabilitation practice, it must not only demonstrate technical accuracy and consistency but also align with the clinical workflow, such as constraints in time, training, space, and cost. The developed UWB/MIMU system in this research is tailored for use in real-world rehabilitation environments, including outpatient clinics, physiotherapy centers, and patient homes. The system's modular design, small sensor nodes, wireless architecture, and high level of automation make it flexible, as rehabilitation clinicians can configure the sensor placements to suit the specific assessment needs. Compared to optical motion capture systems, which take extensive setup time (typically 30 to 60 minutes per session, only for setting up) [218], this system only requires a minimal setup time of less than 10 minutes, enabling more frequent and larger volume assessments. Besides, the absence of fixed infrastructure provides the possibility of scaling this system beyond the clinical setting. The cost of this sensor system is expected to be much lower than the current optical marker-based instrumented gait analysis systems, as all the components of these sensors are less expensive and could further be reduced in cost if produced in large quantities.

From a healthcare cost perspective, the implementation of cost-effective, portable systems could improve care efficiency and reduce the associated healthcare costs. Objective assessments reduce unnecessary treatments, enable earlier discharge, as well as support better and more targeted interventions [14,15]. For example, long-term monitoring of movement quality at home can detect improvement or deterioration before it becomes visible in clinical visits, allowing therapists to modify protocols proactively. These insights could eventually reduce hospital readmissions, therapy costs, and long-term disability [15], which is a priority for aging populations and healthcare systems currently under pressure. Overall, the integrated UWB/MIMU system developed here is not only technically innovative but clinically

practical. The developed sensor system's consistent estimates, minimal setup time, real-time capability, and potential for remote deployment position it as a promising candidate for integration into modern, technology-supported rehabilitation workflows.

7.3 General Implications beyond 3D AHM

While the core focus of this research was the clinical 3D AHM, the technological advancements presented in this research have broader implications for domains that rely on short-range position estimation and swarm topology-based sensor networks. These methods address fundamental challenges (e.g., optimal physical integration of UWB and MIMU sensor nodes with optimized time-critical data recording, mitigation of distance estimation bias and drift, and developing optimal multi-sensor data fusion) that also arise in ergonomics, injury prevention, robotics, autonomous vehicles, and tracking applications.

Typical examples specifically in healthcare and ergonomics are active exoskeletons and orthotic devices. Similarly, ergonomic assessment systems in occupational health could benefit, where precise segmental position estimates are needed to quantify awkward postures, repetitive strain risks, or load distribution during manual handling tasks, especially since MIMU-only systems often fail due to drift in these environments [219]. In robotics applications, UMIMU sensors could provide alternative/additional data for improved endpoint position estimation for more lightweight construction of robot arms, where diminished rigidity in the robot arms decreases endpoint position estimation precision using a traditional robot arm joint odometer. Another example is in accurate relative positioning is critical for multi-robot or drone swarms in GNSS-denied environments [220], and integrated UWB/MIMU sensors have been identified as a suitable basis for such swarm localization due to their high precision. Integrated UWB/MIMU-based positioning has even been demonstrated by swarms of inventory drones in warehouses, achieving decimeter-level accuracy in real-world industrial settings [220]. This underscores that the technological advancements from the present work are broadly applicable beyond the domain of 3D AHM.

The novel insights into the UWB distance estimation error behavior at short ranges and on the human body (Chapter 3) could enable the design of adaptive positioning algorithms capable of dynamically adjusting the model parameters based on the inter-node distance ranges. Applications such as drone swarms, autonomous ground vehicles, or warehouse robots operating in dense formations could switch between short-range and long-range error models in real time to enhance robustness and accuracy under varying spatial configurations [221,222]. The distance calibration method introduced in this research (Chapter 4) is generalizable and adaptive, enabling error values to be assigned to each individual UWB sensor node. This characteristic allows the calibrated system to compensate for pairwise sensor errors during dynamic operation, which is applicable not only in clinical wearables but also in industrial and robotics settings that utilize UWB positioning systems [155,223,224]. In addition, this calibration method can be extended to any other ranging modalities similar to UWB that measure the distance between two points, as the calibration is based only on the distance measures of the UWB sensor.

The swarm-based position estimation method (Chapter 5) further extends its relevance beyond the intended clinical 3D AHM application, offering a robust position estimation algorithm that can be used for UWB sensors with the swarm topology framework, as observed in applications of multi-robot or drone coordination [222,224]. Similar to the calibration method, this swarm position estimation method is not restricted to UWB measurements, instead can be applied to any similar technology that measures multiple distances between an interconnected network of sensors.

Though the position estimation algorithms based on the EKF sensor fusion approach proposed in this research (Chapter 6) were specifically tuned for clinical 3D AHM application, their structural framework may be transferable to other short-range, body-worn, or swarm-based systems where drift suppression and consistent tracking are required. Similar Kalman filter-based UWB/IMU fusion methods have been shown to automatically correct inertial drift and reject NLOS measurement spikes, greatly improving long-term stability of position estimation over single-sensor solutions [225]. This implies that any platform combining UWB and MIMU sensors that ranges from an individual's wearable navigation device to a team of

robots or UAVs localizing cooperatively could employ the same fusion framework to constrain drift and maintain accuracy.

Beyond robotic and autonomous navigation domains, these contributions resonate in fields like sports analytics and pedestrian navigation. Integrated UWB/MIMU-based tracking systems are rapidly gaining popularity for sports performance analysis, where athletes wear them to capture high-resolution motion data. This integrated system is capable of real-time player localization, offering a cost-effective alternative to camera-based tracking or optical motion capture [226]. In parallel, injury prevention programs in sports and occupational contexts can leverage precise positional monitoring to detect high-risk movement patterns, such as knee valgus during landing [227]. Wearable UWB/MIMU systems could provide reliable feedback in field-based or workplace settings, reducing the dependency on lab-only biomechanical analyses. Integrated UWB/MIMU wearable systems have already proven effective for pedestrian tracking, using sensor fusion to exploit complementary strengths and improve accuracy in position tracking [105,155]. By applying the EKF-based methods from this research, an indoor pedestrian navigation device can continuously correct inertial drift with UWB ranging updates, enabling reliable position estimates in environments where GPS is unreliable. These broader implications emphasize the versatile nature of the foundational technologies developed in this research, highlighting their potential utility in a wide range of position estimation applications beyond the clinical domain.

7.4 Limitations

While this research provides several technical advancements in wearable position estimation for 3D AHM, there are some limitations that should be acknowledged to guide interpretation and inform future directions. A key limitation lies in the validation methodology of the final integrated sensor fusion algorithm (Chapter 6), which relied on synthetic UWB data generated from an optical marker-based motion capture system (VICON). Although the synthetic data was carefully modeled to include realistic bias and noise levels based on empirical UWB characterization, it does not capture the full complexity of live UWB measurements during actual human motion. Especially, these synthetic data may not accurately constitute all possible movement scenarios, such as those of certain patient groups. As such, the

proposed UMIMU fusion algorithm's performance still needs to be validated with real on-body UWB and MIMU data in real-time conditions. This step is essential to confirm its accuracy and consistency under conditions representative of a clinical use case scenario.

Chapter 3 of this thesis provides a detailed characterization of UWB behavior under body-induced NLOS conditions, showing that distance estimates are not only noisier with a higher random error component but also exhibit consistent positive bias when body segments obstruct the LOS. However, these findings have not yet been fully incorporated into the EKF framework of the proposed UMIMU fusion algorithm validated in Chapter 6. Specifically, the current validation of the UMIMU fusion algorithm assumes that the UWB measurement biases are less than or equal to 2cm (based on the calibration results in Chapter 4), which is not the case during NLOS. As a result, the performance of the integrated sensor system may degrade in uncontrolled settings, such as in rehabilitation clinics or home environments where partial occlusions could occur. To address this limitation, the fusion algorithm should be extended with adaptive filtering or error state adjustment strategies that detect and compensate for NLOS to improve the performance in uncontrolled environments.

Another limitation concerns the assumption of full or near-complete swarm connectivity in the position estimation algorithm presented in Chapter 5. In real-world 3D AHM scenarios, body occlusions and NLOS conditions can disrupt certain UWB ranging pairs, effectively reducing the mesh network to a sparse connectivity matrix. This would lower the redundancy of inter-node distances that the swarm-based algorithm relies on, and may consequently degrade the accuracy or consistency of position estimates. While the algorithm is mathematically robust to partial missing pairs, systematic evaluation of its performance under varying levels of connectivity loss was not conducted in this thesis. Future work should therefore test and adapt the algorithm to operate reliably under sparse or dynamically changing connectivity conditions, possibly through adaptive weighting strategies informed by error models of NLOS behavior.

The swarm-based position estimation from UWB distance estimates alone (Chapter 5) relies on a non-linear optimization method that scales with the number of ranging

pairs used in the sensor system, thereby making it more computationally demanding than the traditional trilateration-based method. This method is one of the key components of the sensor fusion-based position estimation in Chapter 6, which can also increase the overall computation time of the proposed UMIMU fusion algorithm. This would currently limit the real-time tracking with a delay of a few seconds. However, in rehabilitation practices, the real-time tracking is more flexible, for instance, in clinical gait retraining or therapist-guided functional task assessment, the feedback provided within a few minutes after each measurement is considered sufficiently real-time to support decision making [228]. Thus, the integrated UWB/MIMU sensor system developed in this thesis may already be clinically useful for session-based monitoring, but it is not sufficient for a continuous gait retraining-based application that requires live feedback. To expand the use case also to live feedback applications, further improvements in computational efficiency are needed. This could include exploring algorithmic refinements, such as reducing the number of inter-node distance combinations used in optimization to eliminate less reliable measurements, or hardware improvements, such as utilizing better CPUs.

7.5 Future research

The ultimate intention of this research is the transition of the integrated UWB/MIMU sensor system developed in this research into a clinically deployable solution. To achieve this, several additional research steps need to be taken. These steps will be discussed in short-term, mid-term, and long-term steps. The pathway to clinical deployment of UWB/MIMU gait analysis technology involves a systematic expansion from technical refinement to real-world validation. In the short term, the focus is on addressing the immediate limitations of the research, perfecting accuracy, and reliability in controlled clinical settings. The mid-term will bridge the gap to clinical reality by improving algorithms and testing with specific patient groups. The long-term objectives ensure that the system meets the required clinical accuracy in complex environments, is adopted in daily practice, and continues to evolve with emerging techniques.

7.5.1 Short-term: Technical validation with real-world data along with a sensor fusion algorithm and sensor firmware refinement

The short-term future research should mainly focus on addressing the key limitations identified in this research. Specifically, the synthetic data-based validation of the position estimation algorithm in Chapter 6 enabled a sensitivity analysis by controlling bias and random error levels around the error levels already achieved after swarm calibration in Chapter 3. However, it does not capture the full complexity of live UWB measurements during actual human motion, such as NLOS introduced by body segments and all possible movement scenarios. Therefore, the priority is to acquire real-time UWB/MIMU data with the current validated nine integrated UWB/MIMU sensor configurations from healthy subjects performing a few clinical tasks with both LOS and NLOS situations. Eventually, the integrated sensor system should be validated with this on-body combined LOS and NLOS situations. This would define the performance benchmark of this system in a clinical situation and would help identify additional challenges in an actual clinical situation.

The next key limitation to be addressed is the lack of NLOS detection or compensation within the UMIMU fusion framework. Algorithmic improvements should focus on a sensor fusion method with smart mechanisms to handle non-line-of-sight (NLOS) conditions. For example, a loosely coupled Kalman Filter that detects and rejects faulty UWB ranges while using UWB updates to correct MIMU drift has been shown to improve positioning accuracy by over 60% compared to MIMU alone dead-reckoning [108]. Similarly, an extended Kalman Filter strategy that dynamically adjusts measurement noise based on NLOS detection achieved a ~46% accuracy gain over conventional fusion in field tests [229]. The current sensor fusion framework developed in this research is already designed to include these adaptations as a tuning of the covariance matrices based on the measurement quality of the UWB and MIMU sensors. With the lack of real UWB data, this feature is not validated in the currently developed algorithm. Therefore, in the immediate future with acquired real UWB data, the system should incorporate either skipping UWB measurements with NLOS detected or an adaptive filtering that can increase the filter covariance during suspected NLOS, or applying outlier rejection to suppress

UWB measurement outliers and MIMU drift. In addition, the comprehensive error characterization of the UWB sensors provided in Chapter 3 could be exploited for classifying each range update as LOS, partial-LOS or NLOS and include appropriate bias corrections to further enhance the position estimation algorithm.

The current firmware implemented in the developed integrated UWB/MIMU sensor platform is optimized primarily to ensure efficient and collision-free ranging between the sensor nodes, enabling the reliable capturing of measurement data (accelerometer, gyroscope, magnetometer, and quaternion data). Future improvements could be expected from research into assessing the presence and characteristics of ranging errors from the UWB distance data, providing insights into the NLOS situation. This additional data about the nature of the UWB ranging could significantly enhance adaptive filtering strategies that either skip the NLOS data points or allow the fusion process to dynamically adjust covariance matrices based on NLOS conditions, as previously suggested. By the end of this phase, the goal is a prototype that is technically sound and easy to deploy in controlled environments, with clearly validated accuracy and consistency for the clinical 3D AHM use case.

7.5.2 Mid-term: Software optimization along with clinical validation

An important mid-term future work involves compensating for position estimation errors induced by human body occlusion during movement. In the current research, UWB/MIMU fusion was implemented using an Extended Kalman Filter (EKF), which relies on a state-space model with process and measurement noise assumed to be zero-mean Gaussian with known covariances. While this framework is powerful for handling random noise and drift, it does not explicitly capture systematic biases not introduced by dynamic, self-occluding anatomical segments. As demonstrated in the error characterization presented in Chapter 3 of this thesis, ranging errors due to NLOS conditions are not random but are strongly influenced by the geometry and size of the body segments causing the occlusion. These occlusion events would follow repeatable, phase-locked temporal structures within cyclic motions such as walking or running. Therefore, future investigations on correction models that leverage this cyclicity and understandings about the errors as shown in Chapter 3 would be a promising extension in improving the accuracy in

complex environments. Such correction models would complement the physics-based EKF pipeline by adding a data-driven correction layer capable of adapting to anatomical variability and task-specific movement patterns, ultimately leading to more accurate and robust spatial tracking of body segments in human movement analysis.

The technical validations along with the sensor firmware refinements mentioned previously (Section 7.5.1) would only make the integrated UWB/MIMU sensor system more accurate, consistent, and reliable. However, for successful clinical implementation, it is also essential for the sensor system to be appropriately validated for clinical full-body movement analysis (clinical validation) as per the criterion mentioned by Baker. et.al.,2006 [29], elaborated in Chapter 1: Section 1.3. Therefore, in this mid-term phase, the system should undergo extensive testing with diverse patient populations and settings. This should include conducting pilot trials in hospital gait labs and rehabilitation centers with participants such as post-stroke patients, older adults at risk of falling, and other clinical groups. The aim must be to validate that the UWB/MIMU system can capture pathological gait characteristics as accurately as it does healthy gait and to assess the clinical relevance of the derived metrics. These studies will help refine the algorithms (e.g., adjusting filter parameters or sensor placement) to handle atypical gait patterns. They will also reveal any usability issues in a clinical workflow. Ultimately, a mid-term milestone is a version of an integrated sensor system that can be deployed in a real clinic or home environment for days at a time, with all components working together effectively.

7.5.3 Long-term: Real-time clinical integration and feedback-driven rehabilitation

In the long run, the integrated UWB/MIMU gait analysis system should be validated in clinical trials and eventually adopted in routine care. A key objective is to demonstrate clinical efficacy by showing that using the system can improve patient outcomes (e.g., faster rehabilitation progress, fewer falls due to early detection of gait deterioration) or provide diagnostic insights not available through standard care.. The long-term goal is also to improve this accuracy further through improved algorithms and calibration, such that even in cluttered or furnished environments, the system should achieve sub-centimeter precision for gait metrics. With achieved

high accuracy and consistency, clinical trials could then focus on how the system's measurements and real-time feedback translate to clinical decision-making and patient improvement. For example, trials may examine whether rehabilitation programs that incorporate UWB/MIMU-based feedback lead to better mobility outcomes compared to programs that rely on periodic visual gait assessments. In parallel, longitudinal studies might use the system for remote monitoring and tracking patients post-discharge in their homes to see if early warnings from gait data can predict falls or health declines. Such evidence will be crucial for clinicians to trust and adopt the technology.

Smooth integration into everyday clinical practice requires training clinicians and therapists to use the technology effectively. User interfaces will need to be refined for simplicity with a clinician-friendly dashboard that automatically highlights abnormal gait parameters or changes over time, rather than requiring raw data interpretation [230]. The system should function as a plug-and-play tool in clinics where a therapist can quickly strap the sensors on a patient, have them walk in the gym area for a few minutes, and immediately obtain gait quality metrics and fall risk indicators. To facilitate this, long-term development should incorporate feedback from clinicians collected during the mid-term pilots. Features that save time and effort, such as voice-guided setup, automatic report generation [230], or integration with scheduling software, could be added for smooth adaptability. Besides, the workflow might be adapted such that the system provides decision support, such as alerting if a patient's gait symmetry has significantly worsened since the last session, prompting further evaluation. In rehabilitation wards, the system could run continuously in the background, monitoring patients as they do exercises or walk in hallways, effectively creating a smart environment. This vision aligns with the concept of digital health and smart rehabilitation facilities, where multi-modal sensor networks (wearables, ambient sensors, etc.) work together. The integrated UWB/MIMU system, with its ability to precisely track movement, could become a cornerstone of such environments, complementing camera systems or ambient radars to give a comprehensive view of patient mobility. By the end of this phase, the system is not just a standalone gadget but part of an integrated rehabilitation ecosystem, potentially feeding data into telerehabilitation platforms or home monitoring programs that extend care beyond the hospital.

7.6 Conclusion

This PhD research has made significant contributions to the field of human movement analysis methodology by developing and validating a novel, fully integrated UWB/MIMU sensor system capable of more accurate and highly consistent position estimation for ambulatory 3D analysis of human movement. It addresses the key limitations in wearable motion tracking associated particularly with the lack of reliable spatial information in MIMU-only systems. This was achieved through integration of existing technologies (MIMU integrated with UWB sensors), UWB sensor calibration, swarm-based position estimation from UWB, and finally, a tailored sensor fusion. This research is both timely and important, as clinical practice increasingly shifts toward objective, decentralized, and technology-supported rehabilitation. By demonstrating that wearable systems can approach clinically meaningful accuracy in real-world conditions, this work lays a valuable technical foundation for the future development of clinically relevant movement assessment tools, facilitating reliable patient monitoring and improved rehabilitation outcomes in diverse real-world settings.

Appendix
Bibliography
Summary
Acknowledgement
Author-Bio
and
Progress Range



APPENDIX

A. Empirical Identification of Position Drift Compensation Strategy

A.1 Background

There was a small repeatable drift always observed in the position estimates of the proposed UMIMU fusion algorithm (Figure A1). This indicated the opportunity to identify the behaviour of the drift and utilize it to compensate for the same after each update step in the Extended Kalman Filter (EKF) filter. Such a correction could reduce accumulated errors between Ultrawideband (UWB) measurement updates and further improve the final position estimation accuracy.

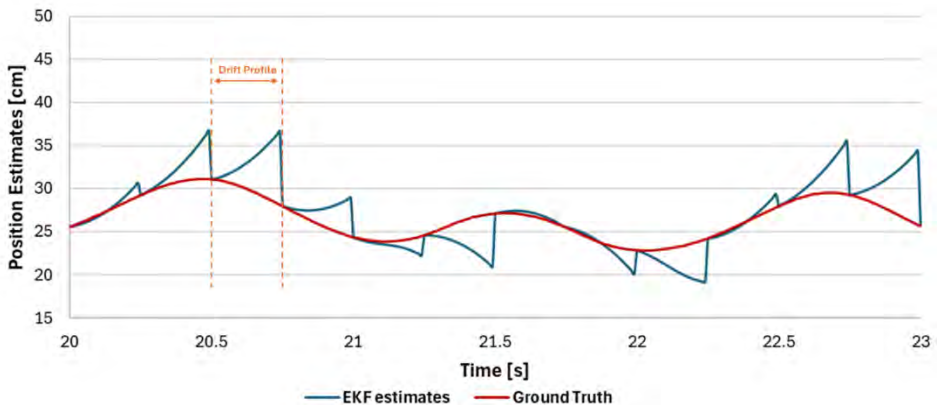


Figure A1: A zoomed region of the position estimates along one of the coordinate axes, showing a typical drift profile between UWB measurement updates. The term drift profile is the interval between two UWB updates, and one of the drift profiles is highlighted between the orange dashed lines.

For this, the position estimation errors from the proposed UMIMU fusion filter were studied to identify the repeatable trend, such that the error compensation can be modelled as a generalized compensation model.

A.2 Method

To investigate the drift behaviour, the UMIMU fusion algorithm position estimation errors from one of the experimental trials (measurement length around 300 seconds) were utilized. These measurement results were from an ideal input UWB data (i.e., clean input UWB distance measure with no bias and random errors) with an update

rate of 4 samples per second (sps), and 6 individual sensor positions as described in the article. A drift profile was defined as the region between two UWB measurement updates (0.25 seconds), where for each interval, the drift was assumed to be zero at the start due to EKF correction by the previous UWB update and accumulated until the next UWB update (Figure A1). With the total duration of around 300 seconds and UWB update rate at 4 sps, a total of 1210 drift profiles were available for analysis per sensor (7260 drift profiles in total).

The mean representative drift profile was obtained by computing the ensemble average over all drift intervals at each time step. From this mean drift profile, the error at the midpoint (time step 11) was extracted and is expressed as a percentage of the final error (time step 24).

A.3 Results

The mean drift curve clearly followed a second-order trend (Figure A2), indicating that drift grows nonlinearly. The midpoint error (time step 11) was consistently less than the final error, with the average value across axes being close to 20% of the final error.

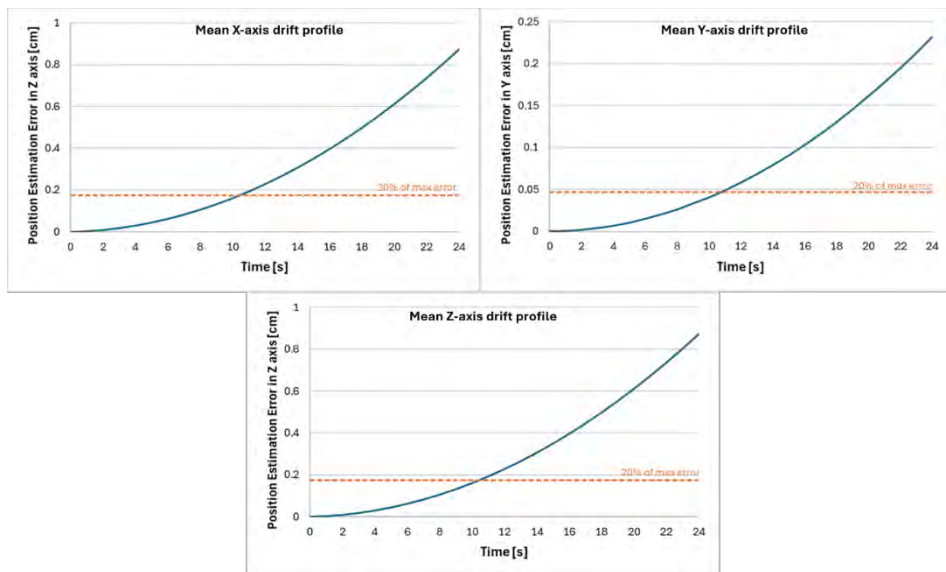


Figure A2: Mean drift curve plot for each coordinate axis, averaged over 7260 drift profiles. The 20% of the final maximum error is represented as the dashed orange line.

Based on the above findings, we chose to use a second-order polynomial to model the drift curve over each EKF prediction interval.

A.4 Conclusion

Though some variation across axes was observed, using 20% as a standard midpoint drift value would be a good approximation that provides a simplified and generalized implementation, while retaining high correction accuracy.

The correction polynomial is constructed using:

- Start point ($t=0$): 0 error (immediately after UWB update),
- Midpoint ($t=11$): 20% of final error (empirically derived),
- End point ($t=24$): actual accumulated error (before next UWB update).

B. Empirical Identification and Validation of Velocity Drift Compensation Strategy

B.1 Background

Similar to the drift observed in position estimates, velocity estimates of the proposed UMIMU fusion algorithm also showed a small repeatable drift (Figure B1). The visual observation of the drift indicated this to be approximately a linear drift. This observed linear behavior aligns closely with trends reported in the literature, particularly in studies utilizing Zero-Velocity-Update (ZUPT) techniques for inertial navigation systems. ZUPT-based methods typically assume a linear growth in velocity drift between known zero-velocity instances and use this assumption to implement linear compensation strategies [44,69,186].

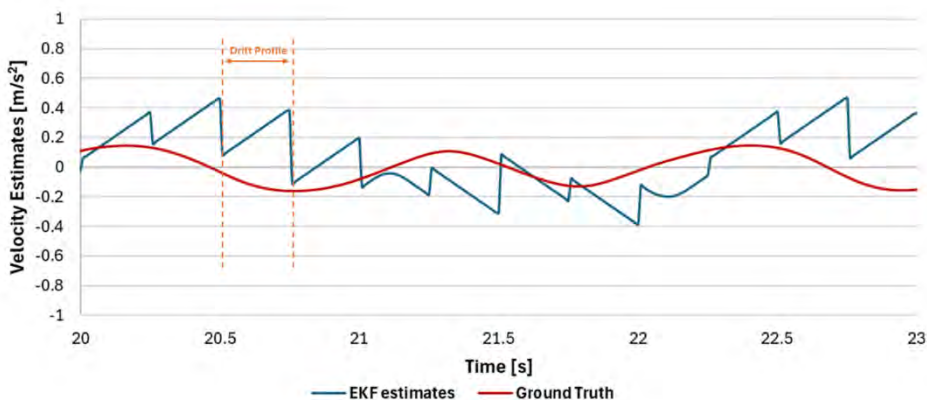


Figure B1: A zoomed region of the velocity estimates along one of the coordinate axes, showing a typical linear drift profile between UWB measurement updates. One of the drift profiles is highlighted between the orange dashed lines.

Within this study, the common assumption of velocity drift being linear between the UWB updates was validated to determine if the linear compensation would be a valid compensation method.

B.2 Method and Results

To investigate the behaviour of velocity drift, data from the UMIMU fusion algorithm were analyzed using one of the experimental trials (measurement length

around 300 seconds). The analysis used ideal UWB inputs (i.e., distance measurements free of bias and random noise) provided at an update rate of 4 samples per second (sps), across 6 sensor nodes, as described in the main article. A velocity drift profile was defined as the interval between two consecutive UWB updates (0.25 seconds), where velocity estimation errors accumulate after each update. It was assumed that the velocity drift is zero immediately following a UWB update due to the EKF correction, and then gradually accumulates until the next update (Figure B1). With a duration of around 300 seconds and 4 updates per second, each sensor contributed 1202 velocity drift profiles, resulting in a total of 7212 drift profiles for analysis.

To characterize the drift pattern, the ensemble average of all velocity drift profiles was computed at each time step within the 0.25-second window and is as seen in Figure B2. The linear fit and coefficient of determination (R^2) of the mean velocity drift curve indicated a strong linearity in all three coordinates.

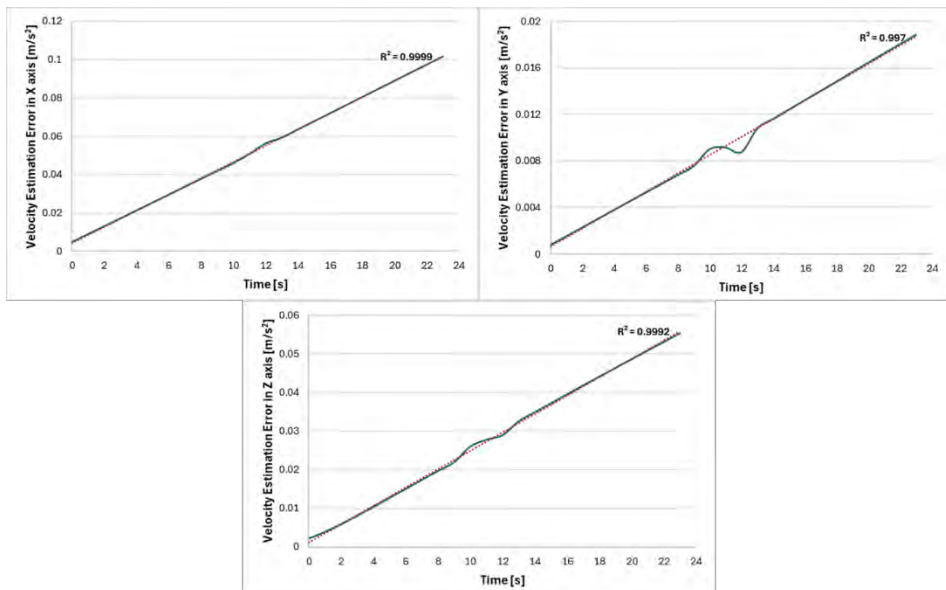


Figure B2: Mean velocity drift curve averaged over 7212 drift segments, shown with the corresponding linear fit (red dotted line [...]) and R^2 values for each axis.

To further validate the linearity assumption empirically, a linear regression model was fitted to the velocity drift for each drift profile, and the R^2 was computed for each coordinate axis per drift profile. The average R^2 across all drift profiles was

found to be 0.93 ± 0.19 for the X-axis, 0.93 ± 0.19 for the Y-axis, and 0.93 ± 0.19 for the Z-axis. These results indicate a strong linearity in the X and Y axes, while a moderate linearity in the Z-axis, supporting the use of linear interpolation for velocity drift compensation. These confirm the assumption of linearity in velocity drift stated in the other ZUPT approaches. In addition, previous ZUPT algorithms [44,186] have demonstrated that linear drift trends in short time windows are sufficiently accurate for improving positional accuracy during human movement.

B.3 Conclusion

Based on these findings, the drift was assumed to be linear for all cases, and a linear velocity drift compensation model was implemented between UWB update steps. Specifically:

- Drift is assumed to be zero at the last UWB update point.
- The drift observed at the current update is estimated from the EKF predicted vs. corrected velocity.
- A linear interpolation is applied across the interval to progressively adjust the velocity estimates, similar to the compensation technique used in ZUPT algorithms.

BIBLIOGRAPHY

1. Pirker, W.; Katzenschlager, R. Gait disorders in adults and the elderly. *Wiener klinische Wochenschrift* **2016**, *129*, 81-95, doi:10.1007/s00508-016-1096-4.
2. Almeheyawi, R.N.; Bricca, A.; Riskowski, J.L.; Barn, R.; Steultjens, M. Foot characteristics and mechanics in individuals with knee osteoarthritis: systematic review and meta-analysis. *Journal of Foot and Ankle Research* **2021**, *14*, doi:10.1186/s13047-021-00462-y.
3. van Meulen, F.B.; Weenk, D.; Buurke, J.H.; van Beijnum, B.J.; Veltink, P.H. Ambulatory Assessment of Walking Balance after Stroke Using Instrumented Shoes. *Journal of NeuroEngineering and Rehabilitation* **2016**, *13*, 48, doi:10.1186/s12984-016-0146-5.
4. Marsh, B.C.; Astill, S.L.; Utley, A.; Ichiyama, R.M. Movement rehabilitation after spinal cord injuries: emerging concepts and future directions. *Brain Res Bull* **2011**, *84*, 327-336, doi:10.1016/j.brainresbull.2010.07.011.
5. Olaya, B.; Moneta, M.V.; Domenech-Abella, J.; Miret, M.; Bayes, I.; Ayuso-Mateos, J.L.; Haro, J.M. Mobility Difficulties, Physical Activity, and All-cause Mortality Risk in a Nationally representative Sample of Older Adults. *J Gerontol A Biol Sci Med Sci* **2018**, *73*, 1272-1279, doi:10.1093/gerona/glx121.
6. Forman-Hoffman, V.L.; Ault, K.L.; Anderson, W.L.; Weiner, J.M.; Stevens, A.; Campbell, V.A.; Armour, B.S. Disability status, mortality, and leading causes of death in the United States community population. *Med Care* **2015**, *53*, 346-354, doi:10.1097/MLR.0000000000000321.
7. Cifuentes, C.A.; Múnera, M.; Sierra M, S.D.; Arciniegas-Mayag, L.; Bautista, M.; Pinto-Bernal, M.J.; Cespedes, N.; Múnera, M.; Cifuentes, C.A. Introduction to robotics for gait assistance and rehabilitation. *Interfacing Humans and Robots for Gait Assistance and Rehabilitation* **2022**, 1-41.
8. Krishnakumar, S.; van Beijnum, B.F.; Baten, C.T.M.; Veltink, P.H.; Buurke, J.H. Estimation of Kinetics Using IMUs to Monitor and Aid in Clinical Decision-Making during ACL Rehabilitation: A Systematic Review. *Sensors (Basel)* **2024**, *24*, doi:10.3390/s24072163.
9. Wang, W.; Niu, Y.; Jia, Q. Physical therapy as a promising treatment for osteoarthritis: A narrative review. *Front Physiol* **2022**, *13*, 1011407, doi:10.3389/fphys.2022.1011407.
10. van Doormaal, M.C.M.; Meerhoff, G.A.; Vliet Vlieland, T.P.M.; Peter, W.F. A clinical practice guideline for physical therapy in patients with hip or knee osteoarthritis. *Musculoskeletal Care* **2020**, *18*, 575-595, doi:10.1002/msc.1492.
11. Wren, T.A.L.; Tucker, C.A.; Rethlefsen, S.A.; Gorton, G.E., 3rd; Ounpuu, S. Clinical efficacy of instrumented gait analysis: Systematic review 2020 update. *Gait Posture* **2020**, *80*, 274-279, doi:10.1016/j.gaitpost.2020.05.031.
12. Hulleck, A.A.; Menoth Mohan, D.; Abdallah, N.; El Rich, M.; Khalaf, K. Present and future of gait assessment in clinical practice: Towards the application of novel trends and technologies. *Front Med Technol* **2022**, *4*, 901331, doi:10.3389/fmedt.2022.901331.
13. Wouda, F.J.; Jaspar, S.; Harlaar, J.; van Beijnum, B.F.; Veltink, P.H. Foot progression angle estimation using a single foot-worn inertial sensor. *J Neuroeng Rehabil* **2021**, *18*, 37, doi:10.1186/s12984-021-00816-4.
14. Muro-de-la-Herran, A.; Garcia-Zapirain, B.; Mendez-Zorrilla, A. Gait analysis methods: an overview of wearable and non-wearable systems, highlighting clinical applications. *Sensors (Basel)* **2014**, *14*, 3362-3394, doi:10.3390/s140203362.

15. Agbemanyole, K.A.; Agbohessou, K.G.; Pons, C.; Lenca, P.; Remy-Neris, O.; Goff-Pronost, M.L. Economic analysis of digital motor rehabilitation technologies: a systematic review. *Health Econ Rev* **2024**, *14*, 52, doi:10.1186/s13561-024-00523-5.
16. Iosa, M.; Picerno, P.; Paolucci, S.; Morone, G. Wearable inertial sensors for human movement analysis. *Expert Rev Med Devices* **2016**, *13*, 641-659, doi:10.1080/17434440.2016.1198694.
17. Kooroor, M.; Durairaj, M.; Karyakarte, M.S.; Zair Hussain, M.; Ashraf, M.; Maguluri, L.P. Sensor-enhanced wearables and automated analytics for injury prevention in sports. *Measurement: Sensors* **2024**, *32*, doi:10.1016/j.measen.2024.101054.
18. Rybníkář, F.; Kačerová, I.; Hořejší, P.; Šimon, M. Ergonomics Evaluation Using Motion Capture Technology—Literature Review. *Applied Sciences* **2022**, *13*, doi:10.3390/app13010162.
19. Aristotle; Peck, A.L.; Forster, E.S. Parts of Animals. Movement of Animals. Progression of Animals. 1937.
20. Clayton, M. Medicine: Leonardo's anatomy years. *Nature* **2012**, *484*, 314-316, doi:10.1038/484314a.
21. Steele, L. Andreas Vesalius and his De humani corporis Fabrica libri septem. *Vesalius: acta internationales historiae medicinae* **2014**, *20*, 5-10.
22. Abu-Faraj, Z.O.; Harris, G.F.; Smith, P.A.; Hassani, S. Human gait and clinical movement analysis. *Wiley Encyclopedia of Electrical and Electronics Engineering* **2015**, 1-34.
23. Schiehlen, W. On the historical development of human walking dynamics. *Pamm* **2011**, *11*, 903-906, doi:10.1002/pamm.201110435.
24. Braun, M. *Picturing time: the work of Etienne-Jules Marey (1830-1904)*; University of Chicago Press: 1992.
25. Basile, M.S.; Coco, M.; Buscemi, A.; Petralia, M.C. Brief review on the historical evolution of kinematics and its application in clinical practice. *Acta Medica Mediterranea* **2018**, *34*, 911-913.
26. Perry, J.; Burnfield, J.M.; Cabico, L.M. *Gait analysis : normal and pathological function*, 2nd ed ed.; SLACK: Thorofare, NJ, 2010.
27. Basmajian, J.V. *Muscles alive : their functions revealed by electromyography*, 3rd ed ed.; Williams & Wilkins: Baltimore, MD, 1974.
28. Winter, D.A. Biomechanics and motor control of human movement. **2009**, doi:10.1002/9780470549148.
29. Baker, R. Gait analysis methods in rehabilitation. *J Neuroeng Rehabil* **2006**, *3*, 4, doi:10.1186/1743-0003-3-4.
30. Colyer, S.L.; Nagahara, R.; Salo, A.I.T. Kinetic demands of sprinting shift across the acceleration phase: Novel analysis of entire force waveforms. *Scand J Med Sci Sports* **2018**, *28*, 1784-1792, doi:10.1111/sms.13093.
31. Eichelberger, P.; Ferraro, M.; Minder, U.; Denton, T.; Blasimann, A.; Krause, F.; Baur, H. Analysis of accuracy in optical motion capture - A protocol for laboratory setup evaluation. *J Biomech* **2016**, *49*, 2085-2088, doi:10.1016/j.jbiomech.2016.05.007.
32. Aurand, A.M.; Dufour, J.S.; Marras, W.S. Accuracy map of an optical motion capture system with 42 or 21 cameras in a large measurement volume. *J Biomech* **2017**, *58*, 237-240, doi:10.1016/j.jbiomech.2017.05.006.

33. Holder, J.; Trinler, U.; Meurer, A.; Stief, F. A Systematic Review of the Associations Between Inverse Dynamics and Musculoskeletal Modeling to Investigate Joint Loading in a Clinical Environment. *Front Bioeng Biotechnol* **2020**, *8*, 603907, doi:10.3389/fbioe.2020.603907.
34. McGinley, J.L.; Baker, R.; Wolfe, R.; Morris, M.E. The reliability of three-dimensional kinematic gait measurements: a systematic review. *Gait Posture* **2009**, *29*, 360-369, doi:10.1016/j.gaitpost.2008.09.003.
35. Challis, J.H. The Variability in Running Gait Caused by Force Plate Targeting. *Journal of Applied Biomechanics* **2001**, *17*, 77-83, doi:10.1123/jab.17.1.77.
36. Roell, M.; Roecker, K.; Gehring, D.; Mahler, H.; Gollhofer, A. Player Monitoring in Indoor Team Sports: Concurrent Validity of Inertial Measurement Units to Quantify Average and Peak Acceleration Values. *Front Physiol* **2018**, *9*, 141, doi:10.3389/fphys.2018.00141.
37. Karoulla, E.; Matsangidou, M.; Frangoudes, F.; Paspalides, P.; Neokleous, K.; Pattichis, C.S. Tracking Upper Limb Motion via Wearable Solutions: Systematic Review of Research From 2011 to 2023. *J Med Internet Res* **2024**, *26*, e51994, doi:10.2196/51994.
38. Sabatini, A.M. Estimating Three-Dimensional Orientation of Human Body Parts by Inertial/Magnetic Sensing. *Sensors (Basel)* **2011**, *11*, 1489-1525, doi:10.3390/s110201489.
39. Vitali, R.V.; McGinnis, R.S.; Perkins, N.C. Robust Error-State Kalman Filter for Estimating IMU Orientation. *IEEE Sensors Journal* **2021**, *21*, 3561-3569, doi:10.1109/jsen.2020.3026895.
40. Roetenberg, D.; Luinge, H.J.; Baten, C.T.; Veltink, P.H. Compensation of Magnetic Disturbances Improves Inertial and Magnetic Sensing of Human Body Segment Orientation. *IEEE Transactions on Neural Systems and Rehabilitation Engineering* **2005**, *13*, 395-405, doi:10.1109/TNSRE.2005.847353.
41. de Vries, W.H.; Veeger, H.E.; Baten, C.T.; van der Helm, F.C. Magnetic Distortion in Motion Labs, Implications for Validating Inertial Magnetic Sensors. *Gait & Posture* **2009**, *29*, 535-541, doi:10.1016/j.gaitpost.2008.12.004.
42. Chow, J.; Hol, J.; Luinge, H. Tightly-Coupled Joint User Self-Calibration of Accelerometers, Gyroscopes, and Magnetometers. *Drones* **2018**, *2*, doi:10.3390/drones2010006.
43. Kaichi, T.; Maruyama, T.; Tada, M.; Saito, H. Resolving Position Ambiguity of IMU-Based Human Pose with a Single RGB Camera. *Sensors (Basel)* **2020**, *20*, doi:10.3390/s20195453.
44. Wahlstrom, J.; Skog, I. Fifteen Years of Progress at Zero Velocity: A Review. *IEEE Sensors Journal* **2021**, *21*, 1139-1151, doi:10.1109/jsen.2020.3018880.
45. Luinge, H.J.; Veltink, P.H.; Baten, C.T. Ambulatory Measurement of Arm Orientation. *Journal of Biomechanics* **2007**, *40*, 78-85, doi:10.1016/j.jbiomech.2005.11.011.
46. Yavuzer, G.; Oken, O.; Elhan, A.; Stam, H.J. Repeatability of Lower Limb Three-Dimensional Kinematics in Patients with Stroke. *Gait & Posture* **2008**, *27*, 31-35, doi:10.1016/j.gaitpost.2006.12.016.
47. Windolf, M.; Gotzen, N.; Morlock, M. Systematic Accuracy and Precision Analysis of Video Motion Capturing Systems--Exemplified on the Vicon-460 System. *Journal of Biomechanics* **2008**, *41*, 2776-2780, doi:10.1016/j.jbiomech.2008.06.024.
48. Picerno, P. 25 years of lower limb joint kinematics by using inertial and magnetic sensors: A review of methodological approaches. *Gait Posture* **2017**, *51*, 239-246, doi:10.1016/j.gaitpost.2016.11.008.

49. Yao, L.; Yao, L.; Wu, Y.W. Analysis and Improvement of Indoor Positioning Accuracy for UWB Sensors. *Sensors* **2021**, *21*, doi:10.3390/s21175731.
50. Yang, X.F.; Wang, J.; Song, D.P.; Feng, B.Z.; Ye, H. A Novel NLOS Error Compensation Method Based IMU for UWB Indoor Positioning System. *IEEE Sensors Journal* **2021**, *21*, 11203-11212, doi:10.1109/JSEN.2021.3061468.
51. Yadav, R.K.; Bhattarai, B.; Gang, H.S.; Pyun, J.Y. Trusted K Nearest Bayesian Estimation for Indoor Positioning System. *IEEE Access* **2019**, *7*, 51484-51498, doi:10.1109/ACCESS.2019.2910314.
52. Buffi, A.; Michel, A.; Nepa, P.; Tellini, B. RSSI Measurements for RFID Tag Classification in Smart Storage Systems. *IEEE Transactions on Instrumentation and Measurement* **2018**, *67*, 894-904, doi:10.1109/tim.2018.2791238.
53. Minne, K.; Macoir, N.; Rossey, J.; Brande, Q.V.D.; Lemey, S.; Hoebeke, J.; Poorter, E. Experimental Evaluation of UWB Indoor Positioning for Indoor Track Cycling. *Sensors (Basel)* **2019**, *19*, doi:10.3390/s19092041.
54. Guang, X.; Gao, Y.; Liu, P.; Li, G. IMU Data and GPS Position Information Direct Fusion Based on LSTM. *Sensors (Basel)* **2021**, *21*, doi:10.3390/s21072500.
55. Weenk, D.; Roetenberg, D.; van Beijnum, B.J.; Hermens, H.J.; Veltink, P.H. Ambulatory Estimation of Relative Foot Positions by Fusing Ultrasound and Inertial Sensor Data. *IEEE Transactions on Neural Systems and Rehabilitation Engineering* **2015**, *23*, 817-826, doi:10.1109/TNSRE.2014.2357686.
56. Hung, T.N.; Suh, Y.S. Inertial Sensor-Based Two Feet Motion Tracking for Gait Analysis. *Sensors (Basel)* **2013**, *13*, 5614-5629, doi:10.3390/s130505614.
57. Li, X.; Wang, Y.; Liu, D. Research on Extended Kalman Filter and Particle Filter Combinational Algorithm in UWB and Foot-Mounted IMU Fusion Positioning. *Mobile Information Systems* **2018**, *2018*, doi:10.1155/2018/1587253.
58. Yu, N.; Li, Y.; Ma, X.; Wu, Y.; Feng, R. Comparison of Pedestrian Tracking Methods Based on Foot- and Waist-Mounted Inertial Sensors and Handheld Smartphones. *IEEE Sensors Journal* **2019**, *19*, 8160-8173, doi:10.1109/jsen.2019.2919721.
59. Li, X.; Wang, Y.; Liu, D. Research on Extended Kalman Filter and Particle Filter Combinational Algorithm in UWB and Foot-Mounted IMU Fusion Positioning. *Mobile Information Systems* **2018**, *2018*, 1-17, doi:10.1155/2018/1587253.
60. Wang, Y.; Li, X. The IMU/UWB Fusion Positioning Algorithm Based on a Particle Filter. *ISPRS International Journal of Geo-Information* **2017**, *6*, doi:10.3390/ijgi6080235.
61. Zhang, H.; Zhang, Z.; Gao, N.; Xiao, Y.; Meng, Z.; Li, Z. Cost-Effective Wearable Indoor Localization and Motion Analysis via the Integration of UWB and IMU. *Sensors (Basel)* **2020**, *20*, doi:10.3390/s20020344.
62. Wen, K.; Yu, K.; Li, Y.; Zhang, S.; Zhang, W. A New Quaternion Kalman Filter Based Foot-Mounted IMU and UWB Tightly-Coupled Method for Indoor Pedestrian Navigation. *IEEE Transactions on Vehicular Technology* **2020**, *69*, 4340-4352, doi:10.1109/tvt.2020.2974667.
63. Brena, R.F.; García-Vázquez, J.P.; Galván-Tejada, C.E.; Muñoz-Rodríguez, D.; Vargas-Rosales, C.; Fangmeyer, J. Evolution of Indoor Positioning Technologies: A Survey. *Journal of Sensors* **2017**, *2017*, 1-21, doi:10.1155/2017/2630413.

64. Hayward, S.J.; van Lopik, K.; Hinde, C.; West, A.A. A Survey of Indoor Location Technologies, Techniques and Applications in Industry. *Internet of Things* **2022**, *20*, doi:10.1016/j.iot.2022.100608.
65. Hashim, H.A.; Eltoukhy, A.E.E.; Vamvoudakis, K.G. UWB Ranging and IMU Data Fusion: Overview and Nonlinear Stochastic Filter for Inertial Navigation. *IEEE Transactions on Intelligent Transportation Systems* **2024**, *25*, 359-369, doi:10.1109/its.2023.3309288.
66. Filippeschi, A.; Schmitz, N.; Miezal, M.; Bleser, G.; Ruffaldi, E.; Stricker, D. Survey of Motion Tracking Methods Based on Inertial Sensors: A Focus on Upper Limb Human Motion. *Sensors (Basel)* **2017**, *17*, doi:10.3390/s17061257.
67. Rekant, J.; Rothenberger, S.; Chambers, A. Inertial Measurement Unit-Based Motion Capture to Replace Camera-Based Systems for Assessing Gait in Healthy Young Adults: Proceed with Caution. *Measurement: Sensors* **2022**, *23*, doi:10.1016/j.measen.2022.100396.
68. Zihajehzadeh, S.; Park, E.J. A Novel Biomechanical Model-Aided IMU/UWB Fusion for Magnetometer-Free Lower Body Motion Capture. *IEEE Transactions on Systems, Man, and Cybernetics: Systems* **2017**, *47*, 927-938, doi:10.1109/TSMC.2016.2521823.
69. Ma, M.; Song, Q.; Gu, Y.; Li, Y.; Zhou, Z. An Adaptive Zero Velocity Detection Algorithm Based on Multi-Sensor Fusion for a Pedestrian Navigation System. *Sensors (Basel)* **2018**, *18*, doi:10.3390/s18103261.
70. Benedetti, M.G.; Beghi, E.; De Tanti, A.; Cappozzo, A.; Basaglia, N.; Cutti, A.G.; Cereatti, A.; Stagni, R.; Verdini, F.; Manca, M.; et al. SIAMOC position paper on gait analysis in clinical practice: General requirements, methods and appropriateness. Results of an Italian consensus conference. *Gait Posture* **2017**, *58*, 252-260, doi:10.1016/j.gaitpost.2017.08.003.
71. Carse, B.; Meadows, B.; Bowers, R.; Rowe, P. Affordable Clinical Gait Analysis: An Assessment of the Marker Tracking Accuracy of a New Low-Cost Optical 3D Motion Analysis System. *Physiotherapy* **2013**, *99*, 347-351, doi:10.1016/j.physio.2013.03.001.
72. van der Kruk, E.; Reijne, M.M. Accuracy of Human Motion Capture Systems for Sport Applications; State-of-the-Art Review. *European Journal of Sport Science* **2018**, *18*, 806-819, doi:10.1080/17461391.2018.1463397.
73. Roetenberg, D.; Veltink, P.H. Camera-Marker and Inertial Sensor Fusion for Improved Motion Tracking. *Gait & posture* **2005**, *22*, 51 - 52, doi:urn:nbn:nl:ui:28-76606.
74. Poulouse, A.; Eyobu, O.S.; Han, D.S. An Indoor Position-Estimation Algorithm Using Smartphone IMU Sensor Data. *IEEE Access* **2019**, *7*, 11165-11177, doi:10.1109/access.2019.2891942.
75. Jimenez, A.R.; Seco, F. Improving the Accuracy of Decawave's UWB MDEK1001 Location System by Gaining Access to Multiple Ranges. *Sensors (Basel)* **2021**, *21*, doi:10.3390/s21051787.
76. Zhang, H.; Zhang, Z.; Gao, N.; Xiao, Y.; Meng, Z.; Li, Z. Cost-Effective Wearable Indoor Localization and Motion Analysis via the Integration of UWB and IMU. *Sensors (Switzerland)* **2020**, *20*, doi:10.3390/s20020344.
77. Wen, K.; Yu, K.G.; Li, Y.B.; Zhang, S.B.; Zhang, W.W. A New Quaternion Kalman Filter Based Foot-Mounted IMU and UWB Tightly-Coupled Method for Indoor Pedestrian Navigation. *IEEE Transactions on Vehicular Technology* **2020**, *69*, 4340-4352, doi:10.1109/TVT.2020.2974667.

78. Feng, D.; Wang, C.; He, C.; Zhuang, Y.; Xia, X.G. Kalman-Filter-Based Integration of IMU and UWB for High-Accuracy Indoor Positioning and Navigation. *IEEE Internet of Things Journal* **2020**, *7*, 3133-3146, doi:10.1109/JIOT.2020.2965115.
79. Geary, R.C. The Ratio of the Mean Deviation to the Standard Deviation as a Test of Normality. *Biometrika* **1935**, *27*, 310-332, doi:10.2307/2332693.
80. Youssef, J.; Denis, B.; Godin, C.; Lesecq, S. Pedestrian Tracking Solution Combining an Impulse Radio Handset Transmitter with an Ankle-Mounted Inertial Measurement Unit. *International Journal of Navigation and Observation* **2012**, doi:10.1155/2012/603254.
81. Zihajehzadeh, S.; Yoon, P.K.; Park, E.J. A Magnetometer-Free Indoor Human Localization Based on Loosely Coupled IMU/UWB Fusion. *Annual International Conference of the IEEE Engineering in Medicine and Biology Society* **2015**, *2015*, 3141-3144, doi:10.1109/embc.2015.7319058.
82. Zihajehzadeh, S.; Yoon, P.K.; Kang, B.S.; Park, E.J. UWB-Aided Inertial Motion Capture for Lower Body 3-D Dynamic Activity and Trajectory Tracking. *IEEE Transactions on Instrumentation and Measurement* **2015**, *64*, 3577-3587, doi:10.1109/TIM.2015.2459532.
83. Kok, M.; Hol, J.D.; Schon, T.B. Indoor Positioning Using Ultrawideband and Inertial Measurements. *IEEE Transactions on Vehicular Technology* **2015**, *64*, 1293-1303, doi:10.1109/TVT.2015.2396640.
84. Yoon, P.K.; Zihajehzadeh, S.; Kang, B.S.; Park, E.J. Robust Biomechanical Model-Based 3-D Indoor Localization and Tracking Method Using UWB and IMU. *IEEE Sensors Journal* **2017**, *17*, 1084-1096, doi:10.1109/JSEN.2016.2639530.
85. Chen, P.; Kuang, Y.; Chen, X. A UWB/Improved PDR Integration Algorithm Applied to Dynamic Indoor Positioning for Pedestrians. *Sensors (Switzerland)* **2017**, *17*, doi:10.3390/s17092065.
86. Li, X.; Wang, Y.; Khoshelham, K. UWB/PDR Tightly Coupled Navigation with Robust Extended Kalman Filter for NLOS Environments. *Mobile Information Systems* **2018**, *2018*, doi:10.1155/2018/8019581.
87. Wang, Y.; Li, X. Graph-Optimization-Based ZUPT/UWB Fusion Algorithm. *ISPRS International Journal of Geo-Information* **2018**, *7*, doi:10.3390/ijgi7010018.
88. Xu, Y.; Tian, G.; Chen, X. Enhancing INS/UWB Integrated Position Estimation Using Federated EFIR Filtering. *IEEE Access* **2018**, *6*, 64461-64469, doi:10.1109/ACCESS.2018.2878101.
89. Xu, Y.; Ahn, C.K.; Shmaliy, Y.S.; Chen, X.Y.; Li, Y.Y. Adaptive Robust INS/UWB-Integrated Human Tracking Using UFIR Filter Bank. *Measurement* **2018**, *123*, 1-7, doi:10.1016/j.measurement.2018.03.043.
90. Tian, Q.; Wang, K.I.K.; Salci, Z. A Low-Cost INS and UWB Fusion Pedestrian Tracking System. *IEEE Sensors Journal* **2019**, *19*, 3733-3740, doi:10.1109/JSEN.2019.2894714.
91. Xu, Y.; Shen, T.; Chen, X.Y.; Bu, L.L.; Feng, N. Predictive Adaptive Kalman Filter and Its Application to INS/UWB-integrated Human Localization with Missing UWB-based Measurements. *International Journal of Automation and Computing* **2019**, *16*, 604-613, doi:10.1007/s11633-018-1157-4.

92. Xu, Y.; Ahn, C.K.; Shmaliy, Y.S.; Chen, X.; Bu, L. Indoor INS/UWB-Based Human Localization with Missing Data Utilizing Predictive UFIR Filtering. *IEEE/CAA Journal of Automatica Sinica* **2019**, *6*, 952-960, doi:10.1109/JAS.2019.1911570.
93. Tian, Q.; Wang, K.I.K.; Salcic, Z. Human Body Shadowing Effect on UWB-Based Ranging System for Pedestrian Tracking. *IEEE Transactions on Instrumentation and Measurement* **2019**, *68*, 4028-4037, doi:10.1109/TIM.2018.2884605.
94. Ferreira, A.G.; Fernandes, D.; Catarino, A.P.; Rocha, A.M.; Monteiro, J.L. A Loose-Coupled Fusion of Inertial and UWB Assisted by a Decision-Making Algorithm for Localization of Emergency Responders. *Electronics* **2019**, *8*, doi:10.3390/electronics8121463.
95. Li, B.; Hao, Z.; Dang, X. An Indoor Location Algorithm Based on Kalman Filter Fusion of Ultra-wide band and Inertial Measurement Unit. *AIP Advances* **2019**, *9*, doi:10.1063/1.5117341.
96. Wang, Y.; Li, X.; Khoshelham, K.; Li, P. Robust Iterated Extended Kalman Filter Algorithm for Foot-Mounted Inertial Measurement Units/Ultrawideband Fusion Positioning. *Journal of Applied Remote Sensing* **2019**, *13*, doi:10.1117/1.JRS.13.024510.
97. Zhang, Y.; Tan, X.L.; Zhao, C.S. UWB/INS Integrated Pedestrian Positioning for Robust Indoor Environments. *IEEE Sensors Journal* **2020**, *20*, 14401-14409, doi:10.1109/JSEN.2020.2998815.
98. Xu, Y.; Shmaliy, Y.S.; Hua, L.; Ma, L.; Zhuang, Y. Decision Tree-Extended Finite Impulse Response Filtering for Pedestrian Tracking over Tightly Integrated Inertial Navigation System/Ultra wide band Data. *Measurement Science and Technology* **2020**, *32*, doi:10.1088/1361-6501/abb38a.
99. Xu, Y.; Li, Y.; Ahn, C.K.; Chen, X. Seamless Indoor Pedestrian Tracking by Fusing INS and UWB Measurements via LS-SVM Assisted UFIR Filter. *Neurocomputing* **2020**, *388*, 301-308, doi:10.1016/j.neucom.2019.12.121.
100. Tian, Q.; Wang, K.I.K.; Salcic, Z. An INS and UWB Fusion-Based Gyroscope Drift Correction Approach for Indoor Pedestrian Tracking. *Sensors (Switzerland)* **2020**, *20*, 1-16, doi:10.3390/s20164476.
101. Tian, Q.; Wang, K.I.K.; Salcic, Z. A Resetting Approach for INS and UWB Sensor Fusion Using Particle Filter for Pedestrian Tracking. *IEEE Transactions on Instrumentation and Measurement* **2020**, *69*, 5914-5921, doi:10.1109/TIM.2019.2958471.
102. Guo, S.; Zhang, Y.; Gui, X.; Han, L. An Improved PDR/UWB Integrated System for Indoor Navigation Applications. *IEEE Sensors Journal* **2020**, *20*, 8046-8061, doi:10.1109/JSEN.2020.2981635.
103. Xu, Y.; Shmaliy, Y.S.; Ahn, C.K.; Chen, X.; Guo, H.; Zhuang, Y. Blind Robust Multi-Horizon EFIR Filter for Tightly Integrating INS and UWB. *IEEE Sensors Journal* **2021**, *21*, 23037-23045, doi:10.1109/JSEN.2021.3105566.
104. Ali, R.; Liu, R.; Nayyar, A.; Qureshi, B.; Cao, Z. Tightly Coupling Fusion of UWB Ranging and IMU Pedestrian Dead Reckoning for Indoor Localization. *IEEE Access* **2021**, *9*, 164206-164222, doi:10.1109/ACCESS.2021.3132645.
105. Kim, D.H.; Pyun, J.Y. NLOS Identification Based UWB and PDR Hybrid Positioning System. *IEEE Access* **2021**, *9*, 102917-102929, doi:10.1109/ACCESS.2021.3098416.

106. Wang, Y.; Li, X. An Improved Robust EKF Algorithm Based on Sigma Points for UWB and Foot-Mounted IMU Fusion Positioning. *Journal of Spatial Science* **2021**, *66*, 329-350, doi:10.1080/14498596.2019.1632754.
107. Xu, Y.; Cao, J.; Shmaliy, Y.S.; Zhuang, Y. Distributed Kalman Filter for UWB/INS Integrated Pedestrian Localization under Colored Measurement Noise. *Satellite Navigation* **2021**, *2*, doi:10.1186/s43020-021-00053-z.
108. Naheem, K.; Kim, M.S. A Low-Cost Foot-Placed UWB and IMU Fusion-Based Indoor Pedestrian Tracking System for IoT Applications. *Sensors* **2022**, *22*, doi:10.3390/s22218160.
109. Liu, Y.; Zhang, Y.; Jiang, Y.; Liu, W.; Yang, F. UWB-INS Fusion Positioning Based on a Two-Stage Optimization Algorithm. *Tehnicki Vjesnik* **2023**, *30*, 185-190, doi:10.17559/TV-20221019035741.
110. Tian, Q.; Wang, K.I.K.; Salcic, Z. An INS and UWB Fusion Approach with Adaptive Ranging Error Mitigation for Pedestrian Tracking. *IEEE Sensors Journal* **2020**, *20*, 4372-4381, doi:10.1109/JSEN.2020.2964287.
111. Lian Sang, C.; Adams, M.; Hormann, T.; Hesse, M.; Pormann, M.; Ruckert, U. Numerical and Experimental Evaluation of Error Estimation for Two-Way Ranging Methods. *Sensors (Basel)* **2019**, *19*, doi:10.3390/s19030616.
112. Mazhar, F.; Khan, M.G.; Sällberg, B. Precise Indoor Positioning Using UWB: A Review of Methods, Algorithms and Implementations. *Wireless Personal Communications* **2017**, *97*, 4467-4491, doi:10.1007/s11277-017-4734-x.
113. Barker, S.; Craik, R.; Freedman, W.; Herrmann, N.; Hillstrom, H. Accuracy, Reliability, and Validity of a Spatiotemporal Gait Analysis System. *Medical Engineering & Physics* **2006**, *28*, 460-467, doi:10.1016/j.medengphy.2005.07.017.
114. Volpi, A.; Tebaldi, L.; Matrella, G.; Montanari, R.; Bottani, E. Low-Cost UWB Based Real-Time Locating System: Development, Lab Test, Industrial Implementation and Economic Assessment. *Sensors (Basel)* **2023**, *23*, doi:10.3390/s23031124.
115. Li, J.; Xue, J.; Fu, D.; Gui, C.; Wang, X. Position Estimation and Error Correction of Mobile Robots Based on UWB and Multisensors. *Journal of Sensors* **2022**, *2022*, doi:doi:10.1155/2022/7071466.
116. Waqar, A.; Ahmad, I.; Habibi, D.; Phung, Q.V. A range error reduction technique for positioning applications in sports. *The Journal of Engineering* **2021**, *2021*, 73-84, doi:10.1049/tje2.12010.
117. Otím, T.; Bahillo, A.; Díez, L.E.; Lopez-Iturri, P.; Falcone, F. Impact of Body Wearable Sensor Positions on UWB Ranging. *IEEE Sensors Journal* **2019**, *19*, 11449-11457, doi:10.1109/jsen.2019.2935634.
118. Otím, T.; Díez, L.E.; Bahillo, A.; Lopez-Iturri, P.; Falcone, F. Effects of the Body Wearable Sensor Position on the UWB Localization Accuracy. *Electronics* **2019**, *8*, doi:10.3390/electronics8111351.
119. Yogesh, V.; Buurke, J.H.; Veltink, P.H.; Baten, C.T.M. Integrated UWB/MIMU Sensor System for Position Estimation towards an Accurate Analysis of Human Movement: A Technical Review. *Sensors* **2023**, *23*, doi:10.3390/s23167277.

120. Naheem, K.; Kim, M.S. A Robust Indoor Pedestrian Localization Approach Against Human Body Shadowing for UWB-Enabled Smartphones. *IEEE Transactions on Instrumentation and Measurement* **2024**, *73*, 1-13, doi:10.1109/tim.2024.3368497.
121. Feng, D.; Peng, J.; Zhuang, Y.; Guo, C.; Zhang, T.; Chu, Y.; Zhou, X.; Xia, X.-G. An Adaptive IMU/UWB Fusion Method for NLOS Indoor Positioning and Navigation. *IEEE Internet of Things Journal* **2023**, *10*, 11414-11428, doi:10.1109/jiot.2023.3245144.
122. De Cock, C.; Tanghe, E.; Joseph, W.; Plets, D. Robust IMU-Based Mitigation of Human Body Shadowing in UWB Indoor Positioning. *Sensors (Basel)* **2023**, *23*, doi:10.3390/s23198289.
123. Jie, H.; Yishuang, G.; Pahlavan, K. Toward Accurate Human Tracking: Modeling Time-of-Arrival for Wireless Wearable Sensors in Multipath Environment. *IEEE Sensors Journal* **2014**, *14*, 3996-4006, doi:10.1109/jsen.2014.2356857.
124. Haggenmiller, A.; Krogius, M.; Olson, E. Non-parametric Error Modeling for Ultra-wideband Localization Networks. In Proceedings of the 2019 International Conference on Robotics and Automation (ICRA), Montreal, Canada, 20/05/2019, 2019; pp. 2568-2574.
125. Chen, J.; Ye, Y.; Pahlavan, K. UWB characteristics of creeping wave for RF localization around the human body. In Proceedings of the 2012 IEEE 23rd International Symposium on Personal, Indoor and Mobile Radio Communications-(PIMRC), 2012; pp. 1290-1294.
126. Wang, F.; Tang, H.; Chen, J. Survey on NLOS Identification and Error Mitigation for UWB Indoor Positioning. *Electronics* **2023**, *12*, doi:10.3390/electronics12071678.
127. Nkrow, R.E.; Silva, B.; Boshoff, D.; Hancke, G.; Gidlund, M.; Abu-Mahfouz, A. NLOS Identification and Mitigation for Time-based Indoor Localization Systems: Survey and Future Research Directions. *ACM Computing Surveys* **2024**, doi:10.1145/3663473.
128. Barbieri, L.; Brambilla, M.; Trabattoni, A.; Mervic, S.; Nicoli, M. UWB Localization in a Smart Factory: Augmentation Methods and Experimental Assessment. *IEEE Transactions on Instrumentation and Measurement* **2021**, *70*, 1-18, doi:10.1109/tim.2021.3074403.
129. Nam, S.-C.; Choi, H.-B.; Ko, Y.-B. On mitigation of ranging errors for through-the-body NLOS conditions using convolutional neural networks. In Proceedings of the 2022 24th International Conference on Advanced Communication Technology (ICACT), 2022; pp. 141-144.
130. Zhu, J.; Kia, S.S. *UWB ranging aided pedestrian geolocation with GPB-based Filtering for LoS and NLoS Measurement processing*; University of California Irvine, Mechanical and Aerospace Eng. Dept. of Univ. of California, Irvine, CA 92697, United States, 2020; pp. 781-787.
131. Zhu, J.N.; Kia, S.S. Bias Compensation for UWB Ranging for Pedestrian Geolocation Applications. *IEEE SENSORS LETTERS* **2019**, *3*, doi:10.1109/LENS.2019.2936007.
132. Sung, S.; Kim, H.; Jung, J.-I. Accurate Indoor Positioning for UWB-Based Personal Devices Using Deep Learning. *IEEE Access* **2023**, *11*, 20095-20113, doi:10.1109/access.2023.3250180.
133. De Cock, C.; Tanghe, E.; Joseph, W.; Plets, D. Semi-Unsupervised Mitigation of Human Body Shadowing for Indoor UWB pedestrian tracking. In Proceedings of the 2023 13th International Conference on Indoor Positioning and Indoor Navigation (IPIN), 2023; pp. 1-7.
134. Hamie, J.; Denis, B.; D'Errico, R.; Richard, C. On-body TOA-based ranging error model for motion capture applications within wearable UWB networks. *Journal of Ambient Intelligence and Humanized Computing* **2013**, *6*, 603-612, doi:10.1007/s12652-013-0215-6.

135. Smaoui, N.; Gnawali, O.; Kim, K. Study and Mitigation of Platform Related UWB Ranging Errors. In Proceedings of the International Conference on COMMunication Systems & NETWORKS (COMSNETS), 2020; pp. 346-353.
136. Kılıc, Y.; Ali, A.J.; Meijerink, A.; Bentum, M.J.; Scanlon, W.G. The effect of human-body shadowing on indoor UWB TOA-based ranging systems. In Proceedings of the 9th Workshop on Positioning, Navigation and Communication, 2012; pp. 126-130.
137. Neiryneck, D.; Luk, E.; McLaughlin, M. An Alternative Double-Sided Two-Way Ranging Method. In Proceedings of the 2016 13th workshop on positioning, navigation and communications (WPNC), 2016; pp. 1-4.
138. APS014 Application Note, Antenna Delay Calibration of DW1000-Based Products and Systems. Available online: <https://www.gorvo.com/products/d/da008449> (accessed on June 25, 2023).
139. DWM1000 Data Sheet. Available online: <https://www.gorvo.com/products/p/DWM1000#documents> (accessed on March 20, 2024).
140. Schmid, L.; Salido-Monz' u, D.; Wieser, A. Accuracy Assessment and Learned Error Mitigation of UWB ToF Ranging. *2019 International Conference on Indoor Positioning and Indoor Navigation (IPIN) 2019*, 1-8.
141. Schön, T.B.; Hol, J.D.; Kok, M. Using Inertial Sensors for Position and Orientation Estimation. *Foundations and Trends® in Signal Processing* **2017**, *11*, 1-153, doi:10.1561/2000000094.
142. De Preter, A.; Goysens, G.; Anthonis, J.; Swevers, J.; Pipeleers, G. Range Bias Modeling and Autocalibration of an UWB Positioning System. In Proceedings of the 2019 International Conference on Indoor Positioning and Indoor Navigation (IPIN), Pisa, Italy, 2019; pp. 1-8.
143. Shalaby, M.A.; Cossette, C.C.; Forbes, J.R.; Ny, J.L. Calibration and Uncertainty Characterization for Ultra-Wideband Two-Way-Ranging Measurements. In Proceedings of the 2023 IEEE International Conference on Robotics and Automation (ICRA), London, United Kingdom, 2023; pp. 4128-4134.
144. Shah, S.; Chaiwong, K.; Kovavisaruch, L.-O.; Kaemarungsi, K.; Demeechai, T. Antenna Delay Calibration of UWB Nodes. *IEEE Access* **2021**, *9*, 63294-63305, doi:10.1109/access.2021.3075448.
145. Cano, J.; Pages, G.; Chaumette, E.; LeNy, J. Clock and Power-Induced Bias Correction for UWB Time-of-Flight Measurements. *IEEE Robotics and Automation Letters* **2022**, *7*, 2431-2438, doi:10.1109/lra.2022.3143202.
146. Sidorenko, J.; Schatz, V.; Scherer-Negenborn, N.; Arens, M.; Hugentobler, U. Decawave UWB Clock Drift Correction and Power Self-Calibration. *Sensors (Basel)* **2019**, *19*, doi:10.3390/s19132942.
147. Alavi, B.; Pahlavan, K. Modeling of the TOA-based distance measurement error using UWB indoor radio measurements. *IEEE communications letters* **2006**, *10*, 275-277, doi:10.1109/LCOMM.2006.1613745.
148. Cheraghinia, M.; Shahid, A.; Luchie, S.; Gordebeke, G.-J.; Caytan, O.; Fontaine, J.; Herbruggen, B.V.; Lemey, S.; Poorter, E.D. A Comprehensive Overview on UWB Radar: Applications, Standards, Signal Processing Techniques, Datasets, Radio Chips, Trends and Future Research Directions. *IEEE Communications Surveys & Tutorials* **2024**, 1-1, doi:10.1109/comst.2024.3488173.

149. Hapsari, G.I.; Munadi, R.; Erfianto, B.; Irawati, I.D. Future Research and Trends in Ultra-Wideband Indoor Tag Localization. *IEEE Access* **2024**, *1*-1, doi:10.1109/access.2024.3399476.
150. Zafari, F.; Gkelias, A.; Leung, K.K. A Survey of Indoor Localization Systems and Technologies. *IEEE Communications Surveys & Tutorials* **2019**, *21*, 2568-2599, doi:10.1109/comst.2019.2911558.
151. Lyu, Y.; Wei, M.; Li, S.; Wang, D. A fusion positioning system with environmental-adaptive algorithm: IPSO-IAUKF fusion of UWB and IMU for NLOS noise mitigation. *Measurement: Sensors* **2025**, *38*, doi:10.1016/j.measen.2025.101864.
152. Cheng, L.; Fu, Z. An adaptive Kalman filter loosely coupled indoor fusion positioning system based on inertial navigation system and ultra-wide band. *Measurement* **2025**, *244*, doi:10.1016/j.measurement.2024.116412.
153. Wang, X.; Gao, F.; Huang, J.; Xue, Y. UWB/LiDAR Tightly Coupled Positioning Algorithm Based on ISSA Optimized Particle Filter. *IEEE Sensors Journal* **2024**, *24*, 11217-11228, doi:10.1109/jsen.2024.3366941.
154. Xu, Y.; Chen, Z.; Zhao, M.; Tang, F.; Li, Y.; Liu, J.; Kato, N. UVtrack: Multi-Modal Indoor Seamless Localization Using Ultra-Wideband Communication and Vision Sensors. *IEEE Open Journal of the Computer Society* **2025**, *6*, 272-281, doi:10.1109/ojcs.2025.3531442.
155. Al-Okby, M.F.R.; Junginger, S.; Roddelkopf, T.; Thurow, K. UWB-Based Real-Time Indoor Positioning Systems: A Comprehensive Review. *Applied Sciences* **2024**, *14*, doi:10.3390/app142311005.
156. Yogesh, V.; Grevinga, L.; Voort, C.; Buurke, J.H.; Veltink, P.H.; Baten, C.T.M. Novel calibration method for improved UWB sensor distance measurement in the context of application for 3D analysis of human movement. *Engineering Science and Technology, an International Journal* **2024**, *58*, doi:10.1016/j.jestch.2024.101844.
157. Sang, C.L.; Adams, M.; Hesse, M.; Hörmann, T.; Korthals, T.; Rückert, U. A comparative study of UWB-based true-range positioning algorithms using experimental data. In Proceedings of the 2019 16th Workshop on Positioning, Navigation and Communications (WPNC), 2019; pp. 1-6.
158. Sahinoglu, Z.; Gezici, S.; Güvenc, I. *Ultra-wideband positioning systems: theoretical limits, ranging algorithms, and protocols*; Cambridge university press: 2008.
159. Jing, L.; Zhang, J.-F. LS-Based Parameter Estimation of DARMA Systems with Uniformly Quantized Observations. *Journal of Systems Science and Complexity* **2021**, *35*, 748-765, doi:10.1007/s11424-021-0314-y.
160. Shu, B.; Li, C.; Wang, H.; Li, H. An Improved Chan-Taylor Hybrid Location Algorithm Based on UWB. In Proceedings of the 2024 6th International Conference on Electronic Engineering and Informatics (EEI), 2024; pp. 1783-1789.
161. Han, H.; Wang, J.; Liu, F.; Zhang, J.; Yang, D.; Li, B. An Emergency Seamless Positioning Technique Based on ad hoc UWB Networking Using Robust EKF. *Sensors (Basel)* **2019**, *19*, doi:10.3390/s19143135.
162. Liu, A.; Wang, J.; Lin, S.; Kong, X. A Dynamic UKF-Based UWB/Wheel Odometry Tightly Coupled Approach for Indoor Positioning. *Electronics* **2024**, *13*, doi:10.3390/electronics13081518.
163. Fontaine, J.; Che, F.; Shahid, A.; Van Herbruggen, B.; Ahmed, Q.Z.; Bin Abbas, W.; De Poorter, E. Transfer Learning for UWB Error Correction and (N)LOS Classification in Multiple

- Environments. *IEEE Internet of Things Journal* **2024**, *11*, 4085-4101, doi:10.1109/jiot.2023.3299319.
164. Waqar, A.; Ahmad, I.; Habibi, D.; Phung, Q.V. Analysis of GPS and UWB positioning system for athlete tracking. *Measurement: Sensors* **2021**, *14*, doi:10.1016/j.measen.2020.100036.
165. Guo, H.; Li, M.; Zhang, X.; Gao, X.; Liu, Q. UWB indoor positioning optimization algorithm based on genetic annealing and clustering analysis. *Front Neurobot* **2022**, *16*, 715440, doi:10.3389/fnbot.2022.715440.
166. Cretu-Sircu, A.L.; Schioler, H.; Cederholm, J.P.; Sircu, I.; Schjorring, A.; Larrad, I.R.; Berardinelli, G.; Madsen, O. Evaluation and Comparison of Ultrasonic and UWB Technology for Indoor Localization in an Industrial Environment. *Sensors (Basel)* **2022**, *22*, doi:10.3390/s22082927.
167. Cho, J.; Jeong, S.; Lee, B. A Study on Anchor Placement and 3D Positioning Algorithm for UWB Application in Small Sites. *KSCE Journal of Civil Engineering* **2024**, *28*, 4575-4587, doi:10.1007/s12205-024-2107-z.
168. Zhao, M.; Chang, T.; Arun, A.; Ayyalasomayajula, R.; Zhang, C.; Bharadia, D. ULoc. *Proceedings of the ACM on Interactive, Mobile, Wearable and Ubiquitous Technologies* **2021**, *5*, 1-31, doi:10.1145/3478124.
169. Zhou, N.; Si, M.; Li, D.; Seow, C.K.; Mi, J. An Indoor UWB 3D Positioning Method for Coplanar Base Stations. *Sensors (Basel)* **2022**, *22*, doi:10.3390/s22249634.
170. Nocedal, J.; Wright, S.J. Numerical optimization. **2006**.
171. Yogesh, V.; Rook, J.W.A.; Keizers, T.; Voort, C.; Buurke, J.H.; Veltink, P.H.; Baten, C.T.M. UWB distance estimation errors in (non-)line of sight situations within the context of 3D analysis of human movement. *Engineering Research Express* **2024**, *6*, doi:10.1088/2631-8695/ad7e7e.
172. Guo, H.; Song, S.; Yin, H.; Ren, D.; Zhu, X. Optimization of UWB indoor positioning based on hardware accelerated Fuzzy ISODATA. *Sci Rep* **2024**, *14*, 17985, doi:10.1038/s41598-024-68998-0.
173. Huang, Y.; Cao, B.; Wang, A. Design a novel algorithm for enhancing UWB positioning accuracy in GPS denied environments. *Sci Rep* **2024**, *14*, 23895, doi:10.1038/s41598-024-74773-y.
174. Favata, A.; Gallart-Agut, R.; Pàmies-Vilà, R.; Torras, C.; Font-Llagunes, J.M. IMU-Based Systems for Upper-Limb Kinematic Analysis in Clinical Applications: A Systematic Review. *IEEE Sensors Journal* **2024**, *24*, 28576-28594, doi:10.1109/jsen.2024.3436532.
175. van Amstel, R.N.; Dijk, I.E.; Noten, K.; Weide, G.; Jaspers, R.T.; Pool-Goudzwaard, A.L. Wireless inertial measurement unit-based methods for measuring lumbopelvic-hip range of motion are valid compared with optical motion capture as golden standard. *Gait Posture* **2025**, *120*, 72-80, doi:10.1016/j.gaitpost.2025.04.003.
176. Liu, S.; Zhang, J.; Zhang, Y.; Zhu, R. A wearable motion capture device able to detect dynamic motion of human limbs. *Nat Commun* **2020**, *11*, 5615, doi:10.1038/s41467-020-19424-2.
177. Gastaldi, L.; Digo, E. Recent Advance and Application of Wearable Inertial Sensors in Motion Analysis. *Sensors (Basel)* **2025**, *25*, doi:10.3390/s25030818.
178. Prisco, G.; Pirozzi, M.A.; Santone, A.; Esposito, F.; Cesarelli, M.; Amato, F.; Donisi, L. Validity of Wearable Inertial Sensors for Gait Analysis: A Systematic Review. *Diagnostics (Basel)* **2024**, *15*, doi:10.3390/diagnostics15010036.

179. Caruso, M.; Sabatini, A.M.; Laidig, D.; Seel, T.; Knaflitz, M.; Della Croce, U.; Cereatti, A. Analysis of the Accuracy of Ten Algorithms for Orientation Estimation Using Inertial and Magnetic Sensing under Optimal Conditions: One Size Does Not Fit All. *Sensors (Basel)* **2021**, *15*, doi:10.3390/s21072543.
180. Khairi, N.; Rahman, A.; bin Abdulrahim, K. A REVIEW OF CURRENT TREND IN INDOOR PEDESTRIAN NAVIGATION. *Journal of Engineering and Technology (JET)* **2024**, *15*, 59–82, doi:10.54554/jet.2024.15.2.004.
181. Wang, Q.; Fu, M.; Wang, J.; Luo, H.; Sun, L.; Ma, Z.; Li, W.; Zhang, C.; Huang, R.; Li, X.; et al. Recent Advances in Pedestrian Inertial Navigation Based on Smartphone: A Review. *IEEE Sensors Journal* **2022**, *22*, 22319–22343, doi:10.1109/jsen.2022.3213836.
182. Elsanhoury, M.; Makela, P.; Koljonen, J.; Valisuo, P.; Shamsuzzoha, A.; Mantere, T.; Elmusrati, M.; Kuusniemi, H. Precision Positioning for Smart Logistics Using Ultra-Wideband Technology-Based Indoor Navigation: A Review. *IEEE Access* **2022**, *10*, 44413–44445, doi:10.1109/access.2022.3169267.
183. Skog, I.; Handel, P. In-Car Positioning and Navigation Technologies—A Survey. *IEEE Transactions on Intelligent Transportation Systems* **2009**, *10*, 4–21, doi:10.1109/tits.2008.2011712.
184. Gustafsson, F. *Statistical Sensor Fusion*, Third Edition ed.; Studentlitteratur: Lund, 2010.
185. Irmischer, I.J.; Clarke, K.C. Measuring and modeling the speed of human navigation. *Cartography and Geographic Information Science* **2017**, *45*, 177–186, doi:10.1080/15230406.2017.1292150.
186. Aristizabal Pla, G.; Martini, D.N.; Potter, M.V.; Hoogkamer, W. Assessing the validity of the zero-velocity update method for sprinting speeds. *PLoS One* **2024**, *19*, e0288896, doi:10.1371/journal.pone.0288896.
187. Ghattas, J.; Jarvis, D.N. Validity of inertial measurement units for tracking human motion: a systematic review. *Sports Biomech* **2024**, *23*, 1853–1866, doi:10.1080/14763141.2021.1990383.
188. Guo, L.; Xiong, S. Accuracy of Base of Support Using an Inertial Sensor Based Motion Capture System. *Sensors (Basel)* **2017**, *17*, doi:10.3390/s17092091.
189. Mohamed Refai, M.I.; van Beijnum, B.F.; Buurke, J.H.; Veltink, P.H. Portable Gait Lab: Tracking Relative Distances of Feet and CoM Using Three IMUs. *IEEE Trans Neural Syst Rehabil Eng* **2020**, *28*, 2255–2264, doi:10.1109/TNSRE.2020.3018158.
190. Zhou, H.; Stone, T.; Hu, H.; Harris, N. Use of multiple wearable inertial sensors in upper limb motion tracking. *Med Eng Phys* **2008**, *30*, 123–133, doi:10.1016/j.medengphy.2006.11.010.
191. Anderson, B.; Shi, M.; Tan, V.Y.F.; Wang, Y. Mobile Gait Analysis Using Foot-Mounted UWB Sensors. *Proceedings of the ACM on Interactive, Mobile, Wearable and Ubiquitous Technologies* **2019**, *3*, 1–22, doi:10.1145/3351231.
192. Berner, K.; Cockcroft, J.; Louw, Q. Kinematics and temporospatial parameters during gait from inertial motion capture in adults with and without HIV: a validity and reliability study. *Biomed Eng Online* **2020**, *19*, 57, doi:10.1186/s12938-020-00802-2.
193. Fehr, K.H.; Bartloff, J.N.; Wang, Y.; Hetzel, S.; Adamczyk, P.G. Estimation of minimum foot clearance using a single foot-mounted inertial sensor and personalized foot geometry scan. *Sci Rep* **2024**, *14*, 13640, doi:10.1038/s41598-024-63124-6.

194. Germanotta, M.; Mileti, I.; Conforti, I.; Del Prete, Z.; Aprile, I.; Palermo, E. Estimation of Human Center of Mass Position through the Inertial Sensors-Based Methods in Postural Tasks: An Accuracy Evaluation. *Sensors (Basel)* **2021**, *21*, doi:10.3390/s21020601.
195. Kavanagh, J.J.; Menz, H.B. Accelerometry: a technique for quantifying movement patterns during walking. *Gait Posture* **2008**, *28*, 1-15, doi:10.1016/j.gaitpost.2007.10.010.
196. Tesio, L.; Rota, V. The Motion of Body Center of Mass During Walking: A Review Oriented to Clinical Applications. *Front Neurol* **2019**, *10*, 999, doi:10.3389/fneur.2019.00999.
197. Damavandi, M.; Farahpour, N.; Allard, P. Determination of body segment masses and centers of mass using a force plate method in individuals of different morphology. *Med Eng Phys* **2009**, *31*, 1187-1194, doi:10.1016/j.medengphy.2009.07.015.
198. Rossanigo, R.; Caruso, M.; Bertuletti, S.; Deriu, F.; Knaflitz, M.; Della Croce, U.; Cereatti, A. Base of Support, Step Length and Stride Width Estimation during Walking Using an Inertial and Infrared Wearable System. *Sensors (Basel)* **2023**, *23*, doi:10.3390/s23083921.
199. Osoba, M.Y.; Rao, A.K.; Agrawal, S.K.; Lalwani, A.K. Balance and gait in the elderly: A contemporary review. *Laryngoscope Investig Otolaryngol* **2019**, *4*, 143-153, doi:10.1002/lio2.252.
200. McAndrew Young, P.M.; Dingwell, J.B. Voluntary changes in step width and step length during human walking affect dynamic margins of stability. *Gait Posture* **2012**, *36*, 219-224, doi:10.1016/j.gaitpost.2012.02.020.
201. Warmerdam, E.; Wolff, C.; Orth, M.; Pohlemann, T.; Ganse, B. Long-term continuous instrumented insole-based gait analyses in daily life have advantages over longitudinal gait analyses in the lab to monitor healing of tibial fractures. *Front Bioeng Biotechnol* **2024**, *12*, 1355254, doi:10.3389/fbioe.2024.1355254.
202. Peters, D.M.; O'Brien, E.S.; Kamrud, K.E.; Roberts, S.M.; Rooney, T.A.; Thibodeau, K.P.; Balakrishnan, S.; Gell, N.; Mohapatra, S. Utilization of wearable technology to assess gait and mobility post-stroke: a systematic review. *J Neuroeng Rehabil* **2021**, *18*, 67, doi:10.1186/s12984-021-00863-x.
203. Mesquita, I.A.; Fonseca, P.F.P.d.; Pinheiro, A.R.V.; Velhote Correia, M.F.P.; Silva, C.I.C.d. Methodological considerations for kinematic analysis of upper limbs in healthy and poststroke adults Part II: a systematic review of motion capture systems and kinematic metrics. *Topics in Stroke Rehabilitation* **2019**, *26*, 464-472.
204. Held, J.P.O.; Klaassen, B.; Eenhoorn, A.; van Beijnum, B.F.; Buurke, J.H.; Veltink, P.H.; Luft, A.R. Inertial Sensor Measurements of Upper-Limb Kinematics in Stroke Patients in Clinic and Home Environment. *Front Bioeng Biotechnol* **2018**, *6*, 27, doi:10.3389/fbioe.2018.00027.
205. Schwartz, M.H.; Ries, A.J.; Georgiadis, A.G.; Kainz, H. Demonstrating the utility of Instrumented Gait Analysis in the treatment of children with cerebral palsy. *PLoS One* **2024**, *19*, e0301230, doi:10.1371/journal.pone.0301230.
206. Cano-de-la-Cuerda, R.; Vela-Desojo, L.; Moreno-Verdu, M.; Ferreira-Sanchez, M.D.R.; Macias-Macias, Y.; Miangolarra-Page, J.C. Trunk Range of Motion Is Related to Axial Rigidity, Functional Mobility and Quality of Life in Parkinson's Disease: An Exploratory Study. *Sensors (Basel)* **2020**, *20*, doi:10.3390/s20092482.
207. Saes, M.; Mohamed Refai, M.I.; van Beijnum, B.J.F.; Bussmann, J.B.J.; Jansma, E.P.; Veltink, P.H.; Buurke, J.H.; van Wegen, E.E.H.; Meskers, C.G.M.; Krakauer, J.W.; et al. Quantifying

- Quality of Reaching Movements Longitudinally Post-Stroke: A Systematic Review. *Neurorehabilitation and Neural Repair* **2022**, *36*, 183-207, doi:10.1177/15459683211062890.
208. Lin, Y.T.; Lee, H.J. Comparison of the Lower Extremity Kinematics and Center of Mass Variations in Sit-to-Stand and Stand-to-Sit Movements of Older Fallers and Nonfallers. *Arch Rehabil Res Clin Transl* **2022**, *4*, 100181, doi:10.1016/j.arrct.2022.100181.
209. He, J.; Liu, D.; Hou, M.; Luo, A.; Wang, S.; Ma, Y. Analysis of inter-joint coordination during the sit-to-stand and stand-to-sit tasks in stroke patients with hemiplegia. *BMC Sports Sci Med Rehabil* **2023**, *15*, 104, doi:10.1186/s13102-023-00716-1.
210. Felius, R.A.W.; Wouda, N.C.; Geerars, M.; Bruijn, S.M.; van Dieen, J.H.; Punt, M. Beyond gait speed: exploring the added value of Inertial Measurement Unit-based measurements of gait in the estimation of the walking ability in daily life. *BMC Neurol* **2024**, *24*, 129, doi:10.1186/s12883-024-03632-0.
211. Tamburini, P.; Storm, F.; Buckley, C.; Bisi, M.C.; Stagni, R.; Mazza, C. Moving from laboratory to real life conditions: Influence on the assessment of variability and stability of gait. *Gait Posture* **2018**, *59*, 248-252, doi:10.1016/j.gaitpost.2017.10.024.
212. Lockhart, T.E.; Soangra, R.; Yoon, H.; Wu, T.; Frames, C.W.; Weaver, R.; Roberto, K.A. Prediction of fall risk among community-dwelling older adults using a wearable system. *Sci Rep* **2021**, *11*, 20976, doi:10.1038/s41598-021-00458-5.
213. Jafleh, E.A.; Alnaqbi, F.A.; Almaeeni, H.A.; Faqeeh, S.; Alzaabi, M.A.; Al Zaman, K. The Role of Wearable Devices in Chronic Disease Monitoring and Patient Care: A Comprehensive Review. *Cureus* **2024**, *16*, e68921, doi:10.7759/cureus.68921.
214. Dal Farra, F.; Castiglia, S.F.; Buzzi, M.G.; Brasiliano, P.; De Angelis, S.; Paolucci, G.; Vasta, S.; Marangon, G.; Orejel Bustos, A.S.; Bergamini, E.; et al. Test-Retest Reliability and Minimal Detectable Changes for Wearable Sensor-Derived Gait Stability, Symmetry, and Smoothness in Individuals with Severe Traumatic Brain Injury. *Sensors (Basel)* **2025**, *25*, doi:10.3390/s25061764.
215. Loukovitis, A.; Ziagkas, E.; Zekakos, D.X.; Petrelis, A.; Grouios, G. Test-Retest Reliability of PODOSmart((R)) Gait Analysis Insoles. *Sensors (Basel)* **2021**, *21*, doi:10.3390/s21227532.
216. Posada-Ordax, J.; Cosin-Matamoros, J.; Losa-Iglesias, M.E.; Becerro-de-Bengoa-Vallejo, R.; Esteban-Gonzalo, L.; Martin-Villa, C.; Calvo-Lobo, C.; Rodriguez-Sanz, D. Accuracy and Repeatability of Spatiotemporal Gait Parameters Measured with an Inertial Measurement Unit. *J Clin Med* **2021**, *10*, doi:10.3390/jcm10091804.
217. Porciuncula, F.; Roto, A.V.; Kumar, D.; Davis, I.; Roy, S.; Walsh, C.J.; Awad, L.N. Wearable Movement Sensors for Rehabilitation: A Focused Review of Technological and Clinical Advances. *PM R* **2018**, *10*, S220-S232, doi:10.1016/j.pmrj.2018.06.013.
218. Colyer, S.L.; Evans, M.; Cosker, D.P.; Salo, A.I.T. A Review of the Evolution of Vision-Based Motion Analysis and the Integration of Advanced Computer Vision Methods Towards Developing a Markerless System. *Sports Med Open* **2018**, *4*, 24, doi:10.1186/s40798-018-0139-y.
219. Digo, E.; Pastorelli, S.; Gastaldi, L. A Narrative Review on Wearable Inertial Sensors for Human Motion Tracking in Industrial Scenarios. *Robotics* **2022**, *11*, doi:10.3390/robotics11060138.
220. Chen, S.; Yin, D.; Niu, Y. A Survey of Robot Swarms' Relative Localization Method. *Sensors (Basel)* **2022**, *22*, doi:10.3390/s22124424.

221. Sidiropoulos, A.; Bechtsis, D.; Vlachos, D. Implementing an Industry 4.0 UWB-Based Real-Time Locating System for Optimized Tracking. *Applied Sciences* **2025**, *15*, doi:10.3390/app15052689.
222. Amala Arokia Nathan, R.J.; Kurmi, I.; Bimber, O. Drone swarm strategy for the detection and tracking of occluded targets in complex environments. *Communications Engineering* **2023**, *2*, doi:10.1038/s44172-023-00104-0.
223. Xu, N.; Guan, M.; Wen, C. A survey on Ultra Wide Band based localization for mobile autonomous machines. *Journal of Automation and Intelligence* **2025**, doi:10.1016/j.jai.2025.02.001.
224. Xianjia, Y.; Qingqing, L.; Queralt, J.P.; Heikkonen, J.; Westerlund, T. Applications of UWB networks and positioning to autonomous robots and industrial systems. In Proceedings of the 2021 10th Mediterranean Conference on Embedded Computing (MECO), 2021; pp. 1-6.
225. Ji, P.; Duan, Z.; Xu, W. A Combined UWB/IMU Localization Method with Improved CKF. *Sensors (Basel)* **2024**, *24*, doi:10.3390/s24103165.
226. Yang, W.; Wang, J.; Zhao, Z.; Cui, Y. Accuracy of an Ultra-Wideband-Based Tracking System for Time-Motion Analysis in Tennis. *Sensors (Basel)* **2025**, *25*, doi:10.3390/s25041031.
227. Hewett, T.E.; Myer, G.D.; Ford, K.R.; Heidt, R.S., Jr.; Colosimo, A.J.; McLean, S.G.; van den Bogert, A.J.; Paterno, M.V.; Succop, P. Biomechanical measures of neuromuscular control and valgus loading of the knee predict anterior cruciate ligament injury risk in female athletes: a prospective study. *Am J Sports Med* **2005**, *33*, 492-501, doi:10.1177/0363546504269591.
228. Routhier, F.; Duclos, N.C.; Lacroix, E.; Lettre, J.; Turcotte, E.; Hamel, N.; Michaud, F.; Duclos, C.; Archambault, P.S.; Bouyer, L.J. Clinicians' perspectives on inertial measurement units in clinical practice. *PLoS One* **2020**, *15*, e0241922, doi:10.1371/journal.pone.0241922.
229. Zou, A.; Hu, W.; Luo, Y.; Jiang, P. An Improved UWB/IMU Tightly Coupled Positioning Algorithm Study. *Sensors (Basel)* **2023**, *23*, doi:10.3390/s23135918.
230. Harradine, P.; Gates, L.; Metcalf, C.; Bowen, C. Podiatrists' views and experiences of using real time clinical gait analysis in the assessment and treatment of posterior tibial tendon dysfunction. *J Foot Ankle Res* **2021**, *14*, 42, doi:10.1186/s13047-021-00482-8.

SUMMARY

Accurate 3D analysis of human movement (3D AHM) is essential in clinical rehabilitation for understanding movement disorders, tailoring interventions, and monitoring patient progress. It provides insights into the underlying mechanisms of impairment, enabling more targeted treatments. The de facto gold standard for 3D AHM is the optical motion capture systems, which deliver sub-centimeter accuracy in laboratory environments. However, their reliance on dedicated infrastructure, high costs, time-consuming post-processing, and specialized personnel restricts them largely to research settings. In current clinical practice, movement assessment remains mostly dependent on clinical observation and functional outcome tests, which do not provide any insights into the underlying mechanism. This emphasizes the need for objective, portable, cost-effective, and reliable 3D AHM tools that can be used in real-world rehabilitation settings.

Wearable Magnetic Inertial Measurement System (MIMU)-based systems provide a portable, cost-effective, and flexible alternative. They have developed significantly in estimating segment orientations (angular kinematics), with sensor fusion algorithms providing clinically acceptable accuracy. However, their performance in position estimation (spatial kinematics) remains limited due to drift from double integration of the free acceleration. This is a critical shortcoming because many clinically relevant parameters, such as step length, base of support (BoS), center of mass (CoM) trajectory, and joint displacement, rely on accurate positioning of body segments. Therefore, addressing this limitation is important for the broader clinical adoption of wearable systems.

Although algorithmic refinements have improved position estimation performance in MIMU, advancements in algorithm optimizations are reaching their practical limits. Therefore, incorporating supplementary sensors that provide redundant positional information is seen as a promising step. In this context, integrating Ultra-Wideband (UWB) sensors with MIMU sensors offers a promising solution, specifically due to their complementary error characteristics. UWB provides drift-free absolute distance estimates, but are affected by Non-Line-of-Sight (NLOS) situations, while MIMUs are known to suffer from integration drift, but they are not affected by NLOS. These complementary error characteristics make them ideal candidates for improving position estimate quality through sensor fusion.

Though this integrated UWB/MIMU sensor shows great potential for accurate position estimation for 3D AHM applications, they have not yet been utilized for 3D AHM applications. Instead, they have been widely used only for pedestrian tracking and large-scale localization applications, which typically involve (much) larger distances than those measured between points on the body in human movement analysis applications.. Therefore, this PhD thesis focuses on the development and validation of an integrated, portable UWB/MIMU wearable system with multiple sensors in the body, tailored for use in 3D AHM applications. The scope of this work is limited to technology development alone, with specific focus on improving position estimation accuracy and exploring the integrated sensor system's feasibility for accurate and consistent position estimation in 3D AHM..

Initial feasibility exploration was done through a comprehensive review of existing research (**Chapter 2**). This review confirmed that most studies employing integrated UWB/MIMU sensor systems were focused on localization or pedestrian tracking applications, with very few exploring their application for ambulatory 3D AHM. The accuracies achieved in estimating positions were limited to the tracking applications, tested in large-scale indoor environments, and the general achieved position estimation errors so far in the existing applications were around 10 cm, with very few studies capable of achieving position estimation errors around 5 cm in controlled environments. Also, several methodological gaps were identified that limit the clinical relevance of existing integrated UWB/MIMU sensor systems. Specifically, these integrated sensor systems described in the literature were not well-characterized under conditions relevant to clinical human movement assessment. Only a few studies clearly report the systematic versus random error components in their systems, making it difficult to assess their true accuracy and reliability under varying conditions. These critical limitations motivated the development of a fully integrated UWB/MIMU sensor platform along with position estimation methods optimally suited for on-body measurement in 3D HMA applications. The nature of the impact of these limitations on position estimation with UMIMUs is central to the subsequent studies in this research.

The fully integrated UWB/MIMU sensor system was developed on a single physical platform, named the UMIMU sensor system. The MIMU sensors in the UMIMU sensor system were well studied and have been extensively validated for 3D AHM

applications, unlike the UWB sensor technology. Therefore, systematic experiments were conducted to evaluate and characterize the distance estimation using only the UWB of the UMIMU sensor system, specifically in the context of 3D AHM application settings (**Chapter 3**). This study examined the behavior of UWB in static and dynamic measurements under Line-of-sight (LOS) conditions, as well as measurements under NLOS situations caused by (simulated) human body segments, all under the relevant 3D AHM settings. The evaluation indicated significant residual bias errors of around 6 cm that persisted in the UWB distance measurement, even after applying the factory-recommended antenna delay calibration procedure, as previously reported in the literature. It was observed that the NLOS conditions caused by human segments led to systematic overestimations, particularly when larger segments (e.g., trunk) were involved. These effects were repeatable, suggesting the potential for error modeling and mitigation in future fusion algorithms. In addition, optimal sensor placement and orientation on the human body were identified for better distance measurement in **Chapter 3**, based on the sensor behavior analysis.

The findings on the presence of significant systematic errors in the distance measurement, even after applying the recommended antenna delay calibration procedure, indicated a need for an additional ranging calibration procedure. In **Chapter 4**, a novel generalizable calibration procedure was developed, namely, the Distance-Bias Calibration method. This Distance-Bias Calibration method applied a non-linear optimization model assuming the existence of a sensor-specific bias error component contributing to the bias error in all distance estimates in which a sensor is participating. This calibration procedure also provided data on the effective sensor center location within the sensor node casing, between which the distance was estimated. Experimental validation showed that systematic distance errors could be reduced to sub-centimeter levels (≤ 0.5 cm), representing a significant advancement over previously reported UWB calibration results. The distance-bias calibration method focuses exclusively on systematic errors, and the random error components remain unchanged.

In the next step, position estimation using the UMIMU system based on the optimized UWB distance measurements was investigated. Published methods for position estimation using UWB sensors primarily rely on distance measurements in

a star topology (**Chapter 2**). Existing position estimation algorithms estimate positions based on geometric relationships between the fixed anchors and the mobile tag, with algorithms such as trilateration and least square approaches. These position estimation methods do not utilize the information on inter-node distances between all the non-fixed sensor nodes, typically available when a swarm topology is deployed. In this research, a swarm topology was implemented to fully exploit the redundant information it provides. This extra data was exploited in the position estimation through a non-linear optimization approach that utilizes all the inter-node distances for the position estimation (**Chapter 5**). The swarm optimization-based position estimation approach showed significant improvement in the position estimation accuracy when compared to the traditional trilateration-based position estimation, achieving mean position errors of 6.5 cm versus 8.8 cm for trilateration. A sensitivity analysis for position estimate errors as a function of realistic estimate error statistics provided additional insights into the performance of the proposed swarm optimization-based position estimation approach.

As a final step, this research combined the UWB data with MIMU data using a data fusion approach based on an Extended Kalman filter (EKF) called the UMIMU fusion algorithm, specifically tuned for conditions to be encountered in the intended clinical 3D AHM application (**Chapter 6**). Using synthetically generated UWB distance estimates modeled on VICON-derived reference positions and measured UWB error statistics, the proposed UMIMU fusion algorithm was validated across varying levels of bias and random errors in distance estimation. The proposed data fusion approach largely eliminated integration drift errors in the position estimates, with only minimal residual drift error remaining between the UWB updates. The resulting mean position estimation errors were around 6 cm with an SD of 3 cm, when the UWB distance measurements had less than 1 cm bias and 5 cm noise (values now achievable with the proposed distance-bias calibration method in **Chapter 4**).

The integrated system was shown to address key gaps identified in the literature by improving UWB accuracy (through calibration), enhancing the position estimation robustness (via swarm optimization), and delivering drift-free stability through sensor fusion. In **Chapter 7**, the achieved results and implications for future clinical applications in 3D HMA were discussed in terms of accuracy, consistency, and

practical integration. Although the accuracy still falls short of the benchmarks set by the gold standard, the achieved reasonable accuracy and high consistency make the system promising for future applications such as fall risk assessment, rehabilitation monitoring, and unsupervised training, which justifies further research. Priorities for follow-up research are broadly clear, and initial steps have already been taken in new projects. In addition to further improving accuracy and consistency, a key topic is investigating performance when applied to the human body, with special attention to the effects of (temporary) NLOS situations and strategies to avoid or compensate for them.

In summary, this PhD dissertation supports the feasibility of an integrated, portable UWB/MIMU sensor system for clinical 3D AHM, with consistent, drift-free position estimates. While it does not yet offer a ready-made replacement for laboratory-based 3D AHM, this study represents a significant step toward the actual implementation of wearable sensor technology in clinical practice.

SAMENVATTING

Nauwkeurige 3D-analyse van menselijke beweging (3D AHM) is essentieel in klinische revalidatie voor het begrijpen van bewegingsstoornissen, het optimaliseren van interventies en het monitoren van de voortgang van patiënten. Het biedt inzicht in de onderliggende mechanismen van beperkingen, waardoor gerichtere behandelingen mogelijk worden. De feitelijke gouden standaard voor 3D AHM zijn optische motion capture-systemen, die sub-centimeter nauwkeurigheid leveren in laboratoriumomgevingen. Hun afhankelijkheid van speciale infrastructuur, hoge kosten, tijdrovende nabewerking en gespecialiseerd personeel beperkt hun toepassing echter grotendeels tot onderzoeksomgevingen. In de huidige klinische praktijk is beoordeling van het bewegingspatroon meestal afhankelijk van klinische observatie en functionele testen, die geen inzicht geven in het onderliggende mechanisme. Dit benadrukt de noodzaak van objectieve, draagbare, kosteneffectieve en betrouwbare 3D AHM-instrumenten die kunnen worden gebruikt in revalidatieomgevingen in de echte wereld.

Op draagbare 'Magnetic Inertial Measurement Units' (MIMU) gebaseerde systemen bieden een draagbaar, kosteneffectief en flexibel alternatief. Deze kunnen met behulp van sensorfusie-algoritmen segmentoriëntaties (angulaire kinematica) voldoende accuraat schatten voor zinnige klinische applicatie. De bepaling van segment- en gewrichtspositie (ruimtelijke kinematica) wordt echter geplaagd door sterke groeiende fouten als gevolg van de benodigde dubbele integratie van de vrije versnelling ('integration drift'). Dit is een cruciale tekortkoming, omdat veel klinisch relevante parameters, zoals staplengte, 'Base of Support' (BoS), traject van het lichaamsswaartepunt of 'Center of Mass' (CoM) en gewrichtsverplaatsing, afhankelijk zijn van nauwkeurige positiebepaling van lichaamssegmenten. Daarom is het aanpakken van deze beperking belangrijk voor bredere klinische toepassing van draagbare systemen.

Hoewel algoritmische verfijningen de resultaten van positiebepaling in MIMU hebben verbeterd, bereiken optimalisaties van algoritmen hun praktische grenzen. Een potentiële oplossing vormt het integreren van aanvullende sensoren die een tweede onafhankelijke schatting van sensorpositie leveren. Een veelbelovende optie wordt gevormd door de integratie van Ultra-Wideband (UWB)-sensoren met MIMU-sensoren, met name vanwege hun complementaire foutkenmerken. UWB biedt driftvrije absolute positie-schattingen op basis van afstandsmetingen, maar

wordt verstoord in Non-Line-of-Sight (NLOS)-situaties, terwijl positieschattingen op basis van MIMU's (gebaseerd op verplaatsingsschattingen) last hebben van integratiedrift, maar geen last hebben van verstoring in NLOS situaties. Deze complementaire sterkten en zwakten maken ze ideale kandidaten om een meer nauwkeurige positieschatting te verkrijgen via sensorfusie dan met elk afzonderlijk mogelijk is.

Ondanks dit potentieel voor nauwkeurige positiebepaling bij 3D AHM-toepassingen, worden geïntegreerde UWB/MIMU-sensoren nog niet toegepast voor dergelijke doeleinden. Wel worden ze veel gebruikt voor volgsystemen voor personen en autonome voertuigen, waar het typisch gaat om (veel) grotere afstanden dan de afstanden die gemeten moeten worden tussen plekken op het lichaam in menselijke bewegingsanalyse-applicaties. Daarom richt dit proefschrift zich op de ontwikkeling en validatie van een geïntegreerd, draagbaar UWB/MIMU-systeem met meerdere sensoren op het lichaam, dat specifiek is afgestemd op toepassing in 3D AHM-toepassingen. De nadruk ligt op het realiseren van de benodigde nauwkeurigheid van (driftloze) positiebepaling en het onderzoeken van de haalbaarheid voor consistente en nauwkeurige positiebepaling in typische condities aanwezig in 3D AHM toepassingen. Dit onderzoek richt zich hiermee op het onderzoeken en ontwikkelen van de technologische mogelijkheden van UMIMU systemen binnen de condities van deze toepassing.

Allereerst werd een haalbaarheidsanalyse uitgevoerd via een uitgebreide technische literatuurstudie (**Hoofdstuk 2**). De literatuur richt zich voornamelijk op grootschalige lokalisatie- en voetgangersvolgsystemen, en onderzoekt onvoldoende de nauwkeurigheid en robuustheid onder condities die relevant zijn voor klinische 3D AHM-toepassingen (zoals korte afstanden en partiële of dynamische NLOS-situaties). Slechts enkele studies bereikten positiefouten rond de 5 cm onder gecontroleerde omstandigheden, terwijl de meeste rond de 10 cm bleven. Daarnaast werden methodologische hiaten vastgesteld die de klinische relevantie van de beschreven geïntegreerde UWB/MIMU-systemen beperken. Daarnaast rapporteerden slechts enkele studies duidelijk de structurele versus de willekeurige foutcomponenten, waardoor het moeilijk was om de werkelijke gevonden nauwkeurigheid en betrouwbaarheid te beoordelen. Deze beperkingen vormden de motivatie voor de ontwikkeling van een eigen maximaal geïntegreerd UWB/MIMU-

sensorplatform samen met positiebepalingmethoden optimaal geschikt voor meten op het lichaam in 3D AHM toepassingen. Het karakter van het effect van deze beperkingen op het schatten van positie met UMIMUs staat centraal in de diverse studies in dit onderzoek.

Het volledig geïntegreerd UWB/MIMU-sensorsysteem werd ontwikkeld op één fysiek platform, genaamd het UMIMU-sensorsysteem. De MIMU-sensoren in dit systeem zijn al veelvuldig en uitgebreid bestudeerd en gevalideerd in 3D AHM-toepassingen, dit in tegenstelling tot de (nieuwere) UWB-sensortechnologie. Daarom werden eerst systematische experimenten uitgevoerd om de afstand- en positie-schatting met de alleen UWB-componenten in het UMIMU-systeem apart te evalueren en te karakteriseren, specifiek in de context van 3D AHM toepassing (**Hoofdstuk 3**). Deze studie onderzoekt onder andere het gedrag in statische en dynamische metingen onder Line-of-Sight (LOS)-condities, evenals metingen onder NLOS-situaties veroorzaakt door (fysiek gesimuleerde) menselijke lichaamssegmenten, allemaal onder condities relevante voor 3D AHM applicaties. De evaluatie toonde aan dat er significante resterende systematische (bias) fouten van ongeveer 6 cm aanwezig waren in de UWB-afstandmetingen, zelfs na toepassing van de door de producent aanbevolen kalibratieprocedure voor het instellen van de compensatie voor de antennevertraging, zoals ook eerder in de literatuur gerapporteerd. Er werd vastgesteld dat NLOS-condities veroorzaakt door menselijke segmenten systematische overschattingen veroorzaakten, vooral bij grotere segmenten zoals de romp. Deze effecten waren herhaalbaar, wat wijst op de mogelijkheid tot foutmodellering en mitigatie in toekomstige fusie-algoritmen. Daarnaast werd in **Hoofdstuk 3** de optimale plaatsing en oriëntatie van sensoren op het lichaam geïdentificeerd voor betere afstandsmetingen, gebaseerd op sensoranalyse.

De aanwezigheid van significante systematische fouten in de afstandsmetingen, zelfs na toepassing van de aanbevolen antennevertragingkalibratie, gaf aanleiding tot de ontwikkeling van een aanvullende kalibratieprocedure. In **Hoofdstuk 4** werd een nieuwe, generaliseerbare kalibratiemethode ontwikkeld: de 'Distance-Bias Calibration'-methode. Deze methode past een niet-lineair optimalisatiemodel toe, waarbij wordt aangenomen dat er een sensor-specifieke biascomponent bestaat die bijdraagt aan de fout in alle afstandsmetingen waarin een sensor participeert. Deze

kalibratieprocedure leverde ook gegevens op over de effectieve locatie van het sensorcentrum binnen de behuizing. Dit is de locatie binnen de sensorbehuizing tussen welke de afstand werd gemeten. Experimentele validatie toonde aan dat systematische fouten in afstandsschatting konden worden teruggebracht tot sub-centimeterniveau ($\leq 0,5$ cm), wat een aanzienlijke verbetering betekent ten opzichte van eerder gerapporteerde resultaten. De voorgestelde Distance-Bias Calibration-methode richt zich uitsluitend op systematische fouten; de random foutcomponenten (schattingsruis) blijven onveranderd.

In een volgende stap werd het schatten van posities met het UMIMU-systeem op basis van de geoptimaliseerde UWB-afstandmetingen onderzocht. Gepubliceerde methoden positiebepaling op basis van UWB-sensoren maken vooral gebruik van afstandsmetingen in een ‘ster-topologie’ (**Hoofdstuk 2**). Bestaande algoritmen schatten hierbij posities op basis van geometrische relaties tussen vaste ‘anchor’-sensoren en mobiele ‘tag’-sensoren, onder gebruikmaking van algoritmen zoals trilateratie- en kleinste-kwadratenbenaderingen. Deze methoden maken geen gebruik van de informatie over onderlinge afstanden tussen alle tags, alleen van die tussen tags en anchors. Deze worden wel gebruikt bij gebruik van een ‘zwerm-topologie’. In dit onderzoek werd een zwermtopologie geïmplementeerd om maximaal gebruik te maken van de hierdoor aanwezige redundante informatie. Deze extra gegevens werden benut in de positiebepaling via een niet-lineaire optimalisatiebenadering die alle onderlinge afstanden gebruikt (**Hoofdstuk 5**). De zwerm-gebaseerde positiebepaling toonde een significante verbetering in nauwkeurigheid ten opzichte van traditionele trilateratie, met gemiddelde positiefouten van 6,5 cm versus 8,8 cm bij trilateratie. De behaalde nauwkeurigheid was ook vergelijkbaar met complexere algoritmen zoals die op basis van Kalman-filters. Een gevoeligheidsanalyse van de fouten in positieschatting als functie van realistische (op experimenten gebaseerde), synthetische gegenereerde foutcondities gaf aanvullende inzichten in de prestaties van de voorgestelde zwerm-gebaseerde positiebepaling.

Als laatste werd vervolgens positieschatting door combinatie van UWB-gegevens met MIMU-gegevens basis van datafusie met een Extended Kalman Filter (EKF), genaamd het UMIMU-fusiealgoritme, onderzocht. Dit algoritme was specifiek afgestemd op de omstandigheden die verwacht worden in de beoogde klinische 3D

AHM-toepassing (**Hoofdstuk 6**). Met gemeten MIMU data en met synthetisch gegenereerde UWB-afstandsschattingen, gemodelleerd op met referentiesysteem VICON gemeten positedata in combinatie met gemeten UWB-foutstatistieken, werd het voorgestelde UMIMU-fusiealgoritme gevalideerd onder verschillende niveaus van bias en random foutcomponenten in de UWB afstandsschatting. De voorgestelde datafusie benadering bleek integratiedriftfouten in de positiebepalingen grotendeels te elimineren; slechts minimale restdriftfouten tussen UWB-updates bleven bestaan, wat resulteerde in gemiddelde positiebepalingsfouten van ongeveer 6 cm met een standaarddeviatie van 3 cm, wanneer de UWB-afstandsmetingen minder dan 1 cm bias en 5 cm ruis bevatten (Dit zijn waarden zoals nu haalbaar met de voorgestelde Distance-Bias Calibration-methode uit **Hoofdstuk 4**).

Het geïntegreerde systeem bleek belangrijke hiaten uit de literatuur aan te pakken door de UWB-nauwkeurigheid te verbeteren (via kalibratie), de robuustheid van positiebepaling te versterken (via zwermoptimalisatie), en driftvrije stabiliteit te leveren via sensorfusie. In **Hoofdstuk 7** werden de behaalde resultaten en implicaties voor toekomstige klinische applicatie in 3D AHM besproken in termen van nauwkeurigheid, consistentie en praktische integratie. Hoewel de nauwkeurigheid nog onder de benchmarks van de gouden standaard ligt, maken de behaalde redelijke nauwkeurigheid en hoge consistentie het systeem veelbelovend voor toekomstige toepassingen zoals valrisicobeoordeling, revalidatiemonitoring en onbegeleide training, hetgeen verder onderzoek rechtvaardigt. Prioriteiten voor vervolgonderzoek zijn in grote lijnen duidelijk en een start hiermee is al gemaakt in nieuwe projecten. Naast het verder verbeteren van nauwkeurigheid en consistentie is een belangrijk onderwerp het onderzoeken van de performance bij toepassing op het menselijk lichaam met speciale aandacht voor de effecten van (tijdelijke) NLOS-situaties en het vermijden hiervan of het compenseren hiervoor.

Samengevat kan worden gesteld dat dit proefschrift vooralsnog de haalbaarheid onderschrijft van een geïntegreerd, draagbaar UWB/MIMU-sensorsysteem voor klinische 3D AHM met consistente, driftvrije positiebepalingen. Hoewel nog geen kant-en-klare aanvulling, of vervanging, is gerealiseerd voor laboratorium gebaseerde 3D AHM, is met deze studie een belangrijke stap gezet op weg naar daadwerkelijke toepassing van draagbare sensortechnologie in de klinische praktijk.

ACKNOWLEDGEMENTS

My PhD journey began even before my official start date in December 2020. It all started with a simple coffee and a conversation at Roessingh Research and Development (RRD), a year before, during my Master's studies at the University of Twente (UT). Then, I met **Ir. Chris Baten**, who generously spent hours explaining his work and possible internship opportunities. What began as my internship on calibrating MIMUs soon evolved into my Master's thesis on UWB/MIMU integration for sports player tracking in volleyball. Around this time, Chris had applied for the INSTANT project, and when he suggested that I continue as a junior researcher if the grant came through, I did not hesitate. The enthusiasm I had for working with him and on this topic eventually set the foundation for my PhD.

First and foremost, I would like to express my heartfelt gratitude to **Chris** for giving me my very first opportunity at RRD and later trusting me with the INSTANT project. Thank you for your constant guidance and for your patience with my frequent visits to your office, often armed with new questions or ideas. Our discussions, sometimes stretching well beyond scheduled meetings, were often intense, occasionally argumentative, but always productive, usually ending only when we were both convinced of the solution, or when you got a call about your dinner getting cold. Beyond research, I will fondly remember the lighter moments, such as sharing your passion for photography or hearing stories of your travels, which often turned our meetings into photo-viewing sessions. One of the highlights of my PhD journey was traveling together to Japan for the 3DAHM conference, followed by our adventure exploring the country, an experience filled with fun, learning, and memories I will always cherish. Working with you has been a privilege, and I have learned immensely from both your expertise and your enthusiasm.

I am deeply grateful to my promoters, **prof. dr. Jaap H. Buurke** and **dr. ir. Bert-Jan F. van Beijnum**, for their support and guidance throughout my PhD. **Jaap** was a steady source of encouragement, ensuring that I remained aligned with the project's goals and clinical relevance. He often helped me maintain focus on the main goals while still exploring new ideas. I would also like to acknowledge **prof. dr. ir. Peter H. Veltink**, who was initially one of my promoters. In the early stages of my PhD, his thoughtful feedback and critical reviews of my manuscripts were invaluable in shaping them into publishable articles. Due to his increasing commitments, he stepped down midway, after which Bert-Jan kindly took over.

Bert-Jan not only continued to provide constructive feedback but also played the important role of reminding me to remain focused and not attempt to solve every problem I encountered. Together, they have each contributed in their own way to the completion of this thesis, and I am sincerely thankful for their guidance and support.

My gratitude extends to the members of my graduation committee: **prof. dr. A. Cereatti**, **prof. dr. J.H. Van Dieën**, **prof.dr.ir. G.J.M. Krijnen**, and **prof.dr.ir. J.R. Buitenweg** for kindly agreeing to be part of the committee, to review my dissertation, and for providing constructive feedback that improved this thesis further.

The INSTANT project would not have been possible without the collaboration between all four partner organizations: UT, Saxion, Gabel Systems, and Topvorm Twente. I thank them all for their contributions. My closest collaboration was with Gabel, where I had the privilege to work closely with **Carsten**. From him, I learned a great deal about electronic subsystems, firmware development, and also about the process of introducing products to market, an area in which I initially had little background. I am also grateful to **Neik** and **Adhitya** at Gabel, who helped in the development of the integrated UWB/MIMU sensor system used in my research.

I would like to thank my students who played a central role in shaping parts of this thesis. **Lisanne**, my very first student, worked on her Master's thesis under my supervision, and her efforts contributed significantly to this research. **Jan Willem** and **Thomas** joined later as interns, and both of them were instrumental in carrying out the experimental characterization of the UWB system. Working with the three of you was a truly rewarding and educational experience for me, and I learned as much from supervising you as you hopefully did from the projects themselves. I would also like to thank the other students, **Stephan**, **Thijs**, and **Jos**, for their contributions, whom I supervised in smaller parts of the projects. Your involvement and support in different aspects helped me move this work forward.

At RRD, I was fortunate to work with many supportive colleagues. I would like to first acknowledge **Leendert**, our Lab/technical manager, for his patient help whenever I faced firmware issues with the UWB or was stuck with software debugging. Our technical discussions often sparked new ideas and solutions. His

support in setting up lab measurements was also invaluable. Next, I thank **Erik**, our manager and now the scientific director, for his support and ensuring timelines were met. Thanks to **Jos** and **Wendy** for their ICT support, and specifically, Jos provided his expertise in 3D printing and designing, which helped me improve my skills in 3D design and rapid prototyping. I also extend my thanks to **Inger**, our enthusiastic secretary (now retired), and **Briggett** for being approachable and always ready to help. Finally, I would also like to thank all my other colleagues at RRD for their support, collaboration, and the many ways in which they made my time at RRD an enjoyable and enriching experience.

My fellow junior researchers at RRD made the workplace enjoyable and motivating. Thanks to my wonderful roommates at different points in time, **Robert, Cindy, Kira, and Bouke** made the PhD journey less lonely, even during COVID, when opportunities to be in the office were limited. Thanks to **Bouke**, my paranymph, for the interesting talks and for sharing the unforgettable story of his trek. I will also fondly remember the wine tastings organized by **Lena** and **Cindy**, which were always full of good conversations and a welcome break from research life. I also cherish the coffee breaks, dinner-outings, borrels, and lunch walks shared with **Bouke, Robert, Cindy, Lena, Kira, Marian, Eline, Luca, and Jule**. And of course, the *Integration to the Netherlands & RRD* booklet you all gifted me at my farewell has become my go-to reference guide 😊. Thank you all once again for the wonderful memories.

Although I was not working full-time at the UT, I would also like to thank those at UT who supported me during my PhD. **Sandra**, the secretary, was always approachable and quick to help with all kinds of questions regarding formalities and administration, and I truly appreciated her responsiveness. **Frodo** provided valuable support as well, particularly through his clear presentation on the MDR, which helped me understand the regulatory aspects relevant to my work.

Beyond my academic and professional environment, I am deeply thankful to my friends and family, whose constant support has carried me through this journey. My friends and home away family, currently living in the Netherlands, **Anand** (my other paranymph), **Jegan, Visshnu, Nivedha, Castro, Praveen, Junia, Surya, Kowshik, Nithin, CK, Ashwini, Uthvag, and Priya**, have been a source of

encouragement from the very beginning. In fact, it was **Anand** who first convinced me to apply for a Master's at the University of Twente, setting me on the path that eventually led to this PhD, and my move to the Netherlands. Also, his enthusiasm and outgoing nature introduced me to many of the wonderful friendships I now cherish for life. **Jegan** and **Visshnu** were great travel companions who were pushing me to go on trips to relax, though I suspected they planned to have a free travel planner and designated driver 😊. Together, we shared unforgettable adventures to Iceland, Luxembourg, Croatia, and beyond, trips that were much-needed breaks amidst the hectic PhD workload. I also fondly remember the many board game nights and dinners with **Praveen** and **Junia**, which were always full of laughter and good conversations.

I am also especially grateful for the support of my closest friends back home, namely, **Dinesh, Sudarsan, Arjun, and Raghul**. Their companionship, long phone calls, and small trips provided comfort and encouragement during difficult times. **Dinesh**, in particular, often reminded me how far I had already come, which was always reassuring at times of feeling low or when doubts crept in. **Arjun's** periodic phone calls brought laughter, and his enthusiasm for organizing group calls and planning trips was always motivating, though we all knew it was unlikely to happen 😊. I would also like to extend my thanks to all my other friends from SRM, with whom I share countless memories and whose friendship has continued to support and inspire me throughout this journey.

I sincerely thank my parents-in-law, **Krishnakumar and Jayanthi**, for their encouragement and support throughout this journey. Above all, I am forever indebted to my parents, **Vijayakumari (Mother) and Yogesh (Father)**, for their unconditional love, prayers, and motivation. My mother, in particular, kept a close watch on my PhD progress, often demanding regular updates and checking deadlines more strictly than my supervisors. As a teacher, she always encouraged me to pursue what I truly enjoyed, and it was her push towards curiosity and investigation that led me to take part in school research projects and later embark on a research career. My father has been a constant source of motivation, whose confidence in my abilities and steady encouragement gave me the strength to persevere through challenges. Both my parents have been the foundation of my

journey, and without their support, I could not have reached this milestone. I also extend my heartfelt thanks to all my extended family members for their love, encouragement, and unwavering belief in me.

Finally, my deepest gratitude goes to my wife and best friend, **Sanchana**. She is not only my partner in life but also my collaborator in the INSTANT project at UT, where we had the unique opportunity to work together. Our journey together has been long and special, spanning over 12 years, growing from friends to partners, and now to a married couple. Along the way, we have supported and shaped each other, both personally and professionally. Throughout this journey, she played many roles, from offering professional support in the project to providing unwavering personal encouragement in every phase of my life. She has always believed in me, encouraged me when I doubted myself, and stood by me with love and patience. She has been the most important person in both my life and my PhD journey, and without her support, this thesis would not have been possible.

To all who have been part of this journey (mentors, colleagues, friends, and family), I thank you for shaping not only this thesis but also the person I have become along the way. It is indeed a long list, and I apologize if I have unintentionally missed mentioning anyone by name. Please know that your support, whether big or small, has been woven into every step of this journey, and without it, I would not be standing here today.

ABOUT THE AUTHOR AND
PUBLICATIONS

Vinish Yogesh was born in Vythiry, Kerala, India, in 1996. He earned his Bachelor of Technology in Biomedical Engineering from SRM University, Chennai. As part of a semester-abroad program, he completed his bachelor's thesis at Harvard Medical School in the Division of Engineering in Medicine, where he worked on point-of-care diagnostic devices and lab-on-a-chip systems. He continued working in medical device innovation as a Project Associate at Healthcare Technology Innovation Centre (IIT-Madras), Chennai, where he contributed to the development of various low-cost and portable medical devices, aimed at making healthcare more accessible in remote parts of the world.



In 2018, he moved to the Netherlands to pursue a Master's in Biomedical Engineering with specialization in bio-robotics at the University of Twente. His studies were fully supported by the Orange Tulip Scholarship from Nuffic, which also covered his living expenses, making the program completely funded. Alongside his degree, he completed an additional Honours program in Design Thinking. During his Master's thesis assignment at Roessingh Research and Development (RRD), he worked on sensor fusion for sports tracking applications and came across an opportunity for doctoral research that resonated with his background and interests in medical device development. From 2020, Vinish carried out his PhD research as a Junior researcher (Biomedical Engineer) at RRD, also as a PhD candidate at the University of Twente. His doctoral work focused on the development of wearable sensor systems, advanced signal processing, and sensor fusion for clinical human movement analysis and rehabilitation applications. His work combined algorithm development with experimental validation in clinical and real-world settings, contributing to innovations in wearable healthcare technology.

Vinish has a strong passion for medical device development and aims to continue working on technologies that bring healthcare solutions closer to patients. Beyond research, he loves to travel, explore new technologies, and has a particular interest in following aviation technology and safety developments. He also enjoys sharing experiences with friends and colleagues, embracing the diversity of people and ideas he has encountered throughout his journey.

Journal publications

Yogesh, V.; Grevinga, L.; Voort, C.; Buurke, J.H.; Veltink, P.H.; Baten, C.T.M. Novel calibration method for improved UWB sensor distance measurement in the context of application for 3D analysis of human movement. *Engineering Science and Technology, an International Journal* **2024**, 58, doi:10.1016/j.jestch.2024.101844.

Yogesh, V.; Rook, J.W.A.; Keizers, T.; Voort, C.; Buurke, J.H.; Veltink, P.H.; Baten, C.T.M. UWB distance estimation errors in (non-)line of sight situations within the context of 3D analysis of human movement. *Engineering Research Express* **2024**, 6, doi:10.1088/2631-8695/ad7e7e.

Yogesh, V.; Buurke, J.H.; Veltink, P.H.; Baten, C.T.M. Integrated UWB/MIMU Sensor System for Position Estimation towards an Accurate Analysis of Human Movement: A Technical Review. *Sensors* **2023**, 23, doi:10.3390/s23167277.

Submitted for publication

Yogesh, V.; Beijnum, B.J.V.; Buurke, J.H.; Veltink, P.H.; Baten, C.T.M. Position Estimation with integrated UWB/MIMU sensors in relevance to 3D Analysis of Human Movement.

Yogesh, V.; Beijnum, B.J.V.; Buurke, J.H.; Baten, C.T.M. Position estimation based on UWB swarm optimization and comparison against traditional trilateration.

Conference contributions

Yogesh, V.; Rook, J.W.A.; Keizers, T.; Voort, C.; Buurke, J.H.; Veltink, P.H.; Baten, C.T.M. Comprehensive Study of UWB Distance Estimation Errors in LOS and NLOS Caused by the Human Body in 3D-AHM Scenario (Oral Presentation), *18th International Symposium of 3D Analysis of Human Movement* **2024**, Montevideo, Uruguay.

Yogesh, V.; Buurke, J.H.; Beijnum, B.J.V.; Veltink, P.H.; Baten, C.T.M. Position Estimation with a Swarm of Integrated UWB/MIMU Sensors within the Context of 3D Analysis of Human Movement (Oral Presentation), *18th International Symposium of 3D Analysis of Human Movement* **2024**, Montevideo, Uruguay.

Yogesh, V.; Grevinga, L.; Voort, C.; Buurke, J.H.; Veltink, P.H.; Baten, C.T.M. Novel distance estimate calibration procedure for Ultra-wideband sensor swarm: Towards stable and accurate clinical application in movement analysis (Oral Presentation), *17th International Symposium of 3D Analysis of Human Movement 2022*, Tokyo, Japan.

Yogesh, V.; Grevinga, L.; Voort, C.; Buurke, J.H.; Veltink, P.H.; Baten, C.T.M. Optimal ranging calibration in a swarm configuration of INSTANT integrated ultra-wideband / MIMU sensors for accurate and stable position estimation (Oral Presentation), *9th World Congress of Biomechanics 2022*, Taipei, Taiwan.

Yogesh, V.; Grevinga, L.; Buurke, J.H.; Veltink, P.H.; Baten, C.T.M. Novel technical calibration of ultra-wideband sensors: A step towards accurate and stable human movement analysis (Poster Presentation), *EEMCS day - University of Twente 2022*, Netherlands.

Yogesh, V.; Lankhorts, T.; Baten, C.T.M. Automated monitoring of load exposure and coping in the context of performance in volleyball (Oral Presentation), *8th Dutch BME Conference 2020*, Netherlands.

PROGRESS RANGE

The following publications have been published in the Progress range by Roessingh Research and Development, Enschede, the Netherlands. Copies can be ordered, when available, via info@rrd.nl.

1. Pot, J.W.G.A., Boer H., van Harten, W.H., Hermens, H.J., Seydel, E.R. Comprehensive Need-Assessment. Ontwikkeling van een meetinstrument voor zorgbehoeften en kwaliteitsbeoordeling door patiënten. September 1994, ISBN 90-25452-01-22
2. Van Leerdam, N.G.A., Hermens, H.J. Revalidatietechnologie in Euregio. July 1995, ISBN 90-75452-02-0
3. Duda, L., van Noort, L.O., Röseler, S., Greitemann, B.O.I., van Harten, W.H., Klazinga, N.S. Rehabilitation in Germany and the Netherlands, A comparison of two rehabilitation systems. August 1995, ISBN 90-75452-03-9
4. Hermens, H.J., Nene, A.V., Zilvold, G. Electrophysiological Kinesiology, Proceedings of the 11th congress of the International Society of Electrophysiology and Kinesiology in Enschede, the Netherlands 1996. October 1996, ISBN 90-75452-04-7
5. Van Harten, W.H. Bouwen aan een kwaliteitssysteem in de revalidatiezorg. Een poging tot constructieve technology assessment van een kwaliteitssysteem in een gezondheidszorginstelling. December 1997, ISBN 90-75452-07-1
6. Baardman, G., IJzerman, M.J. Design and evaluation of a hybrid orthosis for people with paraplegia. November 1997, ISBN 90-75452-8-X
7. Hutten, M.M.R. Lumbar Dynamometry: A useful method for assessment of patients with chronic low back pain? November 1999, ISBN 90-75452-13-6
8. Van der Salm, A., van Harten W.H., Maathuis, C.G.B. Ketenkwaliteit Cerebrale Parese Zorg. Een beschrijving van de cerebrale parese zorg en mogelijke verbeteringen hierin. April 2001, ISBN 90-75453-19-5
9. Nederhand, M.J. Muscle activation patterns in post traumatic neck pain. March 2003, ISBN 90-75452-27-6
10. Jannink, M.J.A. Usability of custom-made orthopaedic shoes in patients with degenerative disorders of the foot. September 2004, ISBN 90-75452-28-4
11. Blokhorst, M.G.B.G. State-dependent factors and attention in whiplash associated disorder. January 2005, ISBN 90-365-2111-4
12. Buurke, J.H. Walking after stroke. Co-ordination patterns & functional recovery. February 2005, ISBN 90-365-140-8
13. Van der Salm, A. Spasticity reduction using electrical stimulation in the lower limb of spinal cord injury patients. October 2005, ISBN 90-365-2253-6
14. Snoek, G.J. Patient preferences for reconstructive interventions of the upper limb in tetraplegia. December 2005, ISBN 90-365-2255-2
15. De Kroon, J.R. Therapeutic electrical stimulation of the upper extremity in stroke. December 2005, ISBN 90-365-2269-2
16. Van Dijk, H. Motor skill learning, age and augmented feedback. March 2006, ISBN 90-365-202-9

17. Mes, C.A.J. Improving non-optimal results in chronic pain treatment. January 2007, ISBN 90-365-2435-0
18. Voerman, G.E. Musculoskeletal neck-shoulder pain: a new ambulant myofeedback intervention approach. March 2007, ISBN 90-365-2460-1
19. Kallenberg, L.A.C. Multi-channel array EMG in chronic neck-shoulder pain. March 2007, ISBN 90-365-2459-8
20. Huis in 't Veld, M.H.A. Work-related neck-shoulder pain. The role of cognitive-behavioural factors and remotely supervised treatment. December 2007, ISBN 978-90-365-2584-8
21. Fleuren, J.F.M. Assessment of spasticity. From EMG to patients' perception. October 2009, ISBN 978-90-365-2869-6
22. Reenalda, J. Dynamic sitting to prevent pressure ulcers in spinal cord injured. October 2009, ISBN 978-90-365-2884-9
23. Prange, G.B. Rehabilitation robotics. Stimulating restoration of arm function after stroke. October 2009, ISBN 978-90-365-2901-3
24. Vos-van der Hulst, M. Prognostic factors and underlying mechanisms in chronic low back pain. February 2010, ISBN 978-90-365-2881-8
25. Kottink-Hutten, A.I.R. Assessment of a two-channel implantable peroneal nerve stimulator post-stroke. February 2010, ISBN 978-90-365-2959-4
26. Van Weering, M.G.H. Towards a new treatment for chronic low back pain patients. Using activity monitoring and personalized feedback. May 2011, ISBN 978-90-365-3305-8
27. Gulmans, J. Crossing boundaries. Improving communication in cerebral palsy care. February 2012, ISBN 978-90-365-3305-8
28. Molier, B.I. Influence of augmented feedback on learning upper extremity tasks after stroke. March 2012, ISBN 978-90-365-3293-9
29. Dubbeldam, R. Towards a better understanding of foot and ankle kinematics in rheumatoid arthritis. The effects of walking speed and structural impairments. October 2012, ISBN 978-90-365-3407-9
30. Evering, R.M.H. Ambulatory feedback at daily physical activity patterns. A treatment for the chronic fatigue syndrome in the home environment? April 2013, ISBN 978-90-365-3512-0
31. Malhorta, S. Does spasticity interfere with functional recovery after stroke? A novel approach to understand, measure and treat spasticity after acute stroke. November 2013, ISBN 978-90-365-2567-0
32. Tabak, M. Telemedicine for patients with COPD. New treatment approaches to improve daily activity behaviour. February 2014, ISBN 978-94-6108-590-0
33. Trompetter, H.R. ACT with pain. Measurement, efficacy and mechanisms of Acceptance and Commitment Therapy. September 2014, ISBN 978-90-365-3708-7
34. Op den Akker, H. Smart tailoring of real-time physical activity coaching systems. October 2014, ISBN 978-90-365-3762-9
35. Jansen-Kosterink, S.M. The added value of telemedicine for physical rehabilitation. December 2014, ISBN 978-90-823196-0-6

36. Velstra, I.M. Advanced insights in upper limb function of individuals with cervical spinal cord injury. December 2015, ISBN 978-90-365-3929-6
37. Kloosterman, M.G.M. Keep on rolling. Functional evaluation of power-assisted wheelchair use. June 2016, ISBN 978-90-365-4299-9
38. Prinsen, E.C. Adapting to change. Influence of a microprocessor-controlled prosthetic knee on gait adaptations. December 2016, ISBN 978-90-365-4206-7
39. Wolvers, M.D.J. A coach in your pocket. On chronic cancer-related fatigue and physical behavior. March 2017, ISBN 978-90-365-4299-9
40. Cabrita, M. Active and pleasant ageing supported by technology. November 2017, ISBN 978-90-365-4407-8
41. Haarman, J.A.M. TIBAR. Therapist Inspired Balance Assisting Robot. November 2017, ISBN 978-90-365-4407-8
42. Nijenhuis, S.M. Roll up your sleeves! Technology-supported arm and hand training at home after stroke. April 2018, ISBN 978-90-365-4510-5
43. Cranen, K. Acceptance of telerehabilitation in chronic pain: the patients' perspective. June 2018, ISBN 978-90-365-4555-6
44. Boerema, S.T. Sensing human activity to improve sedentary lifestyle. September 2018, ISBN 978-90-365-4604-1
45. Radder, B. The wearable hand robot. Supporting impaired hand function in activities of daily living and rehabilitation. November 2018, ISBN 978-90-365-4658-4
46. Krabben T. A reaching hand. Towards an active therapeutic device for the upper extremity following stroke. December 2018, ISBN 978-90-365-4660-7
47. Timmerman, J.G. Cancer rehabilitation at home. The potential of telehealthcare to support functional recovery of lung cancer survivors. January 2019, ISBN 978-90-4701-7
48. Nikamp-Simons, C.D.M. The sooner the better?! Providing ankle-foot orthoses in the rehabilitation after stroke. May 2019, ISBN 978-90-365-4747-5
49. Achterkamp, R. Towards a balanced and active lifestyle. June 2019, ISBN 978-94-6323-656-0
50. Engbers, C. Keep Cycling. How technology can support safe and comfortable cycling for older adults. September 2019, ISBN 978-90-365-4848-9
51. Ommeren, A.L. Offering a helping hand. Getting a grip on needs and preferences of stroke patients regarding soft-robotic technology supporting hand function. October 2019, ISBN 978-90-365-4835-9
52. Ter Stal, S. Look who's talking. Appearance of embodied conversational agents in eHealth. March 2021, ISBN 978-90-365-5126-7
53. Beinema, T.C. Tailoring coaching conversations with virtual health coaches. December 2021, ISBN 978-90-365-5260-8
54. Hurmuz, M. Z. M. eHealth-In or out of our daily lives?: Measuring the (non-) use of eHealth in summative evaluations. June 2022, ISBN 978-90-365-5360-5
55. Broekhuis, M. Meet my HUBBI: he's an expert on eHealth usability. September 2022, ISBN 978-90-365-5443-5

56. Schulte, R. V. Up to one's knees in data: Data-driven intent recognition using electromyography for the lower limb. December 2022, ISBN 978-90-365-5486-2
57. Bessler-Etten, J. Safety first in rehabilitation robots! Investigating how safety-related physical human-robot interaction can be assessed. January 2023, ISBN 978-90-365-5503-6
58. Zandbergen, M. A. Moving forwards by going outside: Inertial measurement unit-based monitoring of running biomechanics. February 2023, ISBN 978-920-365-5513-5
59. Marotta, L. Development of inertial sensor-based methods to assess physical fatigue in running applications. February 2023, ISBN 978-90-365-5507-4
60. Tenniglo, M. J. Stiff knee gait in stroke: Walking down the road of different treatment options. December 2023, ISBN 978-94-6419-964-2
61. Oberschmidt, K. Who, When, How - Guiding the active involvement of stakeholders in eHealth Action Research. January 2024, ISBN 978-90-365-5866-2
62. Rikhof, C. Stimulating rehabilitation - A new hybrid rehabilitation device combining robot and functional electrical stimulation for early stroke rehabilitation. December 2024, ISBN 978-90-365-6353-6
63. Brandl, L. Guiding older mourners from online self-help to offline support using algorithmic mental health monitoring. January 2025, ISBN 978-90-365-6436-6
64. Yogesh, V. Towards Accurate 3D Analysis of Human Movement: An Integrated UWB/MIMU Approach. December 2025, ISBN 978-90-365-6990-3

